U.PORTO
FEUP FACULDADE DE ENGENHARIA
UNIVERSIDADE DO PORTO

DEPARTAMENTO DE ENGENHARIA MECÂNICA

BULK TEMPERATURE IN POLYMER-METAL HYBRID GEARS

DIOGO MIGUEL PROENÇA ROCHA

2017

DIOGO MIGUEL PROENÇA ROCHA

BULK TEMPERATURE IN POLYMER-METAL HYBRID GEARS

A DISSERTATION SUBMITTED TO THE
FACULDADE DE ENGENHARIA DA UNIVERSIDADE DO PORTO
FOR THE *PROGRAMA MESTRADO INTEGRADO EM ENGENHARIA MECÂNICA*

Supervisor: Doctor Carlos M. C. G. Fernandes
Co-supervisor: Professor Jorge H. O. Seabra

DEPARTAMENTO DE ENGENHARIA MECÂNICA
FACULDADE DE ENGENHARIA
UNIVERSIDADE DO PORTO

To the memory of my uncle Orlando.

Abstract

The use of polymer in power transmissions is growing fast mainly due to the possibility to work without lubrication, resulting in lighter and cheaper power transmission mechanisms. However, there are some disadvantages, such as polymers' lower heat conductivity and mechanical resistance, hindering its widespread use. In fact, the heat generated by the rubbing surfaces of meshing gears will increase the operating temperature and, therefore, reduce gears life and mechanical resistance. An appropriate solution to the problem consists in using polymer-metal hybrid-gears, enhancing heat conduction by including a metallic insert, obtaining gears with higher load carrying-capacity and efficiency.

This thesis presents the conceptualization, construction and implementation of a Finite Element Method (FEM) model suitable for the calculation of the load carrying capacity of polymer gears, as well as the validation of the results from the model with experimental data from literature.

The concept of thermal contact resistance in the polymer/metal interface is described for the implementation of the hybrid-gear model. The goal is to evaluate the influence of a polymer-metal hybrid-gear on bulk temperature and to conclude if it gives better results than standard polymer gears. Some simulations of gears in dry contact conditions are presented, to allow the comparison with and without metal insert.

The FEM model presented allows to calculate the load carrying capacity of polymer gears whose mechanical properties are critically dependent on the bulk temperature.

Resumo

O uso de engrenagens poliméricas em transmissões de potência tem vindo a crescer devido principalmente à forte possibilidade de trabalhar sem lubrificação, resultando num mecanismo mais leve e acessível. No entanto, existem algumas desvantagens no uso deste tipo de engrenagens, como o condutividade térmica dos polímeros e a sua resitência mecanica, evitando assim o seu mais amplo uso. De facto, o calor gerado pelo atrito entre os dois corpos em contacto irá aumentar a temperatura de funcionamento da engrenagem e, consequentemente, resulta numa redução da vida do engrenamento bem como na redução da sua resistência mecânica. Uma solução passará pelo uso de uma engrenagem híbrida polímero-metal, de forma a aumentar a conductividade térmica com a implementação de um inserto metálico, obtendo uma engrenagem com maior capacidade de carga e mais eficiente.

Esta tese irá apresentar a idealização desta engrenagem híbrida, sua construção e a implementação de um modelo de método de Elementos Finitos (MEF) para calcular a capacidade de carga de engrenagens poliméricas, bem como a validação do modelo criado com resultados retirados da literatura.

O conceito de resistância térmica de contacto entre o polímero e o metal irá ser descrito, para a implementação da engrenagem híbrida. O objectivo deste trabalho resume-se na avaliação da influência de uma engrenagem híbrida polímero-metal na temperatura de massa e concluir se são melhores resultados do que as normais engrenagens poliméricas . Alguns resultados considerando condições de contacto a seco em comparação com uma engrenagem inicial sem inserto às mesmas condições de operação são apresentados.

O modelo MEF apresentado permite calcular a capacidade de carga das engrenagens poliméricas, cujas propriedades mecânicas são criticamente dependentes da temperatura de massa.

Keywords

Hybrid Polymer Gear
Bulk Temperature
FEM
Heat Transfer

Palavras chave

Engrenagens híbridas poliméricas
Temperatura de massa
Métodos dos elementos finitos
Transferência de calor

Acknowledgements

The work presented here is also a combination of knowledge and experience of several individuals, who were part of my journey, leaving their contribution and to whom I would like to express my gratitude.

First of all, a special thank to Faculdade de Engenharia da Universidade do Porto, not only has it been my second home for the past 5 years but also the place where I have grown personally and professionally. Moreover, I would like to thank all the professors that contributed for my greater knowledge and wisdom. To Professor Jorge Seabra, who awoke my curiosity in the field of mechanical contact, I would like to thank for the opportunity and support given.

My sincere thanks to Carlos Fernandes for all the interest, the constant help as well as the perfectionism that inspired me during these past five month. Without his guidance this thesis would not be completed.

To the people I knew in CETRIB, who provided the means for this research and welcomed me as one of their own, allowing me to experience an idea of real life work and leading to a continuous learning opportunity.

To all my friends, Catarina Sena Esteves, Filipa Rocha, Ana Costa, Diogo Santos, Mariana Oliveira and Marta Maurício for all the support and the good times that they provided in this journey. A special gratitude goes to my colleague and friend Mário Correia, for his advice, patience and unconditional friendship. To all my friends that one way or another, were present in my life and that made me a better person.

Nevertheless, a special thanks to The LADs for being my support, for all the memories we shared and true friendship during the tough and good times. Without them my graduation as well as my thesis would not be possible.

Last but not least, a final gratitude to my parents, my brother, my future sister in law, my grandmother, my godson, my godmother and all the rest of my family, for all the unconditional support, for all the words, the affection, the comprehension and the love that they gave me. I am eternally grateful to them, specially to my beloved mother, not in the last five years, but in my whole life, taking care of me and making me better every day.

Contents

List of Figures

List of Tables

List of Symbols

Symbol	Description	Units
α	Gear pressure angle	[°]
α_{mix}	Parameter of the evaluation of the amount of oil mixed with air	[-]
α_{1mix}	Thermal Diffusivity	[m^2/s]
β_{k_i}	Heat thermal distribution partition between pinion and wheel	[-]
β_{zb}	Gear base helix angle	[°]
γ_i	Heat generated coefficient that is transfer for the solids	[-]
Γ_i	Basis function	[-]
ϵ	Value for linear convergence tolerance	[-]
ϵ_1	Addendum contact ratio of pinion	[-]
ϵ_2	Addendum contact ratio of wheel	[-]
ϵ_α	Transverse contact ratio	[-]
ε_c	Contact strain	[-]
ε_{st}	Yield strain	[MPa]
ζ	General physical property	[-]
η	Dynamic viscosity	[Pa·s]
ϑ_{pm}	Peak temperature of melting range	[°C]
ϑ_{zul}	Permissible temperature for continuous running conditions	[°C]
κ	Differential operator with no time differentiation	[-]
λ	Volumetric viscosity	[-]
λ_r	Relaxation factor	[-]
μ	Coefficient of friction of teeth	[-]
μ_{mZ}	Average coefficient of friction along the path of contact	[-]
$\mu_Z(x)$	Meshing gear coefficient of friction along the path of contact	[-]
ν	Kinematic viscosity	[cSt]
$\nu_{air,lub}$	Kinematic viscosity of the air or lubricant	[cSt]
ν_{mix}	Kinematic viscosity of the mixture	[cSt]
ξ	Thermal expansion coefficient	[1/K]
ρ	Density	[kg/m^3]
ρ_{redC}	Equivalent contact radius on the pitch point	[mm]
ρ_i	Density for pinion or wheel	[kg/m^3]
ϱ	Relative mean plate separation	[-]
σ	Root mean square (RMS) roughness	[νm]
σ_s	Effective root mean square (RMS) roughness	[νm]
σ_{st}	Yield stress	[MPa]
ϕ	Unknown evolutionary field	[-]
Φ	Vector of values referent to the unknow field ϕ at nodes	[-]
φ_{2h}	Solution on a grid with average spacing $2h$	[-]

Symbol	Description	Units
φ_{4h}	Solution on a grid with average spacing $4h$	[-]
φ_{extra}	Extrapolated solution from Richardson Extrapolation	[-]
φ_h	Solution on a grid with average spacing h	[-]
ψ	Radius of a contact spot	[mm]
ω	Rotational speed	[rad/s]
Δt	Time step interval	[-]
Δ_{T_c}	Temperature drop	[K/°C]
∇	Spatial differential operator	[-]
a	Hertzian contact half-width	[mm]
A	Coefficient matrix of the element discretization	[-]
A_a	Area of apparent contact	[mm^2]
A_{ij}	Stifness matrix	[-]
a_m	Mean contact spot radius	[m]
A_p	Area of real contact	[mm^2]
b	Gear face width	[mm]
$b_{1,2}$	Thermal contact coefficients	[-]
b_A	Constants terms of the linear system	[-]
c	Radius of an elemental heat channel	[mm]
$c_{1,2}$	Vickers microhardness correlation coefficients	[-]
C_c	Dimensionless thermal contact conductance	[-]
c_p	Heat capacity	[J/kg·K]
c_{p_i}	Heat capacity for pinion or wheel	[J/kg·K]
$c_{p_{mix}}$	Heat capacity of mixture	[J/kg·K]
d	Distribution factor of physical properties at gear side	[-]
D	Gear's diameter	[m]
d_i	Pitch circle diameter	[m]
d_{b1}	Base diameter of the pinion	[mm]
d_v	Vickers indentation diagonal	[m]
d_0	Reference diagonal	[m]
e	Gap distance of the insert from gear sides	[mm]
E	Elastic modulus	[Pa]
$E^{'}$	Effective elastic modulus	[Pa]
E_{int}	Internal energy	[J]
f	Blending parameter	[-]
F_{bn}	Normal force on tooth flank	[N]
F_{bt}	Transverse force on tooth flank	[N]
f_{ep}	Elasto-plastic parameter	[-]
F_i	Force vector	[-]
f_N	Gear normal force per unit of contact length in each meshing position along the path of contact	[N/mm]
F_N	Gear normal force at each meshing position along the path of contact	[N]
h	Heat source	[W/kg]
h_c	Heat transfer coefficient at the interface contact	[W/m^2·K]
H_e	Elastic Microhardness	[Pa]
H_{ep}	Elasto-plastic microhardness	[Pa]
h_g	Heat transfer coefficient of gas conduction at gap	[W/m^2·K]
h_m	Final heat transfer coefficient of meshing tooth faces	[W/m^2·K]
$h_m^{'}$	Heat transfer coefficient of meshing tooth faces when meshing	[W/m^2·K]
H_p	Microhardness on softer surface	[Pa]
H_{poly}	Polymer's elastic modulus	[Pa]

Symbol	Description	Units
h_r	Heat transfer coefficient of non-meshing tooth faces	[W/m^2·K]
h_{rad}	Heat transfer coefficient of radiation within gap	[W/m^2·K]
h_s	Heat transfer coefficient of gear sides	[W/m^2·K]
h_t	Heat transfer coefficient of tip-tooth	[W/m^2·K]
h_{tc}	Total heat transfer coefficient at bodies joint	[W/m^2·K]
H_V	Gear loss factor	[-]
$H_V^{Ohlendorf}$	Gear loss factor according to Ohlendorf	[-]
H_{vick}	Microhardness on a surface layer	[μm]
H_{VL}	Local gear loss factor using rigid load distribution	[-]
I	Enthalpy	[J]
i	Gear transmission ratio	[-]
J_i	Jacobian matrix	[-]
k	Thermal conductivity	[W/m·K]
$k_{air,lub}$	Thermal conductivity of air or lub	[W/m·K]
K_{hs}	Constant for better heaviside strech approximation	[-]
k_i	Thermal conductivity for pinion or wheel	[W/m·K]
k_{mix}	Thermal conductivity of mixture	[W/m·K]
k_s	Effective thermal conductivity	[W/m·K]
$l^i(x)$	Single contact line length	[mm]
L	Length of profilometer trace	[m]
m	Module	[mm]
M	Preconditioner matrix	[-]
m_a	Absolute asperity slope	[-]
m_h	Hartnett parameter	[-]
M_{ij}	Mass matrix	[-]
m_s	Effective absolute asperity slope	[-]
n	Rotational speed	[rpm]
N	Total Gauss-Points	[-]
N^n	Solution vector T_j for its n-th nonlinear iteration step	[-]
Nu	Nusselt number	[-]
p	Pressure	[Pa]
P	Apparent contact pressure	[Pa]
$\bar{p}$	Average contact pressure	[Pa]
Pr	Prandlt number	[-]
p_0	Maximum hertz contact pressure	[Pa]
p_b	Gear base pitch	[mm]
P_{IN}	Gearbox input power	[W]
p_{ord}	Order of the numerical method used	[-]
P_{VD}	Shaft seals power loss	[W]
P_{VL}	Rolling bearings power loss	[W]
P_{VZ0}	Load independent meshing gears power loss	[W]
P_{VZP}	Load dependent meshing gears power loss	[W]
Pr_{mix}	Prandlt number of mixture	[-]
q	Heat flux at contacting joint	[W/m^2]
q_{max}	Maximum instantaneous meshing gears heat flux per unit area on the contact area	[W/m^2]
q_s	Distribution of instantaneous meshing gears heat flux per unit area on the contact area	[W/m^2]
q_{VZP}	Instantaneous meshing gears heat flux per unit area	[W/m^2]
$\bar{q}_{VZP}$	Meshing gears heat flux per unit area averaged over one revolution	[W/m^2]

Symbol	Description	Units
r	Arbitrary radius on the gear side surface	[m]
R	Relative norm	[-]
r_a	Radius of the addendum circle	[m]
r_{den}	Factor between grids densities	[-]
R_q	Root mean square average surface roughness (DIN 4768)	[μm]
R_s	Thermal contact resistance at contact spot	[m^2·K/W]
R_{tc}	Thermal contact resistance	[m^2·K/W]
R_X	Equivalent radius in rolling direction	[m]
Re	Reynolds number	[-]
Re_{mix}	Reynolds number of mixture	[-]
S_f	Material yield/flow stress	[Pa]
SRR	Slide-to-Roll ratio	[%]
T	Absolute temperature	[K]
t	Gap distance from tooth-tip	[mm]
t_f	Time factor	[1/m]
$T_{flash,max}$	Absolute maximum flash temperature	[K]
t	Time	[s]
T_{air}	Temperature of the air	[°C]
T_{amb}	Initial ambient temperature	[°C]
T_B	Absolute bulk temperature	[K]
T_{exp}	Initial oil/wall temperature	[°C]
T_i	Temperature value at iteration cycle i	[-]
T_j	Solution vector	[-]
T_{mix}	Absolute temperature of the mixture oil/air	[K]
T_{oil}	Temperature of the oil	[°C]
T_w	Absolute temperature of the gear wall	[K]
$\vec{u}$	Convection velocity	[m/s]
u_i	General variable at iteration cycle i	[-]
U_S	Entrainment speed	[m/s]
U	Velocity on x direction	[m/s]
v	Circumferential velocity	[m/s]
V	Velocity on y direction	[m/s]
$\dot{V}$	Flow rate lubrication	[l/min]
$v_{\Sigma C}$	Sum of the rolling velocities on the pitch point	[m/s]
$v_{1,2}$	Velocity of the heat source along each tooth face	[mm/s]
v_g	Sliding speed	[m/s]
V_l	Element volume	[m^3]
v_{r_i}	Rolling velocity for pinion or wheel	[m/s]
v_{tb}	Absolute tangential speed on the plane of action	[m/s]
vw	Insert vertical width	[mm]
W	Velocity on z direction	[m/s]
w_t	Tooth width	[mm]
w_x	Insert horizontal width	[mm]
x	Meshing contact position along the path of contact	[mm]
X_L	Coefficient of friction lubricant parameter	[-]
xa	Discretization of each position of the Hertzian band-width over the contact area	[m]
y	Separation of surface and mean plate	[m]
z_1	Number of teeth of pinion	[-]

Chapter 1.

Introduction

1.1. Thesis purpose

The use of polymeric gear for power transmission has been increasing over the years, although with lower mechanical resistances than metal materials such as steel. Some advantages like the possibility of dry running and good vibration damping could increase the adoption of this material for gears.

However, the heat generation problem due to friction between the teeth of the two polymer gear (calculated with the help of a power loss model already validated), along with plastic's low thermal conductivity, can increase the operating temperature of the gear and, therefore, decrease the gear's life and mechanical resistance. In fact, plastic's mechanical properties are dependent on temperature, its load capacity decreasing with increasing temperature.

New hybrid gears, a combination between polymeric and metal gears, have been created to solve the problem. Moreover, the hybrid-gears have already been used in aeronautic, military and even automotive applications [1, 2] to decrease the weight and increase the efficiency of the system [3].

For the study of the advantage of using a hybrid-gear, a study of the temperature distribution/bulk temperature of a gear for certain operating conditions is essential since the field of application of plastic gears is very small due to thermal/load limitations.

The requirement of studying and calculating the load carrying capacity of polymer gears with the reduction of maximum temperature of the gear is essential to for that cause. Therefore, being the main purpose of this thesis the study the influence of the bulk temperature with the implementation of a metallic insert in a polymeric gear (polymer-metal hybrid gear), the creation of a Finite Element Method (FEM) model to perform an analysis on any gear tooth geometry is then necessary to compare with normal steel gears.

As a final outcome, it is intended to show that it is possible to improve heat evacuation and gear life using an hybrid gear concept.

1.2. Tasks Chronogram

The task chronogram, summarised in Table 1.1, was mainly a framework for the beginning of this thesis as well as fixing the objectives to accomplish during the dissertation.

Table 1.1.: Total weeks expected for each task

Task	**Period** [weeks]
Study the state of the art in polymer gears, hybrid gears and heat transfer FEM models	≈ 3
Validate a bulk temperature FEM model for gears with experimental results from literature	≈ 6
Simulate a polymer gear with metallic insert in order to reduce contact bulk temperature	≈ 6
Results analysis and dissertation	≈ 5
Total weeks	≈ 20

1.3. Thesis outline

Chapter 2, entitled **Polymeric Gears**, summarizes, briefly, the use of gears currently, advantages and disadvantages when using polymeric gears, problems and a possible solution.

Chapter 3, entitled **Heat transfer model for gear teeth**, is a review about the load dependent power loss model as well as the theoretical thermal model construction with an analysis of the different heat transfer coefficients and boundary conditions. The concept of flash temperature is presented as an introduction to bulk temperature and the study of transient and steady-state simulations.

Chapter 4, entitled **Model Implementation**, reviews of all the softwares used for the FEM model construction as well as a brief explanation of how the different programs work and their function in the created FEM model.

Chapter 5, entitled **Model Validation**, presents the validation of the numerical results of the FEM model with experimental data from literature.

Chapter 6, entitled **Hybrid Gears**, presents the concept of a polymer gear with a metallic insert. An introduction to the thermal contact concept as well as several metallic insert simulations, in order to reduce the operating temperature, are presented. The main drawback of polymeric gears, discussion of these results and

study of different insert profiles are also included. Finally, a study of the influence of mesh size on the numerical error.

Chapter 7, entitled **Conclusions and future work**, presents the final conclusions of the thesis and suggests possible future work.

Chapter 2.

Polymeric Gears

The study of the heat transfer mechanisms within polymeric gears (with the use of a FEM model) is the major focus of this dissertation. This first Chapter will summarize polymer characteristics, their advantages and disadvantages over typical metallic gears as well as subsequent problems and a new solution (hybrid-gear) in order to reduce the operating temperature, the main drawback of using polymeric gears.

2.1. Polymeric gears in industry

The use of polymer gears is growing fast due to their potential advantages over typical metallic gears: cheaper mass production, operation without lubrication (or so called lubricated for life), interesting for non-lubrication applications (automotive industry, office machines, food industry, textile industry, etc.) [4–6].

2.1.1. Advantages and disadvantages of plastic gears

In fact, if the main objective of the mechanical designer/projector is to have a stronger tooth bending resistance the polymeric gear solution is not always the best solution. However, if dry contact, lower noise or functioning in a corrosive environment are required, the polymeric gear is a very good solution.

The main advantages and disadvantages are listed in Table 2.1.

Naturally, due to the expansion of today's technology a obligation to enhance the performance of machinery is increasing, therefore, improving certain physical characteristics of the mechanism. So, improving the use of polymeric gear can lower the total final weight of mechanism (since they are 1/6 to 1/7 of a steel gear), lower the cost production, lower noise and vibration damping as well as an higher energetic efficiency at the final mechanism. Moreover, if working in an hostile environment (chemical corrosive) polymer gears become the first choice to these applications, for example, it is unsuitable the use of lubricants or metal components in medical applications [3].

Table 2.1.: Advantages and disadvantages of polymeric gears.

Advantages	**Disadvantages**
Possibility of dry contact (lubricated for life)	Lower mechanic resistance
Lower noise	Low heat resistance
Good vibration absorption	High hygroscopicity
Corrosion-proof	Shorter life
Low cost on mass production	Poor thermal conductibility

Table 2.2.: Examples of some polymer properties on typical running conditions [8].

Polymer	ρ [g/cm^3]	ϑ_{pm} [°C]	ϑ_{zul} [°C]	σ_{st} [MPa]	ε_{st} [%]	E [MPa]
PA66	1.13-1.16	225-265	80-100	85/60	5/20	3000/1600/800
PET	1.38-1.40	250-260	100	55-80	4-7	2100-3100
POM	1.39-1.43	164-175	90-100	60-75	15-50	2600-3200

However it is important to notice that polymer mechanical properties are considerably inferior when compared with metal, preventing its wide use; having a Young's modulus that can be 1/75, a tensile strength of about 1/7 and a thermal conductivity of about 1/80 that of steel. Also, temperature drastically changes the mechanical properties of plastics: elastic modulus, tensile strength and even water absorption rate [7].

Some properties are listed in Table 2.2, with a range of values taking into account the normal service conditions. The properties listed are the density (ρ), the peak temperature of melting range (ϑ_{pm}), permissible temperature for continuous running conditions (ϑ_{zul}), yield stress (σ_{st}), yield strain (ε_{st}) and elasticity modulus (E).

The fact that a polymer part is wet, moist or dry has a huge influence over the yield modulus and yield strength as shown in Figure 2.1 [8].

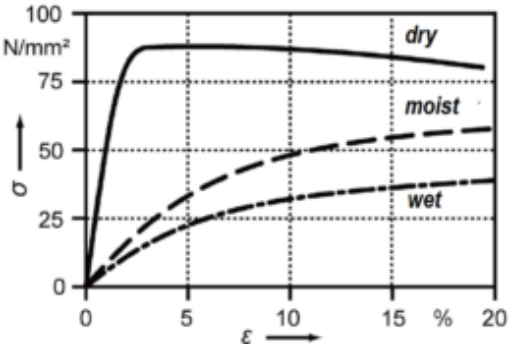

Figure 2.1.: Stress-strain curve for PA66 for dry, wet and moist polymer [8].

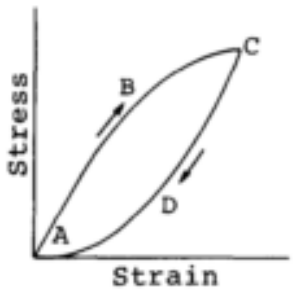

Figure 2.2.: Hysteresis loop of plastic [7].

Since plastic are a visco-elastic materials, certain amount of time is needed in order that they return to their original shape after the load being removed, which results in the tooth's deformation hysteresis loop shown in Figure 2.2. This hysteresis will contribute for the recuperation time of the gear due to the viscosity dissipation [7].

2.1.2. Engineering plastics

The variety of plastic gears used can be divided according to the type of monomers used to build up the polymeric chain and the links between them. Therefore, it is possible to have:

- *"General purpose engineering plastics"* (or E.P.) - with heat resistant temperature of at least 100°C, tensile strength of at least 49 MPa and Young's modulus of at least 2.4 GPa. This type of polymer is used in industrial applications, namely, for structural and mechanical members;

- *"Super-Engineering plastics"* (or S.P.) - suitable for applications where the highest temperatures reach 150°C.

Moreover, the E.P. typically used can be of two types: a thermosetting resin and a thermoplastic resin, both being generally used since they are low-priced gear materials and having a strong strength and heat resistance. In fact, the application of thermosetting resins as well as of thermoplastic resins, such as Polyamide (Nylon or PA) and Polyacetal (POM), is increasing [7].

If the main goal is to lower costs as well as reduce weight, plastic gears have been the tendency for enhancing performance; be it with the application of composite plastic gear with E.P. filled with solid lubricants, for instance carbon fibers, or with S.P.

2.1.3. Manufacturing of plastic gears

The process chosen for the manufacturing of plastic gears depends on gear material, on desired quantity, size and geometry. The most used is injection moulding.

Injection Moulding

If the desired production volumes are big injection moulding is the ideal process. A major limitation is the processing of the final wall thickness. During moulding injection, the shrinkage of the semi-crystalline plastic depends on the wall thickness: for a larger wall thickness, a longer heating cycle is required and more defects will result as a consequence [8].

Casting

Another manufacturing process used is the casting process, which is suitable for gears with large dimensions, although only a few polyamides and polyrethane elastomers can be casted using this process.

Machining

The machining process is used for small and medium series since the tool cost are lower when comparing to injection moulding. The method is the same as for metal gears, this is: gear forming (by milling or broaching) and gear generation processe (hobbing).

2.2. Life-time for plastic gear

The life of gear is dependent on the gear geometry, materials, load torque, gear materials combination, speed, operating temperature, lubrication, etc [8, 9]. The increase the life of the polymeric gears is possible by either reduce the wear on the tooth or decrease the temperature.

The study of a thermal limit for the use of polymers in gears is usually done at a constant maximum power for a certain application [10–14], such as the case of the VDI 2736 method to compare the influence of the tooth geometry on load carrying capacity and life of plastic gears. However, the tooth geometry can be optimized in order to reduce heat dissipation and, consequently, increase the allowable operating temperature [10] and, therefore, maximize the operating life.

2.3. Failure modes for plastic gears

2.3.1. Tooth Temperature

As the subject study of this dissertation is the study of bulk temperature, the tooth temperature is an important subject since the raise in temperature during the contact of the meshing surfaces of the two gears could lead to the degradation of the polymer's mechanical properties, such as stiffness, as well as the reduction of the load capacity. In addition to the poor thermal conductivity of the polymer which tends to evacuate less heat when compared with other materials.

Although the temperature distribution in a plastic gear varies slightly with the kind of plastic being used, the highest temperature tends to be located near the pitch point (where the mechanical resistance is substantially low or due to the temperature increase), as represented in Figure 2.3, where the rolling contact occurs, rather than near the root or tip of the tooth, where the fastest sliding takes place. This distribution field is well explained due to the tooth deformation hysteresis, since the heat is released faster at the tip and at the root because the cooling is easier in these areas [7].

The heat generation in these types of mechanical transmission is essentially due to friction between gear teeth [15–17].

Plastics have high hygroscopy (the capacity of attracting and holding water molecules from surroundings) and also high variation of their mechanical properties

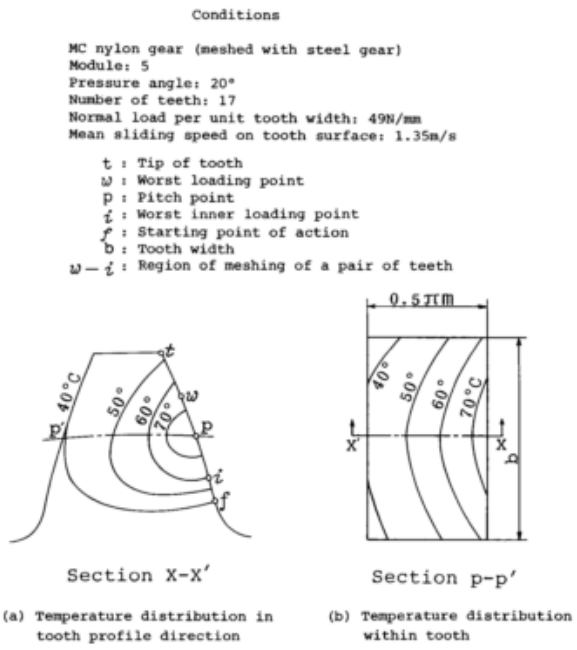

Figure 2.3.: Temperature distribution in tooth profile and within the tooth [8].

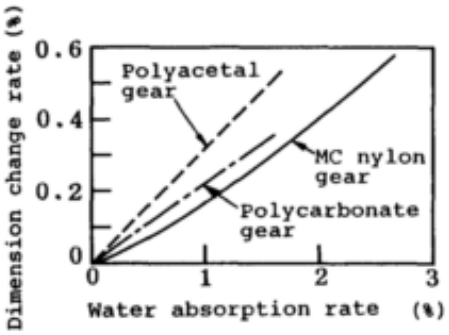

Figure 2.4.: Water absorption rate and volume increase rate of plastic gears [7].

with temperature, so that it is crucial to realize the role of the temperature in the lubrication phenomena to achieve greater load capacity [10–13].

This water absorption capacity results in a reduction of their mechanical resistance as the volume increases (this rise is given in percentage relatively to the initial plastic body) [8].

When comparing, for example, a POM (polyacetal) and a PA (nylon) gear, the dimension change rate is lower for the PA, although they are highly hygroscopic, as shown in Figure 2.4. The POM gear is preferable for runs underwater due to its low hygroscopy when compared to PA [7]. Furthermore, it is important to consider the dilation of the original solid form with the increase of temperature that aggravates the effect of hygroscopy.

Nevertheless, there are some positive effects with the temperature rise, since the absorption of vibrations capacity increases as well [8].

2.3.2. Tooth deflection

As explained earlier the stiffness of a plastic is much lower than steel (almost 1/75 lower) and the tooth deflection must be taken into account.

Taking an example from literature [7], shown at Figure 2.5, as the static load P acts on the plastic gear the tooth deflects more than 30 μm and if the application of the load continues this deflection even increases to 40 μm. If the plastic gear does not suffer a large load during a long time that it is possible after a certain time the deflection decreases and reaches 0, returning to the initial state. However, if the load is large and the time of application is also big a permanent deformation could occur - meaning that the deflection does not reach 0 after the removal of the load.

Figure 2.5, representing the curvature of tooth deflection for POM and for PA, shows that due to the POM's inferior Young's modulus when compared to PA, the POM tooth will experience a greater deflection than the PA one. However, POM

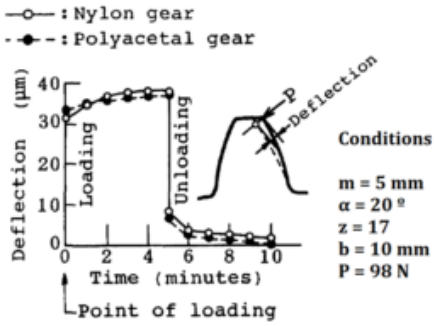

Figure 2.5.: Deflection curve of plastic tooth [7].

has as lower viscosity than PA, so after a certain time, the POM's tooth shows a smaller deflection that the PA tooth.

2.3.3. Wear on plastic gears

Mao et al. [18] proved, with POM, PA and steel gears, that the wear on plastic gears depends a lot on the materials used for the drive/driven combination.

In the cases of POM/POM (or A/A) and PA/PA (or N/N) the wear could be divided into three phases:

- Initial running in - short period, where the wear that occurs is considerable;
- Nearly linear - period where the wear increases progressively until reaching a critical value;
- Final fracture - period after reaching the critical value, and wear rate increases drastically leading to failure.

In fact fracture in plastic gears only occurs when the larger load acts on the addendum flank due to the abnormal wear (which appears near the root of plastic tooth) and the tooth material becomes soft (which is caused by the increase in temperature by rubbing). The abnormal wear of the tooth flank grows between the inner worst point to the root point, spreading to the pitch point and, finally, reaching the outer worst point. As for the normal wear only occurs in between the outer worst point and the tip point [5].

It is understood that the severe wear appears near the root, where the specific sliding speed is large. Moreover, plastic gears mechanical strength decreases with the rise of tooth temperature, so it is becomes difficult to estimate their lives [5].

The number of load cycles to failure have strong dependency on the torque load applied. For a low torque the wear seems to never cause fracture, achieving, therefore, a higher number of load cycles (more than 10^7 cycles). However, when the number of

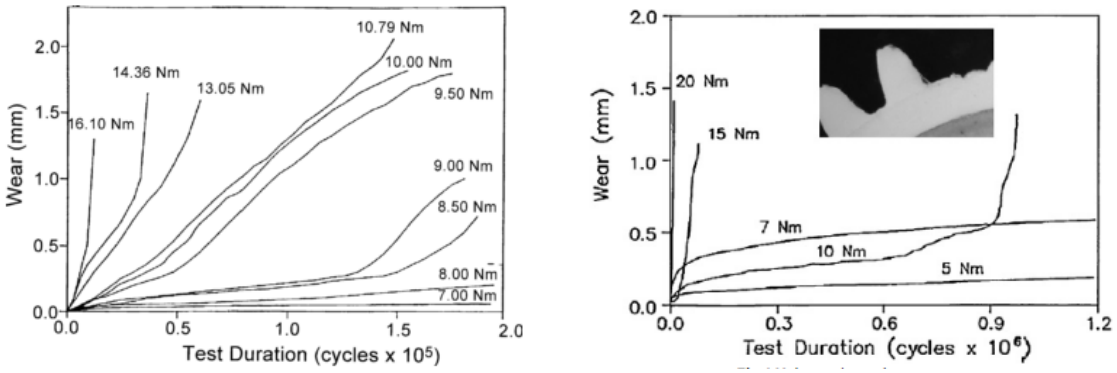

(a) Acetal against acetal.

(b) Nylon against nylon.

Figure 2.6.: Wear on plastic gears at 1000 rpm [18].

loads is less than 10^6 the main life period seems to depend only on the load applied, as the fracture occurs at the pitch point at the driving gear, shown in Figure 2.6.

The combination of PA/POM (nylon driving gear and acetal driven gear) gives similar results when compared with POM/POM combination. However the POM/PA combination resulted in an increase in life of the gear by about 5 times, for the example suggested in [18] with 1000 rpm and 10 Nm as shown in Figure 2.7. (where the horizontal axis corresponds to the life time cycles (10^6)).

When using a plastic gear as wheel and a steel gear as pinion the life of the plastic gear is longer, since the wheel teeth have more time to dissipate heat than the ones from the pinion, resulting on a lower tooth temperature [19].

The direction of sliding speed is different on the driven and on the driving gear (Figure 2.8b), resulting on a wear damage also different (Figure 2.8a). Because of the direction of tooth action in the driven gear is from the side of the tip of the tooth and from the side of the root to the pitch circle, the damage near this pitch

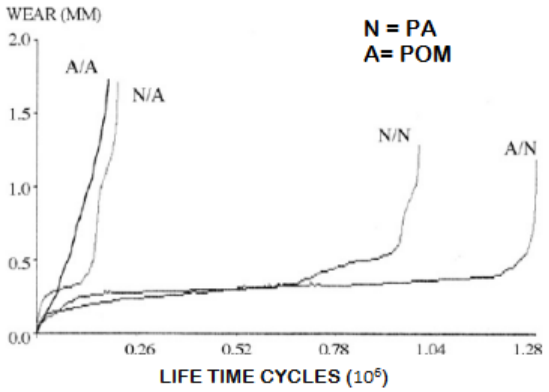

Figure 2.7.: Influence of changing the pair drive/driven gear materials [18].

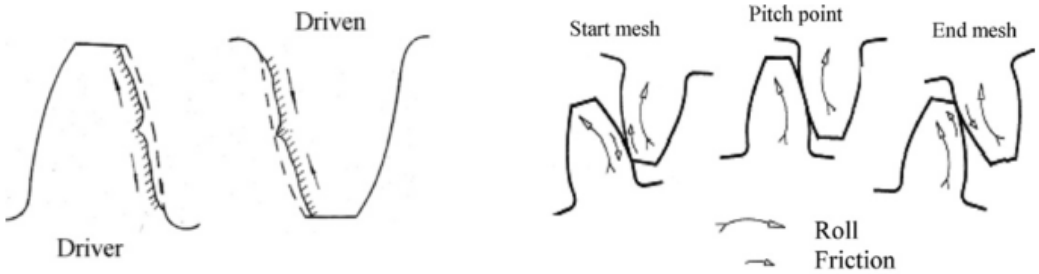

(a) Gear surface wear forms.

(b) Gear rolling/sliding.

Figure 2.8.: Resulting gear surface wear and gear rolling/sliding [20].

circle does not occur.

When combining different materials for the combination of driven/driver gears the lower wear resistance material should be placed as the driven gear.

2.3.4. Failure types and causes

Plastic gear life can be influenced by many factors, some of the common failure modes and causes are listed in Table 2.3.

2.3.5. Lubrication

In fact the lubrication of plastic gear is not as well understood as that of steel gears, since normally when a plastic gear is chosen over a metallic one is, it is due to the possibility of working in dry contact. In this dry run it is possible to work with internal lubricants (fillers) or without internal lubricants. However, there is also the possibility of working with externally lubricated polymeric gears.

Table 2.3.: Failure types and causes [8].

Damage	**Cause**
Partial Melting	Excessive heating of the tooth flanks
Tooth root fracture	Too high stresses
Tooth flank fracture	High Hertzian pressures, combined bending stresses
Pitting	High Hertzian pressure
Tooth wear	Low wear resistance
Tooth deformation	Excessive deformation - high loads

Table 2.4.: Fillers for internal lubrication and its effects [8].

Fillers	**Positive Effects**	**Negative Effects**
Glass, carbon and aramide fibers	Increase of stiffness Tensile Strength Bending	Reduces impact resistance
PTFE	Reduces friction	Reduces impact resistance Decreases bending capacity
PE	Reduces Friction	Reduces impact resistance
Graphite and Boron nitride	Reduces friction Increases thermal conductivity	Reduces impact resistance
Silicone oil	Reduces friction Reduces hardness	
Mineral fillers	Increases thermal conductivity	

Fillers

One major disadvantage linked to the adoption of polymer gears, and the leading problem with its use, is related to the poor thermal conductivity of these materials [5]. The addition of specific additives such as fibres, graphene or carbon nano-tubes can improve the heat conductibility (some effects are listed in Table 2.4), although some attention must be taken into account for the use of this fillers since the benefit of using with a auto-lubricated condition (low coefficient of friction, for instance) fades [21, 22].

Greases

When using synthetic greases, corrosion and volume increase due to moisture absorption are no problem, although the use of mineral greases tends to be better at high pressures. Moreover,the main problem of temperature increase does not affect negatively the grease's lubrication parameters, although it must be guaranteed that the lubricant adheres firmly to the contacting surface and the maximum speed does not exceeds the 5m/s [8].

Oils

The lubricant must be chosen accordingly to the operating temperature of the gears. Synthetic base oils are suitable for use with low operating temperature. Some oils/lubricants suggested by VDI 2736 are shown in Table 2.5.

It is important to take into account the polarity of the lubricant chosen, since the polar polymeric gears should only be lubricated with nonpolar base oils. For

Table 2.5.: Lubricant and operating temperature [8].

$\vartheta_{operating}$ [°C]	Lubricants
$[-80, 20]$	Synthetic base oils
$[20, 60]$	Mineral oils
$[60, 100]$	PAO, ester oils
$[100, 120]$	Ester oils, Silicone oil, PFPE

instance, the POM and PA gears, being polar thermoplastics, the use of non-polar base oil is recommended [8]. In fact, the polarization occurs when a solid material is placed inside an electric field, resulting in electric charges at the surface of the body.

To reduce the effect of the hygrocopy higher viscosity oils must be used since they are less able to penetrate the polymeric gear.

2.4. Solutions

Auto-cooling method

When talking about plastic gears, the temperature reached by the frictional contact between surfaces can be very high and, therefore, cooling the gear is very important. However, normal auto-cooling may not be enough when in presence of high loads and high power losses, so a method by Tsukamoto was suggested to enhance the auto-cooling effect.

Figure 2.9 represent the auto cooling method developed by Tsukamoto, which consists in drilling small holes between the teeth and allowing air to go inside the holes due to the gradient of pressures during rotation and blowing against the tooth flank, increasing the number of cycles from 10^6 to more than 10^7.

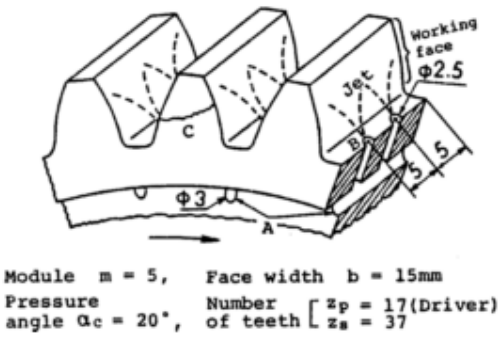

Figure 2.9.: Auto-cooling method by Tsukamoto [19].

Hybrid Gears

In order to solve the above stated problems an innovative design in gear application is needed, taking into consideration the best tooth geometry for the reduction of the power loss and heat generation, the best gear design (allowing the possibility of using new material) and a lower manufacturing process cost than typical machined gears.

In fact, new hybrid gears with metallic inserts on the polymer that increases significantly the heat conduction are already being developed and tested, lowering the operating temperature and, therefore, increasing load capacity for a wider range of application of polymer gears. In the aeronautic, military and automotive fields, gears with metallic tooth and polymeric body [1, 2] have been used, because of the possibility of using lighter material, as the system inertia is drastically reduced, and of having a more responsive and efficient system [3].

As a first approach to this concept of hybrid-gears: the construction of a compound gear with polymeric teeth and a metallic insert/metallic gear-body will improve heat conduction in the gear (and, consequently, better heat removal) and the reduction and control of operating temperature of the polymer at the contact zone and, therefore, the increase of gear life and mechanical resistance.

The first idea of the body of the gear will include a polymeric tooth and a metallic gear, as presented in Figure 2.10, offering the possibility of:

- application at higher speeds than normal polymeric gears;
- dry running with low loads and meshing with metallic gears;

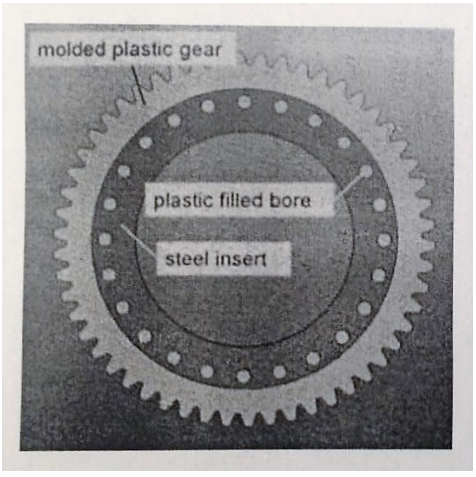

(a) First view.

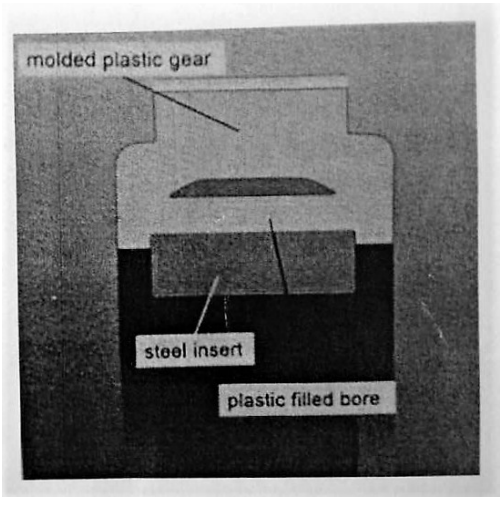

(b) Second view.

Figure 2.10.: Hybrid-gear - metallic gear-body/insert with polymeric gear [14].

- grease lubrication;
- improvement of heat removal and gear's life;
- potential increase in load capacity compared to regular polymeric gears;
- avoiding gear machining.

However, there will be some design challenges at the level of the metallic inserts designs to improve the heat removal as well as the manufacturing challenges due to the modification of the polymer's mechanical properties with the different mould and melt temperatures.

To sum up, this will be the dissertation's purpose: to study bulk temperature distribution on a polymer-metal hybrid-gear and to solve the maximum temperature/gear life problem; thus, to improve the heat evacuation by reducing the maximum and operating temperature and, consequently, raise the operating life time of the gear and mechanical resistance.

Chapter 3.

Heat transfer model for gear teeth

3.1. Introduction

in the previous chapter, polymeric gears' mechanical properties, advantages and problems were generally described, finalizing with a possible solution. Furthermore, in order to study the bulk temperature with the application of the Hybrid-gear solution, it is fundamental to have a notion of the heat transfer and heat generated in the gear when the meshing takes place.

Therefore, the most important task when predicting the bulk temperature on meshing gears is in fact to understand every detail that happens within the gear contact. However, since there is an infinite number of possible combinations of gears, seals, rolling bearings, oils or even operating conditions, there is a large number of variables affecting the power loss and, therefore, its efficiency.

The power loss inside a gearbox can be divided in two major groups that are also branched in other sub-groups, as shown in Figure 3.1 [23]. The first group can be designated as the load dependent losses, directly influenced by the applied load torque, due to gears (P_{VZP}) and rolling bearings (P_{VL}). The second group, labelled as load independent losses, which are dependent on rotating speed, gearbox geometry and oil physical properties, such as its viscosity and density [24]. The power loss due to seals (P_{VD}), rolling bears (P_{VL}) and gears (P_{VZ0}) are load independent losses.

Load dependent power losses, normally, represent the main source of energy

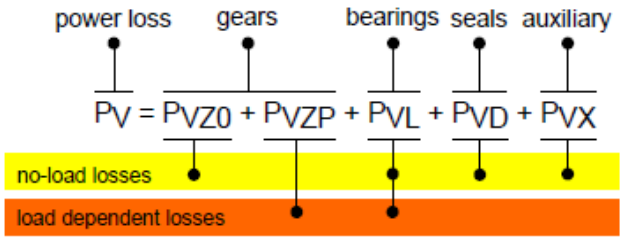

Figure 3.1.: Power loss contributions [23].

dissipation under torques and rotational speeds since the load independent losses have less influence, although with the use of dip lubrication and with very high speeds these last type of losses may have a huge influence.

3.2. Power loss model

When the contact between two gears takes place some amount of energy is dissipated. This energy will consequently decrease the efficiency of the gearbox and can be determined by the power loss model. In fact the load dependent gear losses being the main cause for the heat dissipation by frictional contact this power loss model will only consider them.

3.2.1. Load dependent gear losses - P_{VZP}

The load dependent gear losses can be divided into rolling losses and sliding losses. However, the rolling losses are almost negligible and can be disregarded.

Sliding losses

The most crucial source of power loss in a gear transmission is the contact between meshing teeth, mainly in cases which velocity is not very high. Buckingham [25] introduced the first theoretical approach to calculate the efficiency of meshing gears, assuming a constant coefficient of friction along the path of contact (μ_{mZ}). Afterwards, Ohlendorf [26] was able to develop the following formula for the meshing gears power loss:

$$P_{VZP} = P_{IN} \cdot H_V \cdot \mu_{mZ} \tag{3.1}$$

Where the P_{IN} refers to the input power, the μ_{mz} to the average coefficient of friction and H_V the gear loss factor. This last, gear loss factor (H_V), can be obtained using the Ohlendorf's equation(3.2):

$$H_V^{Ohlendorf} = (1+i) \cdot \frac{\pi}{z_1} \frac{1}{\cos\beta_{zb}} \left(1 - \epsilon_\alpha + \epsilon_1^2 + \epsilon_2^2\right) \tag{3.2}$$

Where i is the gear transmission ratio, z_1 is the number of teeth of pinion, β_{zb} is the gear base helix angle, ϵ_α is the transverse contact ratio, ϵ_1 and ϵ_2 is the addendum contact ratio of pinion and wheel, respectively.

However, the tooth geometry implies a variation of the relative velocity of the surfaces along the path of contact (as shown in Figure 3.3 as well as the direction of sliding on a tooth surface for driver and driven gear in Figure 3.2) [27] and, as sliding speed increases, the coefficient of friction increases too.

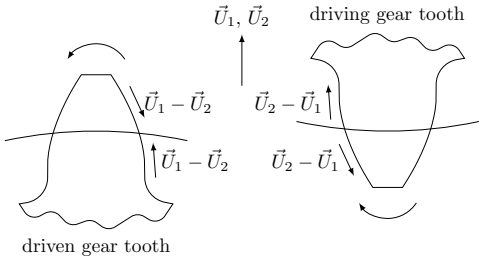

Figure 3.2.: Direction of sliding on a tooth surface [27].

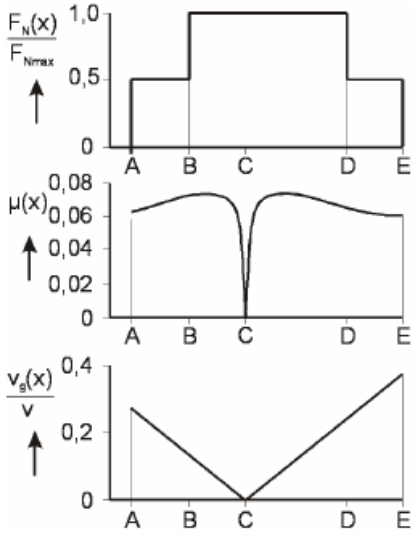

Figure 3.3.: Load, friction coefficient and sliding speed along the path of contact [23].

Considering the coefficient of friction constant along the path of contact is a good approximation. The coefficient of friction becomes close to zero at the pitch point, but the variation of coefficient of friction away from the pitch is very small. Therefore, based on the principle of constant coefficient of friction along the path of contact, Niemann and Winter [28], Henriot [29] and other were able to introduce different approaches for the prediction of load dependent power loss.

Ohlendorf's gear loss factor [26] is the most used to calculate the gear loss factor, in fact it is based on the load distribution at the path of contact between spur gears and is described by equation (3.3) and Figure 3.3 [23].

$$F_N(x,y) = F_{bn} \cdot \frac{1}{\sum_{i=1}^{n} l^i(x,y)} \tag{3.3}$$

Where the F_N is the gear normal force at each meshing position along the path of contact, taking into consideration the F_{bn} (normal force on tooth flank), the l^i single contact line length for both x and y directions.

The power loss at each point can be calculated and by integrating we can obtain

the power loss along the path of contact, according to equation (3.4).

$$P_{VZP}(x) = F_N(x) \cdot v_g(x) \cdot \mu_Z(x) \tag{3.4}$$

Coefficient of friction for lubricated contacts

If the coefficient of friction is considered as constant value along the path of contact (μ_{mZ}), the power loss can be calculated by equation (3.5).

$$P_{VZP} = \mu_{mZ} \cdot P_{in} \cdot \underbrace{\frac{1}{p_b} \int_0^b \int_A^E \frac{f_N(x,y)}{F_{bt}} \cdot \frac{v_g(x,y)}{v_{tb}} \quad \mathrm{dxdy}}_{H_{VL}} \tag{3.5}$$

The last equation is valid for both spur and helical gears with the contribution of the average coefficient of friction (μ_{mZ}), input power (P_{in} - obtained by the product of the transverse force - F_{bt} - on tooth flank and the respective absolute tangential velocity - v_{tb}) and the gear loss factor (H_{VL}) considering only the geometry of the gear tooth [30]. To calculate the local gear loss factor the method proposed by *Marques et al.*, taking into consideration the elastic deformation of the tooth [31], can be used.

More recently, Xu Hai proposed a coefficient of friction based on the results of an EHL model (numerical results) that were validated with experimental traction curves, leading to the function presented on equation (3.6) [32].

$$\mu_Z(x)^{Xu} = e^{f_{Xu}} \cdot p_0^{b2} \cdot |SRR|^{b3} \cdot U_s^{b6} \cdot \eta^{b7} \cdot R_X^{b8} \tag{3.6}$$

Where the the parameter f_{Xu} is calculated by equation (3.7) and the exponents for the Xu equation are presented on Table 3.1.

$$f_{Xu} = b_1 + b_4 \cdot |SRR| \cdot p_0 \cdot \log(\eta) + b5 \cdot \exp(-|SRR| p_0 \log(\eta)) + b_9 \cdot \exp(R_q) \tag{3.7}$$

Xu's equation wasn't able to produce acceptable correlation with experiments, therefore, it was adjusted for the lubricants used leading to a factor written in equation (3.8) and a local meshing gear coefficient of friction as presented at equation (3.9) [33]:

$$\mu_Z(x)^X = X_L^X \cdot \mu_Z(x)^{Xu} \tag{3.8}$$

$$\mu_Z(x)^F = X_L^F \mu_{mZ} \tanh\left(\frac{\varepsilon_\alpha}{\varepsilon_\alpha - 1} \cdot |SRR|(x)\right) \tag{3.9}$$

Table 3.1.: Paramenters for Xu Hai equation.

b1	-8.916465
b2	1.03303
b3	1.036077
b4	-0.354068
b5	2.812084
b6	-0.100601
b7	0.752755
b8	-0.390958
b9	0.620305

Where the average coefficient of friction (μ_{mZ}) along the path of contact is given by Schlenk's equation (3.10) [34], with $X_L = 1$ for non additised mineral oils. The factor $X_L^{X,F}$ needs calibration with experimental results with:

$$\mu_{mZ} = 0.048 \cdot \left(\frac{F_{bt}/b}{v_{\Sigma C} \cdot \rho_{redC}} \right)^{0.2} \eta^{-0.05} \cdot R_a^{0.25} \cdot X_L \tag{3.10}$$

$$X_L^{X,F} = \frac{P_{VZP}^{EXP}}{\frac{1}{p_b} \int_A^E F_N(x)\, v_g(x) \cdot \mu_Z^{X,F}(x) dx} \tag{3.11}$$

Coefficient of friction for dry contacts

One major advantage of using polymeric gears is the option not to use a lubricant. In fact, it is possible to work on a situation of dry contact, where there is no fluid in contact with the two contacting surfaces and the coefficient of friction between the rubbing surfaces has a constant value over the path of contact and only depends on the materials in contact, as we can see in Table 3.2.

Table 3.2.: Dry coefficient of friction (μ) for different materials [9].

Pairing	μ
plastic/steel	0.20
PA/PA	0.40
POM/POM	0.21
POM/PA	0.18
PA/PBT	0.35
POM/PBT	0.18

3.3. Thermal Model

3.3.1. Concept of Flash Temperature

Typically, rubbing surfaces, such as meshing gear teeth and cams, etc., are difficult to understand not only because the heat generation is caused by the frictional energy generated by the sliding motion of the two contact surfaces (proportional to the slide-to-roll ratio), but also because the heat shared by the surfaces in a not known ratio, as explained before on this chapter [35].

The increase of a surface's temperature through the generation of frictional heat caused by sliding action in the contact area between the two rubbing surfaces is defined as the flash temperature. In fact, nowadays, engineers' main focus is to solve the loading and speed problems due to scuffing by selecting properly the material for both surface or even the shape of these rubbing surfaces. Therefore, a simplistic study is not enough for the forecast of the friction coefficient, since the increase in temperature could lead to the destruction of the rubbing surfaces and, therefore, result in adhesion of the surface, for example [35].

3.3.2. Thermal model equations

It is crucial to know the mechanical, physical and rheological properties since their temperature dependency and their affect the contact behavior. Considering a steady state situation, without external heat source and with constant pressure along the film lubricant the energy behavior can be described by the following equation:

$$\begin{aligned}\rho\left[U\left(\frac{\partial E_{int}}{\partial x}\right)+V\left(\frac{\partial E_{int}}{\partial y}\right)+W\left(\frac{\partial E_{int}}{\partial z}\right)\right]+\rho\cdot p\left[U\frac{\partial}{\partial x}\left(\frac{1}{\rho}\right)+V\frac{\partial}{\partial y}\left(\frac{1}{\rho}\right)+W\frac{\partial}{\partial z}\left(\frac{1}{\rho}\right)\right]=\\ \left[\frac{\partial}{\partial x}\left(k\frac{\partial T}{\partial x}\right)+\frac{\partial}{\partial y}\left(k\frac{\partial T}{\partial y}\right)+\frac{\partial}{\partial z}\left(k\frac{\partial T}{\partial z}\right)\right]+\lambda\left(\frac{\partial U}{\partial x}+\frac{\partial V}{\partial y}+\frac{\partial W}{\partial z}\right)^2+\\ +2\eta\left[\left(\frac{\partial U}{\partial x}\right)^2+\left(\frac{\partial V}{\partial y}\right)^2+\left(\frac{\partial W}{\partial z}\right)^2+\frac{1}{2}\left[\left(\frac{\partial W}{\partial x}+\frac{\partial U}{\partial z}\right)^2+\left(\frac{\partial V}{\partial x}+\frac{\partial U}{\partial y}\right)^2+\left(\frac{\partial V}{\partial x}+\frac{\partial W}{\partial y}\right)^2\right]\right]\end{aligned} \tag{3.12}$$

where the four terms represent implicit thermodynamic phenomena, which are convection, adiabatic compression, conduction and viscous dissipation (usually represented by ϕ), respectively. The variables used in the previous equation represent the following physical quantities:

E_{int} - Internal energy;

T - Temperature;

U,V,W - Velocities on x, y and z directions, respectively;

ρ - Density;

η - Dynamic viscosity;

λ - Volumetric viscosity ($3\lambda+2\eta=0$);

k - Thermal conductivity.

For the case of a EHD (Elasto-Hydrodynamic) contact certain approximations are made in order to simplify the problem, such as:

1. The velocity **W** in the contact thickness direction is negligible because of the very small lubricant film thickness (normally less than 1 μm). So, **W=0**

2. The significant velocity gradients only occur at the 0Z direction,according to Reynold's equation. Thus,

$$\frac{\partial U}{\partial x} = \frac{\partial U}{\partial y} = 0 \quad \text{and} \quad \frac{\partial V}{\partial x} = \frac{\partial V}{\partial x} = 0 \tag{3.13}$$

3. The thermal conductivity **k** is constant in the interior of the EHD contact.

Therefore, the energy equation takes the simple from equation (3.14):

$$\rho\left[U\frac{\partial E_{int}}{\partial x} + V\frac{\partial E_{int}}{\partial y}\right] + \rho \cdot p\left[U\frac{\partial}{\partial x}\left(\frac{1}{\rho}\right) + V\frac{\partial}{\partial y}\left(\frac{1}{\rho}\right)\right] = k\left[\frac{\partial^2 T}{\partial x^2} + \frac{\partial^2 T}{\partial y^2} + \frac{\partial^2 T}{\partial z^2}\right] + \eta\left[\left(\frac{\partial U}{\partial z}\right)^2 + \left(\frac{\partial V}{\partial z}\right)^2\right] \tag{3.14}$$

Finally, taking into account that the internal energy (E_{int}) can be described as a function of the enthalpy **I** and considering the thermal expansion coefficient, ξ, the therms ∂E/∂x and ∂E/∂y can be obtained by:

$$\frac{\partial E_{int}}{\partial x} = c_p\frac{\partial T}{\partial x} - \frac{\xi}{\rho}T\frac{\partial p}{\partial x} - p\frac{\partial}{\partial x}\left(\frac{1}{\rho}\right) \tag{3.15}$$

$$\frac{\partial E_{int}}{\partial y} = c_p\frac{\partial T}{\partial y} - \frac{\xi}{\rho}T\frac{\partial p}{\partial y} - p\frac{\partial}{\partial y}\left(\frac{1}{\rho}\right) \tag{3.16}$$

Thus, reorganizing the therms on the last equation, it is possible to obtain the thermal behavior in the case of an Elasto-hydrodynamic (EHD) contact described by equation (3.17):

$$\underbrace{\xi \cdot T \cdot \left(U\frac{\partial p}{\partial x} + V\frac{\partial p}{\partial y} \right)}_{\text{compression}} + \underbrace{\eta \cdot \left[\left(\frac{\partial U}{\partial z} \right)^2 + \left(\frac{\partial V}{\partial z} \right)^2 \right]}_{\text{fluid friction}} =$$

$$\underbrace{\rho \cdot c_p \cdot \left(U\frac{\partial T}{\partial x} + V\frac{\partial T}{\partial y} \right)}_{\text{heat convection}} - \underbrace{k \cdot \left[\frac{\partial^2 T}{\partial^2 x} + \frac{\partial^2 T}{\partial^2 y} + \frac{\partial^2 T}{\partial^2 z} \right]}_{\text{heat conduction}} \quad (3.17)$$

As matter of fact these four terms refer to the fundamental heat transfer modes that occurs in a lubricant film. The first therm represent heating by compression, the second term refers to the heat due to viscosity dissipation and the last ones represents the cooling by convection and by conduction, respectively.

Thermal behavior

As written previously, the heat source of gear meshing is due to the friction heat generated by the relative sliding between the tooth surfaces during meshing. At high speeds significant temperatures will be reached at the points close to the path of the heat source, in a very thin layer, where the heat source will penetrate perpendicularly to the surface.

Assuming a band-shaped heat source with a proper distribution of the heat flux and moving at a uniform speed along the body, as shown at Figure 3.4, the flash temperatures (superimposed on the initial bulk temperature) will have the highest values at the surface affected by the heat source.

In cases of gear teeth, as *H. Blok* described, the flash temperature equation has to take account of the complicated phenomenon of heat partitioning between the meshing tooth faces of the total heat generated. However, at the interface of the two contacting tooth surfaces, at each instant, there should not be a discrepancy in the temperature between the two contacting areas.

The maximum flash temperature can be obtained using equation (3.18)

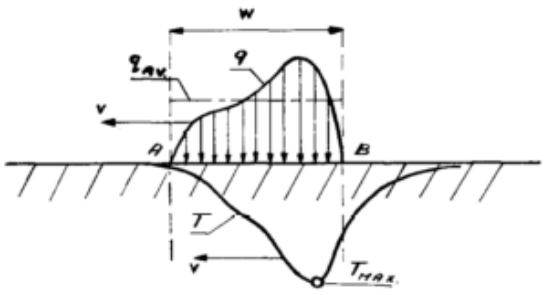

Figure 3.4.: Band-shaped heat source [35].

$$T_{flash,max} = 1.11 \cdot \mu \cdot W \cdot \frac{|b_1\sqrt{v_1} - b_2\sqrt{v_2}|}{w_t} \tag{3.18}$$

Where $W = w_t \cdot \bar{p}$, if the $\bar{p}$ represents the average contact pressure, denotes the load per unit tooth width, b_i are the thermal contact coefficients (calculated at the end of this chapter) and v_i referring to the velocity that the heat source moves along the tooth faces [35].

Furthermore, the heat generated could be divided in two types over time: the bulk temperature and the flash temperature.

Transient Problem

According to energy conservation, Fourier's law and the transient differential equation, the distribution of the three dimensional temperature within the meshing gear is governed by equation (3.19):

$$\underbrace{k \cdot \left(\frac{\partial^2 T}{\partial x^2} + \frac{\partial^2 T}{\partial y^2} + \frac{\partial^2 T}{\partial z^2}\right)}_{\text{Heat Conduction}} = \underbrace{\rho \cdot c_p \left(\frac{\partial T}{\partial t}\right)}_{\text{Transient Therm}} \tag{3.19}$$

Therefore, the flash temperature field is a function of space (x,y and z) and of time (t) - $T = T(x, y, z, t)$. According to Blok the transient term is only observed on the meshing surface, normally called "thermal skin", in fact bellow this skin the transient effect is negligible [35], as discussed previously. However, if the time elapsed after the motion of the heating source is sufficiently high, the temperature distribution registered within the body will be quasi-steady. The last condition is only true if the operating conditions are steady, such as having the heat source per unit time constant.

Steady State (Quasi-steady State)

As said before, if the elapsed time is long enough the temperature solution reached will be quasi-steady, the friction heat generated and the cooling heat dissipation of the gear tend to balance and the temperature change of all the teeth is the same, so the bulk temperature will be space dependent only ($T_B = T_B(x, y, z)$) and the last term at equation (3.19) will be null - $\partial T/\partial t=0$, obtaining:

$$k \cdot \left(\frac{\partial^2 T_B}{\partial x^2} + \frac{\partial^2 T_B}{\partial y^2} + \frac{\partial^2 T_B}{\partial z^2}\right) = 0 \tag{3.20}$$

3.3.3. Boundary Conditions

The bulk temperature solution is assumed to remain constant at any point on the gear as the time required for one revolution of a high-speed gear is much smaller

than the time needed for any change in the gear bulk temperature. In this way, it is possible to infer that the temperature distribution on each gear tooth can be presumed to be equal and only one needs to be analyzed.

In order to solve the above stated differential equations, it becomes indispensable to describe and to determine the boundary conditions for the different surfaces of the single tooth model, shown in Figure 3.5.

A gear is usually lubricated by oil but it can also be unlubricated. Under this circumstances the surrounding medium's temperatures should be adapted accordingly. If oil lubrication is used, the surrounding medium temperature is approximated to be the same as the oil ($T_{mix} = T_{oil}$); as for in case of dry contact, the surrounding medium's temperature is accepted to be the same as the air temperature ($T_{mix} = T_{air}$).

Gear Sides

For the gear sides, **s**, which requires knowledge of the initial temperature of the surrounding and the convective heat transfer coefficient of the gear sides (h_s), the boundary condition is given by equation (3.21).

$$-k \cdot \left.\frac{\partial T}{\partial n}\right|_s = h_s \left(T - T_{mix}\right) \tag{3.21}$$

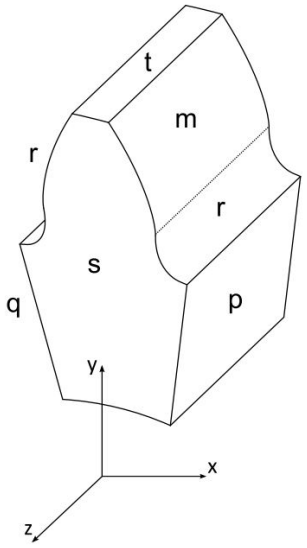

Figure 3.5.: Single Tooth Model.

Non-Meshing Tooth Surfaces

For then non-meshing tooth surfaces, **r**, which also requires the initial oil temperature of the surrounding and the convective heat transfer coefficient of the non-meshing surfaces (h_r)is given by equation (3.22).

$$-k \cdot \left.\frac{\partial T}{\partial n}\right|_r = h_r \left(T - T_{mix}\right) \tag{3.22}$$

Tooth-Tip Surface

For the tooth-tip surface, **t**, which requires knowledge of the temperature of the ambient and the convective heat transfer coefficient for the tooth-tip surface (h_t) is given by equation (3.23).

$$-k \cdot \left.\frac{\partial T}{\partial n}\right|_t = h_t \left(T - T_{mix}\right) \tag{3.23}$$

Meshing Tooth Surface

For the meshing face, **m**, which requires to know the temperature of the surrounding, the convective heat transfer coefficient for the meshing face (h_m) and also the gear power loss (q_{ZVP}) due to friction is given by equation (3.24).

$$-k \cdot \left.\frac{\partial T}{\partial n}\right|_m = h_m \left(T - T_{mix}\right) - q_{VZP} \tag{3.24}$$

Inner Hole of the Gear

For the inner hole of the gear, the interference between the lower part of the gear and shaft, the heat conduction will be neglected and considered an adiabatic surface (∂T/∂n=0), a Neumann boundary condition, due to the faraway distance between the meshing surface and the lower part of the gear.

Tooth Sections

Finally, for the tooth sections, **p** and **q**, assuming the same bulk temperature profile under the steady-state conditions for all the pinion or wheel teeth, a Neumann boundary condition for the temperature gradient along the circumferential direction n on both p and q is imposed, as well as the same temperature for the two sections,

as presented in next equations:

$$T\Big|_p = T\Big|_q \tag{3.25}$$

$$\frac{\partial T}{\partial n}\Big|_p = -\frac{\partial T}{\partial n}\Big|_q \tag{3.26}$$

3.3.4. Heat Transfer Coefficients

The analysis and calculation of the convective heat transfer coefficients is a fundamental point when studying the the gear's temperature distribution. The heat transfer depends on lubrication method and operating conditions.

Gear Sides

For the gear sides the heat transfer coefficient, h_s, will depend on the flow regime. In order to simplify calculations, the gear will be approximated as a rotating disk [36], as shown at Figure 3.6. So, as it depends on the flow regime, the flow along the gear side surface can be divided into laminar and turbulent flow according to the Reynolds number (Re), which is given by equation (3.27):

$$Re = \frac{\omega \cdot r^2}{\nu_{mix}} \tag{3.27}$$

where the ω is the rotational speed, r an arbitrary radius on the gear side surface, ν_{mix} the kinematic viscosity of the fluid.

However, the above calculation would not be accurate for the gear sides since there is a possibility of there being a mixture of oil and air, depending on the lubrication method used. Therefore, when predicting the fluid properties, the following general equation is used for every physical property to be determined.

$$\zeta_{mix} = \alpha_{mix} \cdot d \cdot \zeta_{air} + (1 - \alpha_{mix} \cdot d) \cdot \zeta_{oil} \tag{3.28}$$

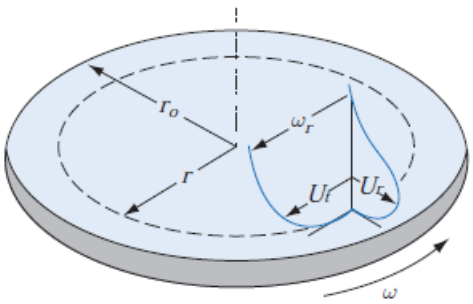

Figure 3.6.: Velocity profile for a rotating disk model [36].

The factor d is the ratio between the arbitrary radius (r) and the radius of the addendum circle (r_a), as shown in equation (3.29). The parameter α_{mix} needs to be determined experimentally and it depends on the operating conditions, for instance on the lubrication method used.

$$d = \frac{r}{r_a} \tag{3.29}$$

However, if a dry contact is used, there is no need to calculate new fluid properties since there is only one fluid - air. Therefore, the properties of the fluid are easily obtained by consulting the Table in Appendix E [37], provided that the initial temperature of air and the external pressure at the gearbox is known.

The heat transfer coefficient can be estimated by using the equation (3.30) proposed by *Hartnett et al.* [38].

$$h_s = Nu \cdot k_{mix} \cdot \sqrt{\frac{\omega}{\nu_{mix}}} \tag{3.30}$$

The Nusselt number (Nu) depends on the Reynolds number of the mixture (Re_{mix}) and the Prandtl number (Pr), given by equations (3.31) and (3.32).

$$Re_{mix} = \frac{r^2 \cdot \omega}{\nu_{mix}} \tag{3.31}$$

$$Pr_{mix} = \frac{\eta \cdot c_{p_{mix}}}{k_{mix}} \tag{3.32}$$

The heat transfer coefficient will be determined according to the flow regime established:

1. The values for **Laminar Flow** ($Re_{mix} < 2 \times 10^5$) are presented in *Hartnett et al*'s work [38], showing the heat transfer coefficient for this regime is independent of radius and is given by equation (3.33) in case of oil lubrication and in case of dry contact conditions equation (3.34) (for Re$<4.3 \times 10^6$) [39, 40].

$$h_s = 0.308 \cdot k_{mix} \cdot (m_h + 2)^{0.5} \cdot Pr_{mix}^{0.5} \cdot \left(\frac{\omega}{\nu_{mix}}\right)^{0.5} \tag{3.33}$$

$$h_s = 0.36 \cdot \frac{k_{air}}{D} \left(\frac{\omega \cdot D^2}{\nu_{air}}\right)^{0.2} \tag{3.34}$$

2. For the **Transition Regime** ($2 \times 10^5 \leq Re_{mix} \leq 2.5 \times 10^5$) the heat transfer coefficient is driven by equation (3.35), based on the measurements of *Boguslawski* and *Popiel* [41].

$$h_s = 10 \times 10^{-19} \cdot k_{mix} \cdot \left(\frac{\omega}{\nu_{mix}}\right)^4 \cdot r^7 \tag{3.35}$$

3. Finally, for **Turbulent Flow** ($Re_{mix} > 2.5 \times 10^5$) the heat transfer coefficient is given by Dorfman's equation (3.36) [42] in the case of oil lubrication while for dry contact situation equation (3.37) (for Re>4.3×10^6) [39, 40] is used.

$$h_s = 0.0197 \cdot k_{mix} \cdot (m_h + 2)^{0.2} \cdot Pr_{mix}^{0.6} \left(\frac{\omega}{\nu_{mix}}\right)^{0.8} \cdot r^{0.6} \tag{3.36}$$

$$h_s = 0.0195 \cdot \frac{k_{air}}{r} \cdot \left(\frac{\omega \cdot r^2}{\nu_{air}}\right)^{0.8} \tag{3.37}$$

The parameter m_h is the exponent in the assumed the wall temperature distribution given by equations (3.38) and (3.39) [38].

$$T_w - T_{mix} = Ar^{m_h} \tag{3.38}$$

$$m_h = \log_r \left(\frac{T_w - T_{mix}}{A}\right) \tag{3.39}$$

where the T_{mix} and the T_w are the ambient temperature and the wall temperature, respectively. These temperature are previously assumed, although the calculation of the tooth wall temperature is an iterative process, the final result is not different by assuming these temperatures.

Non-meshing tooth surfaces

According to *Shunlei* [43], the heat transfer coefficient for the non-meshing tooth surface, h_r, is between half or a third of the maximum value for the heat transfer coefficient of gear sides (h_s) as presented in equation (3.40).

$$\frac{max(h_s)}{3} \leq h_r \leq \frac{max(h_s)}{2} \tag{3.40}$$

Tooth-tip Surface

Based on *Shunlei*'s work [43], the heat transfer coefficient of the gear tip surface, h_t, is the maximum value found on the range of the heat transfer coefficients for the gear sides (h_s) as presented in equation (3.41).

$$h_t = \max(h_s) \tag{3.41}$$

Meshing Tooth Surface

At the meshing tooth surface there will be two different phenomena when the meshing tooth is outside of the contact and when it is actually in contact.

The first one corresponds to most of the time within the gear rotation since the meshing tooth time is very short compared to the gear rotation time. So, the heat transfer coefficient is equal to the non-meshing tooth surface (h_r) during this time. The following principles were adopted: *DeWinter*, *Blok* and *Heijningen* [44–46] suggested, for oil jet lubrication, different heat transfer coefficients should be calculated taking into account the fling-off mechanism.

Nevertheless, the heat transfer coefficient for the meshing tooth while in mesh, $h_{m'}$, will be given by equation (3.42) [47, 48]:

$$h_{m'} = 0.228 \cdot Re^{0.731} \cdot Pr^{1/3} \cdot \frac{k}{d_i} \tag{3.42}$$

where d_i is the pitch circle diameter.

To quantify the time cycle period where the tooth is in mesh the parameter t_f taken into consideration (equation (3.43)):

$$t_f = \frac{1}{z_i} \tag{3.43}$$

where z is the gear number of teeth. Furthermore, the real heat transfer coefficient for the meshing tooth region, h_m , is obtained by equation (3.44):

$$h_m = t_f \cdot h_{m'} + (1 - t_f) \cdot h_r \tag{3.44}$$

3.3.5. Friction Heat Flux

Assuming that all the power loss is converted into heat, so the local heat power generation per unit width is given by equation (3.45):

$$q_{VZP_i}(x) = \gamma_k \cdot \beta_{k_i} \cdot p_0(x) \cdot \mu(x) \cdot v_g(x) \tag{3.45}$$

where γ_k is the amount of heat generated that is transferred to the solids, which generally has its value in the range between 0.9 and 0.95 [49] and β_k is the distribution coefficient of friction heat flux between the contacting bodies (the pinion and the wheel), which can be calculated using the following equation(3.46) [49].

$$\beta_{k_i} = \frac{b_i}{b_1 + b_2}, \text{ with } \quad b_i = \sqrt{k_i \cdot c_{p_i} \cdot \rho_i \cdot v_{r_i}} \tag{3.46}$$

For the quasi steady-state conditions, the bulk temperature was a steady-state temperature field and therefore the average heat flux per unit area, at each point

along the path of contact, was applied according to equation (3.47).

$$\bar{q}_{VZP_i}(x) = \frac{a(x) \cdot \omega_i}{\pi \cdot v_{r_i}} \cdot q_{VZP_i}(x) \tag{3.47}$$

Transient Problem

Due to the relative sliding friction, the heat is generated in the contact area. In fact, the flash temperature rise is generated by the heat, q_s, instantaneously and locally by friction from the speed movement along the path of contact, as shown at Figure 3.7. The distribution of the moving heat source is given by equation (3.48).

$$q_s = q_{max}\sqrt{1 - \left(\frac{x}{a_i}\right)^2} \tag{3.48}$$

where a_i is the Hertzian contact semi-width.

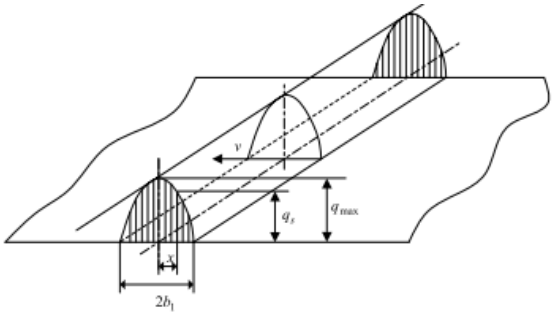

Figure 3.7.: Moving heat distribution on the contact area [50].

Chapter 4.

Model Implementation

4.1. Introduction

In the previous chapter it was described how to theoretically calculate the different heat transfer coefficients, the boundary conditions applied to the different surfaces of the single tooth model and the power loss models to calculate the heat generation due to friction.

This chapter will describe the algorithm implementation, following the flowchart shown in Figure 4.1, as well as a brief explanation of the different software packages used.

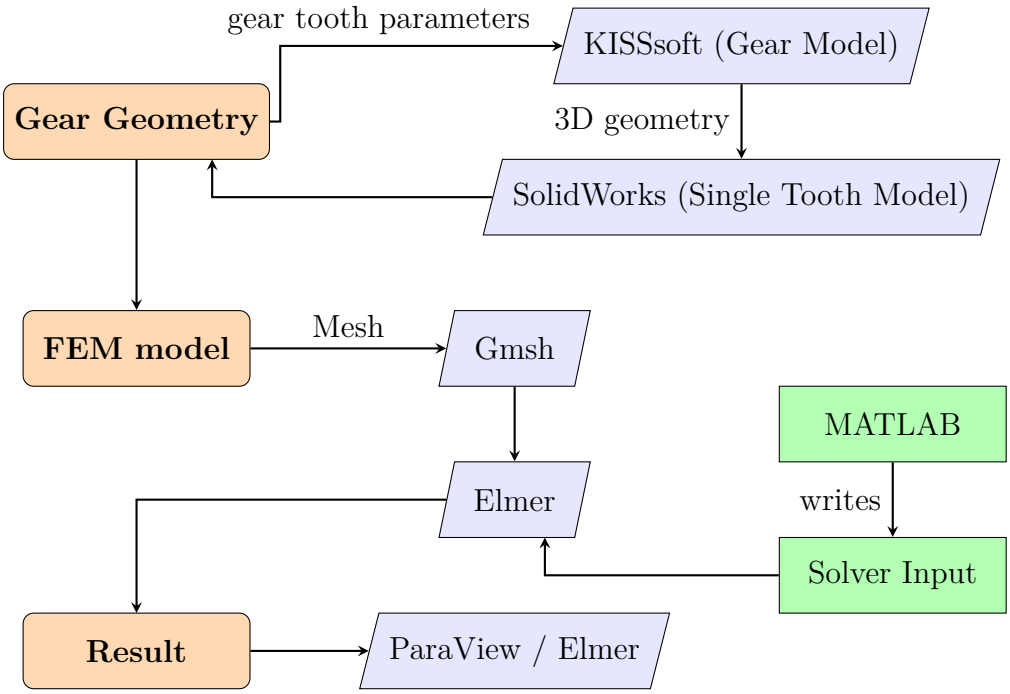

Figure 4.1.: Flowchart of the model implementation used

4.2. Gear Geometry

The creation of the gear geometry will regard the use of the KISSsoft software, for calculation of the gear tooth's parameters and exportat of the 3D gear model to the SolidWorks software, with which the 3D tooth model will be obtained.

4.2.1. Gear Parameters and Model (KISSsoft)

The KISSsoft program works based on the international standards, offering an extensive range of options to optimize the process of dimensioning machinery elements. This program executes a fast and an accurate force calculus and reports with detailed information about safety factors and the equipment safety life [51]. Finally, it offers the possibility to export to any 3D CAD software to easily integrate them into SolidWorks or any other similar package, with a simple STEP file.

This STEP (*"Standard for the Exchange of Product Model Data"*) file, created by ISO (*"International Standard Organization"*), is an uniform standard file that can be read by all CAD softwares. When exporting the file to Solidworks all gears' lines are generated either with polylines or circular approximation or even splines, resulting on the gear model shown in Figure 4.2.

4.2.2. Gear Tooth Model (SolidWorks)

Afterwards, the use of Solidworks is essential since it will be the step to begin the FEM model mesh generation. Solidworks offers features to create the possibility to sketch over a plane and even use the function *"Extrude Cute"* to cut off the excess material. This last function was extremely important for the isolation of the single

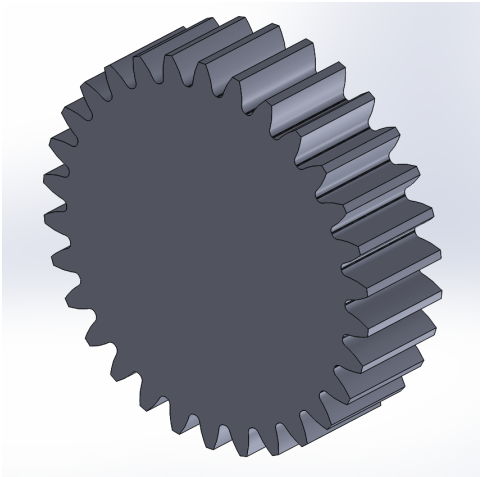

Figure 4.2.: Gear model exported from KISSsoft to SolidWorks.

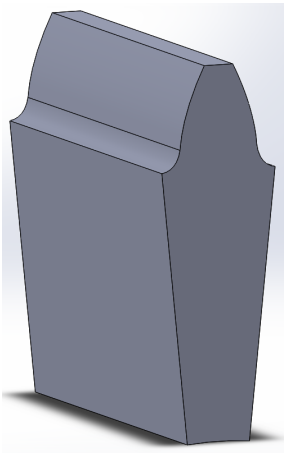

Figure 4.3.: Single tooth model created - SolidWorks.

tooth from the gear along with the creation of the inner diameter, where the shaft will be placed, Figure 4.3.

4.3. FEM model

At the creation of the FEM model used in the simulations, the exported file from Solidworks will be first introduced into Gmsh software for mesh generation. Then with the mesh generated, it is possible to use MATLAB in order to write in the solver input file (SIF), which will be read by ElmerSolver, with different heat transfer and heat frictional fluxes obtained by the created MATLAB function.

4.3.1. Mesh Generation (Gmsh)

The STEP file previously created for a tooth model will look like Figure 4.4 in the Gmsh interface.

Gmsh is an open source software for three-dimensional finite element grid generation with a build-in CAD engine and post-processor. Its main goal is to provide a fast, light and simple meshing tool with parametric input and advanced visualization capabilities.

This program has four main modules: Geometry, Mesh, Solver an Post-Processing, where all the instructions are prescribed either by using the graphical user interface (GUI) or in text files using Gmsh's own language [52].

Gmsh uses the boundary representation to describe geometries, where the models are created in the following order: points, oriented lines (for instance line segments, circles, splines, ...), oriented surfaces (ruled surfaces, plane surfaces, ...) and, finally, volumes.

GEO file

Before starting with the mesh generation directly in the SolidWorks exported STEP file, a GEO file is created to better control in the final grid. This GEO file contains all the coding information of all the points, lines, surfaces and volumes, which will result in the Figure 4.5 on the Gmsh interface. An example of the GEO file coding language generated for the present case is presented in Appendix A. This last file, an ASCII (*"American Standard Code for Information Interchange"*) file, is easily opened and edited with any text editor, includes a set of declarations that allow Gmsh to reconstruct the geometry, effectively allowing the user to save the geometry.

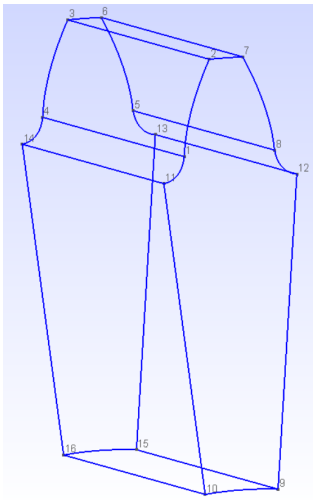

Figure 4.4.: Single tooth model created (STEP) - Gmsh.

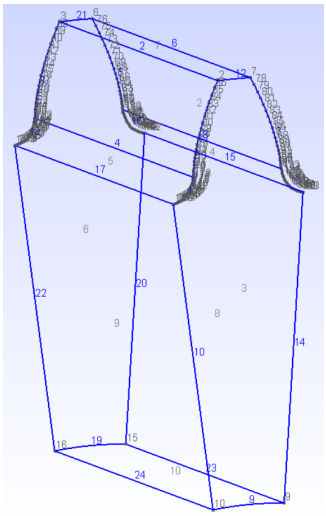

Figure 4.5.: Single tooth model created (GEO) - Gmsh.

Mesh

The finite element mesh is generated by dividing a subset of the three-dimensional space by elementary geometrical elements (lines, triangles, quadrangles, tetrahedra, hexahedra and pyramids).

While in mesh generation there is the need to first discretize lines, then with the line's mesh, it is possible to mesh the surface, and, finally, with the mesh of the surfaces the meshing of volumes is done.

Gmsh's mesh module reorganizes several 1D, 2D and 3D meshing algorithms, all of them producing mesh conforming the two main algorithms: *unstructured* (spawning triangle and quadrangles in 2D and tetrahedra in 3D) and *structured*(originating triangle in 2D and tetrahedra, hexahedra and pyramids in 3D).

Due to the complex geometry of the tooth and its geometrical tolerance, instead of using the *structured grid*, the *unstructured grid* of Gmsh, with the help of "Automatic" algorithm (combinating the use of the "Delaunay" algorithm for plane surfaces and "MeshAdapt" algorithm for all the other surfaces), was used in order to create the mesh, resulting on the mesh represented in Figure 4.6.

In the end, the mesh can be exported as a MSH file (containing one mandatory section with information about the file format followed by several optional sections defining the nodes, elements, region names, periodicity relations and post-processing datasets) and read by the ElmerFEM program.

For further information on the*structured grid* and the *unstructured grid* algorithms used, the Appendix B summarizes their function as well as their disadvantages and advantages.

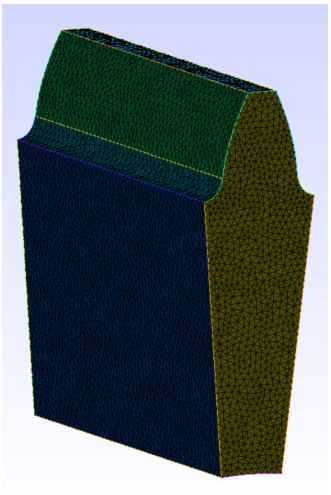

Figure 4.6.: Mesh of single tooth model with 128812 elements - Gmsh.

4.3.2. Solver Input File (MATLAB)

With mesh generation and exportation done, the next step is to obtain the different heat transfer coefficients and heat fluxes for each boundary condition, to establish the operation conditions, etc, in order to write the Solver input file obtained with the use of the MATLAB program.

In this case, MATLAB was used as an interface for the user, creating the bridge between the user/programmer and ElmerSolver. The MATLAB *model* is used to create the ElmerSolver input file. In order to generate the input file, the following data is necessary:

- **Gear Calculation** - selection of the gear geometrical properties and material;

- **Operating Conditions** - selection of the rotational speed, the load torque, the lubrication method (dry or lubricated) and the implementation of a metallic insert. Moreover, the initial temperature conditions need to be established, they differ if it is a dry contact simulation (T_{exp} as initial wall temperature and the T_{amb} as initial ambient temperature) or a lubricated simulation (T_{exp} as initial oil temperature and T_{amb} as initial ambient temperature) and depend on reference temperature (T_{ref}). Finally, the discretization of the path of the contact as well as the calculation of the rolling and sliding velocities, the friction coefficient, forces and local pressures must be performed;

- **Lubricant** - selection of the lubricant and its corresponding properties (kinematic viscosity, density, conductivity, etc.);

- **Power Loss Model** - the heat generated by the friction of the meshing gears is used instead of the Elmer predefined frictional heating, since the power loss model has been validated with experimental work [23], calculating the load dependent power loss due to the gears , P_{VZP}, using equation (3.4);

- **Heat Transfer Coefficients** - calculating the several heat transfer coefficients taking into account the possible presence of oil lubrication (varying the heat transfer coefficient for gear sides with ratio of the arbitrary radius and addendum radius using equations (3.29),(3.33),(3.35) and (3.36), the ratio parameter between air and oil,the physical properties of the mixture air and oil using the general equation (3.28) as well as all the others heat transfer coefficients explained in the previous Chapter 3) or dry contact (also spelt out in Chapter 3).

Polynomial approximation

Heat flux at the meshing gear, generated by the frictional contact of the two rubbing surfaces, and the heat transfer coefficient from the gear sides boundary condition are continuous. Therefore, in order to get a close approximation the path of contact needed to be discretized using an interpolating function that can calculate for each node the expected value.

This approximation is possible with the help of polynomials functions, which are in function of the radius (geometrical location) or the time (in case of a transient simulation) for an easier application of boundary conditions. Therefore, using the MATLAB base function *polyfit* - *"p=polyfit(x,y,n)"*, polynomial curve fitting - returning the coefficients for the polynomial of n degree that best fits, and *polyval* - *"y=polyval(p,x)"*, polynomial evaluation - returning the value of a polynomial of degree n evaluated at x [53].

Approximation of the average heat flux - Steady State

The average heat flux ($\bar{q}_{VZP_i}$) applied to the wheel and pinion is obtained by equation (3.47) and its approximation will use polynomial functions of the contact radius (with help of the division into streches), clearly shown for an example of average heat flux in Figure 4.7.

This approximations is possible with the use of four Heaviside step functions along with the definition of five points on the path of contact. This division is explained by the meshing of one or two pair of teeth in contact. So, when gears start to mesh, two pair of teeth are in contact (from the start -A- to point B), followed by the initiation

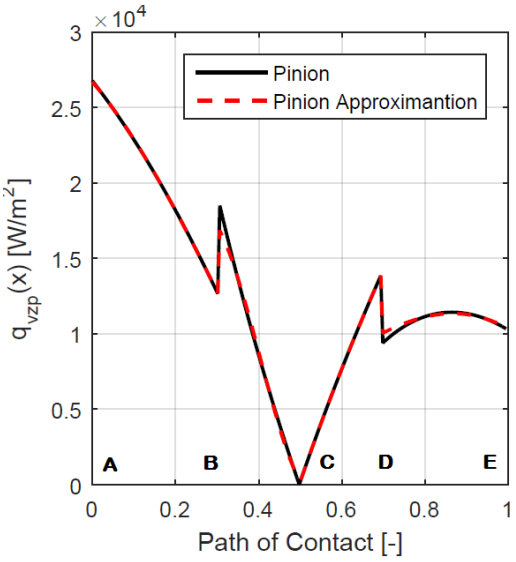

Figure 4.7.: Average pinion heat flux approximation example.

of the contact with a single pair of teeth (which is divided into two streches (point B to point C and C to point D) to better approximate the continuous function), finishing with a double pair of teeth in contact (point$D$ to point E).

Calculated the index for each radius, in MATLAB language:

```
indexA=sum(raioc =< raioA);
indexB=sum(raioc =< raioB);
indexC=sum(raioc =< raioC);
indexD=sum(raioc =< raioD);
indexE=sum(raioc =< raioE)
```

For establishing the polynomial coefficients, in MATLAB language:

```
qcof1=polyfit(raioc(1,indexA:indexB),qVZP(1,indexA:indexB),2);
qcof2=polyfit(raioc(1,indexB:indexC),qVZP(1,indexB:indexC),3);
qcof3=polyfit(raioc(1,indexC:indexD),qVZP(1,indexC:indexD),3);
qcof4=polyfit(raioc(1,indexD:indexE),qVZP(1,indexD:indexE),2);
```

Where the Heaviside Step functions, in MATLAB language:

```
HeaviSide0=tanh(1000*Khs.*(raioc-(raioA-1e-4)));
HeaviSide1=(-tanh(1000*Khs.*(raioc-(raioB)))+1).*,...
   (tanh(1000*Khs.*(raioc-(raioA-1e-4)))+1)/4;
HeaviSide2=(-tanh(Khs.*(raioc-raioC))+1).*,...
   (tanh(1000*Khs.*(raioc-(raioB)))+1)/4;
HeaviSide3=(-tanh(1000*Khs.*(raioc-(raioD)))+1).*,...
   (tanh(1000*Khs.*(raioc-(raioC-1e-4)))+1)/4;
HeaviSide4=(tanh(1000*Khs.*(raioc-(raioD)))+1)/2;
```

The final result for the average heat flux, in MATLAB language:

```
qvzpaverage=HeaviSide0.*(HeaviSide1.*(polyval(qcof1,raioc))+ ,...
    HeaviSide2.*(polyval(qcof2,raioc))+, ...
    HeaviSide3.*(polyval(qcof3,raioc))+, ...
    HeaviSide4.*(polyval(qcof4,raioc)));
```

where *Khs* is a constant to improve the approximation, *raioc* is the discretized contact radius between *raioA* and *raioE*.

Local Heat Flux Approximation - Transient State

As for the transient simulation, the time variable was considered and, therefore, the polynomial approximations are in function of meshing time.

The meshing time for each contact radius is discretized by the use of the following MATLAB code, being the result shown in Figure 4.8.

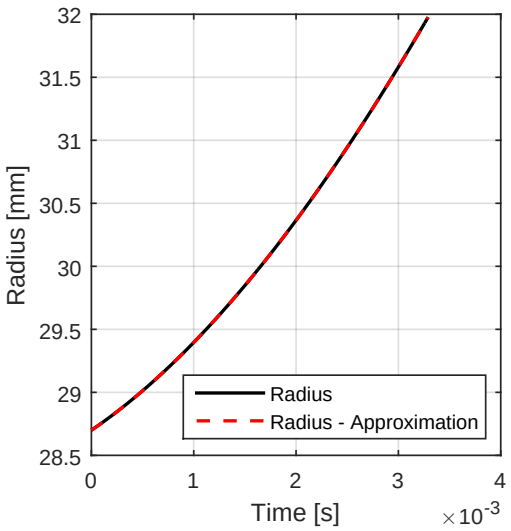

Figure 4.8.: Contact radius approximation example.

```
for i=1:length(x(1,:)):
    time_trans(1,i)=(2+(x(1,i)/1000)/(omega(1,1)*db(1)/2000));
end
```

where x is the discretized path of contact coordinate, ω_1 is the rotational speed for pinion and d_b its primitive diameter. Polynomial approximation and value in MATLAB code:

```
timedis2=polyfit(time_trans(1,:),(raioc(1,:)/1000),4);
raio_time=polyval(timedis2,time_trans);
```

As for approximation of the calculation of Hertzian half-width for each meshing time with its polynomial approximation is shown in Figure 4.9. The approximation was done taking into account the two points of transition in the path of contact.

For the discretization of Hertzian half-width field for each meshing time, in MATALB language:

```
for i=1:length(a{1,1}(1,:)
  xa(i,:)=linspace(-a{1,1}(1,i),a{1,1}(1,i),21);
end
xa(:,11)=0
```

For establishing the connection between meshing time and the Hertzian halft-width, the polynomial coefficients in MATLAB language:

```
atempocof1=polyfit(time_trans(1,indexA:indexB),a{1,1}(1,indexA:indexB),3);
atempocof2=polyfit(time_trans(1,indexB:indexD),a{1,1}(1,indexB:indexD),6);
atempocof3=polyfit(time_trans(1,indexD:indexE),a{1,1}(1,indexD:indexE),3);
```

Where the Heaviside Step function in MATLAB code:

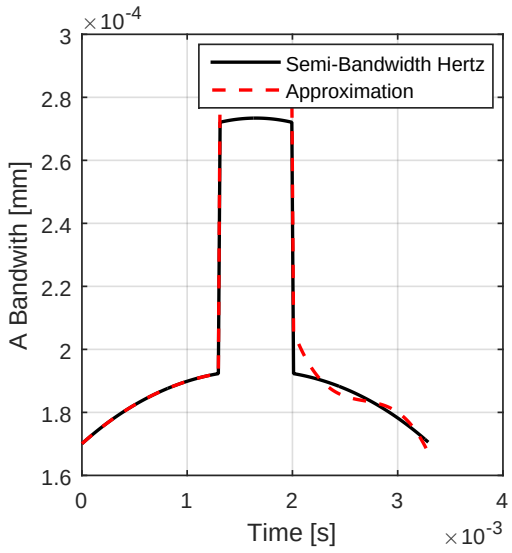

Figure 4.9.: Hertzian half-width approximation example.

```
ahs_0=tanh(1000*Khs.*(time_trans-(time_trans(1,indexA)-1e-3)));
ahs_1=(-tanh(1000*Khs.* (time_trans-(time_trans(1,indexB)+0.1e-4)))+1), ...
  .* (tanh(1000*Khs.*(time_trans-(time_trans(1,indexA)-1e-3)))+1)/4;
ahs_2=(-tanh(1000*Khs.*(time_trans-(time_trans(1,indexD)+1.8e-6)))+1), ...
  .* (tanh(1000*Khs.*(time_trans-((time_trans(1,indexB)+0.1e-4))))+1)/4;
ahs_3=(tanh(1000*Khs.*(time_trans-(time_trans(1,indexD)+1.8e-6)))+1)/2;
```

The final result for the Hertzian half-width, in MATLAB code:

```
a_temp=ahs_0.*ahs_1.*(polyval(atempocof_1,time_trans)), ...
+ahs_2.*(polyval(atempocof_2,time_trans)), ...
+ahs_3.*(polyval(atempocof_3,time_trans))
```

Finally, the polynomial and Heaviside step functions approximations for the local heat flux, taking into account the same steps as for the average heat flux Heaviside step function, is shown in Figure 4.10.

For the approximation of the heat flux applied locally, the polynomial coefficients in MATLAB code:

```
tempcof_1=polyfit(timetrans(1,indexA:indexB),q_VZP(1,indexA:indexB),3);
tempcof_2=polyfit(timetrans(1,indexB:indexC),q_VZP(1,indexB:indexC),6);
tempcof_3=polyfit(timetrans(1,indexC:indexD),q_VZP(1,indexC:indexD),3);
tempcof_4=polyfit(timetrans(1,indexD:indexE),q_VZP(1,indexD:indexE),3);
```

Where the Heaviside step functions in MALTAB language:

```
hs_0temp=tanh(1000*Khs.*(time_trans-(time_trans(1,indexA)-1e-3)));
hs_1temp=(-tanh(1000* Khs.*(time_trans-(time_trans(1,indexB)+0.1e-4)))+1).*, ...
  (tanh(1000*Khs.* (time_trans-(time_trans(1,indexA)-1e-3)))+1)/4;
hs_2temp=(-tanh(1000*Khs.*(time_trans-(time_trans(1,indexC)+2.5e-6)))+1).*, ...
```

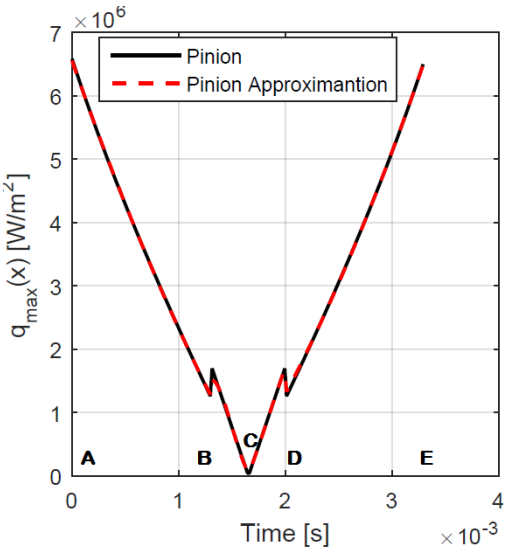

Figure 4.10.: Maximum local heat flux example.

```
  (tanh(1000*Khs.*(time_trans-((time_trans(1,indexB)+0.1e-4))))+1)/4;
hs_3temp=(-tanh(1000*Khs.*(time_trans-(time_trans(1,indexD)+1.8e-6)))+1).*, ...
  (tanh(1000*Khs.*(time_trans-((time_trans(1,indexC)+3.5e-6))))+1)/4;
hs_4temp=(tanh(1000*Khs.*(time_trans-(time_trans(1,indexD)+3.5e-6)))+1)/2;
```

The final result for the maximum heat flux locally in order of the meshing in MATLAB code:

```
qvzp_temp=hs_0_temp.*hs_1_temp.*(polyval(tempcof_1,time_trans))+, ...
   hs_2temp.*(polyval(tempcof_2,time_trans))+, ...
   hs_3temp.*(polyval(tempcof_3,time_trans))+, ...
   hs_4temp.*(polyval(tempcof_4,time_trans));
```

Heat transfer coefficients approximation

For the approximation of the heat transfer coefficients a code was created in order to read all the mesh nodes and only consider the nodes placed at the gear sides. Following the next equation for each contact radius, if gear lubricated contact is

simulated:

$$\mathrm{d} = 2000 \cdot \frac{\mathrm{r}}{\mathrm{d}_{a1}} \tag{4.1}$$

$$\rho_{\mathrm{mix}} = (1 - (\alpha_{\mathrm{mix}} \cdot \mathrm{d})) \cdot \rho_{lub} + \mathrm{d} \cdot (\alpha_{\mathrm{mix}}) \cdot \rho_{\mathrm{air}} \tag{4.2}$$

$$\nu_{\mathrm{mix}} = \mathrm{d} \cdot \alpha_{\mathrm{mix}} \cdot \nu_{\mathrm{air}} + (1 - (\alpha_{\mathrm{mix}} \cdot \mathrm{d})) \cdot \nu_{\mathrm{lub}} \tag{4.3}$$

$$\mathrm{k}_{\mathrm{mix}} = \mathrm{d} \cdot (\alpha_{\mathrm{mix}}) \cdot \mathrm{k}_{\mathrm{air}} + (1 - (\alpha_{\mathrm{mix}} \cdot \mathrm{d})) \cdot \mathrm{k}_{lub} \tag{4.4}$$

$$c_{p_{\mathrm{mix}}} = \mathrm{d} \cdot (\alpha_{\mathrm{mix}}) \cdot c_{p_{\mathrm{air}}} + (1 - (\alpha_{\mathrm{mix}} \cdot \mathrm{d})) \cdot c_{p_{lub}} \tag{4.5}$$

$$\alpha_{1mix} = \frac{\mathrm{k}_{\mathrm{mix}}}{\rho_{\mathrm{mix}} \cdot \mathrm{c}_{\mathrm{p}_{\mathrm{mix}}}} \tag{4.6}$$

$$\mathrm{Re}_{\mathrm{mix}} = \frac{(\mathrm{r})^2 \cdot \omega_1}{\nu_{\mathrm{mix}}} \tag{4.7}$$

$$\mathrm{Pr}_{\mathrm{mix}} = \frac{\nu_{\mathrm{mix}}}{\alpha_{1mix}} \tag{4.8}$$

Taking into consideration the different flow regimes for each node we can obtained the heat transfer coefficients. As for the dry contact situation only the physical properties of air are considered for the determination of the heat transfer coefficients.

So, the approximation of the heat coefficients for the gears sides in function of the radius is done by equation (4.9):

$$\mathrm{pcof} = \mathrm{polyfit}(\mathrm{hs}, \mathrm{r}, 2) \tag{4.9}$$

For the non-meshing meshing tooth surfaces, h_r, are equal to a third of maximum heat transfer coefficient at the gear sides and the tooth tip surface takes the maximum value of the gear side heat transfer coefficient.

Finally, for the meshing surface the heat transfer coefficient is calculated and approximated by a polynomial function in function of the contact radius. So,

$$\mathrm{Pr} = \rho_{\mathrm{air/lub}} \cdot \nu_{\mathrm{air/lub}} \cdot \frac{c_{\mathrm{p}_{\mathrm{air/lub}}}}{k_{\mathrm{air/lub}}} \tag{4.10}$$

$$\mathrm{Re} = \left(\frac{\mathrm{r}}{1000}\right)^2 \cdot \frac{\omega_1}{\nu_{\mathrm{air/lub}}} \tag{4.11}$$

$$\mathrm{h}_{\mathrm{m}}^{'} = 0.228 \cdot \mathrm{Re}^{0.731} \cdot \mathrm{Pr}^{1/3} \cdot \frac{k_{\mathrm{air/lub}}}{\left(\frac{\mathrm{d}_1}{1000}\right)} \tag{4.12}$$

$$t_f = \frac{1}{z_i} \tag{4.13}$$

$$\mathrm{h}_{\mathrm{m}} = t_f \cdot \mathrm{h}_{\mathrm{m}}^{'} + (1 - t_f) \cdot \mathrm{h}_{\mathrm{r}} \tag{4.14}$$

These are the procedures taken in order to write the Solver Input File (SIF) taking into account all boundaries conditions, materials, bodies, equations, solvers, etc. for the study of transient or steady state.

4.3.3. Solver (Elmer FEM)

Elmer is an open source multiphysical simulation software, mainly developed by CSC-IT Center for Science, it includes physical models of fluid dynamics, structural mechanics, electromagnetics, heat transfer and acoustics. These models are described by partial differential equations which Elmer solves by the Finite Element Method (FEM) [54].

The simulation by finite element software is usually based on the use of three software parts [55]:

1. A preprocessor which is used to create a mesh that enables the construction of the spatial discretization over the continuum;

2. In conjunction with the preprocessing a computational PDE (*Partial Differential Equation*) model is created by using a finite element solver. This program needs to continue the computational work by, for example, updating the numerical solution via time-stepping algorithm, nonlinear iterations;

3. A postprocessor, which analyzes the solver output and displays the computational solution in a graphical form.

The Elmer software offers the possibility to use the solver program independently without needing to use the other two components from the conventional three-component division of the finite element software. The graphical user interface ElmerGUI could be used as a first introduction to the program, in the same ways as the Gmsh software.

During preprocessing the Elmer package contains an independent program that can convert other types of mesh files into Elmer format (in this case it can convert the MSH files created by Gmsh) with the possibility to create the mesh directly in the case of simple geometries.

Then the execution of the solver program of Elmer is easily controlled by simply providing a text file as input that can be created directly by using any text editor. After the solver is completed, the usual output of the Elmer solver is a result file that can be read by its postprocessor, although there is the possibility to use other file formats to visualize with alternative software (for example: ParaView).

4.3.4. Governing Equations of Heat Solver Module

The module used to solve the governing equations was the *"HeatSolver"*, described in *"ElmerSolver Manual"* [56].

This module results from the energy conservation as well as Fourier's law to model heat conduction. However the linearity of the equation may be disregarded as the thermal conductivity is temperature dependent.

The incompressible heat equation is given by equation 4.15:

$$\rho \cdot c_p \left(\frac{\partial T}{\partial t} + (\vec{u} \cdot \nabla) T \right) - \nabla \cdot (k \cdot \nabla T) = \overline{\overline{\tau}} : \overline{\overline{\varepsilon}} + \rho \cdot h \tag{4.15}$$

where ρ is the density, c_p is the heat capacity at constant pressure, T is the temperature, $\vec{u}$ is the convection velocity, k the heat conductivity and h the heat source. The first term on the right side of equation (4.15) refers to the frictional viscous heating, which is not considered in the present work, since the power loss model is used as explained earlier. Since the model will only consider solid physical bodies, the gear tooth model, the velocity considered is null ($\vec{u} = 0$).

Solver

Solving the PDE models can be quite challenging and a precise description of the problem must given by the solver input file (SIF file). This file contains fundamental information about the physical model selected, the material parameters, the boundary conditions, the initial conditions, tolerances for iterative solvers, etc.

The solver input file must be organized into different sections, each of them starting with a row with the name of the section, followed by the number of keyword commands and ending with a row containing the word *End*, as example presented in Appendix D. The sections are [56]:

- **Header** - this section contains the location of mesh files;
- **Simulation** - used for general information and not to specify the particular PDE model involved in the simulation, describes the coordinate system used, indicates whether the problem is stationary or evolutionary (Steady State or Transient), the timestepping method, etc;
- **Constants** - defines certain physical constants, for instance the Stefan-Boltzmann constant and the gravity vector;
- **Body** n - associates for each body the equations, the material properties, the body force and the initial conditions;
- **Material** n - describes the material properties (density, enthalpy, viscosity, heat capacity, heat conductivity, etc.);
- **Body Force** n - describes the body forces involved (heat source, frictional heat, joule heat, etc.)
- **Equation** - defines a set of solvers applied to a body or a set of bodies, which with the ability to solve certain physical model (heat equation, etc.);

- **Solver** n - describes the solver control variables, with most of the possible keywords related to linearization procedures of nonlinear models, the selection of solution methods for resulting linear equations, convergence tolerance, etc.;
- **Boundary Condition** n - holds the parameter values for the various boundary conditions types: imposed temperature by Dirichlet boundary condition or the use of flux conditions. The natural boundary condition set is the zero flux condition, if no boundary condition is established;
- **Initial Condition** n - giving initial values, it is important only for evolutionary problems (initial temperature);
- **Component** n - physical entity not associated with the mesh, it could represent the representation of a 0D object such as an electrical component, an equation of state, etc.

Solution Methods for linear systems

The discretization and linearization of the a system containing PDE generally leads to solve linear systems as given by equation (4.16):

$$Ax = b_A \tag{4.16}$$

where A is the coefficient matrix as a result of element discretization. The A and b_A are of orders $n \times n$ and $n \times 1$, respectively. To solve this linear systems, direct methods may be used, determining the solution of the linear system dependent of the machine precision. This method is a very robust way to solve the linear system and has a problem with the expensive time in computational calculus and memory requirement, therefore it is not used for large order linear systems. In this way, using iterative methods is the best method for providing a solution, their efficiency generally work by generating sequences to improve the approximate solutions.

Elmer provides two major groups for the iterative methods that can be used in the solver: the preconditioned Krylov subspace methods or the multilever methods. For the preconditioned Krylov methods ElmerSolver contains the following:

- Conjugate Gradient (CG);
- Conjugate Gradient Square (CGS);
- Biconjugate Gradient Stabilized (BiCGStab);
- BiCGStab(l);
- Transpose-Free Quasi-Minimal Residual (TFQMR);

- etc.

In this thesis the preconditioned Krylov subspace method of BiGStab was used, because of its smoother convergence.

As stopping criterion for the Krylov methods a linear convergence tolerance is fixed as an approximate solution considered to be accurate enough, satisfying the following equation:

$$\frac{\|Ax - b_A\|}{\|b_A\|} \leq \epsilon \tag{4.17}$$

Preconditioners

The performance of the iterative methods created by Krylov is strongly dependent on the spectrum of the coefficient matrix A used, where the rate of convergence is improved by transforming the system into an equivalent system that has more favorable spectral properties (*preconditioning process*), which is based on the following equation:

$$AM^{-1}z = b \tag{4.18}$$

where the preconditioner matrix M is an approximation to A and z is related to the solution x by $z = Mx$.

The possible preconditioners of ElmerSolver are:

- Jacobi;
- ILU;
- ILU(N);
- ILUT.

The preconditioner adopted was ILU0 since it has a good performance at the convergence rate to the solution as well as a low time and low memory spent on building the preconditioner matrix for each iteration. The information of the others preconditioners is shown in Appendix C.

Solution Methods for nonlinear systems

Many problems are not linear by nature, so the ElmerSolver is going to linearize all nonlinear equations following the same form as shown in equation (4.19):

$$A\left(u_{i-1}\right) u_i = b_A\left(u_{i-1}\right) \tag{4.19}$$

where i refers to the iteration cycles. For the nonlinear problems there are two major methods:

- **Picard** linearization;
- **Newton** linearization;

which need a convergence of the nonlinear system tolerance as criterion to stop the iteration process after a relative change of the norm of the variable in analysis between two consecutive iteration is small enough, as shown at equation (4.20):

$$\|T_i - T_{i-1}\| < \epsilon \|T_i\| \tag{4.20}$$

where ϵ is a given fixed value.

In the present work both methods were used, with the change of the Picard iteration method to the Newton iteration method after a certain number of iterations, in order to improve convergence of the iterations.

The steady state convergence tolerance is used to specify the convergence of a steady state, with the condition that all the other convergence tolerances are reached before the whole system is considered converged. This convergence tolerance is given by equation (4.21):

$$T_i^{'} = \lambda_r T_i + (1 - \lambda_r)\, T_{i-1} \tag{4.21}$$

where λ_r is the fixed relaxation factor.

Integration of time-dependent systems

For the solution of time-dependent systems with only first order time derivatives the discretization methods used are:

- Crank-Nicolson Method;
- Backward Differences Formulae (BDF) of several orders.

The numerical solution of a evolutionary field equation is obtained by:

$$\frac{\partial \phi}{\partial t} + \kappa \phi = f \tag{4.22}$$

where the differential operator κ that does not involve differentiation with respect to time t and f is a function of spatial coordinates and time. The spatial discretization leads to:

$$M \frac{\partial \Phi}{\partial t} + K\Phi = F \tag{4.23}$$

where M, K and F result from the discretization of the identity operator, the operator κ and f, respectively, being Φ the vector of values of the unknown field ϕ at the nodes [56].

The first two order of BDF methods to discretize the time derivative are obtained by the following systems:

$$\left(\frac{1}{\Delta t}M + K\right)\Phi^{i+1} = F^{i+1} + \frac{1}{\Delta t}M\Phi^{i} \tag{4.24}$$

$$\left(\frac{1}{\Delta t}M + \frac{2}{3}K\right)\Phi^{i+1} = \frac{2}{3}F^{i+1} + \frac{1}{\Delta t}M\left(\frac{4}{3}\Phi^{i} - \frac{1}{3}\Phi^{i-1}\right) \tag{4.25}$$

where Δt is the time step with Φ^i being the solution at step i and F^i is the value of F at time step i.

All of the BDF methods are implicit in time, its accuracy increases with the higher order, although the recommended BDF order for a first order time integration (as the case of the heat equation module) is the second order.

HeatSolver Module

The linearized PDE for the scalar T in the variational formulation is given by equation (4.26):

$$M_{ij}\frac{\partial T_j}{\partial t} + A_{ij}T_j = F_i \tag{4.26}$$

where M_{ij} is the mass matrix, A_{ij} is the stiffness matrix and F_i is the force vector.

The time-stepping and the coupled solver iteration of the steady state or time level iteration of the several solvers are taken care by the main part of the Elmer Solver. So, the task of the user is to set a defined solver routine that manages to linearize the nonlinear PDE, as is shown at Figure 4.11. In this flowchart, the tasks that are provided by Elmer are seen within the grey area, whereas the white area indicates the source code of the user subroutine.

Heat Conduction Equation Solver - Subroutines

For constant density, ρ, and heat capacity, c_p, equation (4.15) can be rewritten as:

$$\frac{\partial T}{\partial t} - \nabla \cdot \left(\frac{k}{c_p \cdot \rho}\nabla T\right) = \frac{h}{c_p \cdot \rho} \tag{4.27}$$

where T stands for the temperature, k for heat conductivity and h is the heat source.

Therefore, the variational formulation of equation (4.27) after the partial integration of the conduction therm and application of divergence's theorem:

$$\int_{V_l}\frac{\partial T}{\partial t}\Gamma_i \quad \mathrm{d}V_l + \int_{V_l}\frac{k}{c_p \cdot \rho}\nabla T \cdot \nabla\Gamma_i \quad \mathrm{d}V_l = \int_{V_l}\frac{h}{c_p \cdot \rho}\Gamma_i \quad \mathrm{d}V_l + \oint_{\partial V_l}\frac{1}{c_p \cdot \rho}\underbrace{(k \cdot \nabla T) \cdot \vec{n}}_{q_n}\Gamma_i \quad \mathrm{d}A \tag{4.28}$$

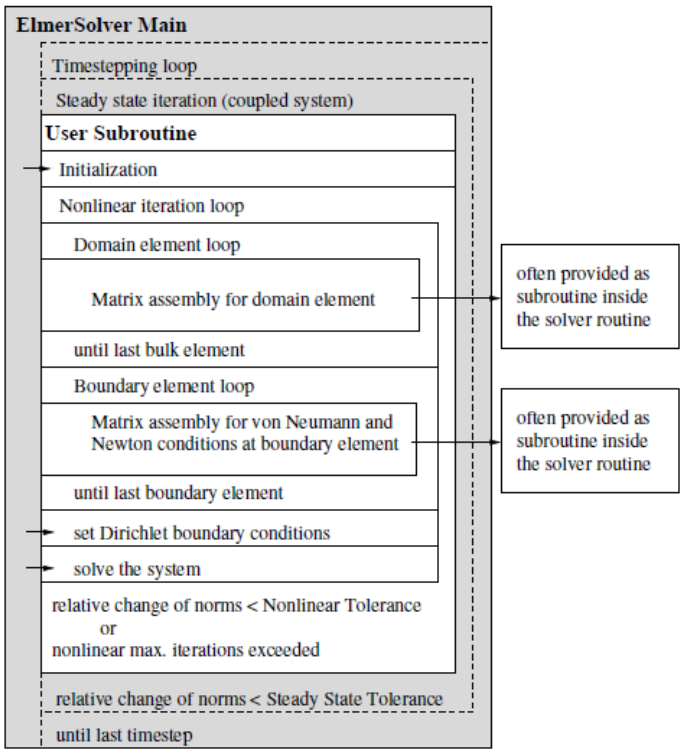

Figure 4.11.: Flowchart of a user defined solver subroutine within ElmerSolver [56].

where Γ_i is the basis-function, V_l and ∂V_l the element volume and its enclosing surface, respectively. According to the Galerkin's method, the variable T is given by:

$$T = T_j \Gamma_j \tag{4.29}$$

leading to the following,

$$M_{ij} = \int_{V_l} \Gamma_j \Gamma_i \quad \mathrm{d}V_l \tag{4.30}$$

$$A_{ij} = \int_{V_l} \frac{k}{c_p \cdot \rho} \nabla\Gamma_j \cdot \nabla\Gamma_i \quad \mathrm{d}V_l \tag{4.31}$$

$$F_i = \int_{V_l} \frac{h}{c_p \cdot \rho} \nabla\Gamma_i \quad \mathrm{d}V_l + \oint_{\partial V_l} \frac{q_n}{c_p \cdot \rho} \Gamma_i \quad \mathrm{d}V_l \tag{4.32}$$

By analyzing Figure 4.11 the solver subroutine consist in:

1. Declaration of the needed variables;
2. Reading information about the nonlinear iteration from the solver input file;
3. Nonlinear iteration loop starts and the linear system solver is initialized;

4. Next loop will get over all active elements in the simulation domain and, after inquiring the number of nodes, the nodal material parameter values (heat capacity, heat conductivity and density) are read in;

5. Composition of elements matrices and force vector (heat source, in this case), has to be read from the body section of the solver input file. After the initialization of the local matrix and vectors to zero, the information about the Gauss-points for integrations is inquired. The integration of the element is done by summing all Gauss points, with the evaluation of the square root of the determinant of the element coordinate system metric tensor $\sqrt{\det\left(J^T \cdot J\right)}$ - Jacobian determinant-, as well as the local basis functions, Γ_i, and their gradient, $\nabla\Gamma_i$. Thereafter, the material parameters for each Gauss-point is also evaluated using the basis function. For example, the local density is given by:

$$\rho\Big|_{GP} = \rho_i \cdot \Gamma_i\Big|_{GP} \tag{4.33}$$

with the sum being taken over the nodal index *i*. Whereas, the force vector is obtained by integrating over the element, which is approximated to sum over all Gauss-Point, as it show on equation (4.34)

$$F_j = \int_{V_l} \frac{h}{\rho \cdot c_p} \quad \mathrm{d}V_l \approx \sum_{t=1}^{N} \left(\sqrt{ds^2}\sqrt{\det\left(J^T \cdot J\right)} \cdot \frac{h}{\rho \cdot c_p} \right)\Big|_{GP} \tag{4.34}$$

where $\sqrt{ds^2}$ is the model coordinate system metric and N the total Gauss-Points that take part of the element. In the same analogy the mass and stiffness matrix are calculated by the following equations;

$$M_{ij} = \int_{V_l} \Gamma_j \cdot \Gamma_i \quad \mathrm{d}V_l \approx \sum_{t=1}^{N} \left(\sqrt{ds^2}\sqrt{\det\left(J^T \cdot J\right)} \cdot \Gamma_j \cdot \Gamma_i \right)\Big|_{GP} \tag{4.35}$$

$$A_{ij} = \int_{V_l} \frac{k}{c_p \cdot \rho} \nabla\Gamma_j \cdot \nabla\Gamma_i \quad \mathrm{d}V_l \approx \sum_{t=1}^{N} \left(\sqrt{ds^2}\sqrt{\det\left(J^T \cdot J\right)} \cdot \frac{k}{c_p \cdot \rho} \nabla\Gamma_j \cdot \nabla\Gamma_i \right)\Big|_{GP} \tag{4.36}$$

6. In case of a transient simulation, a subroutine is generated to take care of the first order time discretization;

7. The local matrix is, then, added to the global coefficient matrix;

8. Looping over all boundary elements to get the contribution of the coefficient matrix and the force vector from a Neumann type of boundary condition (BC). So, there is the need to differentiate the type of boundary conditions, only reading the Neumann BCs, although the force value that will be computed

in the internal subroutine will not be the value for the fixed heat flux, q_n, but the value of the heat flux divided by the its density and heat capacity, as previously explained. If no boundary type condition is established, the assumed BC is a natural boundary condition with zero flux perpendicular to the surface (adiabatic). The contribution to the force vector at the boundary elements is given by the external load given by equation (4.37):

$$F_j = \oint_{V_l} \frac{q_n}{\rho \cdot c_p} \mathrm{d}V_l \approx \sum_{t=1}^{N} \left(\sqrt{ds^2} \sqrt{\det\left(J^T \cdot J\right)} \right) \cdot \frac{q_n}{c_p \cdot \rho} \Big|_{GP} \tag{4.37}$$

The boundary loop is closed and the system vector and system are updated with the current boundary element;

9. Before establishing the Dirichlet condition the assembly of the system matrix is done;

10. By default the system is solved by a subroutine which returns the norm of the N^n solution vector T_j for its n-th nonlinear iteration step. This is implanted by the subroutine to inquire the change of the solution between two steeps. This relative norm is given by:

$$R = 2\frac{|N^{n-1} - N^n|}{N^{n-1} + N^n} \tag{4.38}$$

and if it is smaller than the *Nonlinear System Tolerance* the nonlinear iteration is considered to have converged;

Transient Simulation

In the case of Transient simulation, another aspect requires atention since these type of simulation as evolutionary starts with an existing solution. Therefore, extra conditions are imposed into the the Simulation section of the solver input file:

- Restart file name - *Restart File* = "name of the file".result;
- Restart position - *Restart Position = 0*, which makes sure the results reloaded are the last stored time/iteration level;
- Restart time - *Restart Time = 0*, since the transient simulation will start with the Steady-State result and quite often it has the result of several iterations steps, especially when the differences between the time levels of each simulation is not correctly known. So, with this keyword it is possible to make sure the time simulation is set to the correct time.

For better analysis of the results, a third solver was implemented to change the format of the result to a VTU file, so ParaView would be able to read and make a possible animation of the Transient Simulation.

Chapter 5.

Model Validation

5.1. Introduction

In the preceding chapters (Heat transfer model for gear teeth and Model Implementation) the Finite Element Method model was described. In Chapter 3, the model governing equations for the two states (evolutionary/transient and steady) as well as the boundary conditions and its heat transfer coefficients were theoretically explained. In Chapter 4 the various software used were described, defining the functionality along with a description of the application of each program.

Therefore, this chapter is going to emphasize the validation of the FEM thermal model that was developed and implemented, corroborating the results with experimental work from literature.

5.2. Steady State Model

5.2.1. Case 1 (Spur Gears)

In the paper *"Operating temperatures of oil-lubricated medium-speed gears: numerical models and experimental results"* [57], is a study of the gear geometry, rotational speed and the applied load as well as the lubrication conditions as they influence bulk temperature in high-speed gears.

A spur gear, with the geometric properties listed in Table 5.1, which is made of 665M17(EN-34) steel (the mechanical and thermal properties are described in Table 5.3) and it is lubricated with a Mobil Jet II, whose properties are enumerated in Table 5.2, the operating conditions can be found in Table 5.4.

The mesh was created according to the method described in Chapter 4, resulting in the mesh presented in Figure 5.1.

Table 5.1.: Geometry of spur gear tested at case 1 - steady State [57].

Geometric Data	**Steady - Case 1**	
	Pinion	Wheel
Number of teeth, z [-]	15	16
Module, m [mm]	5.33	
Center distance [mm]	82.55	
Pressure angle, α [°]	26	
Face width [mm]	4.775	
Addendum modification [-]	0	0
Transverse contact ratio, ε_α [-]	1.34	
Surface finish, Ra [μm]	0.6	

Table 5.2.: Properties of lubricating oil (Mobil Jet II) [57].

Oil Type	**Mobil Jet II**
Oil viscosity @ 40°C, ν [cSt]	30
Oil viscosity @ 100°C, ν [cSt]	5.5
Specific heat @ 90°C, c [J/(kg·K)]	2000
Density, ρ [kg/m^3]	998

Table 5.3.: Material properties of pinion steel (665M-17/EN-34) [57].

Steel type	**665M-17 / EN-34**
Young modulus , E [GPa]	185.42
Poisson's ratio, υ [-]	0.30
Density, ρ [kg/m^3]	7870.00
Thermal conductivity, k [W/(m·K)]	41.80
Specific heat, c [J/(kg·K)]	493.00

Table 5.4.: Operating load conditions for case 1 FEM simulation [57]

Operating Conditions	**Torque of driving shaft [Nm]**
A	17.4
B	26.0
C	35.0
D	43.0
E	52.0
F	61.0
G	73.0
With:	
Oil-jet lubrication, $\dot{V}$ [l/min]	0.38
Rotational speed, n [rpm]	2000-10000
Initial oil temperature, T_{exp}[°C]	90
Initial ambient temperature, T_{amb}[°C]	70

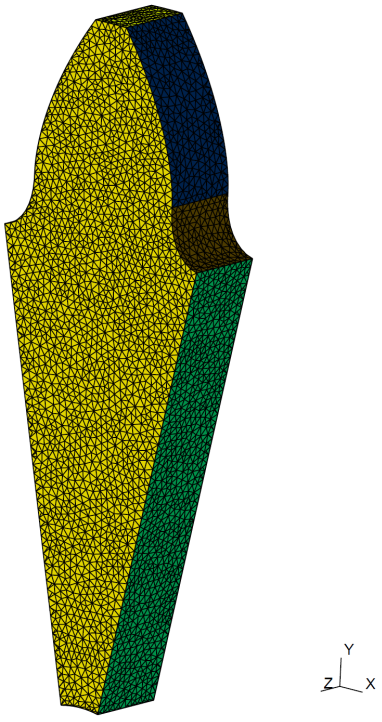

Figure 5.1.: Mesh created on Gmsh with 55539 nodes and 254118 elements.

Table 5.5.: The α_{mix} parameter in function of rotational speed [57].

Rotational Speed [rpm]	α_{mix}
2000	0.3
4000	0.4
6000	0.5

Table 5.6.: The new α_{mix} parameter in function of rotational speed.

Rotational Speed [rpm]	α_{mix}
2000	0.1
4000	0.3
6000	0.4

Determining oil/air phase mixture

A first study was done with the rotating speed of 2000, 4000 and 6000 rpm varying the pinion torque. Using oil-jet lubrication, the parameter α_{mix} is needed in order to make the problem real as the properties of the lubricant used are the result of a mixture between the air in the gearbox and the oil used. This parameter takes into account the volume ratio between air and oil in the mixture, when it takes the value of 1 it represents a situation of dry contact and when it is 0 represents a situation of oil lubrication only. In *Long*'s work [57] the evolution of this parameter with rotational speed is described in Table 5.5.

Using the values suggested by *Long et al.* [57] in the present model lead to values faraway from the experiment. So, a parametric study of the α_{mix} was done, by searching for the value that reduces the difference between FEM model and experiments discrepancy. Therefore, these parameter was study in its total length (between 0.1 and 1). This way the best result was calculated to be the one with least sum of the discrepancies. Therefore, for each rotational speed the parameter is shown in Table 5.6.

Experimental Results VS. FEM model

A comparison between the experimental results and the current FEM model as well as the FEM model presented by *Long et al.* [57] is presented in Figure 5.2. All the temperature results are for the pinion gear.

The error analysis is presented in Table 5.7 with the temperature results from the experimental, paper's FEM and the current FEM model in Table 5.8 (the percentage values are in function of the results taken by each module in comparison with the

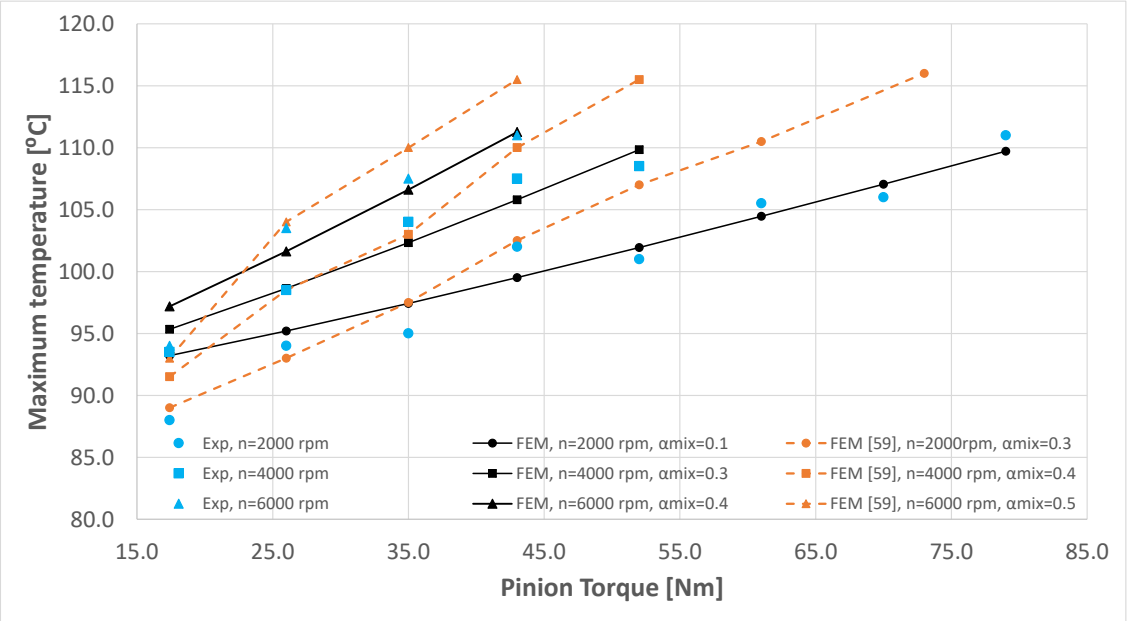

Figure 5.2.: Maximum temperature from experiment, FEM model from [57] and current FEM model.

experimental values).

The main difference between *Long et al.*'s FEM model and the current FEM model is mainly in the power loss model used to calculate the heat flux due to friction.

It is important to notice that the current model has a maximum error lower than 6.5% whereas the paper's FEM model has an maximum error of 9.5%. However, analyzing the current model the values at 17.4 Nm of torque present a higher discrepancy from the experimental result. It was also observed that when the experimental speeds increases the maximum temperature at the same torque is higher, just as expected.

Table 5.7.: Percentage discrepancy Long's between FEM model [57] and current model FEM results and experimental results.

Discrepancy [%]											
Result Origin	**Torque** [Nm]									**Sum**	**Mean**
	17.4	26	35	43	52	61	70	73	79		
N=2000 rpm											
Long et al.'s model [57]	1.14	1.06	2.63	0.49	5.94	4.74	-	9.43	-	25.44	3.63
Current model	6.35	1.34	2.62	2.46	0.91	0.95	-	0.93	1.06	16.60	2.08
N=4000 rpm											
Long et al.'s model [57]	2.14	0.00	0.96	2.33	6.45	-	-	-	-	11.88	2.38
Current model	1.96	0.13	1.60	1.59	1.23	-	-	-	-	6.52	1.30
N=6000 rpm											
Long et al.'s model [57]	1.06	0.48	2.33	4.05	-	-	-	-	-	7.93	1.98
Current model	3.38	1.81	0.83	0.23	-	-	-	-	-	6.26	1.56

Table 5.8.: Result temperature for long's FEM model [57], current FEM model and experiment.

Temperature [°C]									
Result Origin	**Torque** [Nm]								
	17.4	26	35	43	52	61	70	73	79
N=2000 rpm									
Experiment	88.0	94.0	95.0	102.0	101.0	105.5	-	106.0	111.0
Long et al.'s model [57]	89.0	93.0	97.5	102.5	107.0	110.5	116.0	-	-
Current model	93.2	95.2	97.4	99.5	101.9	104.5	-	107.1	109.7
N=4000 rpm									
Experiment	93.5	98.5	104.0	107.5	108.5	-	-	-	-
Long et al.'s model [57]	91.5	98.5	103.0	110.0	115.5	-	-	-	-
Current model	95.3	98.6	102.3	105.8	109.8	-	-	-	-
N=6000 rpm									
Experiment	94.0	103.5	107.5	111.0	-	-	-	-	-
Long et al.'s model [57]	93.0	104.0	110.0	115.5	-	-	-	-	-
Current model	97.18	101.7	106.6	111.3	-	-	-	-	-

Influence of rotational speed, torque and α_{mix}

To study the influence of rotational speed, torque and the α_{mix} parameter it is crucial to analyze the factors independently. So, we will first keep the torque constant and scan the rotational speed and, then, the rotational speed value was kept constant and different torques were considered.

As can be seen in both Figures 5.3a and 5.3b, the maximum bulk temperature increases with either the rotational speed or with thr torque on the driving shaft. However it seems that the parameter α_{mix} has a peculiar behavior when taking as value unity.

In order to infer conclusions on the influence of the α_{mix} parameter, Figure 5.4 presents the results at constant rotational speed and torque. It was observed that the influence of the parameter is greater between 0.9 and 1.0, therefore the existence of oil within the gearbox or its nonexistence is crucial to the heat transfer phenomenon, since a little quantity of oil within the gearbox has a huge influence on the final solution.

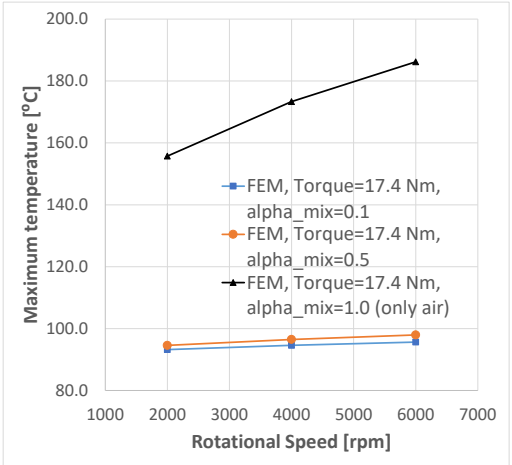

(a) For a fixed torque - 17.4 Nm.

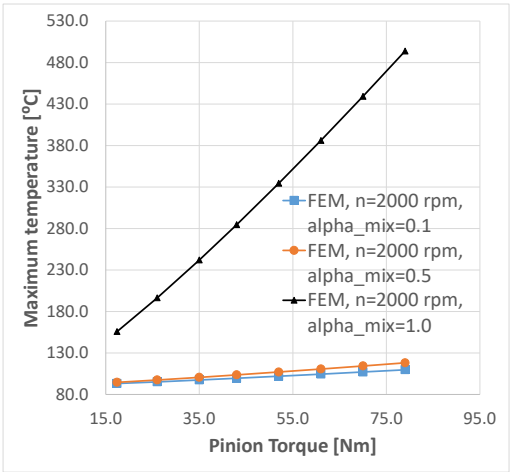

(b) For a fixed rotational speed - 2000 rpm.

Figure 5.3.: Maximum temperature for different conditions.

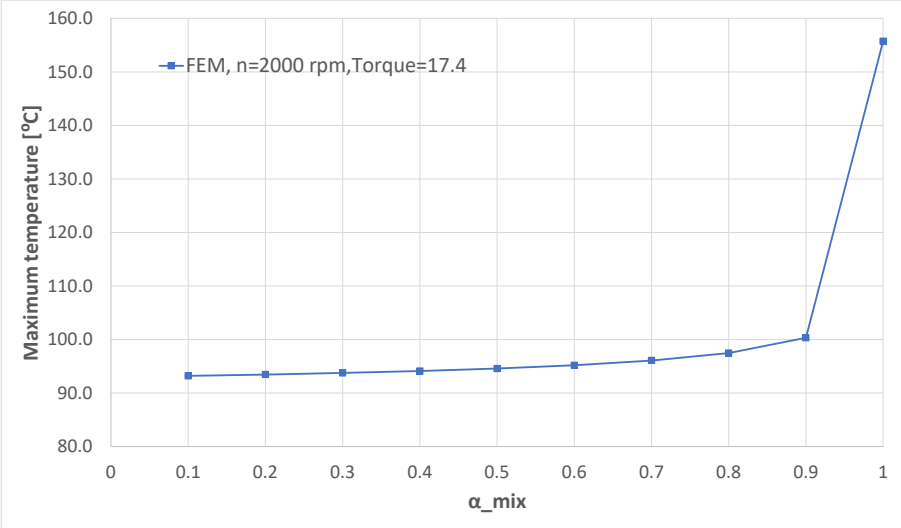

Figure 5.4.: Maximum temperature at 2000 rpm and 17.4 Nm.

Observing Figures 5.5a and 5.5b, which present the Reynolds number and the heat transfer coefficient over the radius of the gear side, respectively, it is obvious that the influence of increasing the amount of oil in the mixture is essential to cool down the gear. Therefore, having a small amount of oil affects dramatically the mixed density since oil density is almost 1000 times higher than the air density. Therefore, the heat transfer coefficient will be affected, depending on the proportion between oil and air in the mixture.

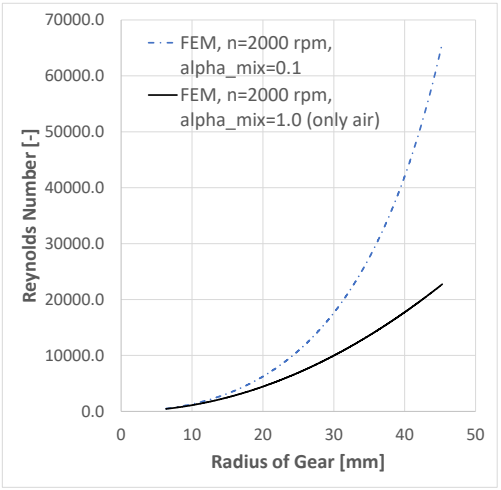

(a) Reynolds number.

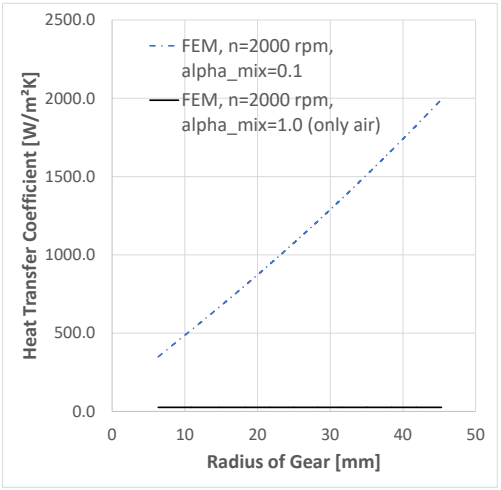

(b) Heat transfer coefficients.

Figure 5.5.: Reynolds and heat transfer coefficients at gear side at 2000rpm and 17.4 Nm.

Finally, considering the average heat flux due to the meshing friction at different speeds, the amount of frictional heat generated increases with the increment of the rotational speed as predicted since the difference between sliding velocities will be greater. Even with the Reynolds number and the heat transfer coefficient increase with the increase of the rotational speed, the frictional heat generated is superior for higher rotational speeds, concluding that the heat transfer coefficient increase is less significant when comparing the rotational speed increase. The average heat fluxes for each rotational temperature are shown in Figures 5.6a, 5.6b and 5.6c.

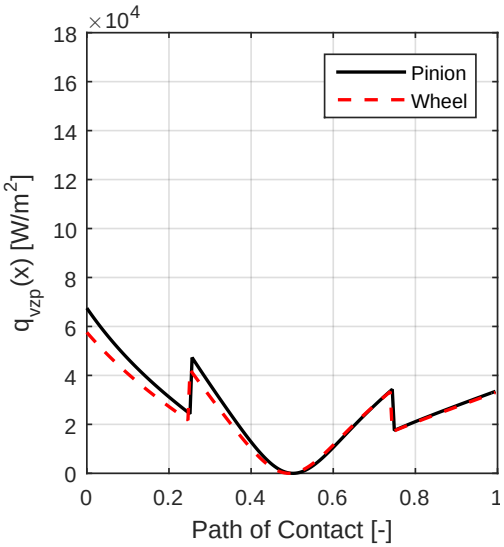

(a) Average heat flux at 2000 rpm.

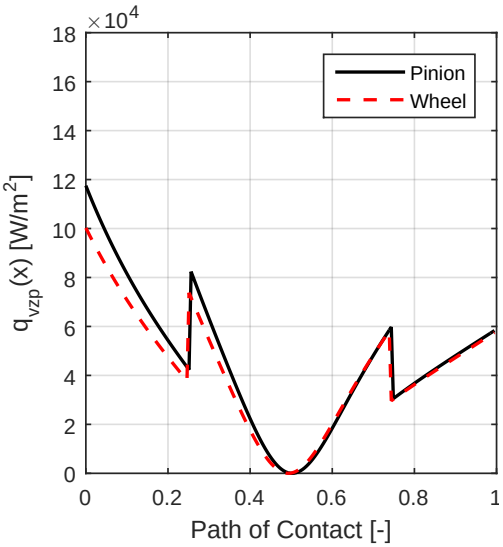

(b) Average heat flux at 4000 rpm.

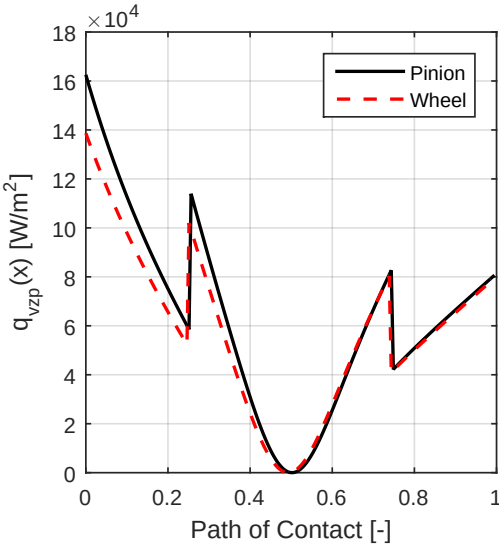

(c) Average heat flux at 6000 rpm.

Figure 5.6.: Average heat flux applied for 2000, 4000 and 6000 rpm at 17.4 Nm.

As explained earlier the approximation taken to describe the continuous average heat flux generated at the meshing surface at 2000 rpm is discretized with the help on the approximation with Heaviside Step functions. These Heaviside functions portrait the different phases during the contact of the two gears. Due to the higher number of teeth on the wheel when comparing to the number of teeth in the pinion, the average frictional heat generated by the pinion is higher than by the wheel.

Figure 5.7 shows the influence of rotational speed on the bulk temperature. It was observed that increasing the rotational speed increases the bulk temperature.

As for the study of the influence of the torque increase at constant speed, Figures

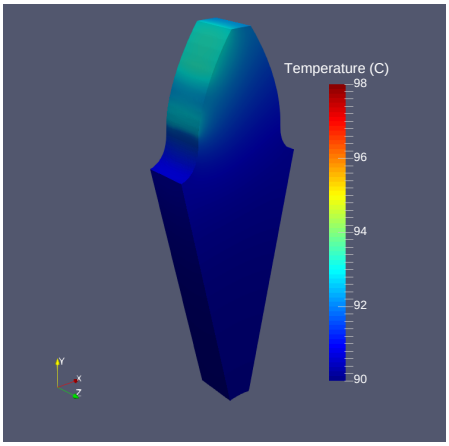

(a) Temperature distribution solution for 2000 rpm.

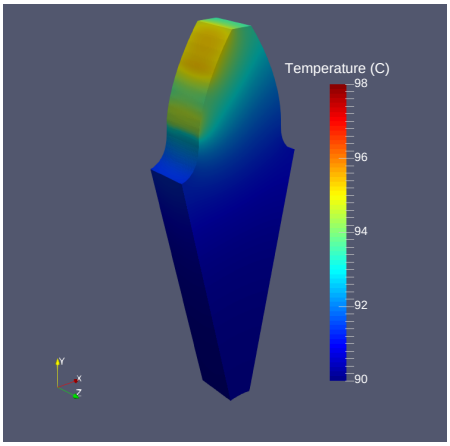

(b) Temperature distribution solution for 4000 rpm.

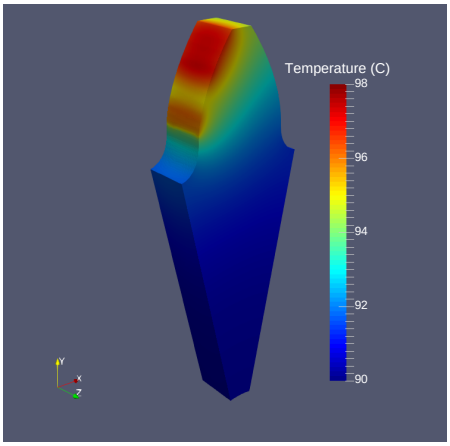

(c) Temperature distribution solution for 6000 rpm.

Figure 5.7.: Bulk temperature field result for 2000, 4000 and 6000 rpm at 17.4 Nm load torque.

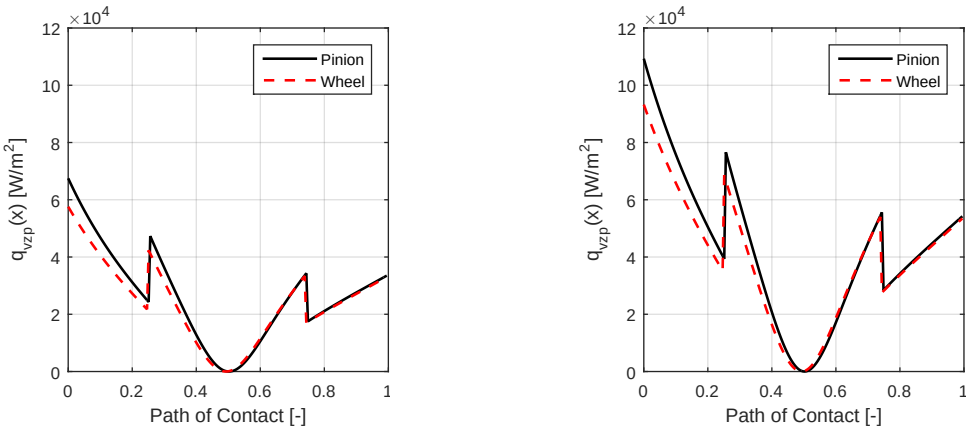

(a) Average heat flux for 17.4 Nm.

(b) Average heat flux for 26 Nm.

Figure 5.8.: Bulk temperature field result for 17.4 and 26 Nm load torque at 2000 rpm.

5.8a and 5.8b show the average heat flux for 17.4 Nm and 26 Nm torque, respectively.

An increment in bulk temperature can also be seen when increasing the load torque at constant rotational speed, Figures 5.9a and 5.9b. In fact, the heat flux generated by friction is higher for highers load torque (increasing the maximum value of the average heat flux from approximately 6.4×10^4 W/m^2 to 11×10^4 W/m^2 for 17.4 Nm and 26 Nm load torque, respectively), while the heat transfer coefficients are kept constant.

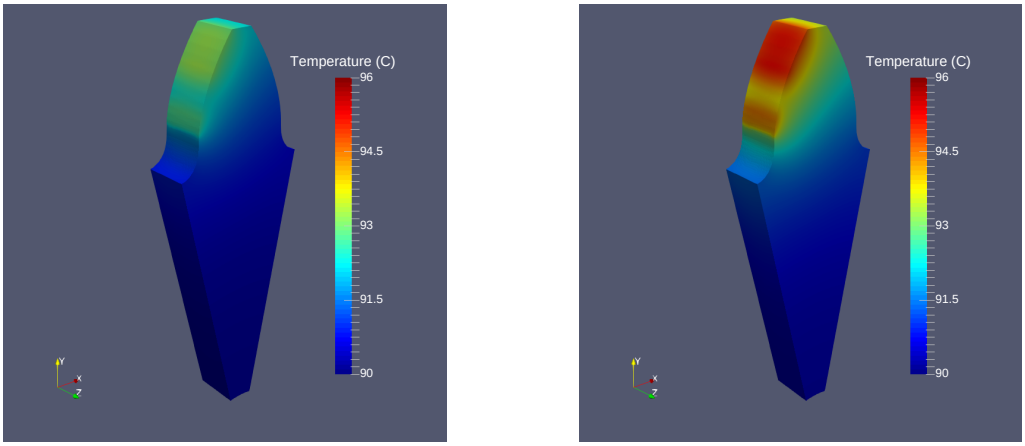

(a) Temperature distribution solution for 17.4 Nm.

(b) Temperature distribution solution for 26 Nm.

Figure 5.9.: Bulk temperature field result for 17.4 and 26 Nm load torque at 2000 rpm.

5.2.2. Case 2 (Scuffing gears)

The paper *"Influence of immersion depth of dip lubricated gears on power loss, bulk temperature and scuffing the load carrying capacity"* [58] is based on a standardized FZG back-to-back scuffing test according to DIN 51534, where two dip-lubricated spur gear pairs are connected by two parallel shafts. The geometric data is listed in Table 5.9. The current simulation used the properties described in Table 5.11. The spur gears are lubricated with a FVA3A ISO VG 100, with properties enumerated in Table 5.10, and are tested for the operating conditions found in Table 5.12.

Following the same procedure for mesh creation described in Chapter 4, the resulting mesh is presented at Figure 5.10.

Table 5.9.: Geometry of spur gear tested at case 2 - steady state [58]

Geometric Data	**Steady - Case 2.** Pinion	Wheel
Number of teeth, z [-]	16	24
Module, m [mm]	4.5	
Center distance [mm]	91.5	
Pressure angle, α [°]	20	
Face width [mm]	14	
Addendum modification [-]	+0.8532	-0.5
Transverse contact ratio, ε_α [-]	1.44	
Surface finish, Ra [μm]	0.5	

Table 5.10.: Properties of lubricating oil (FVA3A ISO VG 100) [58].

Oil Type	**FVA3A ISO VG 100**
Oil viscosity @ 40°C, ν [cSt]	110
Oil viscosity @ 100°C, ν [cSt]	11
Specific heat @ 90°C, c [J/(kg·K)]	2000
Density, ρ [kg/m^3]	900

Table 5.11.: Material properties of pinion steel [58]

Steel type	**Steel**
Young modulus , E [GPa]	210.00
Poisson's ratio, υ [-]	0.30
Density, ρ [kg/m^3]	7870.00
Thermal conductivity, k [W/(m·K)]	41.80
Specific heat, c [J/(kg·K)]	493.00

Table 5.12.: Operating conditions of load cases in the FEM simulation - steady case 2 [58]

Operating Conditions	**Torque of driving shaft [Nm]**
A	95
B	241
C	372
With:	
Circumferential speed, v [m/s]	8.3/20
Initial oil temperature, T_{exp}[°C]	90

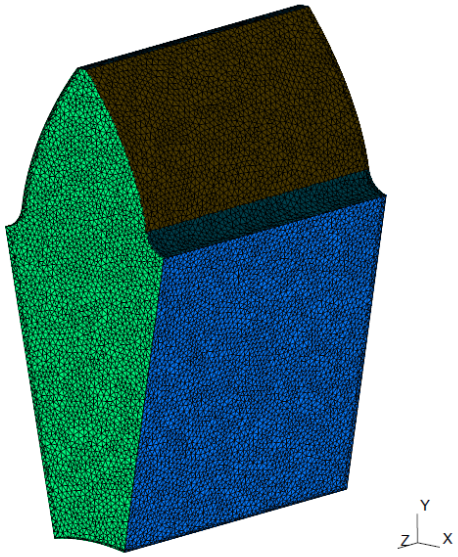

Figure 5.10.: Mesh created on Gmsh with 51142 nodes and 282834 elements.

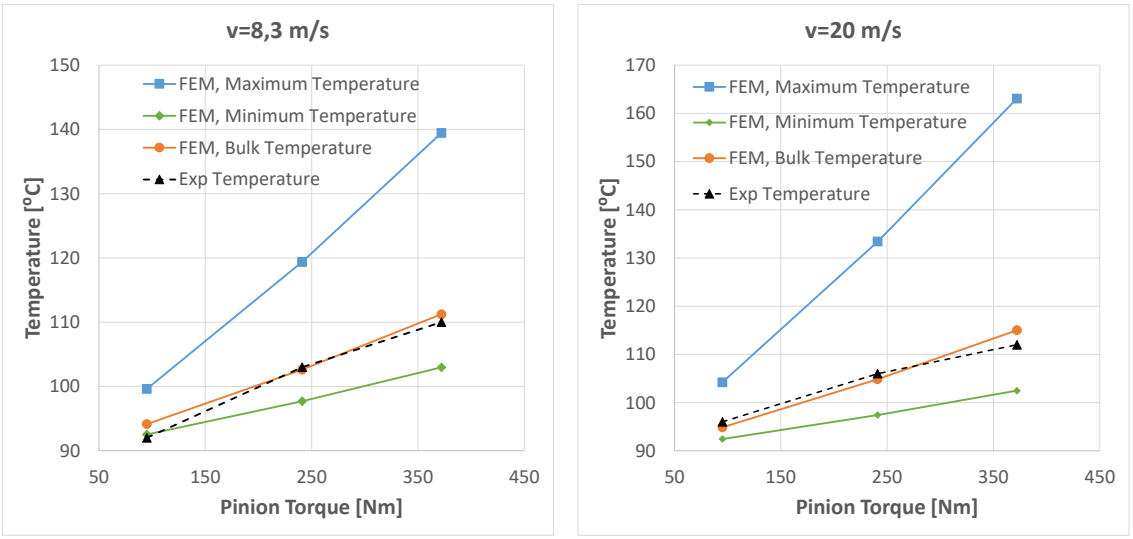

(a) Temperature solution for 8.3 m/s. (b) Temperature solution for 20 m/s.

Figure 5.11.: Bulk temperature field result for 8.3 m/s and 20 m/s circumferential speed at 95, 241 and 372 Nm load torque.

Experimental results VS. FEM

To study if the model behaves properly for high shift gears a scuffing gear was simulated under dip-lubrication, setting the α_{mix} parameter to zero, since the gear tooth will be always totally lubricated (lubricant skin presented in the gear's tooth). The bulk temperature results from the current FEM model taking into consideration the paper's measurement point (between the contact surface and the rest of the gear body).

Taking as reference Figures 5.11a and 5.11b it is possible to infer that with the increase in load torque the bulk temperature is likewise to follow the same pattern: growing with the increment of load torque applied in a pinion.

The error analysis between the current model and the experimental results are listed in Table 5.13, with the deviation being less than 3 %. And where the values for each circumferential speed (8.3 m/s and 20 m/s) are listed in Table 5.14.

Table 5.13.: Percentage discrepancy between current FEM model and experimental results.

Discrepancy [%]					
Result Origin	**Torque** [Nm]			**Sum**	**Mean**
	95	241	372		
v=8.3 m/s					
Current model	2.31	0.38	1.12	3.81	1.27
v=20 m/s					
Current model	1.19	1.08	2.69	4.95	1.65

Table 5.14.: Temperature Results from current FEM model and experimental results.

Temperature [°C]			
Result Origin	**Torque** [Nm]		
	95	241	372
v=8.3 m/s			
Experimental	92.0	103.0	110.0
Current model	94.1	102.6	111.2
v=20 m/s			
Experimental	96.0	106.0	112.0
Current model	94.9	104.9	115.0

Influence of the rotational speed

For the study of the influence of the rotational speed on bulk temperature of scuffing gears, it is necessary to lock the load torque in the simulation. Examining Figure 5.12 and comparing each load torque the bulk temperature behavior looks the same, minimum temperature decreases with rotational speed, but both maximum and bulk temperature increase with speed.

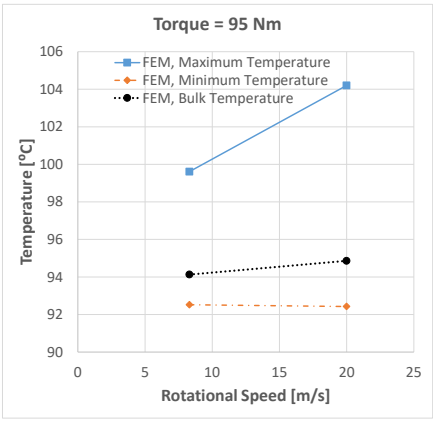

(a) Temperature result at 95 Nm.

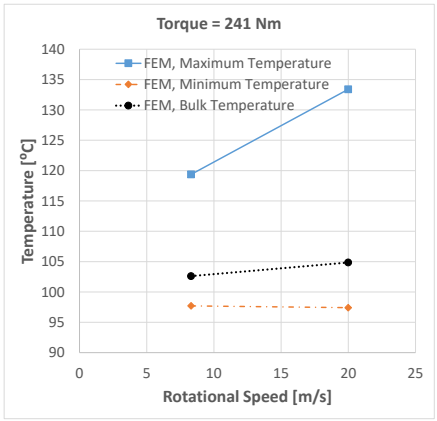

(b) Temperature result at 241 Nm.

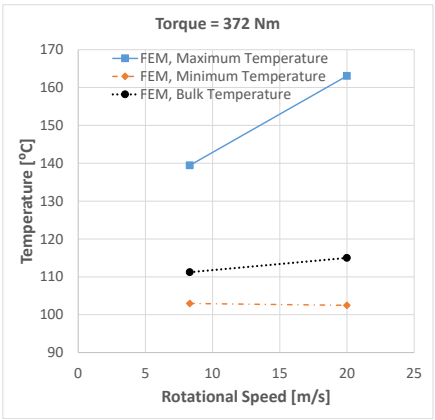

(c) Temperature result at 372 Nm.

Figure 5.12.: Temperature results for 8.3 m/s and 20 m/s at 95, 241 and 372 Nm.

In fact the increase in the heat transfer coefficients is not high enough to offset the effect of a higher power loss. The maximum temperature suffers different percentage increases with rise of load torque, indeed for 95 Nm the percentage increment is approximately 5 %, for 241 Nm it is 12 % and for 372 Nm it is 17 %.

For instance, for a 95 Nm load torque at different circumferential speeds the heat flux will increase (Figures 5.13a and 5.13b), although the Reynolds number at gear sides is higher for higher speeds (Figure 5.14c) and, consequently, the heat transfer

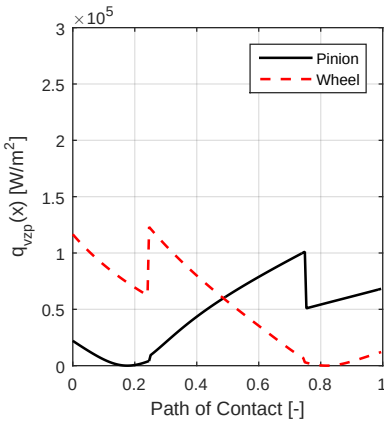

(a) Average heat flux for 8.3 m/s.

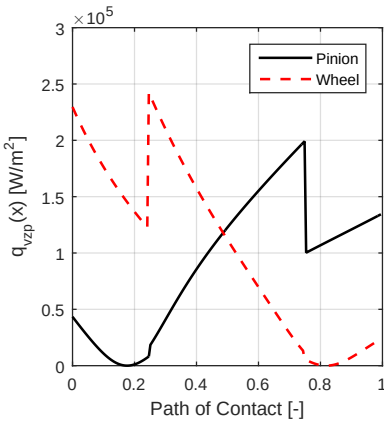

(b) Average heat flux for 20 m/s.

Figure 5.13.: Average heat flux for 8.3 and 20 m/s at 95 Nm.

coefficient is also higher the heat flux imposed in the pinion is also higher. Therefore, resulting on an increase of bulk temperature as shown in Figures 5.14a and 5.14b.

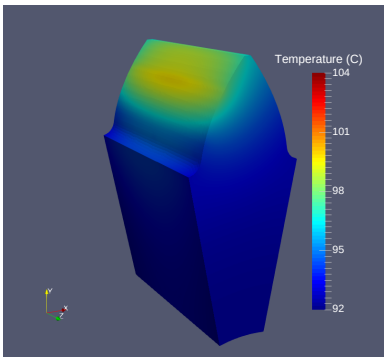

(a) Temperature solution for 8.3 m/s.

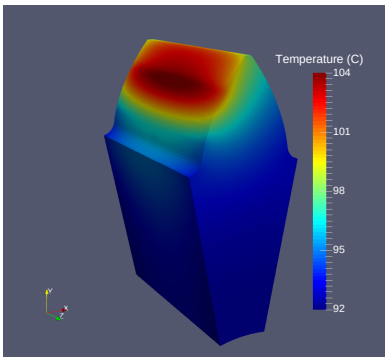

(b) Temperature solution for 20 m/s

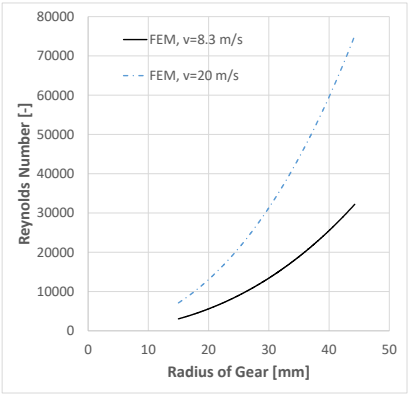

(c) Reynolds number for 8.3 and 20 m/s

Figure 5.14.: Temp. solution and Reynolds number for 8.3 and 20 m/s at 95 Nm.

5.3. Transient Model

5.3.1. Case 1 (Transient temperature in POM or PA gears)

The paper, "A numerical method for polymer composite gear flash temperature prediction" [59], introduced a numerical approximation for the polymer gear flash temperature prediction using the finite different method. *Mao et al.*'s work [59] focuses on the analysis of the flash temperature with Blok's solution provided for the quasi-steady approximation and flash temperature estimation [59].

Since the simulation with POM against POM (mechanical properties in Table 5.16), spur gears with geometric data listed in Table 5.15, with dry contact, no lubricant is used, for the operating conditions established in Table 5.17.

The mesh creation follows the same procedure described in Chapter 4 (see Figure 5.15).

Table 5.15.: Geometry of spur gear tested in case 1 - transient [59].

Geometric Data	**Transient - Case 1**	
	Pinion	Wheel
Number of teeth, z [-]	30	30
Module, m [mm]	2	
Pressure angle, α [°]	20	
Face width [mm]	17	
Addendum modification [-]	0	0
Surface finish, Ra [μm]	0.5	

Table 5.16.: Material properties of pinion polymer used [59].

Polymer type	**Acetal - POM**
Young modulus , E [GPa]	2.69
Poisson's ratio, υ [-]	0.3
Density, ρ [kg/m^3]	1410
Thermal conductivity, k [W/(m·K)]	0.3
Specific heat, c [J/(kg·K)]	1470

Table 5.17.: Operating conditions applied on the FEM simulation - transient Case 1 [59].

Operating Conditions	
Torque of the driving shaft [Nm]	10
Rotational speed, n [rpm]	1000
Initial tooth (wall) temperature, T_{exp}[°C]	20
Friction coefficient, μ [-]	0.21

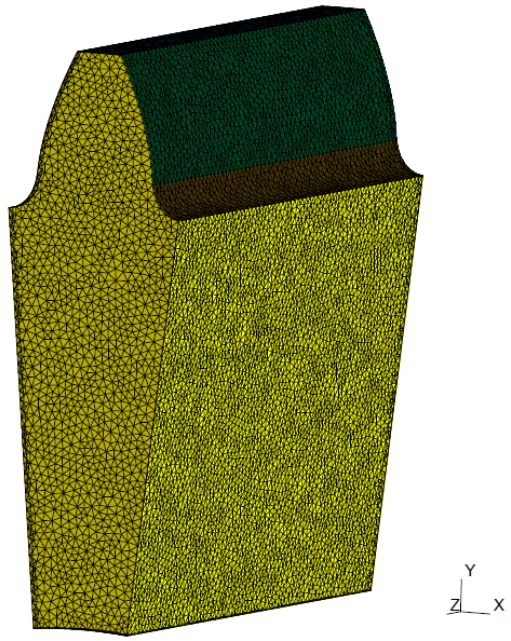

Figure 5.15.: Mesh created on Gmsh with 40636 nodes and 219122 elements.

Generic results

The transient simulation, shown in Chapter 4, will start with an initial temperature solution based on the bulk temperature calculated for a steady state simulation.

In order to simulate the correct continuous and instantaneous heat flux imposed by the transient simulation, the contact line for the path of contact needs to be discretized to interpolate the value of the heat flux at each node.

Starting by calculating the transient time or the meshing time, to ensure continuity, the discretization of the contact line will be the same size as the number of time steps used for the transient simulation.

The case SIF generated, shown in Appendix F for a transient simulation, will start by calculating the time interval and divide it by the number of time steps used.

It is important to remember the main difference between the transient simulation and the quasi steady-state: in the transient simulation the heat flux is applied locally at a given time step, function of time and space, (see Figure 5.16b) instead of an average heat flux for the quasi-steady simulation, which only takes account of the space dependency (see Figure 5.16a).

Figure 5.19 clearly shows the heat flux generated locally is 200 times higher than the average heat flux applied for a steady-state condition. In fact, because of the nature of a transient simulation, the heat flux is dependent not only on space but also on the meshing time; therefore, the contact between the two meshing gears will occur at different contact radius imposed by the meshing time. So, the radius of contact, the Hertzian half-width as well as the heat flux distribution must be

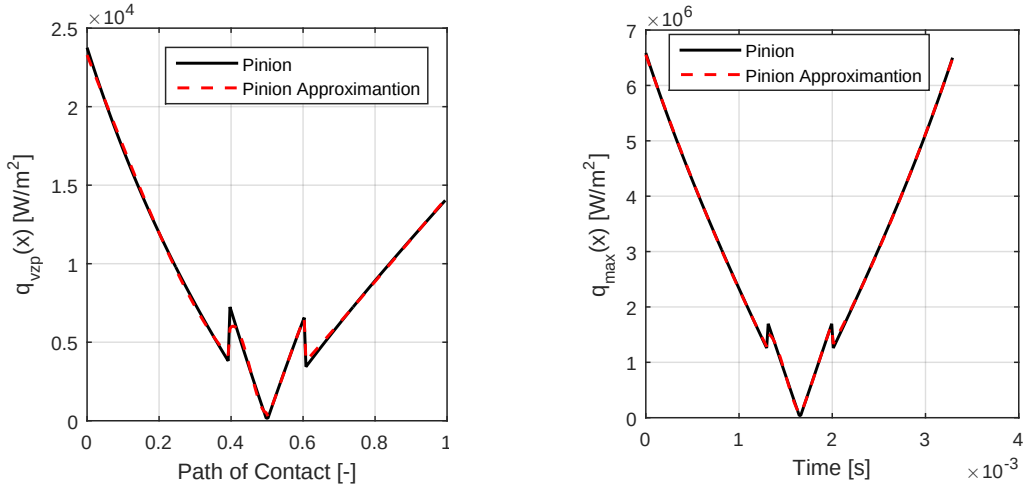

(a) Average heat flux.

(b) Maximum local heat flux.

Figure 5.16.: Average and maximum local heat flux applied for steady or transient simulation.

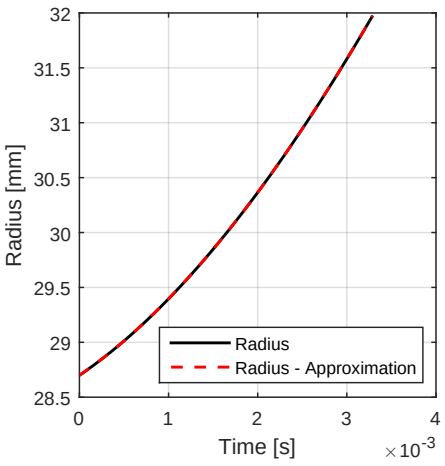

(a) Contact radius approximation.

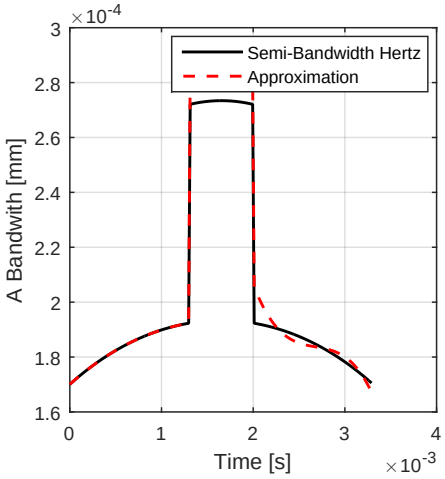

(b) Hertzian half-width approximation.

Figure 5.17.: Approximation of the contact radius and Hertzian half-width over time.

calculated in function of time. The approximations of the contact radius and the Hertzian half-width is presented in Figures 5.17a and 5.17b.

Take for instance, the heat flux applied for the meshing time $t = 3.4898 \cdot 10^{-4}$ s at contact radius $r = 28.9102$ mm, which is represented in Figure 5.18.

Finally, running the transient simulation with the code presented in Appendix F, temperature results along the path of contact can be observed in Figure 5.19, where the bulk temperature distribution is presented in Figure 5.19a and the flash temperature distribution is presented for each meshing position in Figures 5.19b-5.19f.

By analyzing the time steps is clearly that heat source is moving towards the

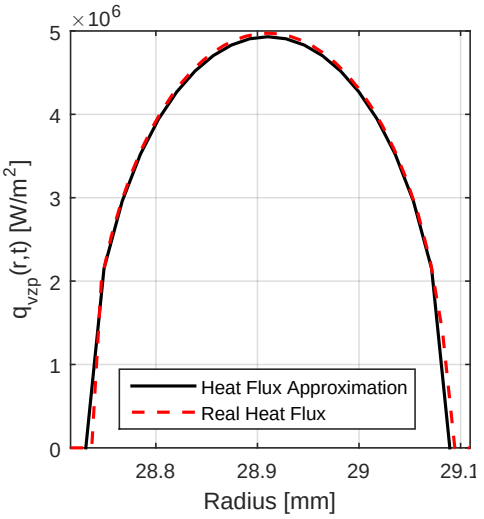

Figure 5.18.: Heat flux distribution applied locally at conctact radius 28.9102 mm.

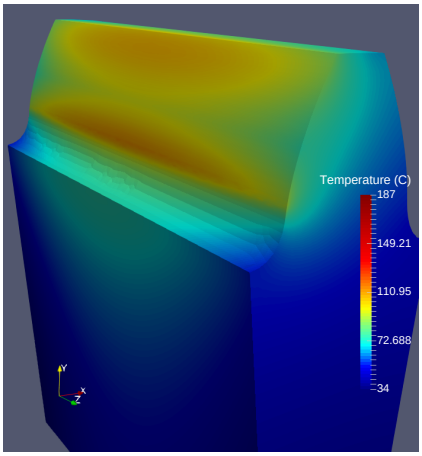

(a) Initial Temperature distribution - Bulk.

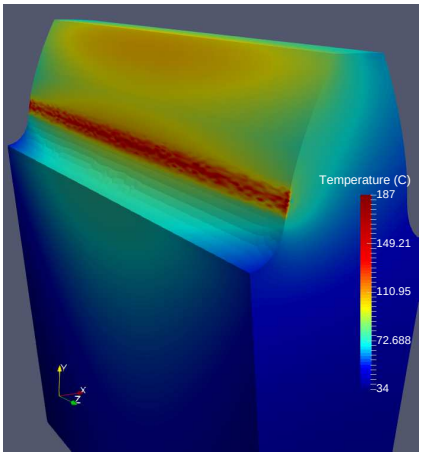

(b) Temperature distribution at 0.000482 s.

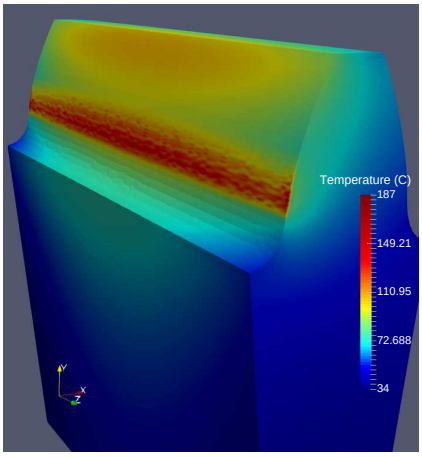

(c) Temperature distribution at 0.001130 s.

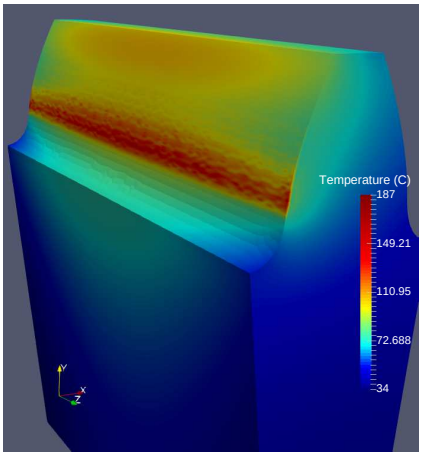

(d) Temperature distribution at 0.001778 s.

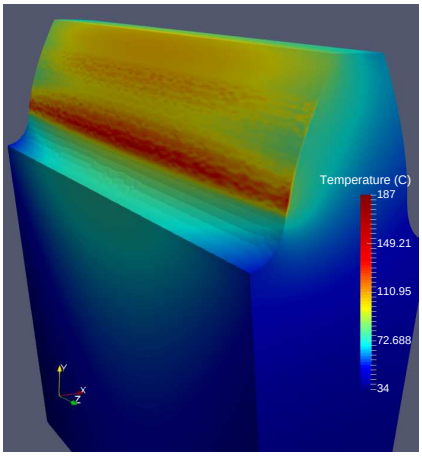

(e) Temperature distribution at 0.002426 s.

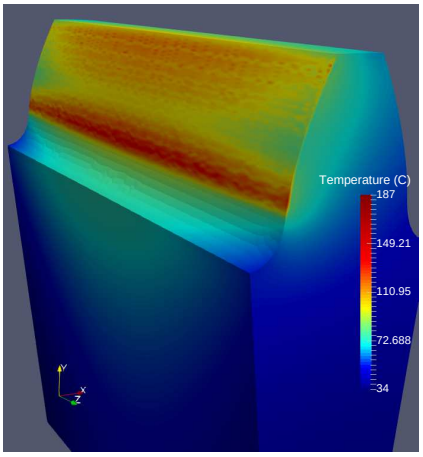

(f) Temperature distribution at 0.003290 s.

Figure 5.19.: Temperature distribution for transient simulation on POM gears for 1000 rpm at 10 Nm.

tooth tip and the maximum temperature and minimum temperature observed is 187°C and 34 °C, respectively. One of the most important conclusions was the non presence of oil at meshing will harshly aggravate the maximum temperature over time and, subsequently, degenerate the gear mechanical properties.

This study of a transient simulation was a qualitative validation since to measure every maximum temperature observed at each contact radius would take too much time. Also, for a much accurate result for this temperature the contact area needs to be more discretized and the simulation done with a computer with higher numerical resources, since the results presented in this work are taken with an everyday work computer.

5.3.2. Case 2 (Transient simulation for metallic spur gear)

The previous example was an transient case for a dry contact with polymeric gears. Although, due to the low discretization and the low thermal properties of the plastic the flash temperature behavior was not validated. The present case will validate the behaviour of the maximum temperature over the path of contact.

In this case the geometry applied was the same first Steady-state case, with the geometrical data presented in Table 5.1, lubricated with the same oil, whose properties listed in Table 5.2 [57], although with different operating conditions as shown in Table 5.18.

Results and discussion

The average heat flux calculated for steady-state is shown in Figure 5.20a, and the maximum heat flux applied locally and for each meshing time is shown in Figure 5.20b.

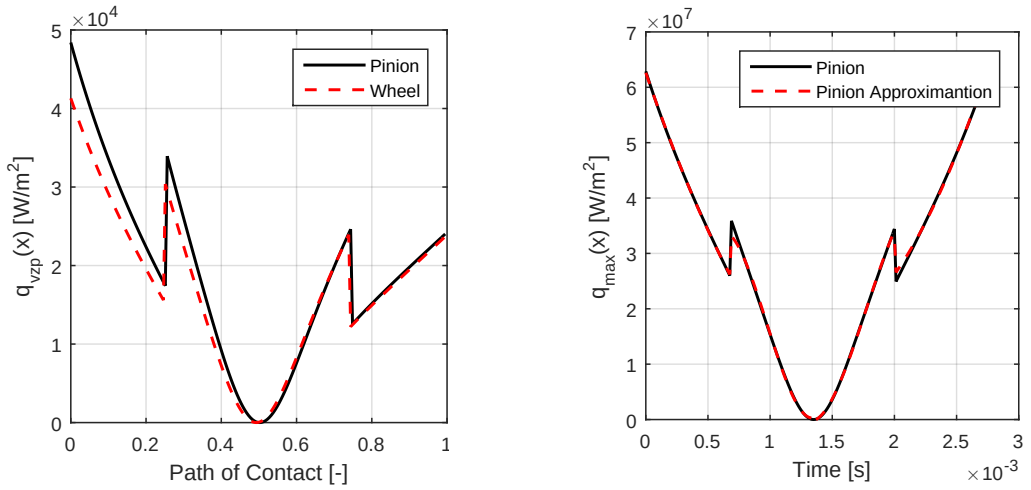

(a) Average heat flux - steady state.

(b) Maximum heat flux - transient state.

Figure 5.20.: Average heat flux and maximum heat flux for 2000 rpm at 13.7 Nm.

Table 5.18.: Operating conditions applied on the FEM simulation - transient case 2.

Operating Conditions	
Torque of driving shaft [Nm]	13.7
Rotational Speed, n [rpm]	2000
Initial Tooth (Oil/Wall) Temperature, T_{exp}[°C]	90
Initial Tooth (Ambient) Temperature, T_{amb}[°C]	70

The maximum temperature results are shown in Figure 5.21 over the meshing time. It is clear that there will be two maximum temperatures along the path of contact, near the tip and root of the meshing gear. A fitted line was added for better view of the maximum temperature results.

It is important to notice that these results were obtained with a usual computer not approximate for difficult numerical calculations and, therefore, a poor discretization of time was employed with only 50 time steps, due to high calculation time. Better results could be obtained with a more discretized time space, although the behavior of the maximum temperature is well represented in Figure 5.21.

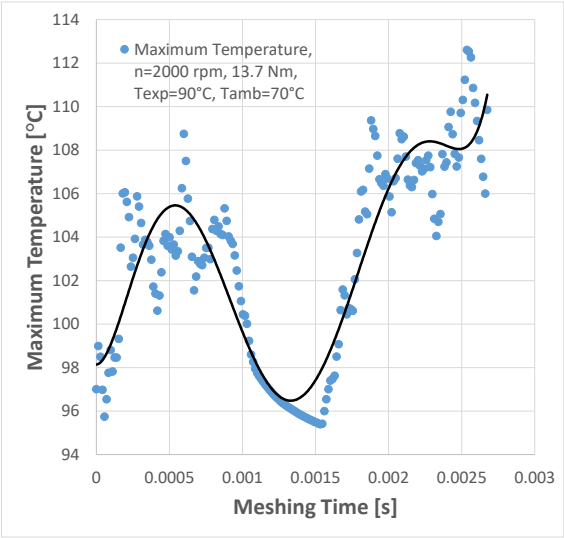

Figure 5.21.: Maximum temperature over time for lubricated gears at 2000 rpm and 13.7 Nm.

Finally, running the transient simulation with the code as presented in Appendix F, temperature results along the path of contact can be observed in Figure 5.22, where the bulk temperature distribution is presented in Figure 5.22a and the flash temperature distribution is presented for each meshing position in Figures 5.22b-5.22f.

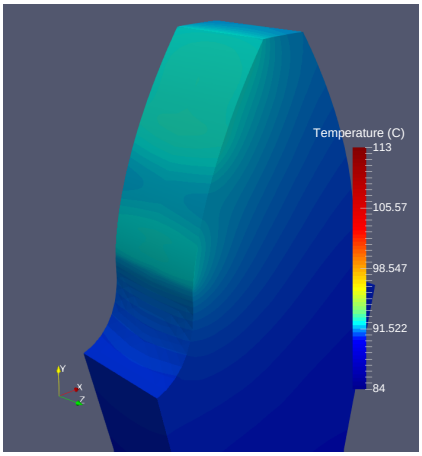

(a) Initial Temperature distribution - Bulk.

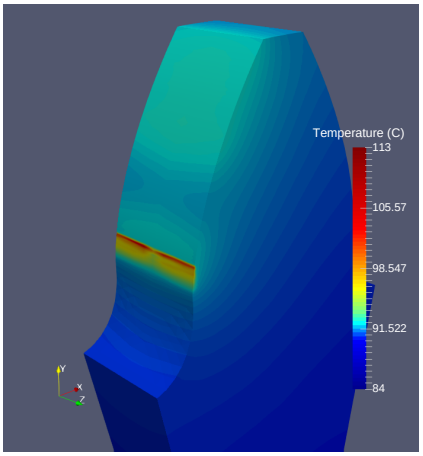

(b) Temperature distribution at 0.000669 s.

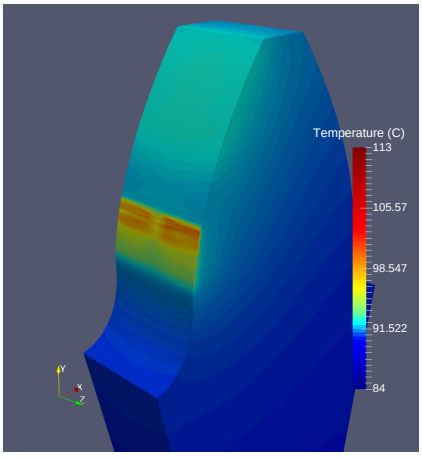

(c) Temperature distribution at 0.001212 s.

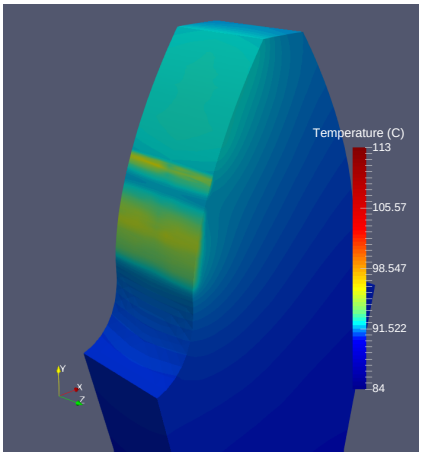

(d) Temperature distribution at 0.001756 s.

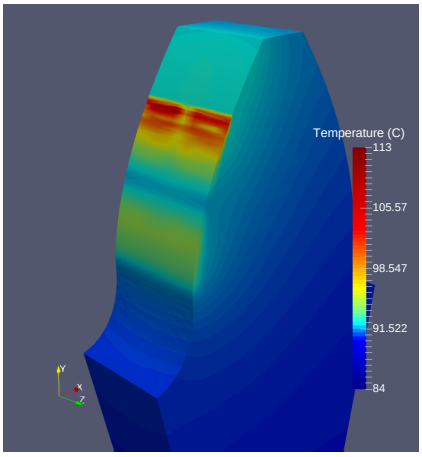

(e) Temperature distribution at 0.002299 s.

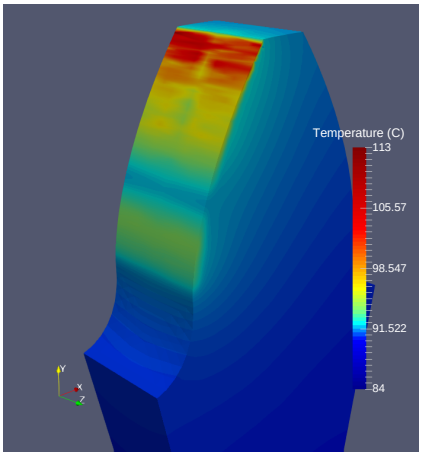

(f) Temperature distribution at 0.002675 s.

Figure 5.22.: Temperature distribution for Transient Case 2 over time for 2000 rpm at 13.7, T_{exp}=90°C and T_{amb}=70°C.

5.4. Closure

The FEM model created for the simulation of the temperature distribution in steady-state and transient-state behaves very well, having small errors when compared with experimental data. However, it is noticed that the current FEM model shows higher numerical errors at low torques (as discussed previously in cases 1 and 2 of steady-state), having less discrepancies with the increase of torque.

For the transient-state simulation, the behaviour of the maximum temperature was validated (having two maximum temperatures at the tip and root of the tooth and a minimum at the pitch point), although the numerical value for each point was not possible due to the time and resources available. In fact, for a better resolution of the numerical values for maximum temperature a higher discretization of the time space as well as better numerical computation resources are needed, since the results were taken with an everyday work computer.

Therefore, it is possible to conclude that the current FEM model is well validated and prepared for the study on the influence of the implementation of a metallic insert in a polymeric body.

Chapter 6.

Hybrid Gears

6.1. Introduction

In the last chapter the validation of the FEM model was presented. The main objective of this thesis was to study the influence of the implementation of a metallic insert over a polymeric gear. This chapter will focus on the implementation of a metallic insert over a standard very widely used gear geometry.

The implementation of an insert over the polymeric gear implies a new boundary condition between metal and plastic. In fact the study of heat transfer mechanisms between two bodies is the main problem in a few areas of engineering, for example in aerospace engineering. Moreover, it is known that plastic gears' mechanical resistance properties are highly dependent on the imposed temperature in the gear, it becomes crucial to control the maximum temperature reached by the gear. Therefore, it is important to study how the bulk temperature is influenced with the implementation of a metallic insert inside the gear tooth.

A general approach for this study starts with a simple insert in the shape of a rectangular cuboid in the middle of the teeth as shown in Figure 6.1, so the symmetry condition over the Cartesian axis of the 3D gear tooth model is preserved.

However, the thermal contact resistance (TCR) is influenced by many factors. Take for instance the variation of thermal contact resistance with roughness and waviness of the contacting surfaces (in case of flat, wavy-smooth or even wavy-rough surface) or the effect of the existence of oxides at the contacting surface level [60].

When analyzing machined surfaces microscopically it is common to observe some defects at a low-scale as result of the tool shape, the machining process or even from the mold itself (also known as roughness) or even at a larger scale because of the heat treatment or vibration. In this way, the imperfections of the surface geometry creates the connection at specific points of the interface between the two bodies in contact.

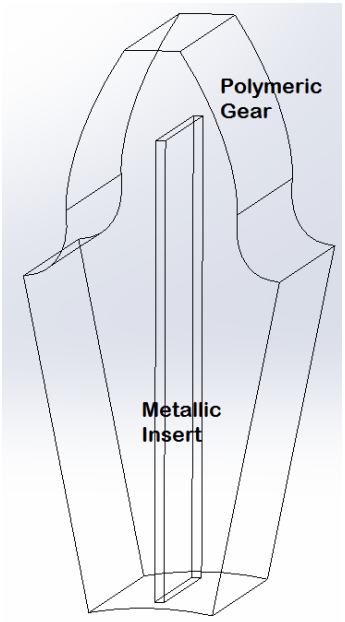

Figure 6.1.: Basic hybrid-gear model implemented.

6.2. Thermal Contact between two bodies

One way to accurately ascertain the temperature distribution between two thick solid bodies in contact is to define a thermal contact conductance/resistance between the temperature drop (as shown in Figure 6.2a) and the heat flux that passes at the apparent cross-section area. The thermal resistance is given by equation (6.1).

$$R_{tc} = \frac{\Delta T_c}{q \cdot A_a} \tag{6.1}$$

$$h_{tc} = h_c + h_{rad} + h_g \tag{6.2}$$

Where the total heat transfer contact coefficient, h_{tc}, is a function of three parts (see Figure 6.2b): conduction through the contacting points(h_c), radiation through the gaps between the two surfaces (h_{rad}) and gas conduction through the gas that fills these gaps (h_g), as shown in equation (6.2).

A hybrid polymer gear can be injected in a mold with the shaft (which carries the metallic inserts), heat transfer through the gas that fills the gaps between the two surfaces will be neglected since the dimensions of these gaps are insignificant. As for the heat transfer from the radiation mode, it is also negligible for the same reason. So, the only heat transfer mode that will be taken into consideration is conduction through the contacting points: $h_{tc} = h_c$.

The heat transfer through the contact is a very complex problem, which can be dependent of certain parameters established by mechanical, thermal or geometric

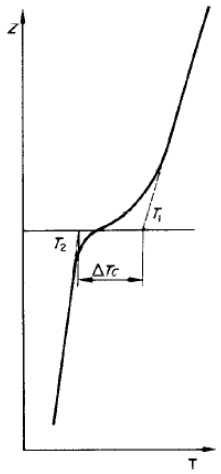

(a) Temperature drop [61].

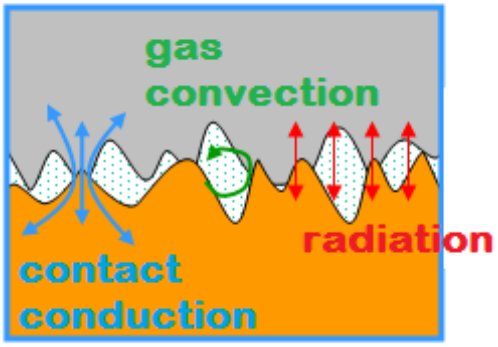

(b) Modes of heat transfer [62].

Figure 6.2.: Temperature drop and fundamentals modes of heat transfer at thermal joint between two bodies.

properties of the contacting surfaces. In fact, the contact resistance is dependent on the gap thickness, the waviness, roughness of the contacting bodies and the thermal conductivities of the solids. Therefore, there will be the need use as simplifying assumptions that the contact is static with no vibration effect present and the solids in contact will have isotropic thermal and physical properties [60].

For the study of the wide variety of polymers' application in thermal designs a portray of the thermal contact conductance is essential to this cause. Therefore the study of this type of contact conductance is normally studied in the interface that relies on: a polymer against metal or a polymer against polymer interface [63].

6.2.1. Thermal resistance models

The constant need to describe and tounderstand the problem of thermal contact conductance lead to formulation of a large number of models. The diverging models are dependent on the deformation of the contacting bodies: elastic (for small ones), plastic (large contact strain) or elasto-plastic model (combination of both).

Effective Surface

For the thermal contact conductance modeling is crucial to calculate two parameters: RMS (Root Mean Square) Roughness, σ, and the absolute asperity slope, m_a given by equations (6.3)-(6.4)

$$\sigma = R_q = \sqrt{\frac{1}{L}\int_0^L y^2 dx} \tag{6.3}$$

$$m_a = \frac{1}{L}\int_0^L \left|\frac{dy}{dx}\right| dx \tag{6.4}$$

If the heights of the two contact surface follow a Gaussian distribution it can be approximated to a single rough surface with a smooth surface as shown in Figure 6.3.

The two parameters, discussed previously (effective RMS roughness - σ_s- and effective absolute mean asperity slope - m_s) [64] are calculated by equation (6.5) and (6.6):

$$\sigma_s = \sqrt{\sigma_1^2 + \sigma_2^2} \tag{6.5}$$

$$m_s = \sqrt{m_1^2 + m_2^2} \tag{6.6}$$

Initial studies of heat flow channel and TCR

The initial study of heat flow between two solid bodies was based on the model of Figure 6.4, which was simplified by Centinkale and Fishenden into a cylinder model [65]. These results show that although the two cylinders may have different conductivity the heat is also conducted from the interstitial gap (adiabatic plane, z=0, see Figure 6.2a).

In practice there is not only one single contact area between the two solid bodies, indeed the contact may be present as a multiple of contact areas distributed over an

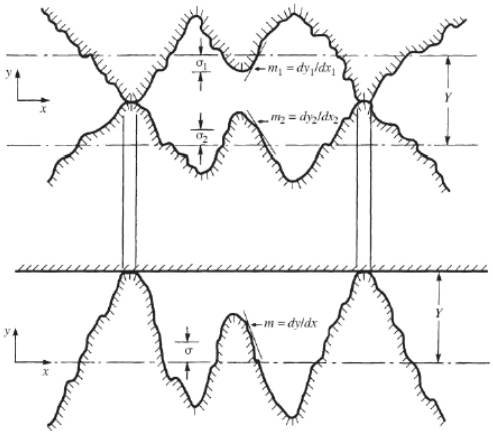

Figure 6.3.: Transformation of two contact surface into one rough surface with an effective RMS roughness and effective absolute mean asperity slope.

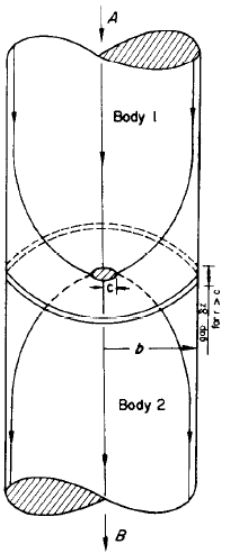

Figure 6.4.: Elemental flow channel.

apparent area of contact (A_a). Yovanovich [66] proposed a general thermal model to for conforming rough surfaces, which describes the constrictions and resistance of a single asperity in contact and extends it to the whole surface. For a single contact spot (i) of the contact between two general surfaces (1 and 2):

$$R_{si} = \frac{\psi_{i1}}{4 \cdot k_1 \cdot A_i} + \frac{\psi_{i2}}{4 \cdot k_2 \cdot A_i} \tag{6.7}$$

Taking into consideration the effective conductivity, because of the symmetry at the interface, $k_s = 2 \cdot k_1 \cdot k_2 / (k_1 + k_2)$, we obtain:

$$R_s = \frac{\psi}{2 \cdot k_s \cdot A_i} \tag{6.8}$$

Finally, to calculate the thermal contact conductance, equation 6.9 is used.

$$h_c = 2 \cdot k_s \frac{c}{b} \times \frac{1}{\psi} \tag{6.9}$$

Where the radius of a contact spot, ψ, is given by $\psi = (1 - \varepsilon)^{1.5}$, being $\varepsilon = c/b = \sqrt{A_r/A_a}$ as the ratio between the real area of contact (A_r) and apparent area of the contact.

6.2.2. Plastic Contact Model (CMY)

Yovanovich [61, 66] was able predict the thermal contact resistance assuming that strain of the contacting asperities is large, implying that the plastic deformation

of the asperities occurs during first loading of the contacting surfaces and that the contacting asperities of the softer surface will suffer plastic deformation.

The important ratio between the real area of contact and the apparent area of contact is proportional to the fraction of the apparent contact pressure -P- and the microhardness of the softer surface - H_p. Some important geometrical parameters are important determined for use with equation (6.9) [61, 66].

$$n_{cb} = \frac{c}{b} = 1/16 \left(\frac{m_s}{\sigma_s}\right)^2 \cdot \frac{exp(-\varrho^2)}{erfc\left(\varrho/\sqrt{2}\right)} \tag{6.10}$$

$$a = \sqrt{\frac{8}{\pi}} \frac{\sigma_s}{m_s} \left(\frac{\varrho^2}{2}\right) \cdot erfc\left(\frac{\varrho}{\sqrt{2}}\right) \tag{6.11}$$

$$\varrho = \sqrt{2} erfc^{-1}\left(\frac{2A_r}{A_a}\right) \tag{6.12}$$

The term ϱ being the relative mean plane separation and the dimensionless thermal contact conductance, given by equation (6.13).

$$C_c = \frac{h_c \sigma_s}{k_s m_s} = 1.25 \cdot \left(\frac{P}{H_p}\right)^{0.95} \tag{6.13}$$

Yovanovich introduced the idea of the microhardness present on a surface layer and found that the microhardness is dependent on the depth of the indentation according to the function $H_{vick} = c_1 \cdot (d_v/d_0)^{c_2}$. Posterior work revealed a relationship to use directly in the equation (6.13):

$$\frac{P}{H_p} = \left[\frac{P}{c_1 \cdot (1.62 \cdot (\sigma_s/m_s))^{c_2}}\right]^{1/(1+0.071c_2)} \tag{6.14}$$

6.2.3. Elastic Contact Model (Mikic)

Mikic [67] was able to determine that the elastic deformation is proportional to the contact pressure by $A_r/A_a = P/\left(E^{'} m_s/\sqrt{2}\right)$, where the effective elastic modulus $(E^{'})$ is calculated with (being ν_p the Poisson's ratio):

$$E' = \frac{E_1 E_2}{E_2\left(1-\nu_{p1}^2\right) + E_1\left(1-\nu_{p2}^2\right)} \tag{6.15}$$

Similarly, to the "plastic microhardness", there is the "elastic microhardness" - H_e- calculated by $H_e = E^{'} m_s/\sqrt{2}$. Moreover, comparing elastic area with the purely plastic deformation, the contact area in plastic deformation is twice as larger as the area in elastic deformation. Some geometric parameters are important to determine using equations (6.16),(6.17) and (6.18) [67]:

$$n_{cb} = \frac{c}{b} = 1/16 \left(\frac{m_s}{\sigma_s}\right)^2 \cdot \frac{exp(-\varrho^2)}{erfc\left(\varrho/\sqrt{2}\right)} \tag{6.16}$$

$$a = \sqrt{\frac{2}{\pi}} \frac{\sigma_s}{m_s} \left(\frac{\varrho^2}{2}\right) \cdot erfc\left(\frac{\varrho}{\sqrt{2}}\right) \tag{6.17}$$

$$\varrho = \sqrt{2} erfc^{-1}\left(\frac{4A_r}{A_a}\right) \tag{6.18}$$

So, the equation of the dimensionless thermal contact conductance for a relative pressure range interval between $10^{-5} \leq P/H_e \leq 0.2$ is given by:

$$C_c = \frac{h_c \sigma_s}{k_s m_s} = 1.54 \cdot \left(\frac{P}{H_e}\right)^{0.94} \tag{6.19}$$

From there on, *Fuller et. al* [68] suggested the change of the elastic contact hardness H_e for the polymer elastic contact hardness, H_{poly}. Rewriting equation (6.19) [68]:

$$H_{poly} = \frac{E_{poly} \cdot m_s}{2.3} \tag{6.20}$$

$$C_c = \frac{h_c \sigma_s}{k_s m_s} = 1.49 \cdot \left(\frac{P}{H_{poly}}\right)^{0.935} \tag{6.21}$$

6.2.4. Elasto-Plastic Model (SY)

Yovanovich and Sridhar [69] were able to describe a wide range of material behaviour from the elastic model studied by Mikic [67] to the plastic model by Cooper and Yovanovich [66]. The relationship between the contact areas and the contact pressure and elasto-plastic microhardness, is given by equation (6.22) [69].

$$H_{ep} = \frac{2.76 \cdot S_f}{\left[1 + \left(\frac{6.5}{\varepsilon_c}\right)^2\right]^{\frac{1}{2}}} \tag{6.22}$$

Where the non-dimensional contact strain is $\varepsilon_c = 1.67 \cdot E' m_s / S_f$ and to calculate the yield/flow stress S_f and the elasto-plastic microhardness (H_{ep}) there is the need to use an iterative procedure until the value converges, starting with an initial guess of H_{ep} as $\sqrt{H_p \cdot H_e}$ (equations (6.23)-(6.29)).

$$S_f = \frac{1}{2.76\sqrt{\frac{1}{H_{ep}^2} - \frac{1}{H_e^2}}} \tag{6.23}$$

$$\varepsilon_c = 1.67 \cdot \frac{E' m_s}{S_f} \tag{6.24}$$

$$f_{ep} = \frac{\left[1 + \left(\frac{6.5}{\varepsilon_c}\right)^2\right]^{0.5}}{\left[1 + \left(\frac{13.0}{\varepsilon_c}\right)^{1.2}\right]^{\frac{1}{1.2}}} \tag{6.25}$$

$$\varrho = \sqrt{2} erfc^{-1} \cdot \left(\frac{1}{f_{ep} \cdot \varepsilon_c} \cdot \frac{2P}{H_{ep}}\right) \tag{6.26}$$

$$a_m = \sqrt{\frac{8 \cdot f_{ep} \cdot \varepsilon_c}{\pi}} \frac{\sigma_s}{m_s} exp\left(\frac{\varrho^2}{2}\right) erfc\left(\frac{\varrho}{\sqrt{2}}\right) \tag{6.27}$$

$$d_v = \sqrt{2\pi} \cdot a_m \tag{6.28}$$

$$H_{ep} = \frac{H_{vick}}{0.9272} \tag{6.29}$$

Where H_{vick} is the Vickers microhardness given by $H_{vick} = c_1 \cdot d_v^{c_2}$.

The geometrical parameter n_{cb} is calculated in the same way as in the past two models, however the dimensionless thermal contact conductance for $\varepsilon_c < 5$ is given by equation (6.30).

$$C_c = \frac{h_c \sigma_s}{k_s m_s} = 1.54 \cdot \left(\frac{P}{H_{ep}}\right)^{0.94} \tag{6.30}$$

6.3. Influence of gear material on non hybrid gears

This section is presented as an visualization of a comparative study for the use of a polymeric or a metallic material in a pinion in dry contact running for a steady state.

6.3.1. C14 gear

The gear used for the study will be a C14 standard pitting gear with the geometric data listed in Table 6.1.

6.3.2. Mesh Generation

Following the same steps described in the Chapter 4, the resulting mesh is shown in Figure 6.5

6.3.3. Material Properties and Operating Conditions

The materials chosen for the gear were steel, POM, copper and aluminum (alu), whose properties are listed in Table 6.2. For this reason, the operating conditions imposed for the analysis are described in Table 6.3.

Table 6.1.: Geometry of a C14 spur gear [10].

Geometric Data	**C14**	
	Pinion	Wheel
Number of teeth, z [-]	16	24
Module, m [mm]	4.5	
Pressure angle, α [°]	20	
Face width [mm]	14	
Addendum modification [-]	0.1817	0.1715
Inner diameter of the shaft [mm]	30	
Surface finish, Ra [μm]	0.5	

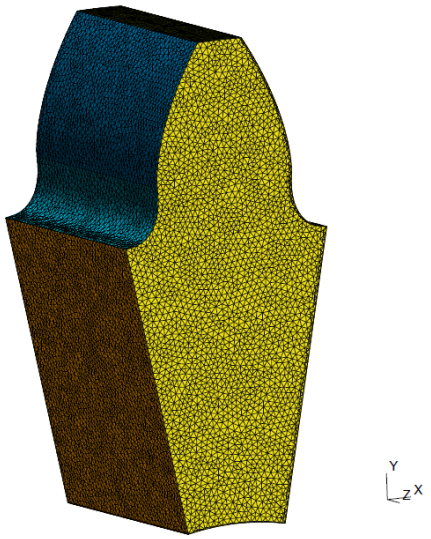

Figure 6.5.: C14 tooth mesh generated with 296620 elements and 49386 nodes.

Table 6.2.: Mechanical and thermal properties of the different materials [70].

Properties	**Copper**	**Aluminum**	**Steel**	**POM**
Young Modulus , E [GPa]	117.00	69.00	210.00	2.69
Poisson's ratio, υ [-]	0.36	0.33	0.30	0.30
Density, ρ [kg/m^3]	8933	2702	7870	1410
Thermal conductivity, K [W/(m·K)]	401.00	237.00	41.80	0.30
Specific heat, c [J/(kg·K)]	385	903	493	1470

Table 6.3.: Operating conditions applied for the dry contact.

Operating Conditions	
Torque of driving shaft [Nm]	10
Rotational Speed, n [rpm]	1000
Initial Tooth (Wall) Temperature, T_{exp}[°C]	20
Initial Tooth (Ambient) Temperature, T_{amb}[°C]	15

6.3.4. Coefficient of friction

Polymeric gears have the possibility to work with dry contact running due to its characteristic of being life-lubricated. This happen essentially due to its low coefficient of friction, as shown in a comparison with other materials, Table 3.2.

6.3.5. Heat Flux Vs. material

As the heat flux generated by friction is dependent on the coefficient of friction, varying the material in study it should have a direct consequence on the heat applied to the meshing surface and it was expected that the material with the highest coefficient of friction would also have the highest heat flux imposed, as shown in Figure 6.6.

6.3.6. Simulation results

Analyzing Figures 6.7a, 6.7b, 6.7c and 6.7d, which show the bulk temperature solution found for the operating conditions stated above for the different materials: POM, steel, copper and aluminum, respectively. The selection of material chosen for a dry contact is quite important, emphasizing the use of polymeric gear for this type of simulation/work.

Moreover, the temperature gradient found for the POM gear tooth is quite high compared to the other situations, as shown at Table 6.4, mostly due to the fact that POM's thermal conductivity is low. In fact, using polymeric gear can decrease the maximum temperature to 32%, 59% and 110% and the minimum temperature to 689 %, 886% and 1210% compared with steel, copper and aluminum, respectively.

The heat transfer coefficient for the gear sides implemented is constant along the gear side, as shown in Figure 6.8,since it is a dry contact simulation and the lubricant used is the ambient air with very low density when comparing with a lubricant oil, for instance, it results that the Reynolds number is almost independent of the radius.

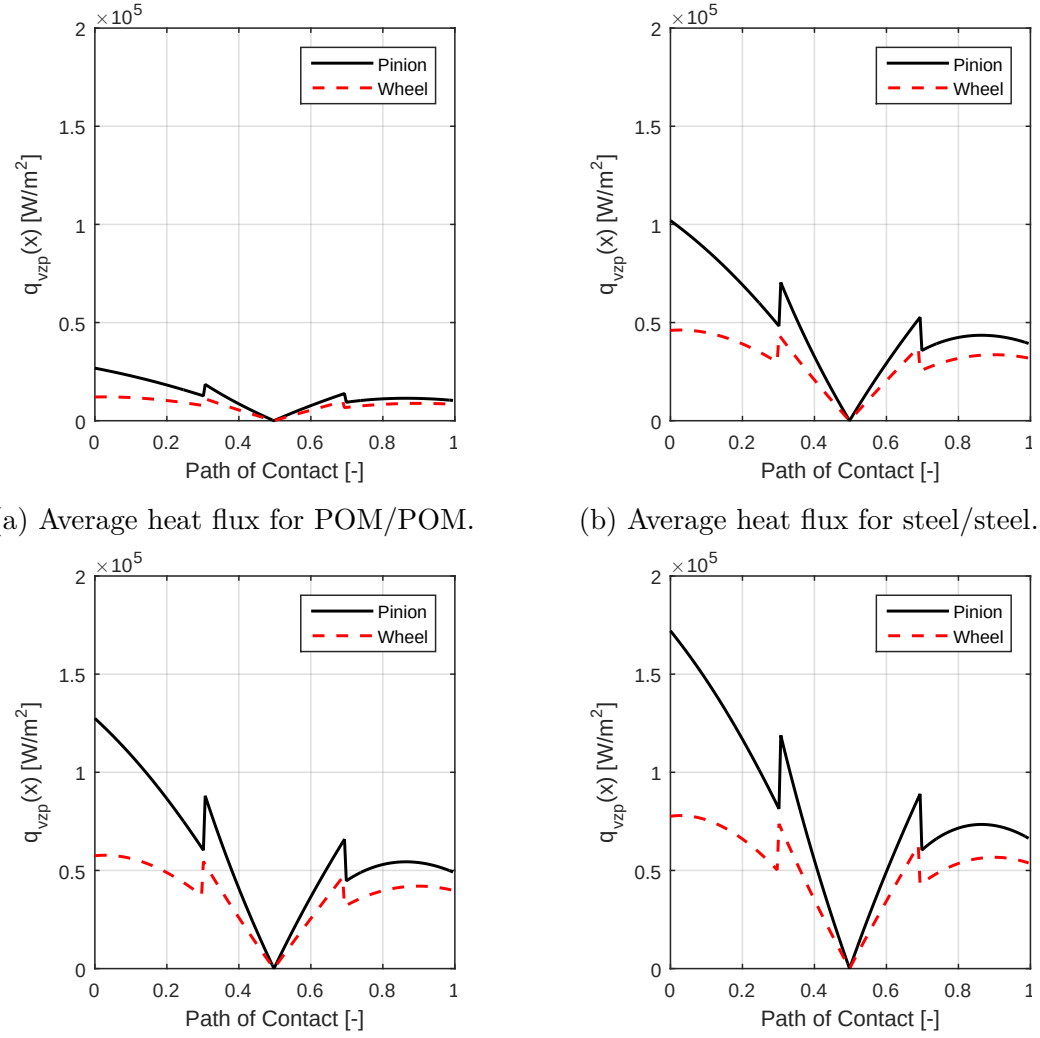

(a) Average heat flux for POM/POM.

(b) Average heat flux for steel/steel.

(c) Average heat flux for copper/copper.

(d) Average heat flux for alu/alu.

Figure 6.6.: Average heat flux applied for the various materials at 1000 rpm and 10 Nm of load torque.

Table 6.4.: Maximum and minimum temperature for different materials.

Material	**Min. Temperature** [°C]	**Max. Temperature** [°C]
POM/POM	22.28	139.40
Steel/Steel	175.87	184.08
Copper/Copper	219.70	221.53
Aluminum/Aluminum	291.78	293.24

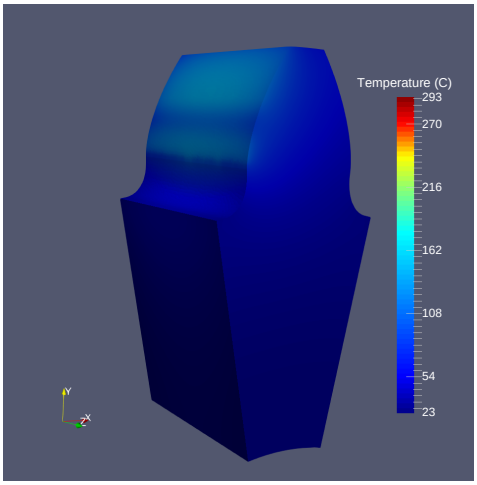

(a) Bulk temperature for POM (T_{max}=139.4°C).

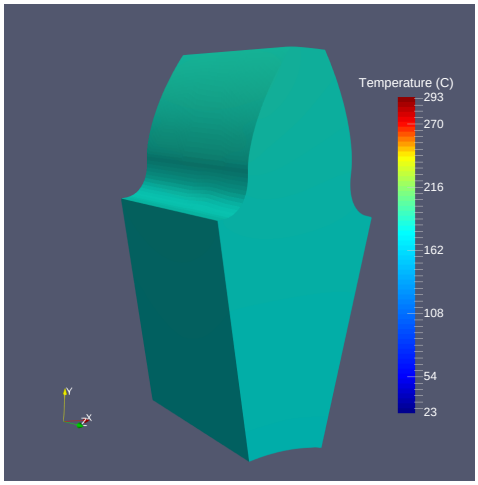

(b) Bulk temperature for steel (T_{max}=184.1°C).

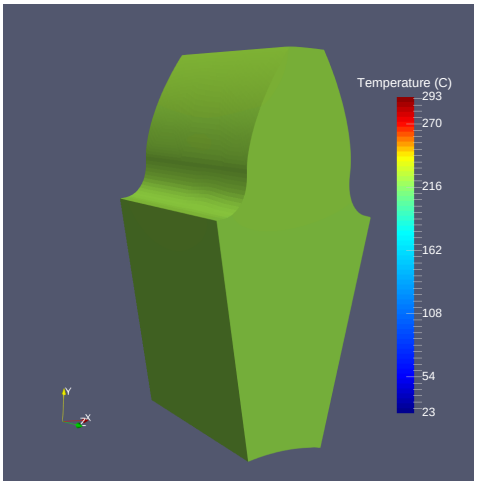

(c) Bulk temperature for copper (T_{max}=221.5°C).

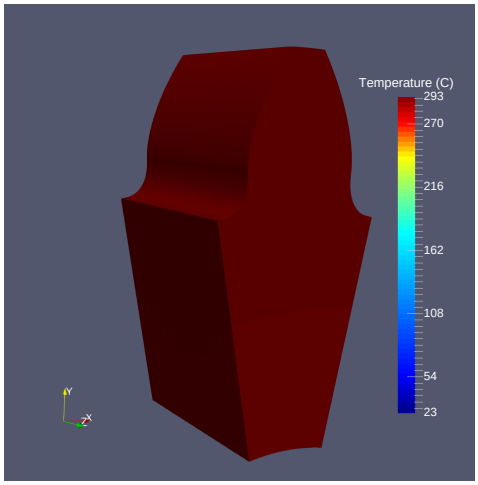

(d) Bulk temperature for aluminum (T_{max}=293.2°C).

Figure 6.7.: Bulk temperature for various materials at 1000 rpm and 10 Nm of load torque.

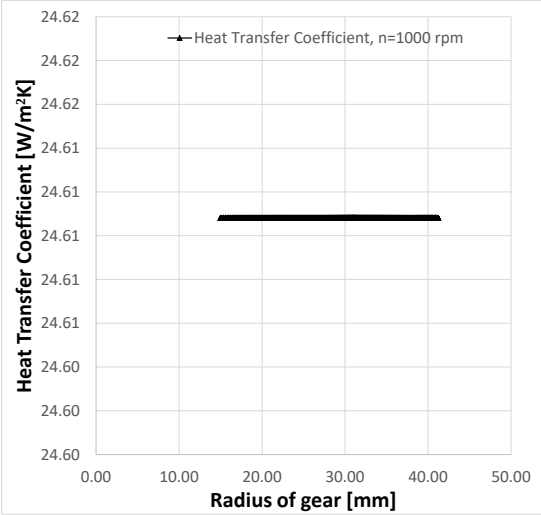

Figure 6.8.: Heat transfer coefficients at gear side for the different materials with dry contact simulation.

6.4. Hybrid-gears concept

6.4.1. Generic Geometrical model and FEM implementation

As explained at the beginning of this Chapter, it is fundamental to control the maximum temperature reached by the gear, since the plastic's mechanical properties are highly dependent on temperature. For this reason a hybrid gear with the implementation of a metallic insert was modeled, as shown in the initial approach in Figure 6.1.

For the creation of the second volume (implementation described in Appendix G) a shared boundary condition for the bottom surface of the gear and the bottom surface of the insert as well as a new boundary condition of heat gap function with the correspondent heat transfer coefficient between the contacting surfaces (thermal contact) have to be defined.

The last function (*"Heat Gap"*) will need some considerations when reading the mesh into Elmer Solver. In order to equalize the temperature solution values of each pair of contacting boundary condition the Elmer Solver needs a duplicated node for each node at the interface, that is, a node with the same coordinates but one for each contacting surface. So, when reading the mesh on Elmer GUI before saving the mesh and nodes files, a new command for the shared boundary condition is applied by adding the two codes: *discont bc_ID* (the nodes at contacting surfaces are duplicated - choosing a boundary condition ID (*bc_ID*)) and *autoclean* (to delete the extra nodes generated at each corner, because there are 3 contacting surfaces on each corner).

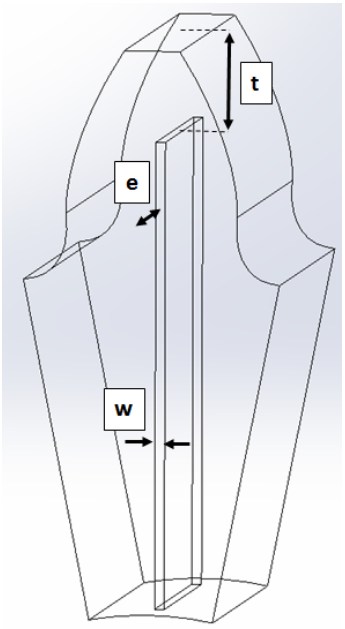

Figure 6.9.: Basic hybrid-gear model implemented with geometrical parameters.

Finally, when studying the different geometries for the implementation of an insert in the gear matrix, it is normal to introduce some variables accounting for the distance between the top of the tooth-tip and the insert upper surface (t), between the gear sides and the sides of the insert (e) as well as the width of insert (w), as shown in Figure 6.9. Such values will be expressed as a function of the module of the gear.

6.4.2. Heat transfer coefficient at the interface polymer/metal

As long as the contact between the two surfaces, polymer and metal, are in good contact, heat is evacuated by the insert as it is evacuated by the hole during the molding process. This temperature drop is caused by the thermal contact resistance (TCR). Therefore, the thermal contact resistance is essential to control solidification, reducing the cooling time and rate.

As explained in the first section of this Chapter, the heat transfer coefficient and, consequently, the TCR is dependent on the contact pressure at the interface between polymer and metal. Typical values of the interface resistance for normal surface finish and moderate contact pressures (from 0.1 Mpa to 10 Mpa) are presented in the Table 6.5 [37].

The contact pressure of the interface is not known. So, the influence of contact pressure on TCR and, consequently, the bulk temperature were studied for the range 0.1-50 MPa.

Table 6.5.: Thermal resistance for metallic interface under vacuum conditions [37].

Thermal Resistance, R_{tc} $\times 10^{-4}$ [m^{2}K/W]		
Contact Pressure	10 kN/m^2	10000 kN/m^2
Stainless Steel	6-25	0.7-40
Copper	1-10	0.1-0.5
Magnesium	1.5-35	0.2-0.4
Aluminum	1.5-5.0	0.2-0.4

Using the elastic contact model, written by *Fuller et al.* [68], the heat transfer coefficient can be calculated by equation (6.21), but the value of the the effective mean asperity slope and effective root mean square roughness has to be calculated with equations (6.5) and (6.6), respectively, for each contact pressure as well as the polymer elastic contact hardness obtained by equation (6.20) with the root mean square roughness and mean asperity slope values listed in Table 6.6.

So, for a given contact pressure, the heat transfer coefficient is given in Table 6.7.

The influence of the contact pressure on the heat transfer coefficients is quite evident. Increasing the contact pressure at the interface from 0.1 MPa to 50 MPa will increase the heat transfer coefficient more than 850%. It is also curious to notice that for different materials the heat transfer coefficient as well as the TCR does not change drastically for the same contact pressure. For a better view on the evolution of TCR with the contact pressure Table 6.8 is presented.

Table 6.6.: Mean asperity slopes and surface finish used [71, 72].

Material	σ [μm]	m_a
POM	1.23	0.41
Steel	0.31	0.09
Copper	0.45	0.15
Aluminum	0.51	0.27

Table 6.7.: Heat transfer coefficient for the contacting pressures for each interface

Heat Transfer Coefficient, h_c [W/m^{2}K]					
Material Interfaces	0.1 MPa	1 MPa	10 MPa	25 MPa	50 MPa
POM/Steel	104.06	895.93	7713.93	18169.79	34738.64
POM/Copper	101.33	872.44	7511.68	17693.38	33827.80
POM/Aluminum	100.58	866.02	7456.36	17563.08	33578.69

Table 6.8.: TCR for the contacting pressures for each interface.

Thermal contact resistance, $R_{tc} \times 10^{-4}$ [m^{2}K/W]					
Material Interfaces	0.1 MPa	1 MPa	10 MPa	25 MPa	50 MPa
POM/Steel	96.10	11.16	1.30	0.55	0.29
POM/Copper	98.69	11.46	1.33	0.57	0.30
POM/Aluminum	99.42	11.55	1.34	0.57	0.30

6.5. Influence of the insert material

To examine the influence of the material of the insert, a fixed geometry of a metallic insert was studied with w_x=0.1 $\cdot$ m =0.45 mm, e=m/2=2.75 mm (for each side) and t =m=4.5 mm, creating the geometry presented in Figure 6.1. The FEM mesh has 338826 elements and 54459 nodes.

Conditions and Geometrical

The analysis done with this chapter for the hybrid gears is for the same operating conditions that was done for non hybrid gears (with a rotational speed n=2000 rpm, a load torque of 10 Nm, a initial wall temperature T_{exp}=20°C and a initial ambient temperature T_{amb}=15°C), creating the same average heat flux in a dry simulation (with μ=0.21) in case of POM/POM materials (as shown in Figure 6.7a), for the same tooth gear geometry were applied.

6.5.1. Influence of material on weight

Beyond the thermal study it was decided to make a study of the mass increment of the gear tooth, presented in Table 6.9, where the middle column gives the insert weight and the final column the total weight of the POM tooth with an insert (as well as the weight increment).

The addition of a metallic insert of aluminum implies an increment of approximately 3% in tooth weight, and 17% or 14% if copper or steel are chosen, respectively.

6.5.2. Tooth temperature results

Figures 6.10a and 6.10b show the maximum and the minimum temperature for each thermal contact resistance (which is imposed by the contact pressure) in a logarithmic scale in the horizontal axis. It is possible to conclude that the steel insert has the worst temperature results for all the pressure contact range. This behaviour could be explained by steel's low thermal properties. However, the same

Table 6.9.: Mass evaluation for the first geometry.

Weight evaluation		
Material	Insert Weight [g]	Total Weight [g]
POM without insert	-	4.078
POM	0.130	4.208
Copper	0.826	4.904 (+ 16.540%)
Aluminum	0.251	4.329 (+ 2.875%)
Steel	0.714	4.792 (+ 13.878%)

behaviour is not seen in the minimum temperature, since the value increases with the decrease of TCR, which is explained by the higher conduction heat at higher TCR and, therefore, increasing the minimum temperature.

The temperature results from Tables 6.10 and 6.11, allow to verify that the best option to decrease the maximum temperature is the copper in comparasion with the temperature results from the initial case (non hybrid gear POM C14), leading the maximum decrease of 8.13% (although the minimum temperature increases with an higher rate than the decreasing rate of the maximum). However, as shown in Table 6.9, the weight increment using copper is higher than with aluminum insert and the temperatures reached are not that different. Nevertheless, the minimum temperature in steel insert is lower than aluminum and copper.

For the same contact pressure, 25 MPa, as shown in Figure 6.11, it is clear that for different insert materials present a slight difference in the temperature result

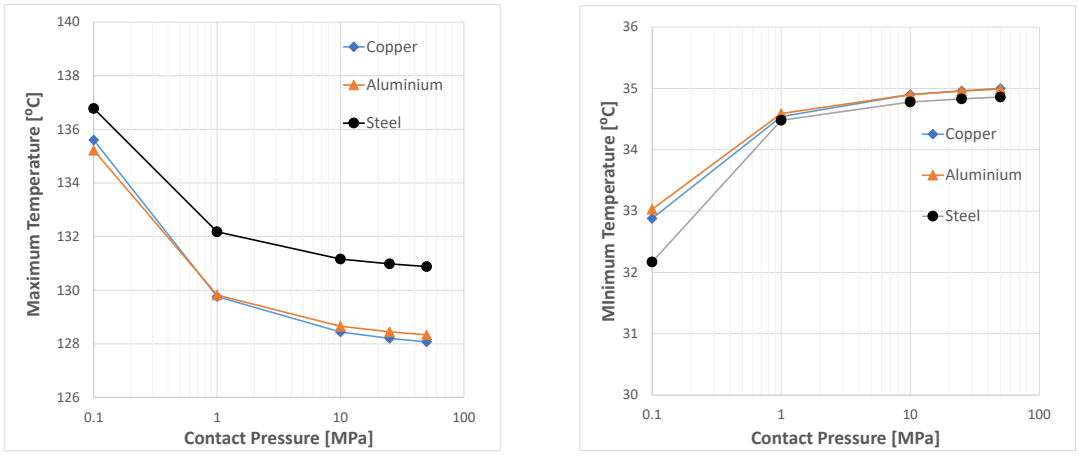

(a) Maximum temperature for each material. (b) Minimum temperature for each material.

Figure 6.10.: Maximum and minimum temperature for each material for the first hybrid gear model.

Table 6.10.: Maximum and minimum temperature for the first geometry.

Temperature evaluation						
Insert Material		**Contact Pressure**				
		0.1 MPa	1 MPa	10 MPa	25 MPa	50 MPa
Copper	max(°C)	135.60	129.76	128.44	128.20	128.07
	min(°C)	32.88	34.54	34.90	34.96	35.00
Aluminum	max(°C)	135.22	129.82	128.65	128.45	128.33
	min(°C)	33.03	34.59	34.90	34.96	34.99
Steel	max(°C)	136.78	132.18	131.16	130.98	130.88
	min(°C)	32.17	34.48	34.78	34.83	34.86

Table 6.11.: Percentage of temperature variation for the first geometry.

Increment of temperature [%]						
Insert Material		**Contact Pressure**				
		0.1 MPa	1 MPa	10 MPa	25 MPa	50 MPa
Copper	max(%)	- 2.73	- 6.92	- 7.86	- 8.03	- 8.13
	min(%)	47.58	55.03	56.64	56.92	57.09
Aluminum	max(%)	- 3.00	- 6.87	- 7.71	- 7.86	- 7.94
	min(%)	48.25	55.25	56.64	56.91	57.05
Steel	max(%)	- 1.88	- 5.18	- 5.91	- 6.04	- 6.11
	min(%)	44.39	54.76	56.10	56.33	56.46

(cut view in Figures 6.11b, 6.11d and 6.11f) for steel, aluminum and copper insert, respectively. This difference is reflected in the rise of the temperature near the tooth-tip because the steel inserts differs from the aluminum and copper ones due to their higher thermal conductivity.

The aluminum solution shows the best scenario for maximum temperature achieved as well as the total weight. This solution will not compromise the maximum temperature reduction since the aluminum and copper have similar thermal behaviour. Finally, the total cost of production and manufacturing of aluminum is lower than that of copper.

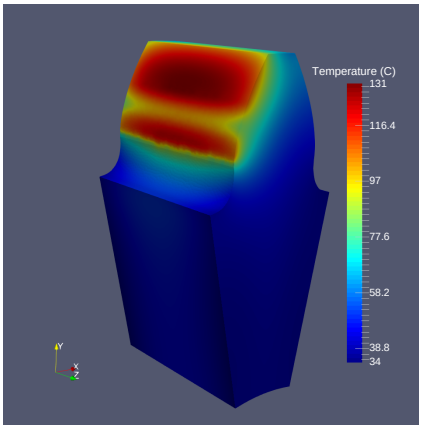

(a) Temperature result - Steel (T_{max}=130.98°C and T_{min}=34.83°C).

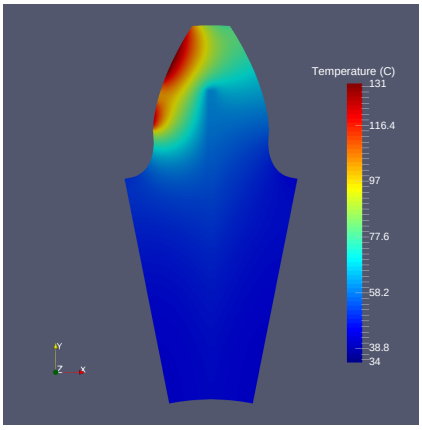

(b) Temperature result insert - Steel (T_{max}=130.98°C and T_{min}=34.83°C).

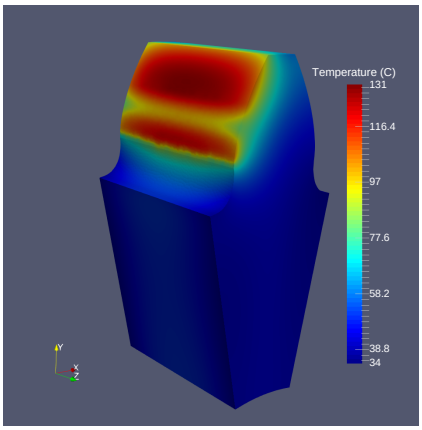

(c) Temperature result - Aluminum (T_{max}=128.33°C and T_{min}=34.96°C).

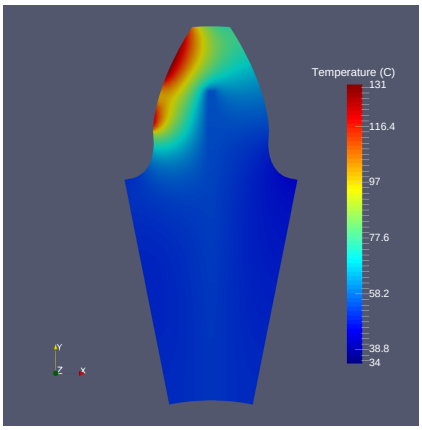

(d) Temperature result insert - Aluminum (T_{max}=128.33°C and T_{min}=34.96°C).

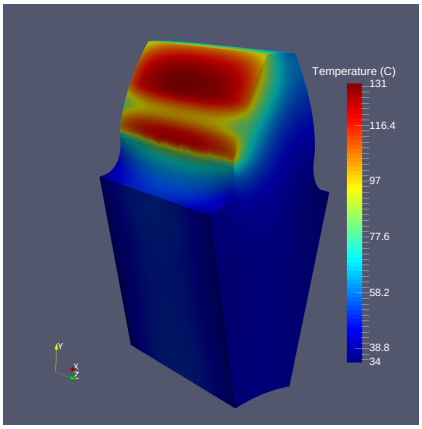

(e) Temperature result - Copper (T_{max}=128.20°C and T_{min}=34.96°C).

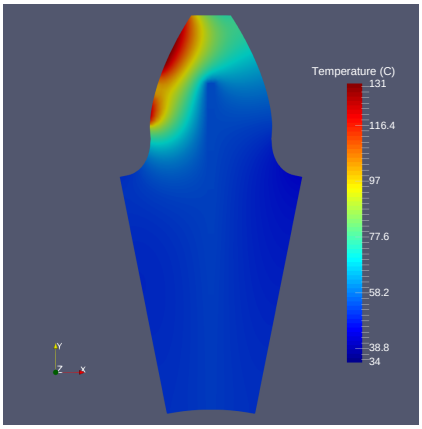

(f) Temperature result insert - Copper (T_{max}=128.20°C and T_{min}=34.96°C).

Figure 6.11.: Temperature distribution for 25 MPa for various insert materials.

6.6. Influence of contact pressure

The test of the impact of the different contact pressures on the temperature distribution is presented in Figures 6.12 and 6.13.

The analysis of Figures 6.12b and 6.12d allow to verify the influence of the contact pressure (0.1 or 1 MPa) on the gradient of bulk temperature of both gear and insert. The insert is able to conduct a higher heat flux with the increase of contact pressure and, therefore, reduce the maximum temperature. However, as a side effect the minimum temperature rises.

The increase of contact pressure (CP) changes the gradient within the metallic insert, which becomes higher. However, comparing the result for 25 and 50 MPa

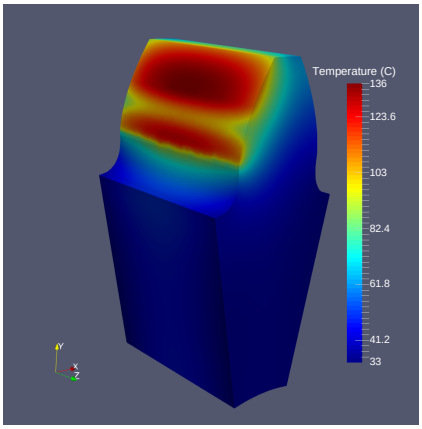

(a) Temperature result - 0.1 MPa (T_{max}=135.22°C and T_{min}=33.03°C).

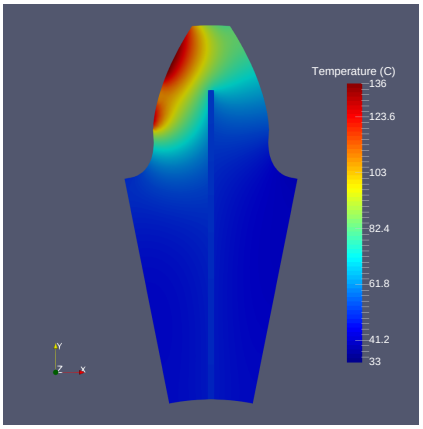

(b) Temperature result insert - 0.1 MPa (T_{max}=135.22° and T_{min}=33.03°C).

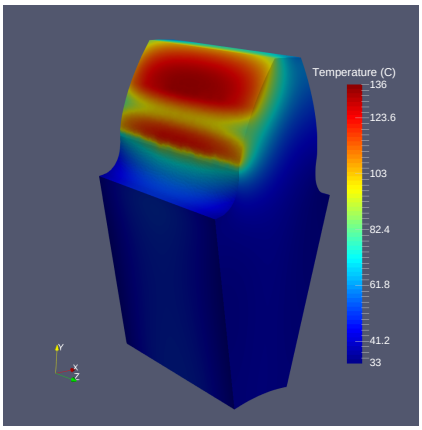

(c) Temperature result - 1 MPa (T_{max}=129.82°C and T_{min}=34.59°C).

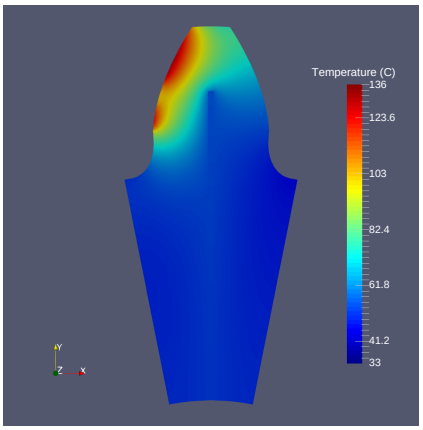

(d) Temperature result insert - 1 MPa (T_{max}=129.82°C and T_{min}=34.59°C).

Figure 6.12.: Temperature distribution for 0.1 and 1 MPa for a aluminum insert with w_x=0.45 mm.

the difference is negligible as already shown in the temperature evaluation in Tables 6.10 and 6.11. Therefore, the next geometry studies will not focus on the influence of the contact pressure of 50 MPa since the capacity to heat evacuation is almost equal to a contact pressure of 25 MPa (however the temperature results reveal that for a contact pressure over 10 MPa, the final result will not change that much, it was decided as a conservative study the contact pressure of 25 MPa).

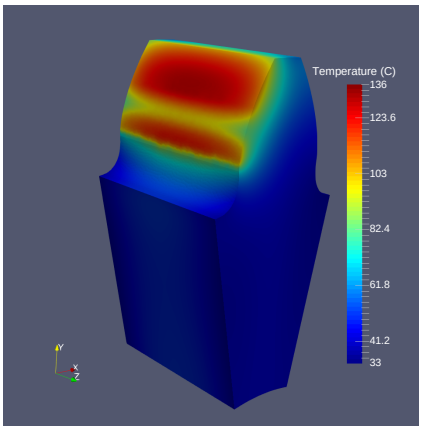

(a) Temperature result - 10 MPa (T_{max}=128.65°C and T_{min}=34.90°C).

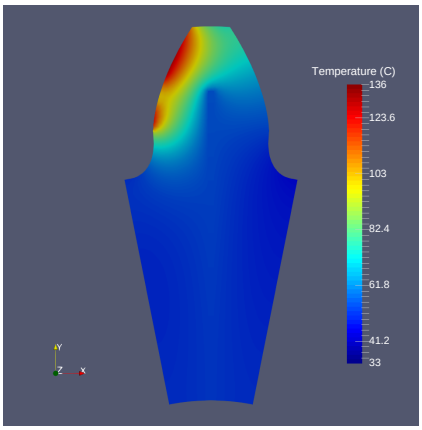

(b) Temperature result insert - 10 MPa (T_{max}=128.65°C and T_{min}=34.90°C).

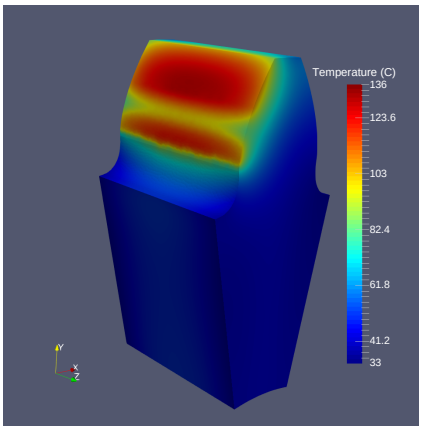

(c) Temperature result - 25 MPa (T_{max}=128.45°C and T_{min}=34.96°C).

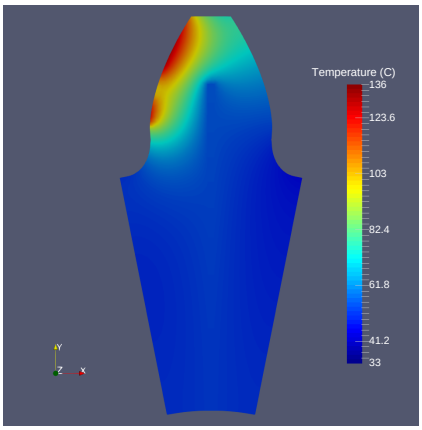

(d) Temperature result insert - 25 MPa (T_{max}=128.45°C and T_{min}=34.96°C).

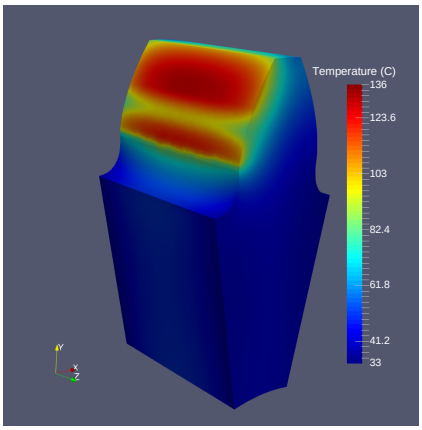

(e) Temperature result - 50 MPa (T_{max}=128.33°C and T_{min}=34.99°C).

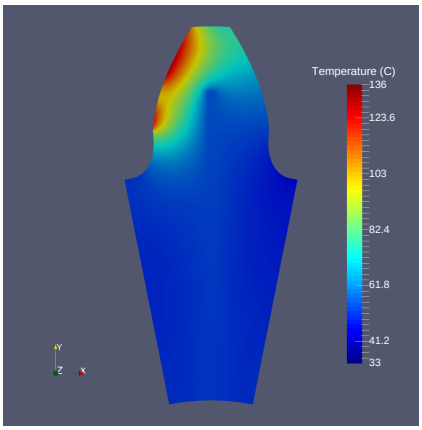

(f) Temperature result insert - 50 MPa (T_{max}=128.33°C and T_{min}=34.99°C).

Figure 6.13.: Temperature distribution for 10, 25 and 50 MPa for an aluminum insert with w_x=0.45 mm.

6.7. Influence of the insert width and the gap to tooth tip and sides

6.7.1. Influence of the insert width - w_x

To examine the influence of the aluminum insert width w_x, the hypothesis of 10%, 25% and 50% of the gear module, respectively 0.45 mm, 1.125 mm and 2.25 mm was considered. A geometry model with a gap distance to the tooth-tip of t=4.5 mm (module) and a gear side distance of e=2.25 mm was used.

Influence on the tooth weight

The use of a wider insert width will considerably raise the weight of the gear as Table 6.12 listed, a increment from approximately of 3% to 14% when multiplying five times the width of the insert.

Tooth temperature results

The TCR is different depending on the contact pressure and the contact area will increase with the insert width increment. Figures 6.14a and 6.14b show the maximum and minimum temperature for different contact pressures and insert widths, respectively, with a logarithmic scale in the horizontal axis. It is possible to infer that with an increase in insert width, the maximum temperature will decrease and the minimum temperature will increase, although at a lower rate.

In Tables 6.13 and 6.14, it is possible to verify that the maximum temperature have maximum decreases of 7.86%, 9.69% and 12.14% when comparing with the

Table 6.12.: Mass evaluation over the insert width variation.

Weight evaluation		
Insert width	Insert Weight [g]	Total Weight [g]
POM Gear without insert	-	4.078
POM Gear	0.130	4.208
w_x=0.450 mm	0.251	4.329 (+ 2.875%)
POM Gear without insert	-	3.883
POM Gear	0.325	4.208
w_x=1.125 mm	0.627	4.510 (+ 7.177%)
POM Gear without insert	-	3.558
POM Gear	0.650	4.208
w_x=2.250 mm	1.254	4.812 (+ 14.354%)

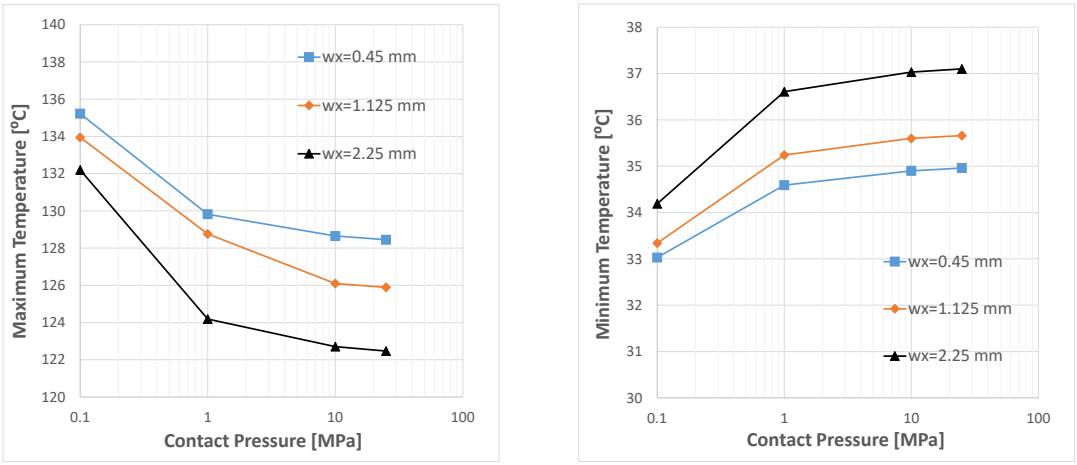

(a) Maximum temperature for each width. (b) Minimum temperature for each width.

Figure 6.14.: Maximum and minimum temperature for each width for the tested contact pressures.

initial case of non hybrid POM gear(reducing from 140°C to 128°C, to 126°C and to 123°C, respectively) for 0.45, 1.125 and 2.25 mm of insert width, respectively. The minimum temperature increases approximately 57% and 67% for 1.25 mm and 2.25 mm insert width (w_x), respectively.

For a better observation of the bulk temperature distribution a comparative study is shown in Figures 6.15 and 6.16 for a 25 MPa contact pressure. The section of the tooth profile through the middle of the insert (Figures 6.15b, 6.15d, 6.16b, 6.16d, 6.16b) shows that the bulk temperature increases and the temperature distribution along the tooth changes since the insert will create a heat sink.

Table 6.13.: Maximum and minimum temperature for the width evaluation.

Temperature evaluation					
Insert width		**Contact Pressure**			
		0.1 MPa	1 MPa	10 MPa	25 MPa
w_x**=0.450 mm**	max(°C)	135.22	129.82	128.65	128.45
	min(°C)	33.03	34.59	34.90	34.96
w_x**=1.125 mm**	max(°C)	133.95	128.76	126.1	125.89
	min(°C)	33.34	35.24	35.60	35.66
w_x**=2.250 mm**	max(°C)	132.20	124.19	122.71	122.47
	min(°C)	34.19	36.61	37.03	37.10

Table 6.14.: Percentage of temperature variation for the width evaluation.

Increment of temperature					
Insert width		**Contact Pressure**			
		0.1 MPa	1 MPa	10 MPa	25 MPa
w_x**=0.450 mm**	max(%)	- 3.00	- 6.87	- 7.71	- 7.86
	min(%)	48.25	55.25	56.64	56.91
w_x**=1.125 mm**	max(%)	- 3.91	- 7.63	- 9.54	- 9.69
	min(%)	49.64	58.17	59.78	60.05
w_x**=2.250 mm**	max(%)	- 5.16	- 10.91	- 11.97	- 12.14
	min(%)	53.46	64.32	66.20	66.52

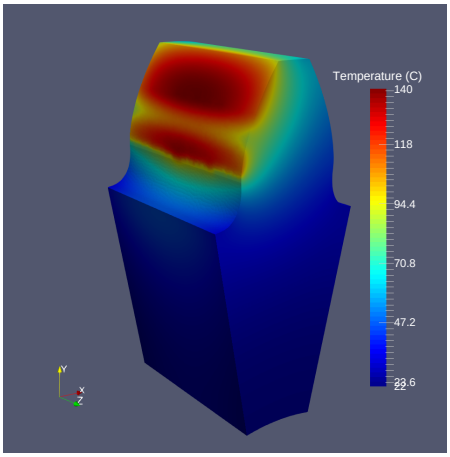

(a) Temperature without insert (T_{max}=139.40°C and T_{min}=22.28°C).

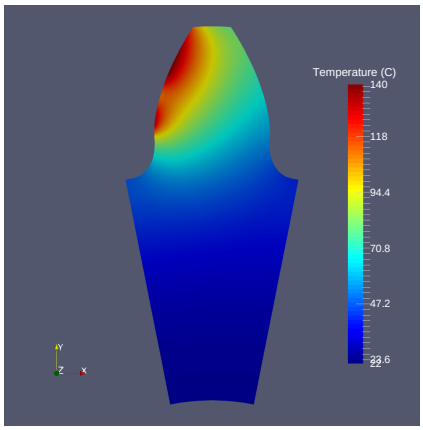

(b) Temperature cut without insert (T_{max}=139.40°C and T_{min}=22.28°C).

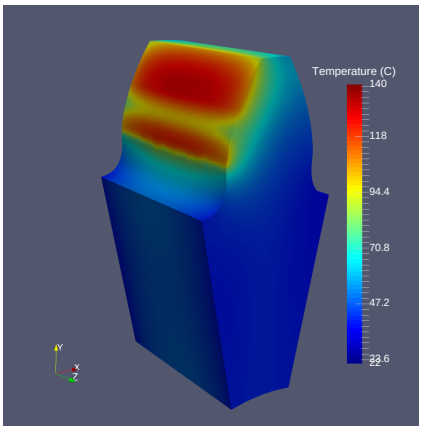

(c) Temperature result, w_x=0.45 mm (T_{max}=128.45°C and T_{min}=34.96°C).

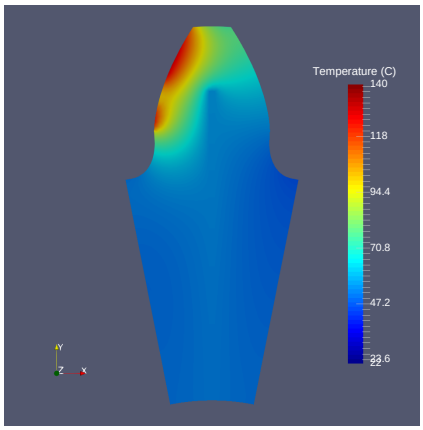

(d) Temperature result insert, w_x=0.45 mm (T_{max}=128.45°C and T_{min}=34.96°C).

Figure 6.15.: Temperature distribution for gear without insert and hybrid-gear with 0.45 mm insert for contact pressure of 25 MPa.

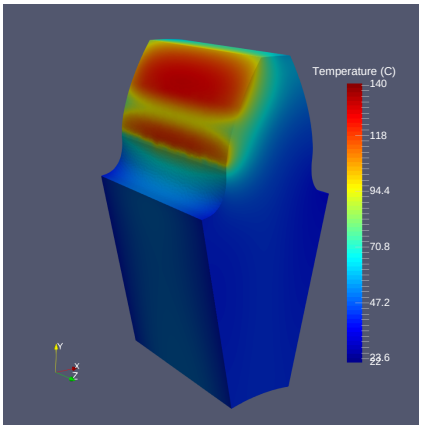

(a) Temperature result, w_x= 1.125 mm (T_{max}=125.89°C and T_{min}=35.66°C).

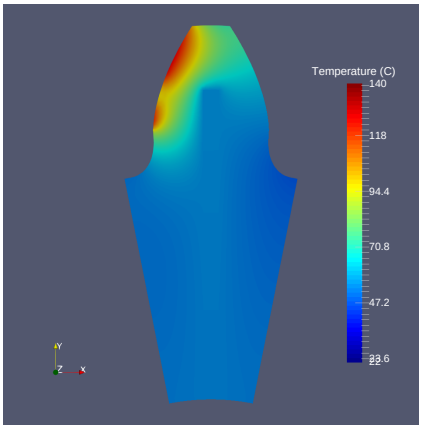

(b) Temperature result insert, w_x= 1.125 mm (T_{max}=125.89°C and T_{min}=35.66°C).

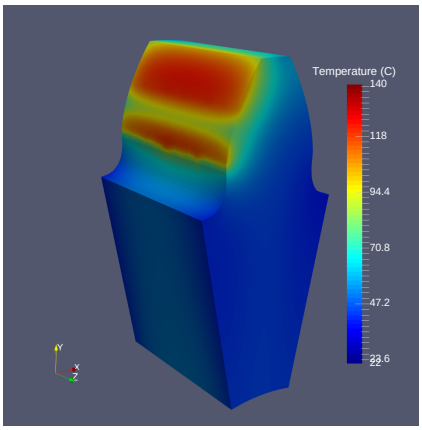

(c) Temperature result, w_x= 2.250 mm (T_{max}=122.47°C and T_{min}=37.10°C).

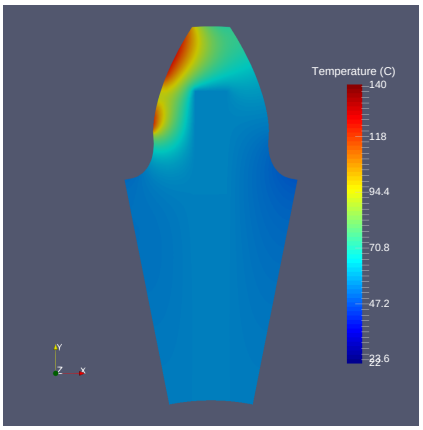

(d) Temperature result insert, w_x= 2.250 mm (T_{max}=122.47°C and T_{min}=37.10°C).

Figure 6.16.: Temperature distribution for hybrid-gear with 1.125 mm and 2.250 mm insert for contact pressure of 25 MPa.

6.7.2. Influence of the gap of the insert from tooth-tip - t

Considering an insert geometry with, w_x=1.125 mm width and the gap for the side of e=2.25 mm, the tooth-tip distance was studied.

Influence on tooth weight

By looking at Table 6.15 it is possible to infer that the use of a taller insert will have an almost insignificant effect on the weight of the gear.

Tooth temperature results

Figures 6.17a and 6.17b present the maximum and minimum temperature respectively for all the contact pressures imposed in a logarithmic scale in the horizontal axis. It is not possible to infer a simple relation of the temperature with the tooth distance since the insert with full height shows better results when compared with the initial case, but worst result than with 2.25 mm of tooth-tip distance (t).

Tables 6.16 and 6.17 present the maximum temperatures which decreased by 9.69% , 14.03% and 10.97% when comparing in the initial non hybrid POM gear (reducing 140 to 126°C, to 120°C and to 124 °C, respectively) for 4.50, 2.25 and 0.00 mm of insert tooth-tip distance, respectively. The minimum temperature increased approximately 60% to 75% (increasing 20°C over to 36°C and 39°C) with the reduction of the insert tooth-tip distance.

A more revealing observation of the effect of the tooth-tip distance on the temperature distribution is shown in Figures 6.18 and 6.19 at a contact pressure of 25 MPa. Looking at Figures 6.18b, 6.18d, 6.19b and 6.19d it is clear that the decrease

Table 6.15.: Mass evaluation over the insert tooth-tip gap variation.

Weight evaluation		
Distance	Insert Weight [g]	Total Weight [g]
POM Gear without insert	-	3.883
POM Gear	0.325	4.208
t=4.500 mm	0.627	4.510 (+ 7.177%)
POM Gear without insert	-	3.850
POM Gear	0.358	4.208
t=2.250 mm	0.692	4.542 (+ 7.938%)
POM Gear without insert	-	3.816
POM Gear	0.392	4.208
t=0.000 mm	0.757	4.573 (+ 8.674%)

Table 6.16.: Maximum and minimum temperature for tooth-tip distance evaluation.

Temperature evaluation					
Distance		**Contact Pressure**			
		0.1 MPa	1 MPa	10 MPa	25 MPa
***t*=4.50 mm**	max(°C)	133.95	128.76	126.1	125.89
	min(°C)	33.34	35.24	35.60	35.66
***t*=2.25 mm**	max(°C)	129.92	120.64	119.94	119.84
	min(°C)	34.89	37.42	37.84	37.91
***t*=0.00 mm**	max(°C)	131.10	124.98	124.22	124.11
	min(°C)	35.71	38.44	38.82	38.88

Table 6.17.: Percentage of temperature variation for tooth-tip distance evaluation.

Increment of temperature [%]					
Distance		**Contact Pressure**			
		0.1 MPa	1 MPa	10 MPa	25 MPa
***t*=4.50 mm**	max(%)	- 3.91	- 7.63	- 9.54	- 9.69
	min(%)	49.64	58.17	59.78	60.05
***t*=2.25 mm**	max(%)	- 6.80	- 13.46	- 13.96	- 14.03
	min(%)	56.60	67.95	69.84	70.15
***t*=0.00 mm**	max(%)	- 5.95	- 10.34	- 10.89	- 10.97
	min (%)	60.28	72.53	74.24	74.51

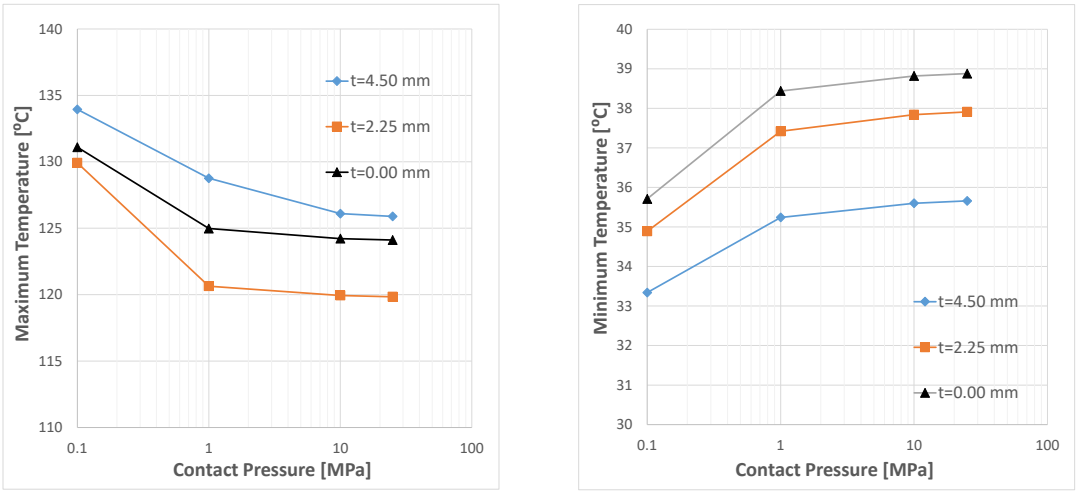

(a) Maximum temperature for each distance. (b) Minimum temperature for each distance.

Figure 6.17.: Maximum and minimum temperature for each tooth-tip distance for the tested contact pressures.

of the tooth-tip distance will create a preferential channel for the heat propagation and, therefore, conducting more heat to insert.

Figures 6.18d, 6.19b and 6.19d show that the temperature within the insert increases as the heat conduction through the insert occurs.

The closer the insert is from the gear tip the highest is the heat evacuation capacity. However, with a complete isolation of the meshing area the heat evacuation capability seems to be reduced (see Figure 6.19d).

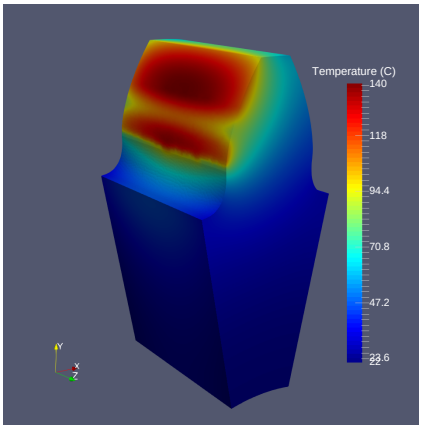

(a) Temperature without insert (T_{max}=139.40°C and T_{min}=22.28°C).

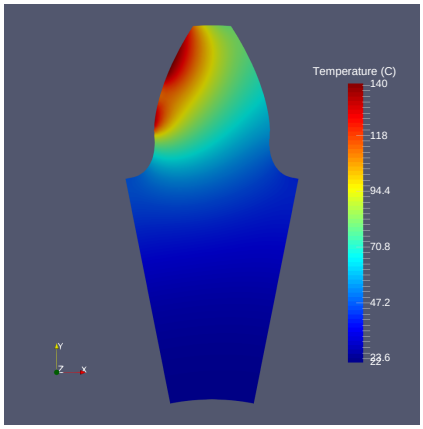

(b) Temperature cut without insert (T_{max}=139.40°C and T_{min}=22.28°C).

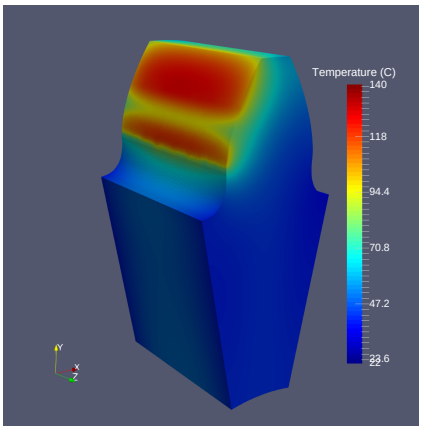

(c) Temperature result, t=4.50 mm (T_{max}=125.89°C and T_{min}=35.66°C).

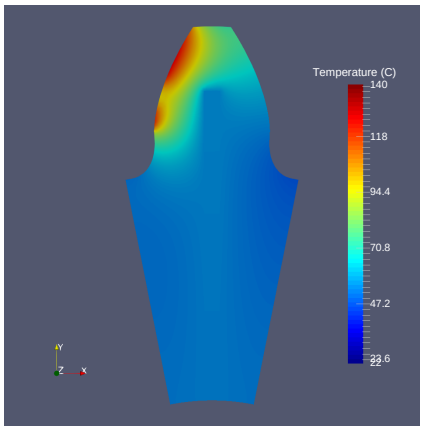

(d) Temperature result insert, t=4.50 mm (T_{max}=125.89°C and T_{min}=35.66°C).

Figure 6.18.: Temperature distribution for gear without insert and hybrid-gear with 4.55 mm tooth-tip distance insert at 25 MPa contact pressure.

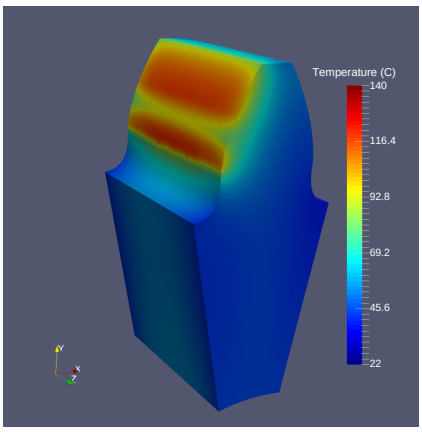

(a) Temperature result, t=2.25 mm (T_{max}=119.84°C and T_{min}=37.91°C).

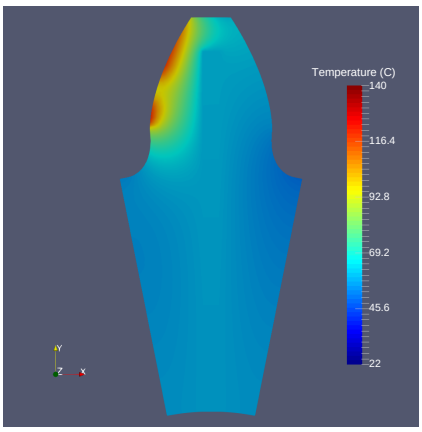

(b) Temperature result insert, t=2.25 mm (T_{max}=119.84°C and T_{min}=37.91°C).

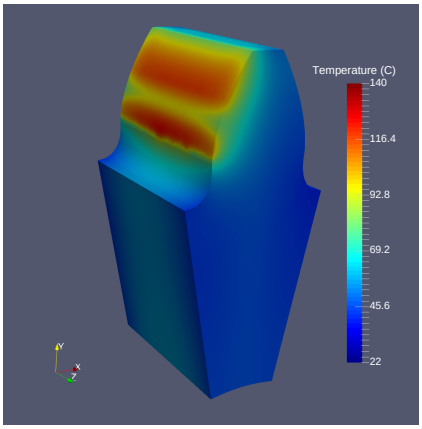

(c) Temperature result, t=0.00 mm (T_{max}=124.11°C and T_{min}=38.88°C).

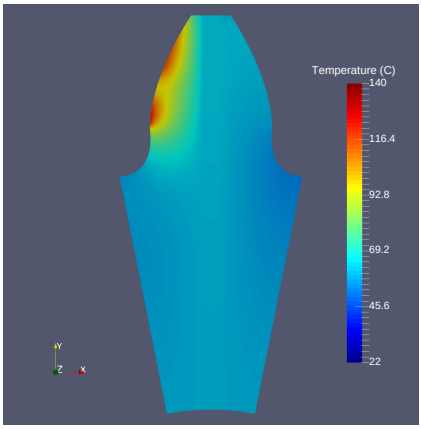

(d) Temperature result insert, t=0.00 mm (T_{max}=124.11°C and T_{min}=38.88°C).

Figure 6.19.: Temperature distribution for hybrid-gear with a 2.25 mm and a 0.00 mm tooth-tip distance at 25 MPa contact pressure.

6.7.3. Influence of the gap of the insert distance from gear sides - e

To study the influence of the gap between gear sides and insert, the insert had the following geometry: width w_x=1.125 mm, gap to tooth tip t=4.50 mm and the gap to the gear sides, e, from the values of 50% and 0% of gear module, that is, 2.25 and 0 mm, respectively.

Influence on the tooth weight

The reduction of the gap between the insert and the gear side will raise the weight of the gear tooth, listed in Table 6.18, by an increment of approximately 7% and 11%.

Tooth temperature results

Figures 6.20a and 6.20b show the maximum and minimum temperatures for a given contact pressure imposed in a logarithmic scale in the horizontal axis. The reduction of the gap to the gear sides promotes a reduction of the maximum temperature while minimum temperature increases (with a lower rate). This is easily explained by the fact that there is an increase of insert material and, therefore, a rise in the heat flux capacity.

Looking in Tables 6.19 and 6.20 the maximum temperatures present a decrease of 9.69% (reducing 140°C to 126°C) and 11.39% (reducing 140°C to 124°C) for 2.25 and 0.00 mm of insert gear sides, respectively, when comparing with the temperature results for the initial non hybrid POM gear. For the minimum temperature the increase is approximately 60% (increasing from 22°C to 36°C) and 57% (increasing 22°C to 35°C), when decreasing the gap between the insert and the gear side.

Table 6.18.: Mass evaluation over the insert sides distance variation.

Weight evaluation		
Distance	Insert Weight [g]	Total Weight [g]
POM Gear without insert	-	3.883
POM Gear	0.325	3.883
e=2.25 mm	0.627	4.510 (+ 7.177%)
POM Gear without insert	-	3.729
POM Gear	0.479	4.208
e=0.00 mm	0.924	4.653 (+10.575 %)

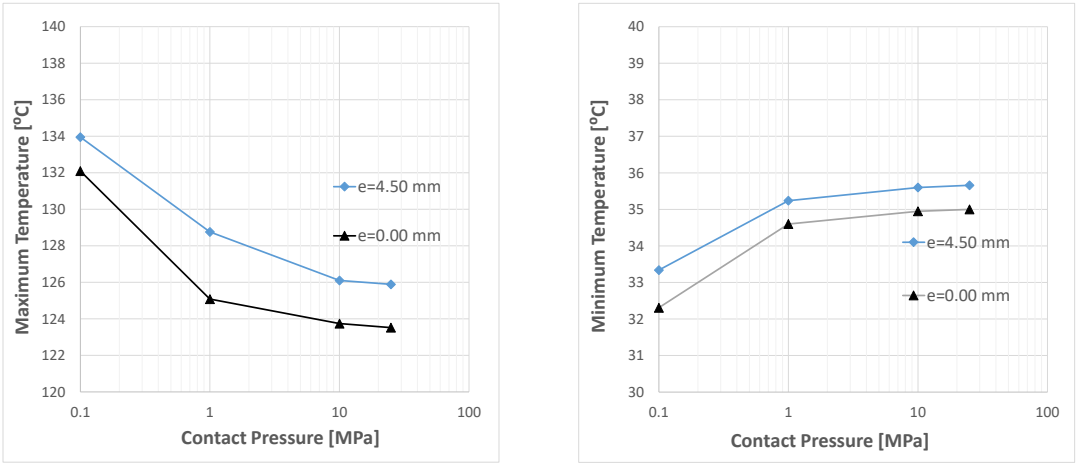

(a) Maximum temperature for each sides distance.

(b) Minimum temperature for each side distance.

Figure 6.20.: Maximum and minimum temperature for each gear side distance for the tested contact pressures.

Table 6.19.: Maximum and minimum temperature for the sides distance evaluation.

Temperature evaluation					
Distance		**Contact Pressure**			
		0.1 MPa	1 MPa	10 MPa	25 MPa
***e*=2.25 mm**	max(°C)	133.95	128.76	126.1	125.89
	min(°C)	33.34	35.24	35.60	35.66
***e*=0.00 mm**	max(°C)	132.09	125.08	123.74	123.52
	min(°C)	32.31	34.60	34.95	35.00

Table 6.20.: Percentage of temperature variation for the sides distance evaluation.

Increment of temperature					
Distance		**Contact Pressure**			
		0.1 MPa	1 MPa	10 MPa	25 MPa
***e*=2.25 mm**	max(%)	- 3.91	- 7.63	- 9.54	- 9.69
	min(%)	49.64	58.17	59.78	60.05
***e*=0.00 mm**	max(%)	- 5.24	- 10.27	- 11.23	- 11.39
	min(%)	45.02	55.30	56.87	57.09

Considering a constant contact pressure (25 MPa), a comparative study between the normal gear tooth (Figures 6.21a and 6.21b) and the hybrid gears with the different gear side distance (2.25 mm in Figures 6.21c and 6.21d or 0.00 mm in Figures 6.21e and 6.21f) is proposed. Analyzing the bulk temperature distribution it is clear that at the base of the gear tooth, the temperatures are in both cases higher than for the non-hybrid gear, however the example with no distance from the gear sides is preferable since the temperature is lower than with a gear distance of 2.25 mm.

It is important to notice that, by expanding the insert to the gear side the temperature near the insert will rise, but the bulk temperature decreases due to the convection between the insert and ambient.

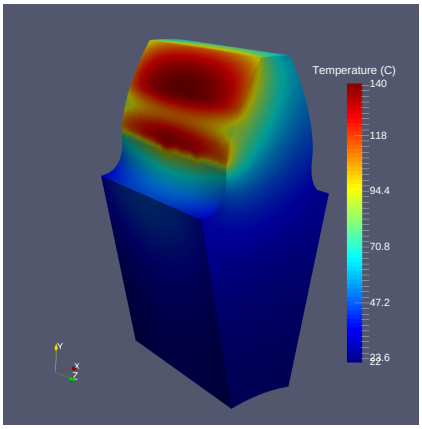

(a) Temperature without insert (T_{max}=139.40°C and T_{min}=22.28°C).

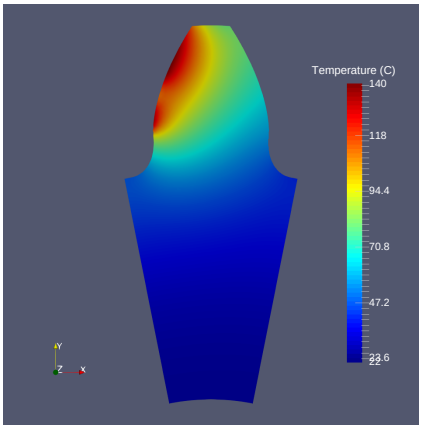

(b) Temperature cut without insert (T_{max}=139.40°C and T_{min}=22.28°C).

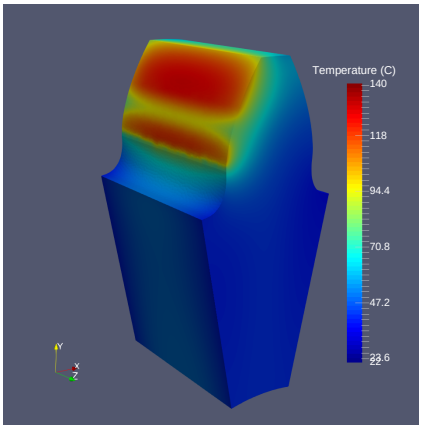

(c) Temperature result, e=2.25 mm (T_{max}=125.89°C and T_{min}=35.66°C).

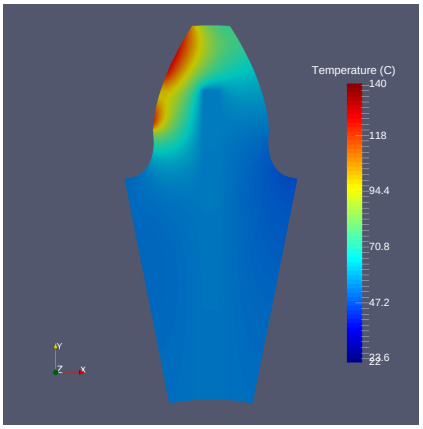

(d) Temperature result insert, e=2.25 mm (T_{max}=125.89°C and T_{min}=35.66°C).

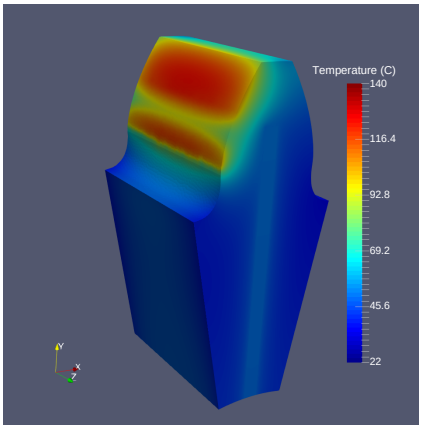

(e) Temperature result, e=0.00 mm (T_{max}=123.52°C and T_{min}=35.00°C).

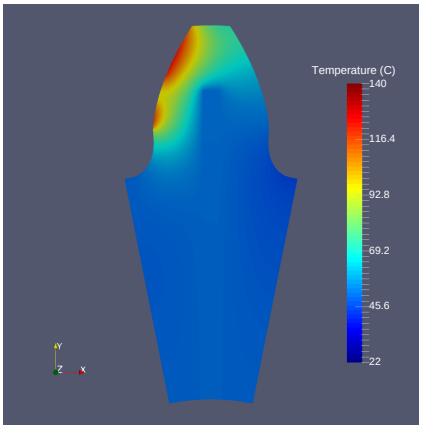

(f) Temperature result insert, e=0.00 mm (T_{max}=123.52°C and T_{min}=35.00°C).

Figure 6.21.: Temperature distribution for normal gear and for hybrid-gear with a 2.25 mm and a 0.00 mm gear side distance at 25 MPa contact pressure.

6.8. Study of the different insert geometries (aluminum)

6.8.1. Explanation and optimization of the insert geometries

In this thesis four different profiles were analyzed: Rectangular Cuboid (like a razor) Profile, T-Profile, Double T-Profile I and Involute Profile. Beginning with a razor shape to study the influence of the various gap distances (to tooth tip and sides) and insert width, as detailed explained in Appendix I.

Then, in a approach to get more heat evacuated, the T-Profile was created, due to its closeness to the heat source. Then a Double T-Profile I was created, to reduce the maximum temperature by inducing heat evacuation through two platforms at the level of the two critical points (root and tip of the gear tooth). The optimized geometry for the Double T-Profile I was studied through the analysis of the tooth temperature, with the variation of the vertical width of the insert's "platforms" (vw), the horizontal insert width as well as the extension of this platforms, as detailed study in the Appendix I.

Finally, a different approach was used with the implementation of a insert profile that follows the flank and face surfaces, an Involute Profile.

Rectangular Cuboid (Razor)

The geometry chosen for the comparative study, between the different profiles, for the Razor insert shape was with the w_x=1.125 mm, e=0.00 mm and t=4.5 mm. A section of the insert is presented in Figure 6.22a and the 3D model of the resulting hybrid-gear is shown in Figure 6.22b.

T-Profile

As said earlier, the addition of an horizontal "platform" to the initial insert shape (rectangular cuboid) created the insert T-profile. In fact, this insert shape was created to better evacuate heat from the meshing surface, thanks to the closeness of the insert from this surface. For this comparative study, the geometry with w_x=1.125 mm, e=0.00 mm, t=4.5 mm and vertical width vw=1.125 mm was used. The section of this insert profile is shown in Figure 6.22c with the 3D model of the resulting hybrid-gear in Figure 6.22d.

Double T-Profile I

The Double T-Profile I is inspired by the T-Profile but with a different purpose since the addition of the two horizontal "platforms" was in order to increase the

insert's capacity of of evacuating the heat generated at the meshing surface thanks to the proximity to the meshing surface's most critical points (the two maximums temperatures - root and tip of the gear tooth). The geometry used for this study has the optimized geometry with w_x=0.450 mm, e=0.00 mm, t=2.250 mm and vertical width vw=1.125 mm. Creating a double T-profile for that two points by creating a 2D section of the double T-profile insert is in Figure 6.23a and the 3D hybrid-gear model in Figure 6.23b.

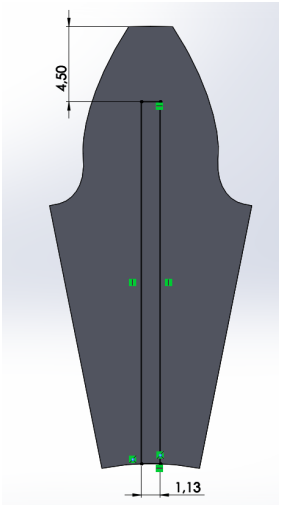

(a) Rectangular Cuboid (Razor) - insert dimensions.

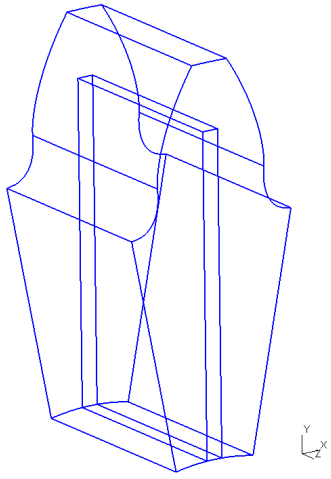

(b) 3D model of rectangular cuboid (razor) hybrid-gear.

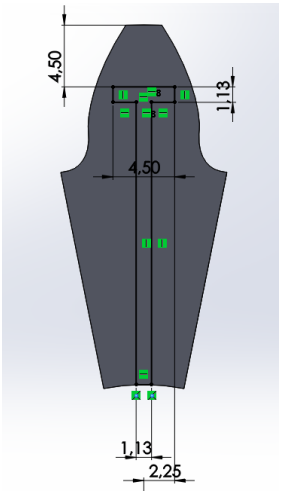

(c) T profile - insert dimensions.

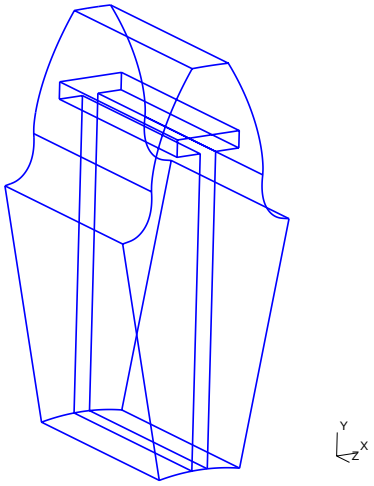

(d) 3D model of T-profile hybrid-gear.

Figure 6.22.: Dimension of the Rectangular Cuboid (Razor) profile and T-Profile insert and respective hybrid-gear 3D models.

Involute Profile

As in the previous approach to the Double T-profile I the extension of the "platforms" suggested a new profile study, one in which the insert follows the gear tooth's flank and face surfaces, as shown in the section in Figure 6.23c and in the 3D resulting hybrid gear model in Figure 6.23d.

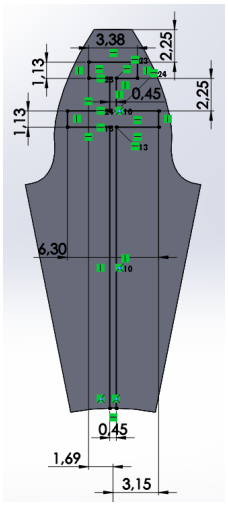

(a) Double T-profile I - insert dimensions.

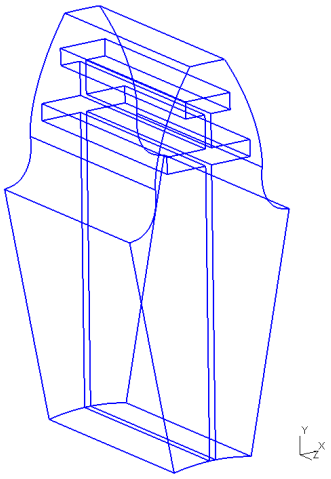

(b) 3D model of Double T-profile I.

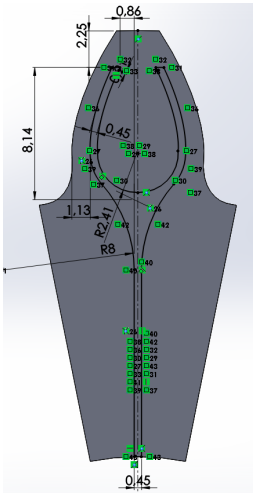

(c) Involute profile - insert dimensions.

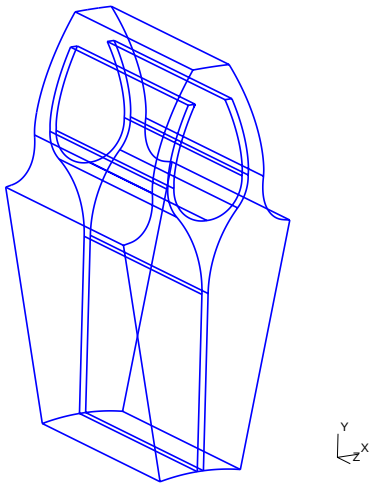

(d) 3D model of involute profile.

Figure 6.23.: Dimension of the Double T-Profile I and Involute insert profile and respective hybrid-gear 3D model.

Table 6.21.: Mass evaluation of the four possible shapes for the insert.

Weight evaluation			
Profile	**Geo.Para. [mm]**	**Insert Weight** [g]	**Total Weight** [g]
POM Gear without insert	-	-	3.729
POM Gear	-	0.479	4.208
Rectangular Cuboid (Razor)	e=0.000 w_x=1.125 t=4.500	0.924	4.653 (+ 10.575%)
POM Gear without insert	-	-	3.655
POM Gear	-	0.553	4.208
T-Profile (vw=1.125)	e=0.000 w_x=1.125 t=4.500	1.067	4.722 (+ 12.215%)
POM Gear without insert	-	-	3.803
POM Gear	-	0.405	4.208
Double T-Profile I (vw=1.125)	e=0.000 w_x=0.450 t=2.250	0.781	4.584 (+ 8.935%)
POM Gear without insert	-	-	3.818
POM Gear	-	0.390	4.208
Involute Profile	e=0.000 w_x=0.450 t=2.250	0.752	4.570 (+ 8.603%)

6.8.2. Influence on tooth weight

The weight evaluation of the four insert profiles is presented in Table 6.21.

It is possible to conclude that the total weight of the gear tooth with the different insert profiles does not change that much, the maximum weight corresponding to the T-Profile (an increment of 12.215%, increasing from 4.207g to 4.722g, of total weight when compared to the initial non hybrid POM gear.

6.8.3. Influence on tooth temperature

Table 6.22 shows maximum and minimum temperatures as well as the percentages of increment and reduction of each geometry when comparing with the initial result obtained for the non hybrid POM gear. It is possible to notice that, using the Involute profile or the Double T-Profile I, the reduction in maximum temperature is about 28% (reducing the temperature from 140° C to 100-101° C), although with an increase in minimum temperature of 90 and 83%, respectively (increasing the

temperature from 22° C to 42-40° C). The reduction of maximum temperature when using a Razor or a T-Profile for the insert is much smaller, 11 and 17%, approximately.

Figures 6.24a and 6.24b present the maximum and minimum temperature for all contact pressures tested, respectively, in a logarithmic scale in the horizontal axis. It is possible to conclude that the T-profile was able to evacuate more heat from the meshing surface by relocating the insert closer to this surface, reducing the maximum temperature, although the minimum temperature was increased with the a better reduction of this maximum temperature.

As for the Double T-Profile I, as was as expected, it is one of the two best solutions since it was able to evacuate even more of the heat, therefore, to decrease the maximum temperature further. However, the same conclusion about the minimum temperature can be deduced for this insert profile, since the minimum temperature was increased.

Finally, the Involute Profile was the best solution, with the highest reduction of the maximum temperature and, therefore, enhancing the mechanical properties of the gear tooth. But it is important to note that the minimum temperature is much higher in value.

This imolies that when the contact area increases, the maximum temperature will be lower, whereas the minimum temperature will be higher.

Table 6.22.: Temperature evaluation of the four possible shapes for the insert.

Temperature [°C]			
Profile	**Geo.Para. [mm]**	**Maximum Temp.**	**Mininum Temp.**
Initial Gear	-	139.40	22.28
Rectangular Cuboid (Razor)	e=0.000 w_x=1.125 t=4.500	123.52 (- 11.39%)	35.00 (+ 57.09%)
T-Profile (vw=1.125)	e=0.000 w_x=1.125 t=4.500	115.88 (- 16.87%)	37.59 (+ 68.72%)
Double T-Profile I (vw=1.125)	e=0.000 w_x=0.450 t=2.250	100.66 (- 27.79%)	40.09 (+ 82.63%)
Involute Profile	e=0.000 w_x=0.450 t=2.250	99.64 (- 28.32%)	42.27 (+ 89.72%)

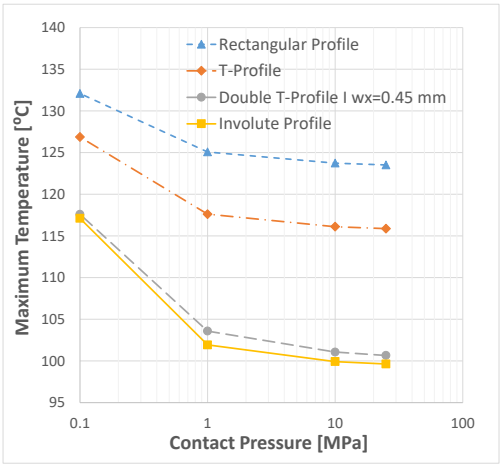

(a) Maximum temperature for each insert shape.

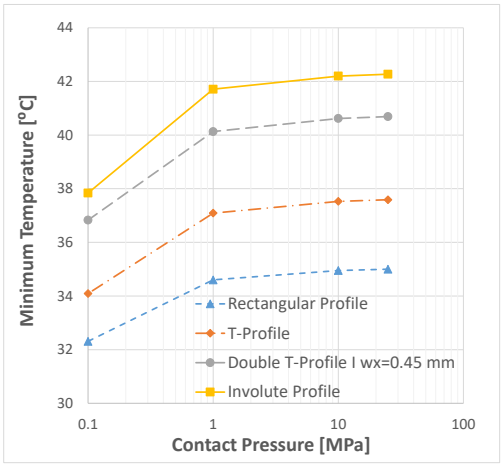

(b) Minimum temperature for each insert shape.

Figure 6.24.: Maximum and minimum temperature of the four types of insert geometries for the tested contact pressures.

A more revealing observation of the effect of the different profiles on the temperature distribution is shown in Figures 6.25 and 6.26 for a contact pressure of 25 MPa. Figures 6.25d, 6.26b, 6.26d and 6.26f show that the temperature within the insert increases as the heat conduction through the insert occurs, being higher with a better heat evacuation efficiency. The Double T-Profile I and the Involute Profile show the most homogeneous temperature distribution within the tooth gear, although with a higher minimum temperature as shown of the blue light tone color at the tooth body.

As for Figures 6.25c, 6.26a, 6.26c and 6.26e, they show the difference between the profiles at the meshing surface more clearly. The Double T-Profile I and the Involute profile show almost no reddish and orangery color at the surface mesh, having a more critical location at the tip of the tooth or at its root, respectively.

It is possible to conclude that the implementation of either of these aluminum inserts will decrease the maximum temperature and possibly enhance the mechanical properties of the polymer, resulting in a higher gear's life time.

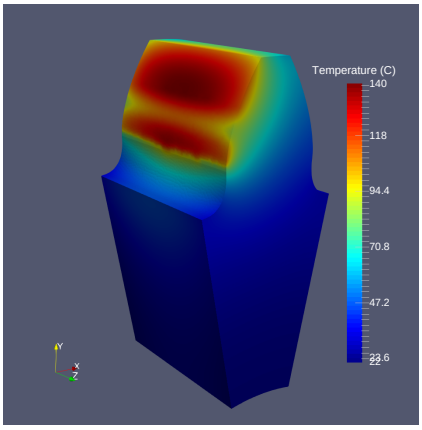

(a) Temperature without insert (T_{max}=139.40°C and T_{min}=22.28°C).

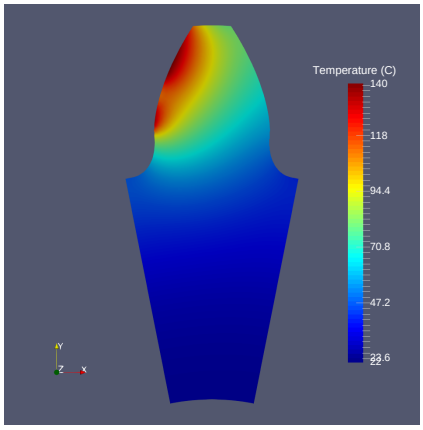

(b) Temperature cut without insert (T_{max}=139.40°C and T_{min}=22.28°C).

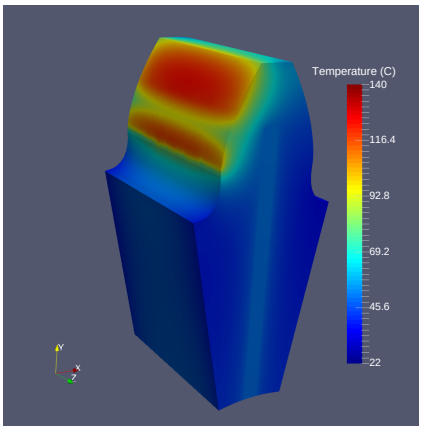

(c) Temperature result, Razor (T_{max}=123.52°C and T_{min}=35.00°C).

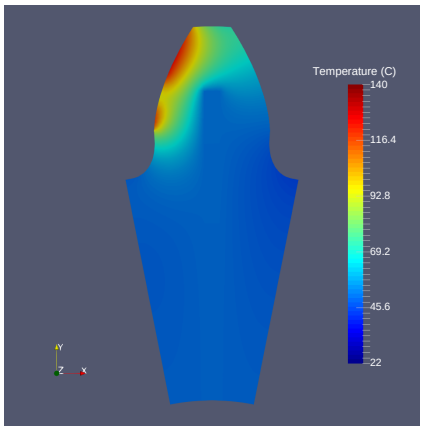

(d) Temp. Insert result - Razor (T_{max}=123.52°C and T_{min}=35.00°C).

Figure 6.25.: Temperature distribution for a POM gear and Rectangular cuboid (razor) Profile hybrid gear at 25 MPa.

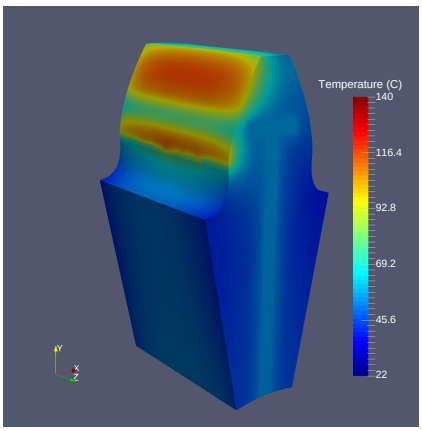

(a) Temperature result - T-profile (T_{max}=115.88°C and T_{min}=37.59°C).

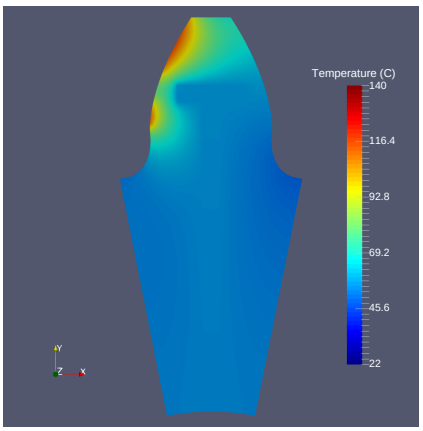

(b) Temperature result insert - T-Profile (T_{max}=115.88°C and T_{min}=37.59°C).

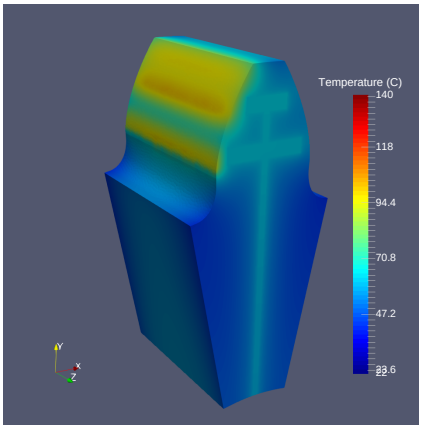

(c) Temp. result - Double T-profile I (T_{max}=100.66°C and T_{min}=40.69°C).

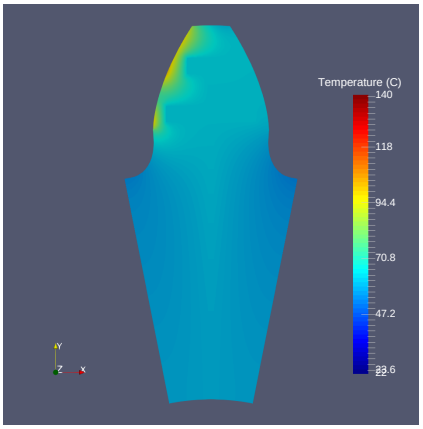

(d) Temp. result insert - Double T-profile I (T_{max}=100.66°C and T_{min}=40.69°C).

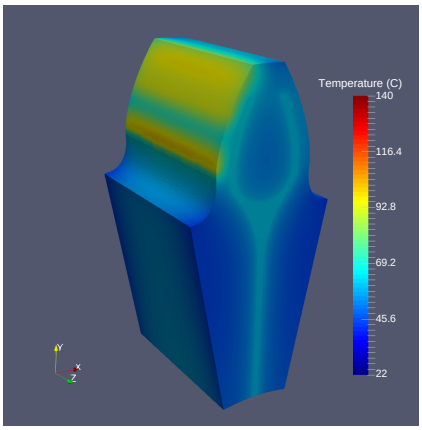

(e) Temperature result - involute (T_{max}=99.64°C and T_{min}=42.27°C).

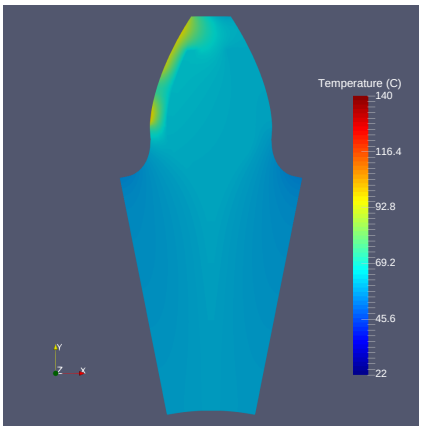

(f) Temperature result insert - involute (T_{max}=99.64°C and T_{min}=42.27°C).

Figure 6.26.: Temperature distribution for a T-Profile, a Double T-profile I and a Involute Profile at 25 MPa.

6.9. Mesh Influence

During this chapter, Chapter 6, different studies were made to analyze the influence of the material for the tooth insert and of the different geometries of insert on the maximum and minimum temperatures.

The simulation of the different insert geometries required the creation of several meshes for each profile used. Therefore, due to a high demand of computational resource of the solver used for the simulations, an estimation of the numerical error associated with the previous meshes by using the Richardson extrapolation method was studied.

6.9.1. Richardson extrapolation method

According to *Feldman*'s work [73] one way to calculate the numerical errors is to use a technique called the Richardson Extrapolation. The main idea behind this method is that when a monotone convergence is obtained after comparing three different grids, which will have a constant refinement ratio amongst them, it is possible to extrapolate the numerical value free of discretization errors. If the numerical monotone convergence is not observed it can mean one of two things: either the grids are not refined enough to estimate the numerical error or the numerical error is much larger than expected, which can be solved by refining the mesh.

The extrapolation solution (φ_{extra}) independent of the mesh size can be calculated using equation (6.31).

$$\varphi_{extra} = \varphi_h + \frac{\varphi_h + \varphi_{2h}}{r_{den}^{p_{ord}} - 1} \tag{6.31}$$

where the φ_h is the solution on a grid with an average spacing h (refined mesh); r_{den} is the factor for the grid density increment (for instance, if the space between nodes on each coordinate from the 3D coordinate system is halved, this is, $r_{den} = 2$) and p_{ord} is the order of the numerical method, which can be calculated by equation (6.32)

$$p_{ord} = \frac{\log_{10}\left(\frac{\varphi_{2h} - \varphi_{4h}}{\varphi_h - \varphi_{2h}}\right)}{\log_{10}\left(r_{den}\right)} \tag{6.32}$$

Where φ_{2h} is the solution on a grid with an average spacing of 2h (which is the mesh normally used for the results and analysis); φ_{4h} is the solution on a grid with average spacing of 4h (which is the coarse mesh).

It is recommended that the consecutive spacings of 4h, 2h and h be at least 50% more nodes in each direction than its original grid.

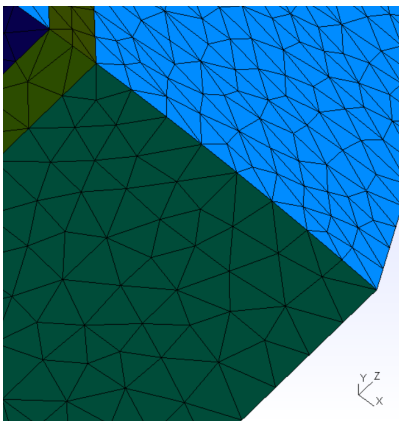

Figure 6.27.: Involute profile mesh normally used for the past simulations (2h).

6.9.2. Mesh numerical errors

Involute profile

It is expected that using the involute profile insert, analyzed in the final section of Chapter 6, the worst element distortion is present due to the curvature of the cup profile. Therefore, the study of influence of the mesh will focus on the involute profile as an example of the procedure to calculate the numerical error.

Mesh used

As explained earlier the consecutive spacing between the 4h, 2h and h grids have to be at least 50% more in each direction than the original mesh created, meaning that the normal mesh used cannot be highly refined, otherwise the refined mesh will take too much time to calculate the solution.

Assuming the above statement, the normal mesh created for the simulation of the involute profile was achieved with the help of the variable "cl_1" (which defines the mesh element size at that point as explained when creating the GEO file for the Gmsh software) using the value of 0.35, resulting in a mesh with 299712 elements and 47056 nodes. The total number of triangular elements at the bottom side, represented in Figure 6.27, after the insert, is 8.

For this case, the consecutive spacing between the comparative grids was set to be 75% higher ($r_{den} = 1.75$). So, for the grid with the least refinement was used a "cl_1" of 0.20, resulting in a mesh with 110169 elements and 17277 nodes. The total number of triangular elements at the bottom of the gear model, represented in Figure 6.28a, after the insert, is 5. Finally, for the grid with finest refinement the mesh was created with the value "cl_1"=0.15, resulting in a mesh with 1620669 elements and 253990 nodes. The total number of triangles at the bottom of the gear

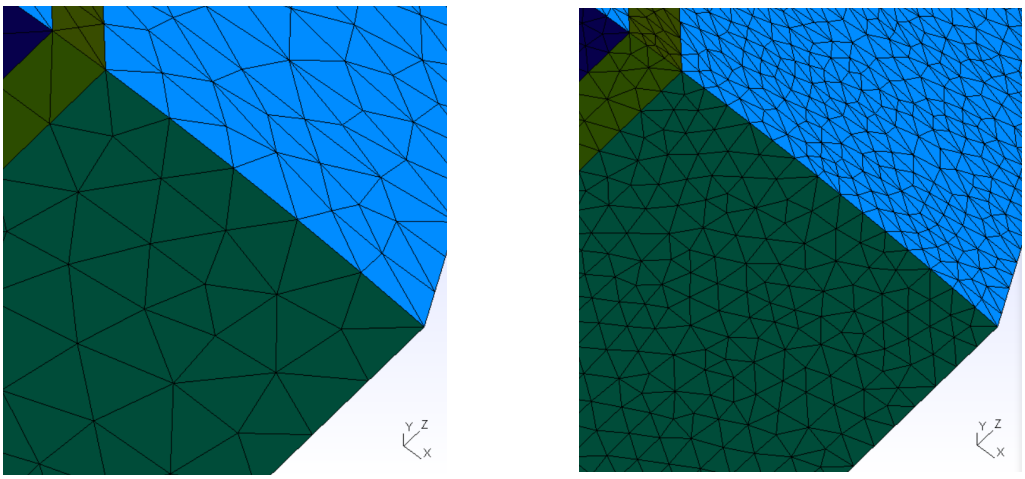

(a) Coarse mesh (4h). (b) Refined mesh (h).

Figure 6.28.: Involute profile meshes created for the Richardson extrapolation (4h and h).

Table 6.23.: Numerical error, extrapolated values and grid solution for the maximum temperature for the cup profile at 25 MPa.

Maximum Temperature [°C]				
$\varphi_{\mathbf{h}}$	$\varphi_{\mathbf{2h}}$	$\varphi_{\mathbf{4h}}$	$\varphi_{\mathbf{extra}}$	Error [%]
98.45	99.64	102.25	96.86	2.87

model mesh created, represented in Figure 6.28b, after the insert, is 14.

Numerical order, error and extrapolated value

Due to the low order of the numerical method, since the equation solved is a heat equation with only conductive heat transfer mode, the value for p_{ord} is expected to be 1. For this case, the maximum temperature being the object of study, the values to compare will be the maximum temperatures of a hybrid tooth with a contact pressure in the insert assumed to be 25 MPa.

The numerical method to solve the equations is of first order ($k \cdot \partial T/\partial x = 0$) and using equation (6.32) the value to the numerical order was of 1.4035. So, since it is near of 1, this last result is taken as acceptable.

Finally, the value of p_{ord} is assumed to be 1, since the numerical method order was also 1, to simplify the calculation of the extrapolation as well as the numerical error. Their values can be found in the Table 6.23 with the inclusion of the solution for each grid used.

Presentation of all numerical errors and extrapolated values

All the meshes used during profile geometry testing were submitted to the same numerical error study proceeding firstly with the creation of the normal mesh, then to the creation of the other two mesh sizes: better and worst refinement over the original mesh created. The same spacing between compared grids was guaranteed during these meshes' generation, with the triangular elements from the bottom of the gear body after the insert being 14, 8 and 5 for the grid with the refined mesh, the normal mesh and the coarse mesh, respectively, using for this the manipulation of the variable "cl_1". The number of nodes as well as the number of elements of each mesh created for all the tested profiles are listed in Table 6.24.

Then, after all meshes were generated, the simulations for each mesh of each profile was executed using for this study a constant contact pressure of 25 MPa. Afterwards, with p=1, the extrapolated value was calculated, and, therefore, the numerical error was also obtained, as presented in Table 6.25 (including the value of the maximum temperature of each insert geometry used).

To sum up, all the numerical errors calculated were very low as expected since the numerical equation in study is of first order, although the worst numerical error obtained was of 2.87% for the involute insert. Moreover, the numerical error could be decreased either with the use of a refined mesh or using a structured mesh (this type of mesh creation takes a lot of time, since the possible volumes that could be generated are with 4 to 8 corner points and the gear body volume cannot be generated as one volume but a group of different volumes).

Table 6.24.: Number of nodes and elements for all geometries grids created.

Insert Type	**Geo. Para.** [mm]	$\varphi_{\mathbf{h}}$		$\varphi_{\mathbf{2h}}$		$\varphi_{\mathbf{4h}}$	
		Nodes	**Elements**	**Nodes**	**Elements**	**Nodes**	**Elements**
Initial Gear	-	241696	1487640	49386	296620	16623	97358
Rectangular Cuboid (Razor)	e=2.250 w_x=0.450 t=4.500	255219	1599739	54459	338826	16553	101734
Rectangular Cuboid (Razor)	e=2.250 w_x=2.250 t=4.500	255776	1606149	54038	336447	16133	101886
Rectangular Cuboid (Razor)	e=2.250 w_x=1.125 t=4.500	260505	1626352	55449	366446	16215	101987
Rectangular Cuboid (Razor)	e=2.250 w_x=1.125 t=2.250	257109	1618525	54424	339983	16433	101192
Rectangular Cuboid (Razor)	e=2.250 w_x=1.125 t=0.000	258925	1631655	54167	338682	16100	100335
Rectangular Cuboid (Razor)	e=0.000 w_x=1.125 t=4.500	255153	1625982	54906	345006	16555	102765
T-Profile (vw=1.125)	e=0.000 w_x=1.125 t=4.500	263864	1673400	54833	346263	17005	106395
Double T-Profile (vw=1.125)	e=0.000 w_x=1.125 t=2.250	265313	1688701	55282	350994	17348	109343
Double T-Profile I (vw=1.125)	e=0.000 w_x=1.125 t=2.250	267192	1706006	55827	356164	17328	109868
Double T-Profile I (vw=1.125)	e=0.000 w_x=0.788 t=2.250	265783	1697300	54988	350645	17216	109360
Double T-Profile I (vw=1.125)	e=0.000 w_x=0.675 t=2.250	262259	1676794	55103	351478	17732	112271
Double T-Profile I (vw=1.125)	e=0.000 w_x=0.450 t=2.250	264237	1687615	56052	357838	17809	113197
Double T-Profile I (vw=0.450)	e=0.000 w_x=0.450 t=2.250	261093	1665985	56022	358149	18106	115573
Involute Profile	e=0.000 w_x=0.450 t=2.250	253990	1620669	47056	299712	17277	110169

Table 6.25.: Numerical error of maximum temperature at 25 MPa all geometries tested.

Maximum Temperature [°C]						
Insert Type	**Geo. Para.** [mm]	$\varphi_{\mathbf{h}}$	$\varphi_{\mathbf{2h}}$	$\varphi_{\mathbf{4h}}$	$\varphi_{\mathbf{extra}}$	**Error** [%]
Initial Gear	-	138.63	139.4	143.94	137.60	1.31
Rectangular Cuboid (Razor)	e=2.250 w_x=0.450 t=4.500	127.98	128.45	129.20	127.35	0.86
Rectangular Cuboid (Razor)	e=2.250 w_x=2.250 t=4.500	122.26	122.47	122.58	121.98	0.40
Rectangular Cuboid (Razor)	e=2.250 w_x=1.125 t=4.500	125.36	125.89	127.87	124.65	0.99
Rectangular Cuboid (Razor)	e=2.250 w_x=1.125 t=2.250	119.31	119.84	119.31	118.6	1.04
Recatangular Cuboid (Razor)	e=2.250 w_x=1.125 t=0.000	123.15	124.11	129.15	121.87	1.84
Rectangular Cuboid (Razor)	e=0.000 w_x=1.125 t=4.50	122.99	123.52	124.13	122.28	1.01
T-Profile (vw=1.125)	e=0.000 w_x=1.125 t=4.500	115.26	115.88	115.95	114.43	1.26
Double T-Profile (vw=1.125)	e=0.000 w_x=1.125 t=2.250	106.31	107.36	113.61	104.91	2.34
Double T-Profile I (vw=1.125)	e=0.000 w_x=1.125 t=2.250	97.85	98.82	99.35	96.79	2.10
Double T-Profile I (vw=1.125)	e=0.000 w_x=0.788 t=2.250	98.83	99.59	99.90	97.82	1.81
Double T-Profile I (vw=1.125)	e=0.000 w_x=0.675 t=2.250	98.97	99.82	100.58	97.84	2.03
Double T-Profile I (vw=1.125)	e=0.000 w_x=0.450 t=2.250	99.98	100.66	100.98	99.073	1.60
Double T-Profile I (vw=0.450)	e=0.000 w_x=0.450 t=2.250	101.90	102.93	105.88	100.53	2.39
Involute Profile	e=0.000 w_x=0.450 t=2.250	98.45	99.64	102.25	96.86	2.87

Table 6.26.: Maximum and minimum temperature at 25 MPa over all insert material tested.

Temperature Results [°C]				
Insert Material	**Max. Temp.**	**Min. Temp.**	**Temp. Reduction** [%]	**Weight Increment** [%]
Initial Gear	139.40	22.28	-	-
Copper	128.07	35.00	-8.13	16.54
Aluminum	128.33	34.99	-7.94	2.88
Steel	130.88	34.86	-6.11	13.89

6.10. Closure

To sum up, the implementation of a metallic insert in the hybrid-gear helped capture and dissipate the heat flux generated by friction over the meshing surface and, therefore, increasing the gear's operating life as well as its mechanical properties (since they are dependent on temperature).

The temperature results as a function of the materials used for the insert are listed at Table 6.26, justifying the use of an aluminum insert for the hybrid gear.

For a better reading of the geometric profile tested, Table 6.27 was created, summarizing all the result found for all the geometries tested. For a more detailed description of the geometry results, ith discussion and respective optimization, Appendix I was written.

Table 6.27.: Maximum and minimum temperature at 25 MPa over all geometries tested .

Temperature Results				
Insert type	**Geo. Para.** [mm]	**Max. Temp.** [°C]	**Min. Temp.** [°C]	**Reduction** [%]
Initial Gear	-	139.40	22.28	-
Rectangular Cuboid (Razor)	e=2.250 w_x=0.450 t=4.500	128.45	34.96	-7.86
Rectangular Cuboid (Razor)	e=2.250 w_x=2.250 t=4.500	122.47	37.40	-12.14
Rectangular Cuboid (Razor)	e=2.250 w_x=1.125 t=4.500	125.89	35.66	-9.69
Rectangular Cuboid (Razor)	e=2.250 w_x=1.125 t=2.250	119.84	37.91	-14.03
Rectangular Cuboid (Razor)	e=2.250 w_x=1.125 t=0.000	124.11	38.88	-10.97
Rectangular Cuboid (Razor)	e=0.000 w_x=1.125 t=4.500	123.52	35.00	-11.39
T-Profile (vw=1.125)	e=0.000 w_x=1.125 t=4.500	115.88	37.59	-16.87
Double T-Profile (vw=1.125)	e=0.000 w_x=1.125 t=2.250	107.36	39.06	-22.98
Double T-Profile I (vw=1.125)	e=0.000 w_x=1.125 t=2.250	98.82	40.83	-29.11
Double T-Profile I (vw=1.125)	e=0.000 w_x=0.788 t=2.250	99.59	40.77	-28.56
Double T-Profile I (vw=1.125)	e=0.000 w_x=0.675 t=2.250	99.82	40.75	-28.39
Double T-Profile I (vw=1.125)	e=0.000 w_x=0.450 t=2.250	100.66	40.69	-27.79
Double T-Profile I (vw=0.450)	e=0.000 w_x=0.450 t=2.250	102.93	40.15	-26.16
Involute Profile	e=0.000 w_x=0.450 t=2.250	99.64	42.27	-28.32

Chapter 7.

Conclusions and future work

7.1. Conclusions

This work, discussed in a systematic and planned way the implementation of a FEM model to predict the exact bulk temperature distribution over a gear tooth. The model allowed to study the influence of the gear geometry as well as the influence of a metallic insert which was the main objective of the work.

In Chapter 1, a general description about steel and polymeric gears was done focusing on the disadvantages and advantages of each one. A possible solution to the problems associated to the use of a plastic gear were also presented and an introduction to the hybrid-gear as solution was shown.

The theoretical thermal model, based on a power loss model already experimentally validated, focusing on the heat generated by the friction between the two meshing surfaces of the gear bodies (load dependent gear losses) were presented in Chapter 3. A description of the boundary conditions was explained in this Chapter, more specifically: the thermal equations, the heat transfer coefficient and the heat fluxes applied over each boundary. Moreover, the introduction of the concept of the flash temperature and the differences of the quasi-steady state and a transient heat problem.

The FEM computational implementation with multiple softwares packages used for the mesh creation, the Solver used for the FEM equation solution and the functions for the calculation of the heat transfer coefficients and heat fluxes can be found in Chapter 4.

The validation of the FEM model constructed with experimental data from literature as well as numerical data was discussed in Chapter 5, showing a very good correlation with the experimental data for the steady-state (dip lubrication and oil jet lubrication) and transient-state (dry contact for polymeric and metallic gear)

cases.

At the beginning of Chapter 6 the concept of hybrid-gear was introduced presenting the heat transfer mechanism over the metal/polymer interface (Thermal Contact Resistance - TCR). The major advantage of polymeric gear is its use without lubrication, since it is lubricated for life. So, a comparative study with a C14 standard gear between a plastic gear and three other metallic materials for a dry contact simulation was presented.

An introduction to the study of the influence of the material for the insert of the hybrid-gear was done as well as the influence of the contact pressure on the interface of polymer/metal (resulting that the aluminum was the best scenario due to its low weight, high thermal conductivity and production cost). An analysis of the geometric parameters of the insert, such as the insert horizontal width, the length to the gear side and the height to the tooth-tip of the gear was detailed explained.

Finally, the examination of various possible geometries for the insert in order to solve the heat dissipation problem was study, starting of with the developing geometries with increasing complexity: from a simple razor to a involute one. A reduction of the maximum temperature of 28% was achieved (140°C to 101°C, using a Double T-Profile) in comparison to the baseline (all polymer gears).

At the end of this chapter a new profile for the insert was studied, called involute profile, since it begin as a singular body at the shaft/gear interface and, then, divided into two involutes that follows the tooth's flank and face surfaces. However, no significant differences on the numerical values from the Double T-profile were observed.

It is important to notice that the temperature distribution for the hybrid gear was smoother than the one found for the initial polymeric gear. However, in order to decrease the maximum temperature it was observed that the minimum temperature of the gear body increased 80% (22 °C to 40 °C) due to higher thermal conductivity, leading to a distribution of temperature more uniform.

Finally, the influence of the mesh size on the numerical error was studied. The Richardson extrapolation method was used in order to calculate the numerical error for different mesh refinements. It was found that due to the low order of the heat conduction problem, the numerical error of the mesh refinement used for this work was very low, lower than 3%.

The present work allowed to validate a FEM model able to simulate accurate results both for the transient and steady state problems as well as lubricated and dry contact for determinate operating conditions.

The implementation of the metallic insert of aluminum lead to a double T-profile or an involute that allowed achieving a reduction of the maximum temperature.

The present work clearly shows that the use a metallic insert on a polymer gear will decrease the operating temperature and possibly increase the gear's load capacity and life.

7.2. Future Work

Several topics addressed in this dissertation require further analysis and development:

- The introduction of all power losses (including the rolling bearing power losses, seals losses, the auxiliary as well as the no-load losses) on the power loss model implemented for a more accurate and powerful model to predict the bulk temperature distribution.
- A creation of a new profile of insert with a combination of the involute profile with the double T-profile to further the decrease the maximum temperature as well as the creation of other profiles.
- The study of the same geometries with different hybrid-gear body materials with higher thermal conductivity, rather than using POM (acetal).
- Begin the experimental work with analysis of the real contact pressure on the interface of polymer/metal to get an accurate final result (as explained, the study of bulk temperature was done over range of contact pressure and not at one specific value).
- Study the possibility of adding a material with higher thermal conductivity for the gear body as well as to study a method of cooling the insert, for example the of a water circulation system inside the insert to further reduce the bulk temperature.

Bibliography

[1] G. D. Roberts, R. R. Sinnamon, B. D. D. D. B. Stringer, L. W. Kohlman, Hybrid gear preliminary results - application of composites to dynamic mechanical components, NASA - Scientific and Technical Information Office 1 (2013) 72–79.

[2] C. N. D. Fh, P. B. Höhn, P. Karsten, Prospects of compound-gears for e-mobility applications, Conference on Future Automotive Technology: Focus Electromobility 1 (2013) 1–5.

[3] J. L. Elmquist, Deciding when to go plastic, Gear Technology 1 (2014) 46–47.

[4] N. Tuskamoto, Investigation about the strength of plastic gears: 6th report, endurance limit and damage state of nylon gear for power transmission, Bull. JSME 28 (241) (1985) 1528–1534.

[5] K. Terashima, N. N. N. Tsukamoto, J. Shi, Development of plastic gear for power transmission: Abnormal wear on the tooth fracture near pitch point, Bull. JSME 29 (251) (1986) 1598–1604.

[6] N. Tsukamoto, T. Yano, H. Sakai, Noise and transmission efficiency under deformation of tooth form of nylon gear, JSME 25 (207) (1982) 1465–1473.

[7] N. Tsukamoto, Argument on plastic gears for power transmission, JSME International Journal 38 (1) (1995) 1–8.

[8] Vdi 2736: Blatt 1. thermoplastische zahnräder. werkstoff, werstoffauswahl, herstellverfahren, herstellgenauigkeit, gestalten., Tech. rep., VDI Richtlinien., Dusseldorf: VDI-Verlag GmbH (2014).

[9] Vdi 2736: Blatt 2, thermoplastische zahnräder, stirnradgkeitsberechnung, tragfähigkeitsberechnung, Tech. rep., VDI Richtlinien, Dusseldorf: VDI-Verlag GmbH (2014).

[10] A. F. Lourenco, Testing of low-loss polymer gears, Master's thesis, Faculdade de Engenharia da Universidade do Porto (2015).

[11] K. Terashima, N. Tsukamoto, N. Nishida, Development of plastic gears for power transmission : Design on load-carrying capacity, JSME 29 (250) (1986) 1326–1329.

[12] K. Terashima, N. Tsukamoto, N. Nishida, Development of plastic gears for power transmission : Economical methods for increasing load-carrying capacity, JSME 29 (247) (1986) 256–259.

[13] N. Tsukamoto, H. M. T. Taki, N. Nishida, A study on strength design methods of plastic gears (2nd report, estimation of operation life of plastic gears in an elevated temperature environment), Trans. Japan Soc. Mech. Eng. Ser. C. 56 (521) (1990) 131–135.

[14] T. Hubert, M. Bauser, C. Hasl, T. Tobie, K. Stahl, Load carrying capacity of cylindrical plastic gears, International Conference on High Performance Plastic Gears (2015) 1273–1282.

[15] B. R. Höhn, K. Michaelis, T. Vollner, Thermal Rating of Gear Drives: Balance Between Power loss and Heat Dissipation, 1996.

[16] C. M. C. G. Fernandes, R. C. Martins, J. H. O. Seabra, Coefficient of friction equation for gears based on a modified hersey parameter, Tribol. Int. 101 (2016) 204–217.

[17] C. M. C. G. Fernandes, L. B., J. S., R. C. Martins, J. H. O. Seabra, Energy efficiency test in a full scale wind turbine gearbox, Tribol. Int. 101 (2016) 375–382.

[18] K. Mao, W. Li, C. Hooke, D. Walton, Friction and wear behaviour of acetal and nylon gears, Wear 267 (1-4) (2009) 639–645.

[19] N. Tsukamoto, K. Terashima, Development of plastic gears for power transmission: various methods of lengthening the life of plastic gears and their effect, JSME 29 (247) (1986) 249–255.

[20] K. Mao, A new approach for polymer composite gear design, WEAR (262) (2007) 432–411.

[21] W. Cheewawuttipong, D. Fuoka, S. Tanoue, H. Uematsu, Y. Lemoto, Thermal and mechanical properties of polypropylene/boron nitride composites, Energy Procedia 34 (2013) 808–817.

[22] M. S. Wirth, R. T. Seidler, Determination of load carrying capacity characteristic values for plastic gears, International Conference on High Performance Plastic Gears (2015) 1273–1282.

[23] B. Höhn, K. Michaelis, M. Hinsterstoiber, Optimization of gearbox efficiency, Goriva i maziva 48 (4) (2009) 462–480.

[24] B. R. Höhn, K. Michaelis, T. Vollmer, Thermal rating of gear drives: Balance between power loss and heat dissipation, 1996.

[25] E. Buckingham, Analytical mechanics of gears - Dover Book for Engineers, McGraw-Hill Book Co, 1949.

[26] H. Ohlendorf, Verlustleistung and erwärmung von stinrädern, Ph.D. thesis, TU München (1958).

[27] J. A. de Sousa Ferreira Brandão, Gear tooth flank damage prediction using high-cycle fatigue and wear models, Ph.D. thesis, Faculdade de Engenharia da Universidade do Porto (2013).

[28] G. Niemann, H. Winter, Maschinenelement: Band 2: Getriebe allgemein, Zahnradgetriebe - Grundlagen, Stirnradgetriebe, Measchinenelemente, 1989.

[29] G. Henriot, Traité Theéorique et pratique des engenages, 1978.

[30] C. M. C. G. Fernandes, P. M. T. Marques, R. C. Martins, J. H. O. Seabra, The influence of gear loss factor on the power loss prediction, Mechanical and Machine Sciences 24 (2) (2015) 799–806.

[31] P. M. T. Marques, R. C. Martins, J. H. O. Seabra, Power loss and load distribution models including frictional effects for spur and helical gears, Mechanism and Machine Theory 96 (Part 1) (2016) 1–25.

[32] X. Hai, Development of a general mechanical efficiency prediction methodology for gear pairs, Ph.D. thesis, The Ohio State University (2005).

[33] C. M. C. G. Fernandes, R. C. Martins, J. H. O. Seabra, Coefficient of friction equation for gears based on modified harsey parameter, Tribology International 101 (2016) 204–217.

[34] L. Schlenk, Unterscuchungen zur fresstragfähigkeit von grozahnrädern, Ph.D. thesis, TU München (1994).

[35] H. Blok, The flash temperature concept, Wear 6 (1963) 483–494.

[36] F. Kreith, R. M. Manglik, M. S. Bohn, Principles of Heat Transfer, 7th Edition, Global Energineering, 2011.

[37] T. L. Bergam, A. S. Lavine, F. P. Incropera, D. P. Dewitt, Fundamentals of Heat and Mass Transfer, 7th Edition, John Wiley & Sons, 2011.

[38] J. P. Hartnett, E. C. Deland, The influence of the prandtl number on the heat transfer from rotating nonisothermal disk and cones, Journal of Heat Transfer 83 (1) (1961) 95–96.

[39] E. C. Cobb, O. A. Saunders, Heat transfer from rotating disk, Proc. R. Soc. London Ser. A. 220 (1956) 343–351.

[40] C. Wagner, Heat transfer from rotating disk to ambient air, J. Appl. Phys. 19 (1948) 837–841.

[41] O. Z. C. Popiel, L. Boguslawski, Load heat-transfer coefficient on the rotating disk in still air, International Journal Heat Mass Transfer 18 (1975) 167–170.

[42] L. A. Dorfman, Hydrodynamic Resistance and the Heat Loss of Rotating Solids, 1963.

[43] Y. Shunlei, The simulation analysis of transient temperature of spiral bevel gear based on finite element method, Techonologies & Products J (2010) 43–48.

[44] A. DeWinter, H. Blok, Fling-off cooling of gear teeth, Journal of Engineering for Industry 96 (1) (1974) 60–70.

[45] G. J. J. van Heijningen, H. Blok, Continuous as against intermittent fling-off cooling of gear teeth, Journal of Lubrication Technology 96 (4) (1974) 529.

[46] G. J. J. van Heijningen, Fling-off cooling of gear teeth, Tribology International 17 (1984) 11–18.

[47] R. F. Handschuh, T. P. Kicher, A method for thermal analysis of spiral bevel gears, Lewis Research Center 118 (1994) 580–585.

[48] R. F. Handschuh, Thermal behavior of spiral bevel gears, Lewis Research Center 1 (1995) 52.

[49] B. Luo, W. Li, Influence factors on bulk temperature field of gear, Journal of Engineering Tribology (2016) 1350650116684275.

[50] L. Jie, Z. Lei, Z. Qi, Comparison and analysis on different finite element model of gear interfacial contact temperature, IEEE Computer Society 3 (2010) 132–136.

[51] KISSsoft, The kisssoft interface to solidworks, acessed: 31/05/2017 `http://www.kisssoft.ch/english/products/pdf/SolidWorks_Flyer.pdf`.

[52] C. Geuzaine, J.-F. Remacle, Gmsh reference manual, acessed: 31/05/2017 `http://gmsh.info/doc/texinfo/gmsh.pdf` (May 2017).

[53] Mathworks help - documentation, https://www.mathworks.com/help (2017).

[54] CSC, Elmer, acessed: 31/05/2017 https://www.csc.fi/web/elmer.

[55] D. Kuzmin, J. Hämäläinen, Finite Element Methods for Computational Fluid Dynamic - A pratical guide, Society for Industrial and Applied Mathematic, 2015.

[56] J. Ruokolainen, M. Malinen, P. Raback, T. Zwinger, A. Pursula, M. Byckling, ElemerSolver Manual, 2015, http://www.csc.fi/elmer.

[57] H. Long, A. A. Lord, D. T. Gethin, B. J. Roylance, Operating temperatures of oil-lubircated medium-speed gears: numerical model and experimental results, IMechE 217 (2003) 87–106.

[58] B.-R. Höhn, K. Michaelis, H.-P. Otto, Influence of immersion depth of dip lubricated gears on power loss, bulk temperature and scuffing load carrying capacity, Int. J. Mech. Mater Des. 4 (2007) 145–156.

[59] K. Mao, A numerical method for polymer composite gear flash temperature prediction, WEAR 262 (2007) 1321–1329.

[60] Various, Spacecraft Thermal Control Handbook - Volume I: Fundamental Technologies, Vol. I, The Aerospace Press, 2002.

[61] M. G. Cooper, B. B. Mikic, M. M. Yovanovich, Thermal contact conductance, int. J. Heat Mass Transfer. 12 (1969) 279–300.

[62] D. D. S. for Precision Engineering), Thermal contact conduction, acessed: 31/05/2017 http://www.dspe.nl/knowledge-base/thermomechanics/chapter-1---basics/1-2-heat-transfer/thermal-contact-conduction/.

[63] J. Gibbins, Themal contact resistance of polymer interfaces, Master's thesis, University of Waterloo (2006).

[64] J. A. Greenwood, J. B. P. Williamson, Contact of nominally flat surfaces, Proceedings of the Royal Society of London 295 (1966) 300–319.

[65] T. N. Cetinkale, M. Fishenden, Thermal conductance of metal surfaces in contact, International Conf. of Heat Transfer (1951) 271–275.

[66] M. M. Yovanovich, Thermal contact correlations. progress in aeronautics and aerodynamics: Spacecraft radiative transfer and temperature control, American Institute of Aeronautics and Astronautics 20 (1982) 102–150.

[67] B. Mikic, Thermal contact conductance: theoretical considerations, Int. Journal of Heat and Mass Transfer 17 (2) (1974) 205–214.

[68] J. J. Fuller, E. E. Marotta, Thermal contact conductance of metal/polymer joints: an analytical and experimental investigation, Journal of Thermophysics and Heat Transfer 15 (2) (2001) 228–238.

[69] M. R. Sridhar, M. M. Yovanovich, Elastoplastic contact conductance model for isotropic, conforming rough surfaces and comparison with experiments, Journal of Heat Transfer 118 (1) (1996) 3–9.

[70] E. ToolBox, Engineering toolbox, acessed: 31/04/2017 `http://www.engineeringtoolbox.com/`.

[71] M. Bahrami, M. M. Yovanovich, E. E. Marotta, Thermal joint resistance of polymer-metal rough interfaces, Journal of Electronic Packaging 128 (1) (2006) 23–29.

[72] E. C. for space standardization, Space Engineering - Threaded fasteners handbook, ECSS (Apr. 2010).

[73] J. Feldman, Richardson extrapolation, `http://www.math.ubc.ca/~feldman/m256/richard.pdf` (2003).

[74] C. Geuzaine, J. F. Remacle, Gmsh: a three-dimensional finite element mesh generator with built-in pre- and post-processing facilities, International Journal for Numerical Methods in Engineering 79 (11) (2009) 1309–1331.

[75] P. J. Frey, P.-L. George, Mesh Generation: Application to finite elements, HERMES Science Publishing, 200.

[76] S. Rebay, Efficient unstructured mesh generation by means of delaunay triangulation and bowyer-watson algorithm, J. Comput. Phys. 106 (1993) 25–138.

[77] C. Geuzaine, J.-F. Remacle, Gmsh 3.0, acessed: 31/05/2017 `http://gmsh.info/doc/texinfo/` (May 2017).

[78] H. Si, Tetgen: a quality tetrahedral mesh generator and three-dimensional delaunay triangulation, ACM Transactions on Mathematical Software 41 (11) (2015) 1–36.

[79] J. Schoeberl, Netgen, an advancing front 2d/3d-mesh generator based on abstract rules, Comput. Visual. Sci. 1 (1997) 41–52.

Appendix

Appendix A.

Example of Code for GEO file

Code created for the example at Chapter 4:

```
cl = 0.35;
Point(1) = {-1.864846548753691, 28.23849052887923, -8.499999999999996, cl};
Point(2) = {-0.6906349915675416, 31.99004578862652, -8.5, cl};
Point(3) = {-0.6906349915675427, 31.99004578862652, 8.5, cl};
Point(4) = {-1.864846548753695, 28.23849052887921, 8.499999999999996, cl};
Point(5) = {1.864846548753698, 28.23849052887923, 8.500000000000004, cl};
Point(6) = {0.6906349915675242, 31.99004578862652, 8.500000000000004, cl};
Point(7) = {0.6906349915675257, 31.99004578862652, -8.5, cl};
Point(8) = {1.8648465487537, 28.23849052887921, -8.500000000000004, cl};
Point(9) = {1.5039087595186, 14.92441819445714, -8.500000000000007, cl};
Point(10) = {-1.5039087595186, 14.92441819445714, -8.500000000000007, cl};
Point(11) = {-2.744770193028943, 27.2384198503888, -8.5, cl};
Point(12) = {2.74477019302896, 27.2384198503888, -8.5, cl};
Point(13) = {2.74477019302896, 27.2384198503888, 8.5, cl};
Point(14) = {-2.744770193028958, 27.2384198503888, 8.5, cl};
Point(15) = {1.5039087595186, 14.92441819445714, 8.5, cl};
Point(16) = {-1.5039087595186, 14.92441819445714, 8.5, cl};
p1 = newp;
Point(p1 + 1) = {-1.853469184205896, 28.32211555246558, -8.499999999999998};
Point(p1 + 2) = {-1.844762921032103, 28.40905162880364, -8.499999999999998};
Point(p1 + 3) = {-1.836188607753355, 28.50370968344115, -8.499999999999998};
Point(p1 + 4) = {-1.824901110785217, 28.61024514437904, -8.499999999999998};
Point(p1 + 5) = {-1.809199193475622, 28.73056183105078, -8.499999999999998};
Point(p1 + 6) = {-1.788696640609108, 28.86416069551368, -8.499999999999998};
Point(p1 + 7) = {-1.762897529456859, 29.01071270176168, -8.499999999999998};
Point(p1 + 8) = {-1.731225569870119, 29.17003278946764, -8.499999999999998};
Point(p1 + 9) = {-1.693104471700131, 29.34193589830439, -8.499999999999998};
Point(p1 + 10) = {-1.647955660741566, 29.52623993413103, -8.499999999999998};
Point(p1 + 11) = {-1.595195497613744, 29.72275018554846, -8.499999999999998};
Point(p1 + 12) = {-1.534288668166774, 29.9311717554823, -8.499999999999998};
Point(p1 + 13) = {-1.464709180287872, 30.15119376065824, -8.499999999999998};
Point(p1 + 14) = {-1.385931041864253, 30.38250531780196, -8.499999999999998};
Point(p1 + 15) = {-1.297428260783133, 30.62479554363916, -8.499999999999998};
Point(p1 + 16) = {-1.198674844931726, 30.87775355489552, -8.499999999999998};
Point(p1 + 17) = {-1.089144802197248, 31.14106846829675, -8.499999999999998};
```

```
Point(p1 + 18) = {-0.9683121404669144, 31.41442940056854, -8.5};
Point(p1 + 19) = {-0.8356508676279406, 31.69752546843656, -8.5};
Spline(1) = {1, p1 + 1, p1 + 2, p1 + 3, p1 + 4, p1 + 5, p1 + 6, p1 + 7, p1 + 8, p1 + 9, p1 + 10,
p1 + 11, p1 + 12, p1 + 13, p1 + 14, p1 + 15, p1 + 16, p1 + 17, p1 + 18, p1 + 19, 2};
Line(2) = {2, 3};
p3 = newp;
Point(p3 + 1) = {-0.8356508676279426, 31.69752546843656, 8.5};
Point(p3 + 2) = {-0.9683121404669173, 31.41442940056853, 8.5};
Point(p3 + 3) = {-1.089144802197251, 31.14106846829675, 8.499999999999998};
Point(p3 + 4) = {-1.19867484493173, 30.87775355489552, 8.499999999999998};
Point(p3 + 5) = {-1.297428260783137, 30.62479554363915, 8.499999999999998};
Point(p3 + 6) = {-1.385931041864257, 30.38250531780195, 8.499999999999998};
Point(p3 + 7) = {-1.464709180287876, 30.15119376065822, 8.499999999999998};
Point(p3 + 8) = {-1.534288668166778, 29.93117175548229, 8.499999999999998};
Point(p3 + 9) = {-1.595195497613748, 29.72275018554845, 8.499999999999998};
Point(p3 + 10) = {-1.64795566074157, 29.52623993413101, 8.499999999999998};
Point(p3 + 11) = {-1.693104471700135, 29.34193589830438, 8.499999999999998};
Point(p3 + 12) = {-1.731225569870125, 29.17003278946763, 8.499999999999998};
Point(p3 + 13) = {-1.762897529456867, 29.01071270176167, 8.499999999999998};
Point(p3 + 14) = {-1.788696640609118, 28.86416069551367, 8.499999999999998};
Point(p3 + 15) = {-1.809199193475634, 28.73056183105077, 8.499999999999998};
Point(p3 + 16) = {-1.824901110785229, 28.61024514437903, 8.499999999999998};
Point(p3 + 17) = {-1.836188607753365, 28.50370968344114, 8.499999999999998};
Point(p3 + 18) = {-1.84476292103211, 28.40905162880363, 8.499999999999998};
Point(p3 + 19) = {-1.853469184205899, 28.32211555246557, 8.499999999999998};
Spline(3) = {3, p3 + 1, p3 + 2, p3 + 3, p3 + 4, p3 + 5, p3 + 6, p3 + 7, p3 + 8, p3 + 9, p3 + 10,
p3 + 11, p3 + 12, p3 + 13, p3 + 14, p3 + 15, p3 + 16, p3 + 17, p3 + 18, p3 + 19, 4};
Line(4) = {4, 1};
p5 = newp;
Point(p5 + 1) = {1.853469184205897, 28.3221155524656, 8.500000000000004};
Point(p5 + 2) = {1.844762921032106, 28.40905162880366, 8.500000000000004};
Point(p5 + 3) = {1.836188607753357, 28.50370968344117, 8.500000000000004};
Point(p5 + 4) = {1.824901110785216, 28.61024514437905, 8.500000000000004};
Point(p5 + 5) = {1.809199193475618, 28.73056183105079, 8.500000000000004};
Point(p5 + 6) = {1.788696640609102, 28.86416069551368, 8.500000000000004};
Point(p5 + 7) = {1.762897529456852, 29.01071270176169, 8.500000000000004};
Point(p5 + 8) = {1.731225569870111, 29.17003278946765, 8.500000000000004};
Point(p5 + 9) = {1.693104471700122, 29.3419358983044, 8.500000000000004};
Point(p5 + 10) = {1.647955660741558, 29.52623993413104, 8.500000000000004};
Point(p5 + 11) = {1.595195497613737, 29.72275018554848, 8.500000000000004};
Point(p5 + 12) = {1.534288668166767, 29.93117175548232, 8.500000000000004};
Point(p5 + 13) = {1.464709180287864, 30.15119376065826, 8.500000000000004};
Point(p5 + 14) = {1.385931041864244, 30.38250531780198, 8.500000000000004};
Point(p5 + 15) = {1.297428260783122, 30.62479554363918, 8.500000000000004};
Point(p5 + 16) = {1.198674844931714, 30.87775355489555, 8.500000000000004};
Point(p5 + 17) = {1.089144802197235, 31.14106846829678, 8.500000000000004};
Point(p5 + 18) = {0.9683121404668994, 31.41442940056856, 8.500000000000004};
Point(p5 + 19) = {0.8356508676279243, 31.69752546843657, 8.500000000000004};
```

Spline(5) = {5, p5 + 1, p5 + 2, p5 + 3, p5 + 4, p5 + 5, p5 + 6, p5 + 7, p5 + 8, p5 + 9, p5 + 10,
p5 + 11, p5 + 12, p5 + 13, p5 + 14, p5 + 15, p5 + 16, p5 + 17, p5 + 18, p5 + 19, 6};
Line(6) = {6, 7};
p7 = newp;
Point(p7 + 1) = {0.8356508676279271, 31.69752546843657, -8.500000000000002};
Point(p7 + 2) = {0.9683121404669035, 31.41442940056855, -8.500000000000002};
Point(p7 + 3) = {1.08914480219724, 31.14106846829677, -8.500000000000002};
Point(p7 + 4) = {1.19867484493172, 30.87775355489554, -8.500000000000004};
Point(p7 + 5) = {1.297428260783129, 30.62479554363917, -8.500000000000004};
Point(p7 + 6) = {1.385931041864251, 30.38250531780196, -8.500000000000004};
Point(p7 + 7) = {1.464709180287872, 30.15119376065824, -8.500000000000004};
Point(p7 + 8) = {1.534288668166774, 29.9311717554823, -8.500000000000004};
Point(p7 + 9) = {1.595195497613744, 29.72275018554845, -8.500000000000004};
Point(p7 + 10) = {1.647955660741566, 29.52623993413101, -8.500000000000004};
Point(p7 + 11) = {1.693104471700129, 29.34193589830437, -8.500000000000004};
Point(p7 + 12) = {1.731225569870117, 29.17003278946762, -8.500000000000004};
Point(p7 + 13) = {1.762897529456857, 29.01071270176166, -8.500000000000004};
Point(p7 + 14) = {1.788696640609107, 28.86416069551365, -8.500000000000004};
Point(p7 + 15) = {1.809199193475622, 28.73056183105077, -8.500000000000004};
Point(p7 + 16) = {1.824901110785219, 28.61024514437903, -8.500000000000004};
Point(p7 + 17) = {1.836188607753359, 28.50370968344115, -8.500000000000004};
Point(p7 + 18) = {1.844762921032107, 28.40905162880365, -8.500000000000004};
Point(p7 + 19) = {1.853469184205899, 28.32211555246559, -8.500000000000004};
Spline(7) = {7, p7 + 1, p7 + 2, p7 + 3, p7 + 4, p7 + 5, p7 + 6, p7 + 7, p7 + 8, p7 + 9, p7 + 10,
p7 + 11, p7 + 12, p7 + 13, p7 + 14, p7 + 15, p7 + 16, p7 + 17, p7 + 18, p7 + 19, 8};
Line(8) = {8, 5};
p9 = newp;
Point(p9 + 1) = {0, 0, -8.500000000000007};
Circle(9) = {9, p9 + 1, 10};
Line(10) = {11, 10};
p11 = newp;
Point(p11 + 1) = {-2.677957226051107, 27.24786703877808, -8.500000000000002};
Point(p11 + 2) = {-2.612186376661775, 27.26252305343384, -8.500000000000002};
Point(p11 + 3) = {-2.547753984845888, 27.28218511972605, -8.500000000000002};
Point(p11 + 4) = {-2.484956390588386, 27.30665046302467, -8.500000000000004};
Point(p11 + 5) = {-2.424089933874209, 27.33571630869968, -8.500000000000004};
Point(p11 + 6) = {-2.365450954688299, 27.36917988212104, -8.500000000000004};
Point(p11 + 7) = {-2.309335793015595, 27.40683840865871, -8.500000000000004};
Point(p11 + 8) = {-2.256040788841038, 27.44848911368266, -8.500000000000004};
Point(p11 + 9) = {-2.20586228214957, 27.49392922256285, -8.500000000000004};
Point(p11 + 10) = {-2.159065757298712, 27.54297500359632, -8.500000000000004};
Point(p11 + 11) = {-2.115496220051438, 27.59570829447749, -8.500000000000004};
Point(p11 + 12) = {-2.075070597558112, 27.65217897683581, -8.500000000000004};
Point(p11 + 13) = {-2.037788889818733, 27.71238705067127, -8.500000000000004};
Point(p11 + 14) = {-2.003651096833302, 27.77633251598388, -8.500000000000004};
Point(p11 + 15) = {-1.972657218601818, 27.84401537277364, -8.500000000000004};
Point(p11 + 16) = {-1.944807255124281, 27.91543562104062, -8.500000000000004};
Point(p11 + 17) = {-1.920101206400693, 27.99059326078473, -8.500000000000004};

Point(p11 + 18) = {-1.89853907243105, 28.0694882920059, -8.500000000000004};
Point(p11 + 19) = {-1.880120853215354, 28.15212071470423, -8.500000000000004};
Spline(11) = {11, p11 + 1, p11 + 2, p11 + 3, p11 + 4, p11 + 5, p11 + 6, p11 + 7, p11 + 8, p11 + 9, p11 + 10, p11 + 11, p11 + 12, p11 + 13, p11 + 14, p11 + 15, p11 + 16, p11 + 17, p11 + 18, p11 + 19, 1};
p12 = newp;
Point(p12 + 1) = {1.04094977927525e-15, 0, -8.5};
Circle(12) = {7, p12 + 1, 2};
p13 = newp;
Point(p13 + 1) = {1.880120853215368, 28.15212071470424, -8.500000000000004};
Point(p13 + 2) = {1.898539072431064, 28.06948829200587, -8.500000000000004};
Point(p13 + 3) = {1.920101206400705, 27.99059326078465, -8.500000000000004};
Point(p13 + 4) = {1.944807255124295, 27.91543562104059, -8.500000000000004};
Point(p13 + 5) = {1.972657218601833, 27.84401537277367, -8.500000000000004};
Point(p13 + 6) = {2.003651096833317, 27.77633251598388, -8.500000000000004};
Point(p13 + 7) = {2.037788889818749, 27.71238705067125, -8.500000000000004};
Point(p13 + 8) = {2.075070597558128, 27.65217897683578, -8.500000000000004};
Point(p13 + 9) = {2.115496220051454, 27.59570829447746, -8.500000000000004};
Point(p13 + 10) = {2.159065757298727, 27.54297500359629, -8.500000000000004};
Point(p13 + 11) = {2.205862282149584, 27.49392922256283, -8.500000000000004};
Point(p13 + 12) = {2.256040788841052, 27.44848911368264, -8.500000000000004};
Point(p13 + 13) = {2.309335793015607, 27.40683840865869, -8.500000000000004};
Point(p13 + 14) = {2.365450954688309, 27.36917988212103, -8.500000000000004};
Point(p13 + 15) = {2.424089933874218, 27.33571630869967, -8.500000000000004};
Point(p13 + 16) = {2.484956390588394, 27.30665046302467, -8.500000000000004};
Point(p13 + 17) = {2.547753984845897, 27.28218511972604, -8.500000000000002};
Point(p13 + 18) = {2.612186376661786, 27.26252305343384, -8.500000000000002};
Point(p13 + 19) = {2.67795722605112, 27.24786703877808, -8.500000000000002};
Spline(13) = {8, p13 + 1, p13 + 2, p13 + 3, p13 + 4, p13 + 5, p13 + 6, p13 + 7, p13 + 8, p13 + 9, p13 + 10, p13 + 11, p13 + 12, p13 + 13, p13 + 14, p13 + 15, p13 + 16, p13 + 17, p13 + 18, p13 + 19, 12};
Line(14) = {9, 12};
Line(15) = {12, 13};
p16 = newp;
Point(p16 + 1) = {2.677957226051119, 27.24786703877808, 8.500000000000002};
Point(p16 + 2) = {2.612186376661784, 27.26252305343384, 8.500000000000002};
Point(p16 + 3) = {2.547753984845895, 27.28218511972605, 8.500000000000002};
Point(p16 + 4) = {2.484956390588391, 27.30665046302467, 8.500000000000004};
Point(p16 + 5) = {2.424089933874214, 27.33571630869968, 8.500000000000004};
Point(p16 + 6) = {2.365450954688304, 27.36917988212103, 8.500000000000004};
Point(p16 + 7) = {2.3093357930156, 27.4068384086587, 8.500000000000004};
Point(p16 + 8) = {2.256040788841043, 27.44848911368264, 8.500000000000004};
Point(p16 + 9) = {2.205862282149573, 27.49392922256283, 8.500000000000004};
Point(p16 + 10) = {2.159065757298714, 27.5429750035963, 8.500000000000004};
Point(p16 + 11) = {2.11549622005144, 27.59570829447746, 8.500000000000004};
Point(p16 + 12) = {2.075070597558113, 27.65217897683578, 8.500000000000004};
Point(p16 + 13) = {2.037788889818733, 27.71238705067126, 8.500000000000004};
Point(p16 + 14) = {2.003651096833301, 27.77633251598389, 8.500000000000004};

Point(p16 + 15) = {1.972657218601818, 27.84401537277368, 8.500000000000004};
Point(p16 + 16) = {1.944807255124286, 27.9154356210406, 8.500000000000004};
Point(p16 + 17) = {1.9201012064007, 27.99059326078467, 8.500000000000004};
Point(p16 + 18) = {1.898539072431055, 28.06948829200589, 8.500000000000004};
Point(p16 + 19) = {1.880120853215357, 28.15212071470426, 8.500000000000004};
Spline(16) = {13, p16 + 1, p16 + 2, p16 + 3, p16 + 4, p16 + 5, p16 + 6, p16 + 7, p16 + 8, p16 + 9, p16 + 10, p16 + 11, p16 + 12, p16 + 13, p16 + 14, p16 + 15, p16 + 16, p16 + 17, p16 + 18, p16 + 19, 5};
Line(17) = {14, 11};
p18 = newp;
Point(p18 + 1) = {-1.880120853215361, 28.15212071470422, 8.499999999999998};
Point(p18 + 2) = {-1.898539072431055, 28.0694882920059, 8.499999999999998};
Point(p18 + 3) = {-1.920101206400695, 27.99059326078472, 8.499999999999998};
Point(p18 + 4) = {-1.944807255124283, 27.91543562104061, 8.499999999999998};
Point(p18 + 5) = {-1.97265721860182, 27.84401537277364, 8.499999999999998};
Point(p18 + 6) = {-2.003651096833304, 27.77633251598387, 8.499999999999998};
Point(p18 + 7) = {-2.037788889818735, 27.71238705067126, 8.499999999999998};
Point(p18 + 8) = {-2.075070597558114, 27.6521789768358, 8.499999999999998};
Point(p18 + 9) = {-2.11549622005144, 27.59570829447749, 8.499999999999998};
Point(p18 + 10) = {-2.159065757298714, 27.54297500359632, 8.499999999999998};
Point(p18 + 11) = {-2.205862282149571, 27.49392922256285, 8.499999999999998};
Point(p18 + 12) = {-2.25604078884104, 27.44848911368265, 8.499999999999998};
Point(p18 + 13) = {-2.309335793015597, 27.4068384086587, 8.499999999999998};
Point(p18 + 14) = {-2.3654509546883, 27.36917988212103, 8.499999999999998};
Point(p18 + 15) = {-2.424089933874211, 27.33571630869968, 8.499999999999998};
Point(p18 + 16) = {-2.484956390588389, 27.30665046302467, 8.499999999999998};
Point(p18 + 17) = {-2.547753984845893, 27.28218511972605, 8.499999999999998};
Point(p18 + 18) = {-2.612186376661783, 27.26252305343384, 8.499999999999998};
Point(p18 + 19) = {-2.677957226051118, 27.24786703877808, 8.5};
Spline(18) = {4, p18 + 1, p18 + 2, p18 + 3, p18 + 4, p18 + 5, p18 + 6, p18 + 7, p18 + 8, p18 + 9, p18 + 10, p18 + 11, p18 + 12, p18 + 13, p18 + 14, p18 + 15, p18 + 16, p18 + 17, p18 + 18, p18 + 19, 14};
p19 = newp;
Point(p19 + 1) = {0, 0, 8.5};
Circle(19) = {15, p19 + 1, 16};
Line(20) = {13, 15};
p21 = newp;
Point(p21 + 1) = {-1.040949779275245e-15, 0, 8.5};
Circle(21) = {6, p21 + 1, 3};
Line(22) = {16, 14};
Line(23) = {15, 9};
Line(24) = {10, 16};
Line Loop(1) = {1, 2, 3, 4};
Ruled Surface(1) = {1};
Line Loop(2) = {5, 6, 7, 8};
Ruled Surface(2) = {2};
Line Loop(3) = {9, -10, 11, 1, -12, 7, 13, -14};
Plane Surface(3) = {3};

```
Line Loop(4) = {15, 16, -8, 13};
Ruled Surface(4) = {4};
Line Loop(5) = {17, 11, -4, 18};
Ruled Surface(5) = {5};
Line Loop(6) = {19, 22, -18, -3, -21, -5, -16, 20};
Plane Surface(6) = {6};
Line Loop(7) = {2, -21, 6, 12};
Ruled Surface(7) = {7};
Line Loop(8) = {20, 23, 14, 15};
Plane Surface(8) = {8};
Line Loop(9) = {10, 24, 22, 17};
Plane Surface(9) = {9};
Line Loop(10) = {23, 9, 24, -19};
Ruled Surface(10) = {10};
Surface Loop(1) = {1, 2, 3, 4, 5, 6, 7, 8, 9, 10};
Volume(1) = {1};
Physical Surface (1)={10};
Physical Surface (2)={8};
Physical Surface (3)={6};
Physical Surface (4)={4};
Physical Surface (5)={5};
Physical Surface (6)={6};
Physical Surface (7)={8};
Physical Surface (8)={1};
Physical Surface (9)={7};
Physical Surface (10)={2};
Physical Volume (1)={1};
```

Appendix B.

Mesh Algorithms

B.1. Unstructured Mesh Algorithm

For all 2D unstructured algorithms a Delaunay mesh that contains all the points of the 1D mesh is initially constructed with a divide-and-conquer algorithm (the missing edges are recovered using edges swaps). After the initial step three different algorithms can be applied to generate the final mesh:

- The "MeshAdapt" algorithm based on the local mesh modifications, using edge swaps, splits and collapses, this is: long edges are split and short are collapsed, and edges are swapped if a better geometrical configuration is obtained [74];
- The "Delaunay" algorithm, inspired by the work of the GAMMA team, where new points are inserted sequentially at the center of the element that has the largest adimensional radius from its center [75];
- The "Frontal" algorithm is inspired by the work of S.Rebay [76];

Each algorithm has its advantages and disadvantages, in fact for very complex curved surfaces the "MeshAdapt" algorithm is the best choice, although when higher quality of the elements used is required the "Frontal" algorithm is preferable. However, if the created meshes of plane surfaces are very large, the "Delaunay" algorithm has the best performance of the three algorithms. When meshing with the Gmsh GUI it is possible to select the "Automatic" algorithm, which will select the "Delaunay" for plane surfaces and "MeshAdapt" for all other surfaces [77].

Finally, the 3D algorithms that are available to use are:

- The "Delaunay" algorithm uses two main steps, where the first is based on the use of the H.Si's Tetgen algorithm [78] to make an initial mesh resulting of the link of all the volumes in the model and then a 3D version of 2D Delaunay algorithm is applied. So for the Delaunay type mesh generation method it is applied the following scheme [75]:

1. Preparation step, where it interprets the data input (point coordinates and boundary entities) and executes the construction of a bounding box and meshing it with a few elements;
2. Construction of the box mesh, insertion of the given point in the box mesh before;
3. Construction of the empty mesh, where it search of the missing specified entities, enforce these items and defines the linked component of the domain;
4. Internal point creation and point insertion;
5. Domain constrictions with the removal of the elements exterior to the domain and classification of the elements with linked components;
6. Optimization.

- The "Frontal" algorithm uses J.Schoeberl's Netgen algorithm [79].

On this behalf, the "Automatic" algorithm was used for a better solution, reaching with the 3D "Delaunay" algorithm a more robust and faster mesh which is able to function with the mechanism of specifying the element size.

B.2. Structured Grids

For the creation of a structured grid the algorithm mostly used is the "Transfinite" algorithm. These algorithm will work based on three base commands. The first part you need to choose the partition of the lines, this is, decide the number of nodes that each line contains so it can be meshed with 1D transfinite algorithm. The second command is to do the same but for surfaces, only defining surfaces with only 3 or 4 boundary nodes. Finally, the third command will create a volume with either 6 or 8 points for it boundary.

Appendix C.

ElmerSolver - Preconditioners

C.1. Additional information

ElmerSolver grants severals ways to obtain preconditioner, which are:

- The more basic preconditioner is the **Jacobi** that simply based on simplifying M as being the diagonal of A;
- The more modern preconditioners are createdby computing incomplete LU factorizations of A, referred as **ILU** preconditioners, where the preconditioner matrix M is given in a $M = LU$ form (L and U the lower and the upper triangular);
- There are several ways to choose the set of matrix positions that allowed to be filled with nonzero elements, the ILU preconditioners of fill level N, the **ILU(N)**, where with:
  - $N = 0$ - accepts nonzero elements in positions in which A has nonzero elements;
  - $N = 1$ - allows nonzero elements in positions that are filled if the first step Gaussian elimination is performed for A;
  - $N = 2$ - allows nonzero elements in positions that are filled if the next step Gaussian elimination is at ILU(1);
  - etc.
- Finally, there is also the possibility that the factorization strategy is based on the numerical tolerances, where the resulting preconditioner is known as **ILUT**, as the creation of the preconditioner Gaussian elimination is executed as the given elements of a row of the LU factorization are obtained uniquely by elements whose value is over the given threshold value accepted in the preconditioner matrix.

As the value of N increases for ILU(N) or threshold values descreases for ILUT the more elements are computed to the factorization, leveling the performance of the preconditioner and lowering the number of iteration needed, although the memory usage grows so as the time spent on building the preconditioner matrix increases too. For direct solver or incomplete factorization preconditioners the bandwidth optimization is recommended (Cuthill-McKee bandwidth optimization).

Appendix D.

Case SIF for Validation of Case 1 (Spur Gears) - Steady State

Code created for the geometry (in Figure D.1) at Chapter 5:

```
Header
CHECK KEYWORDS Warn
Mesh DB "."
Include Path ""
Results Directory ""
End
```

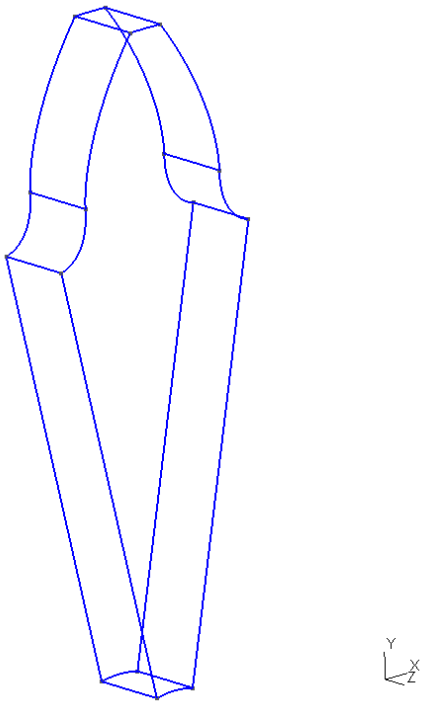

Figure D.1.: Geometry for the validation of Steady State case 1 (spur gears).

```
  Simulation
Max Output Level = 5
Coordinate System = Cartesian
Coordinate Mapping(3) = 1 2 3
Simulation Type = Steady state
Steady State Max Iterations = 2
Output Intervals = 1
Timestepping Method = BDF
BDF Order = 2
Timestep intervals = 1
Timestep Sizes = 1 Solver Input File = case.sif
Output File = case.dat
Post File = case.ep
Coordinate Scaling = 0.001
End

  Constants
Gravity(4) = 0 -1 0 9.82
Stefan Boltzmann = 5.67e-08
Permittivity of Vacuum = 8.8542e-12
Boltzmann Constant = 1.3807e-23
Unit Charge = 1.602e-19
End

  Heat Solver
  Solver 1
Equation = Heat Equation
Procedure = "HeatSolve" "HeatSolver"
Variable = -dofs 1 Temperature
Exec Solver = Always
Stabilize = True
Bubbles = False
Lumped Mass Matrix = False
Optimize Bandwidth = True
Steady State Convergence Tolerance = 1.0e-5
Nonlinear System Convergence Tolerance = 1.0e-7
Nonlinear System Max Iterations = 20
Nonlinear System Newton After Iterations = 3
Nonlinear System Newton After Tolerance = 1.0e-3
Nonlinear System Relaxation Factor = 1
Linear System Solver = Iterative
Linear System Iterative Method = BiCGStab
Linear System Max Iterations = 500
Linear System Convergence Tolerance = 1.0e-10
Linear System Preconditioning = ILU0
Linear System ILUT Tolerance = 1.0e-3
Linear System Abort Not Converged = False
Linear System Residual Output = 1
```

Linear System Precondition Recompute = 1
End

Solver to save values of boundary conditions
Solver 2
Equation = SaveLine
File Append = Logical False
Procedure = "SaveData" "SaveLine"
Filename = temperature_coordinate_1_2.dat
Exec Solver = After Simulation
Save Flux = Logical True
Variable 1 = String Temperature
Variable 2 = Coordinate 1
Variable 3 = Coordinate 2
Variable 4 = Coordinate 3
Update Exported Variables = Logical True
Nonlinear Update Exported Variables = Logical True
End

Solver for output as VTU file format
Solver 3
Exec Solver = After Simulation
Equation = Result Output
Procedure = "ResultOutputSolve" "ResultOutputSolver"
Output Format = Vtu
Output File Name = Temperatures
Scalar Field 1 = Temperature
Single Precision = True
Output Directory = RefinedResults
End

Functions
Radius function definition as the square root of coordinate 1 (x) and coordinate 2 (y):
$ function raio(X) {_raio=$\sqrt{X(0)^2 + X(1)^2}$}

HeaviSide 0 for the imposed Heat Flux (average) from the power loss model:
$ function hs0(X) {_hs0=tanh (1000 · 1000 · ($\sqrt{X(0)^2 + X(1)^2}$-(raioA/1000)))}

HeaviSide 1 for the imposed Heat Flux (average) from the power loss model:
$ function hs1(X) {_hs1=((-tanh (1000· 1000· (($\sqrt{X(0)^2 + X(1)^2}$-raioB/1000))+1)· (tanh (1000· 1000· ($\sqrt{X(0)^2 + X(1)^2}$-(raioA/1000-1e-4)))+1)/4)· ($qcof_1(1)$· (1000· $\sqrt{X(0)^2 + X(1)^2}$)^2+$qcof_1(2)$· 1000· $\sqrt{X(0)^2 + X(1)^2}$+$qcof_1(3)$)}

HeaviSide 2 for the imposed Heat Flux (average) from the power loss model:
$ function hs2(X) {_hs2=((-tanh (1000· ($\sqrt{X(0)^2 + X(1)^2}$-raioC/1000))+1)· (tanh (1000· 1000· ($\sqrt{X(0)^2 + X(1)^2}$-raioB/1000))+1)/4)· ($qcof_2(1)$· (1000· $\sqrt{X(0)^2 + X(1)^2}$)^3+$qcof_2(2)$· (1000· $\sqrt{X(0)^2 + X(1)^2}$)^2+ $qcof_2(3)$ · 1000· $\sqrt{X(0)^2 + X(1)^2}$+$qcof_2(4)$)}

HeaviSide 3 for the imposed Heat Flux (average) from the power loss model:

$ function hs3(X) {_hs3=((-tanh (1000· 1000· ($\sqrt{X(0)^2 + X(1)^2}$-raioD/1000))+1)· (tanh (1000· 1000· ($\sqrt{X(0)^2 + X(1)^2}$-(raioC/1000-1e-4)))+1)/4)· ($qcof_3(1)$· (1000· $\sqrt{X(0)^2 + X(1)^2}$)^3+$qcof_3(2)$· (1000· $\sqrt{X(0)^2 + X(1)^2}$)^2+$qcof_3(3)$· 1000· $\sqrt{X(0)^2 + X(1)^2}$+$qcof_3(4)$)}

HeaviSide 4 for the imposed Heat Flux (average) from the power loss model:

$ function hs4(X) {_hs4=((tanh (1000· 1000· ($\sqrt{X(0)^2 + X(1)^2}$-raioD/1000))+1)/2)· ($qcof_4(1)$· (1000· $\sqrt{X(0)^2 + X(1)^2}$)^2+$qcof_4(2)$· 1000· $\sqrt{X(0)^2 + X(1)^2}$+$qcof_4(3)$)}

HeaviSide for heat transfer coefficients for meshing surface:

$ function ht1(X) {_ht1=((-tanh (1000· 1000· ($\sqrt{X(0)^2 + X(1)^2}$-raioE/1000))+1)· (tanh (1000· 1000· ($\sqrt{X(0)^2 + X(1)^2}$-(raioA/1000)))+1)/4)· ($pcof_3(1)$· (1000· $\sqrt{X(0)^2 + X(1)^2}$)^2+$pcof_3(2)$· (1000· $\sqrt{X(0)^2 + X(1)^2}$)+$pcof_3(3)$)}

Equation 1
Name = "Equation 1"
Active Solvers(3) = 1 2 3
End

Definition of the steel properties:

Material 1
Name = "steel"
Heat Conductivity = 41.8
Heat Capacity = 493
Density = 7870
End
Body Force 1
Name = "BodyForce 1"
End

Meshing surface:

Boundary Condition 7
Target Boundaries(1) = 7
Name = "HeatSource"
Heat Flux = Variable Coordinate 1, Coordinate 2
Real MATC "hs0(tx)· (hs1(tx)+hs2(tx)+hs3(tx)+hs4(tx))"
Heat Transfer Coefficient = Variable Coordinate 1, Coordinate 2
Real MATC "ht1(tx)"
External Temperature = 363.15
End

Symmetry 1:

Boundary Condition 1
Target Boundaries(1) = 1
Name = "HeatFlux"
Heat Flux = 0
Save Line = Logical True

End

Symmetry 2:

Boundary Condition 2
Target Boundaries(1) = 2
Name = "HeatFlux"
Heat Flux = 0
Save Line = Logical True
End

Gear side 1:

Boundary Condition 3
Target Boundaries(1) = 3
Name = "HeatTransferSides"
Heat Transfer Coefficient = Variable Coordinate 1, Coordinate 2
Real MATC "$pcof(1)\cdot$ (raio(tx))^2+$pcof(2)\cdot$ raio(tx)+$pcof(3)$"
External Temperature = 363.15
End

Non-meshing surface 1:

Boundary Condition 4
Target Boundaries(1) = 4
Name = "HeatTransferFaces"
Heat Transfer Coefficient = max(hs)/3
External Temperature = 363.15
End

Non-meshing surface 2:

Boundary Condition 5
Target Boundaries(1) = 5
Name = "HeatTransferFaces"
Heat Transfer Coefficient = max(hs)/3
External Temperature = 363.15
End

Gear side 2:

Boundary Condition 6
Target Boundaries(1) = 6
Name = "HeatTransferSides"
Heat Transfer Coefficient = Variable Coordinate 1, Coordinate 2
Real MATC "$pcof_2(1)\cdot$ (raio(tx))^2+$pcof_2(2)\cdot$ raio(tx)+$pcof_2(3)$"
External Temperature = 363.15
End

Tooth-tip surface:

Boundary Condition 8
Target Boundaries(1) = 8
Name = "HeatTransferFaces"
Heat Transfer Coefficient = max(hs)
External Temperature = 363.15
End

Non-meshing surface 3:
Boundary Condition 9
Target Boundaries(1) = 9
Name = "HeatTransferFaces"
Heat Transfer Coefficient = max(hs)/3
External Temperature = 363.15
End

Adiabatic surface (shaft/gear interface):
Boundary Condition 10
Target Boundaries(1) = 10
Name = "HeatFlux"
Heat Flux = 0
End

Appendix E.

Thermophysical Properties of Air

TABLE A.4 Thermophysical Properties of Gases at Atmospheric Pressure[a]

T (K)	ρ (kg/m^3)	c_p (kJ/kg · K)	$\mu \cdot 10^7$ (N · s/m^2)	$\nu \cdot 10^6$ (m^2/s)	$k \cdot 10^3$ (W/m · K)	$\alpha \cdot 10^6$ (m^2/s)	Pr
Air, $\mathcal{M}$ = 28.97 kg/kmol							
100	3.5562	1.032	71.1	2.00	9.34	2.54	0.786
150	2.3364	1.012	103.4	4.426	13.8	5.84	0.758
200	1.7458	1.007	132.5	7.590	18.1	10.3	0.737
250	1.3947	1.006	159.6	11.44	22.3	15.9	0.720
300	1.1614	1.007	184.6	15.89	26.3	22.5	0.707
350	0.9950	1.009	208.2	20.92	30.0	29.9	0.700
400	0.8711	1.014	230.1	26.41	33.8	38.3	0.690
450	0.7740	1.021	250.7	32.39	37.3	47.2	0.686
500	0.6964	1.030	270.1	38.79	40.7	56.7	0.684
550	0.6329	1.040	288.4	45.57	43.9	66.7	0.683
600	0.5804	1.051	305.8	52.69	46.9	76.9	0.685
650	0.5356	1.063	322.5	60.21	49.7	87.3	0.690
700	0.4975	1.075	338.8	68.10	52.4	98.0	0.695
750	0.4643	1.087	354.6	76.37	54.9	109	0.702
800	0.4354	1.099	369.8	84.93	57.3	120	0.709
850	0.4097	1.110	384.3	93.80	59.6	131	0.716
900	0.3868	1.121	398.1	102.9	62.0	143	0.720
950	0.3666	1.131	411.3	112.2	64.3	155	0.723
1000	0.3482	1.141	424.4	121.9	66.7	168	0.726
1100	0.3166	1.159	449.0	141.8	71.5	195	0.728
1200	0.2902	1.175	473.0	162.9	76.3	224	0.728
1300	0.2679	1.189	496.0	185.1	82	257	0.719
1400	0.2488	1.207	530	213	91	303	0.703
1500	0.2322	1.230	557	240	100	350	0.685
1600	0.2177	1.248	584	268	106	390	0.688
1700	0.2049	1.267	611	298	113	435	0.685
1800	0.1935	1.286	637	329	120	482	0.683
1900	0.1833	1.307	663	362	128	534	0.677
2000	0.1741	1.337	689	396	137	589	0.672
2100	0.1658	1.372	715	431	147	646	0.667
2200	0.1582	1.417	740	468	160	714	0.655
2300	0.1513	1.478	766	506	175	783	0.647
2400	0.1448	1.558	792	547	196	869	0.630
2500	0.1389	1.665	818	589	222	960	0.613
3000	0.1135	2.726	955	841	486	1570	0.536

Appendix F.

Example of Case SIF for Transient Problem

Code created for the first transient example at Chapter 5:

```
timesteps=200
time_interval=min(time_transient)-max(time_transient)
timestep_size=time_interval/(timesteps-1)
```

Header

```
CHECK KEYWORDS Warn
Mesh DB "."
Include Path ""
Results Directory ""
End
```

Simulation

```
Max Output Level = 10
Coordinate System = Cartesian
Coordinate Mapping(3) = 1 2 3
Simulation Type = Transient
Steady State Max Iterations = 50
Output Intervals = 1
Timestepping Method = BDF
BDF Order = 2
Timestep intervals = timesteps-1
Timestep Sizes = timestep_size
Solver Input File = case.sif
Output File = case.result
Post File = case.ep
Coordinate Scaling = 0.001
Restart File = case.result
Restart Time = 1;
End
```

Constants

```
Gravity(4) = 0 -1 0 9.82
Stefan Boltzmann = 5.67e-08
```

```
Permittivity of Vacuum = 8.8542e-12
Boltzmann Constant = 1.3807e-23
Unit Charge = 1.602e-19
End

  Heat Solver
  Solver 1
Equation = Heat Equation
Procedure = "HeatSolve" "HeatSolver"
Variable = -dofs 1 Temperature
Exec Solver = Always
Stabilize = True
Bubbles = False
Lumped Mass Matrix = False
Optimize Bandwidth = True
Steady State Convergence Tolerance = 1.0e-5
Nonlinear System Convergence Tolerance = 1.0e-8
Nonlinear System Max Iterations = 20
Nonlinear System Newton After Iterations = 3
Nonlinear System Newton After Tolerance = 1.0e-3
Nonlinear System Relaxation Factor = 1
Linear System Solver = Iterative
Linear System Iterative Method = BiCGStab
Linear System Max Iterations = 500
Linear System Convergence Tolerance = 1.0e-10
Linear System Preconditioning = ILU0
Linear System ILUT Tolerance = 1.0e-3
Linear System Abort Not Converged = False
Linear System Residual Output = 1
Linear System Precondition Recompute = 1
End
  Solver to save values of boundary conditions
  Solver 2
Equation = SaveLine
File Append = Logical False
Procedure = "SaveData" "SaveLine"
Filename = temperature_coordinate_1_2.dat
Exec Solver = After Timestep
Save Flux = Logical True
Variable 1 = String Temperature
Variable 2 = Coordinate 1
Variable 3 = Coordinate 2
Variable 4 = Coordinate 3
Update Exported Variables = Logical True
End

  Solver for output as VTU file format
  Solver 3
```

Exec Solver = String "after timestep"
Equation = String "ResultOutput"
Procedure = File "ResultOutputSolve" "ResultOutputSolver"
Output File Name = String "temperatures"
Vtu Format = Logical True
Scalar Field 1 = String "Temperature"
Single Precision = True
Output Directory = String RefinedResults
End

Functions

Radius function definition as the square root of coordinate 1 (x) and coordinate 2 (y):

$ function raio(X) {_raio=$\sqrt{X(0)^2 + X(1)^2}$}

HeaviSide 0 for the imposed Heat Flux maximum (locally) from the power loss model:

$ function hs0_temp(X) {_hs0_temp=tanh$(1000 \cdot 1000 \cdot ((X(2)) - (1 - 1e - 3)))$}

HeaviSide 1 for the imposed Heat Flux maximum (locally) from the power loss model:

$ function hs1_temp(X) {_hs1_temp=$(-\tanh(1000 \cdot 1000 \cdot ((X(2)) - (1.0013 + 0.1e - 4))) + 1) \cdot (\tanh(1000 \cdot 1000 \cdot ((X(2)) - (1 - 1e - 3))) + 1)/4 \cdot (507307242576.242 \cdot (X(2))^2 + -1018869821357.73 \cdot (X(2)) + 511568379594.1686)$}

HeaviSide 2 for the imposed Heat Flux maximum (locally):

$ function hs2_temp(X) {_hs2_temp=$(-\tanh(1000 \cdot 1000 \cdot ((X(2)) - (1.0016 + 2.5e - 6))) + 1) \cdot (\tanh(1000 \cdot 1000 \cdot ((X(2)) - (1.0013 + 0.1e - 4))) + 1)/4 \cdot (4.61700554420981e + 16 \cdot (X(2))^3 + -1.38717901817718e + 17 \cdot (X(2))^2 + 1.389259437511046e + 17 \cdot (X(2)) + -4.637809752288777e + 16)$}

HeaviSide 3 for the imposed Heat Flux maximum (locally):

$ function hs3_temp(X) {_hs3_temp=$(-\tanh(1000 \cdot 1000 \cdot ((X(2)) - (1.002 + 1.8e - 6))) + 1) \cdot (\tanh(1000 \cdot 1000 \cdot ((X(2)) - (1.0016 + 3.5e - 6))) + 1)/4 \cdot (-7137205570963148 \cdot (X(2))^3 + 2.145132258916755e + 16 \cdot (X(2))^2 + -2.149109757575865e + 16 \cdot (X(2)) + 7176980595567479)$}

HeaviSide 4 for the imposed Heat Flux maximum (locally):

$ function hs4_temp(X) {_hs4_temp=$(\tanh(1000 \cdot 1000 \cdot ((X(2)) - (1.002 + 3.5e - 6))) + 1)/2 \cdot (588270367939.4791 \cdot (X(2))^2 + -1176093882936.472 \cdot (X(2)) + 587821416685.7053)$}

HeaviSide for heat transfer coefficients for meshing surface:

$ function ht1(X) {_ht1=$((-\tanh(1000 \cdot 1000 \cdot (X - 0.032)) + 1) \cdot (\tanh(1000 \cdot 1000 \cdot (X - (0.028699))) + 1)/4) \cdot (0.00064276 \cdot (1000 \cdot X)^2 + 0.045309 \cdot (1000 \cdot X) + 41.9509)$}

Equation 1
Name = "Equation 1"
Active Solvers(3) = 1 2 3
End

Definition of the steel properties:

Material 1
Name = "mao"
Heat Conductivity = 0.3
Heat Capacity = 1470
Density = 1410
End

Body Force 1
Name = "BodyForce 1"
End

Symmetry 1:
Boundary Condition 1
Target Boundaries(1) = 1
Name = "Sym1"
Heat Flux = 0
Save Line = Logical True
End
Symmetry 2:
Boundary Condition 2 Target Boundaries(1) = 2
Name = "Sym2"
Heat Flux = 0
Save Line = Logical True
End

Gear side 1:
Boundary Condition 3
Target Boundaries(1) = 3
Name = "HeatTransferSides"
Heat Transfer Coefficient = Variable Coordinate 1, Coordinate 2
Real MATC "$9.1113e-11 \cdot (raio1(tx))^2 + -7.9302e-12 \cdot raio1(tx) + 43.6215$"
External Temperature = T_{mix}
End

Non-meshing surface 1:
Boundary Condition 4
Target Boundaries(1) = 4
Name = "HeatTransferFaces"
Heat Transfer Coefficient = max(hs)/3
External Temperature = T_{mix}
End

Non-meshing surface 2:
Boundary Condition 5
Target Boundaries(1) = 5
Name = "HeatTransferFaces"
Heat Transfer Coefficient = max(hs)/3
External Temperature = T_{mix}

End

Gear side 2:

Boundary Condition 6
Target Boundaries(1) = 6
Name = "HeatTransferSides"
Heat Transfer Coefficient = Variable Coordinate 1, Coordinate 2
Real MATC "$-3.4546e-10 \cdot (raio1(tx))^2 + 1.4402e-11 \cdot raio1(tx) + 43.6215$"
External Temperature = T_{mix}
End

Meshing surface:

Boundary Condition 7
Target Boundaries(1) = 7
Name = "HeatSource"
Heat Flux = Variable Coordinate 1, Coordinate 2, Time
Real MATC "$hs0\_temp(tx) \cdot (hs1_temp(tx) + hs2\_temp(tx) + hs3\_temp(tx) + hs4\_temp(tx)) \cdot (int1(tx) \cdot int2(tx) \cdot dist(tx))$"

Heaviside step function 1 of heat flux interval acting

$ function int1(X) {_int1=$-\tanh(1000 \cdot 1000 \cdot (raio(X) - (raio\_time(X) + a(X)))) + 1$}

Heaviside step function 2 of heat flux interval acting

$ function int2(X) {_int2=$(\tanh(1000 \cdot 1000 \cdot (raio(X) - (raio\_time(X) - a(X) + 1e-2))) + 1)/4$}

Distribution of heat flux value of the local heat flux

$ function dist(X) {_dis=$\sqrt{1 - ((raio(X) - raio\_time(X))/a(X)}^2)$}

Function to search for the contact radius for each time

$ function raio_time(X) {_raio_time=$1000 \cdot (-131638.5043 \cdot (X(2))^4 + 523176.335 \cdot (X(2))^3 + -779550.8014 \cdot (X(2))^2 + 516127.1678 \cdot (X(2)) + -128114.1685)$}

Hertzian semi-banwidth at each time

$ function a(X) {_a=$1000 \cdot \tanh(1000 \cdot 2 \cdot ((X(2)) - (1 - 1e-3))) \cdot (((-\tanh(1000 \cdot 2 \cdot ((X(2)) - (1.0013 + 0.1e-4))) + 1) \cdot (\tanh(1000 \cdot 2 \cdot ((X(2)) - (1 - 1e-3))) + 1)/4) \cdot (974.4692 \cdot (X(2))^3 + -2935.7372 \cdot (X(2))^2 + 2948.1007 \cdot (X(2)) + -986.8324) + ((-\tanh(1000 \cdot 2 \cdot ((X(2)) - (1.002 + 1.8e-6))) + 1) \cdot (\tanh(1000 \cdot 2 \cdot ((X(2)) - (1.0013 + 0.1e-4))) + 1)/4) \cdot (-16116030487.7317 \cdot (X(2))^6 + 60747499170.0558 \cdot (X(2))^5 + -63535325929.9268 \cdot (X(2))^4 + -31001662967.8258 \cdot (X(2))^3 + 108482380482.3909 \cdot (X(2))^2 + -76859781232.0283 \cdot (X(2)) + 18282920965.0522) + ((\tanh(1000 \cdot 2 \cdot ((X(2)) - (1.002 + 1.8e-6))) + 1)/2) \cdot (-66379.0653 \cdot (X(2))^3 + 199672.095 \cdot (X(2))^2 + -200208.4374 \cdot (X(2)) + 66915.4092))$}

Radius function definition as the square root of coordinate 1 (x) and coordinate 2 (y):

$ function raio(X) {_raio=$1000 \cdot \sqrt{X(0)^2 + X(1)^2}$}

Heat Transfer Coefficient = Variable Coordinate 1, Coordinate 2
Real MATC "ht1(raio2(tx))"

Radius function definition as the square root of coordinate 1 (x) and coordinate 2 (y):

$ function raio2(X) {_raio2=$\sqrt{X(0)^2 + X(1)^2}$}

Save Line = Logical True
External Temperature = T_{mix}
End

Tooth-tip surface:

Boundary Condition 8
Target Boundaries(1) = 8
Name = "HeatTransferFaces"
Heat Transfer Coefficient = 43.6215
External Temperature = T_{mix}
End

Non-meshing surface 3:

Boundary Condition 9
Target Boundaries(1) = 9
Name = "HeatTransferFaces"
Heat Transfer Coefficient = max(hs)/3
External Temperature = T_{mix}
End

Adiabatic surface (shaft/gear interface):

Boundary Condition 10
Target Boundaries(1) = 10
Name = "HeatFlux"
Heat Flux = 0
End

Appendix G.

GEO file example - Hybrid Gear

The GEO file created for the first hybrid gear presented at Chapter 6:

```
cl_1 = 0.35;
Point(1) = {2.926354830241825, 14.71177920604847, 7, cl_1};
Point(2) = {2.926354830241827, 14.71177920604847, -7, cl_1};
Point(3) = {-2.926354830242031, 14.7117792060485, -7, cl_1};
Point(4) = {-2.926354830242032, 14.7117792060485, 7, cl_1};
Point(5) = {0.225, 14.99831240506748, -4.75, cl_1};
Point(6) = {0.2249999999999642, 14.99831240506747, 4.75, cl_1};
Point(7) = {-0.225, 14.99831240506748, 4.75, cl_1};
Point(8) = {-0.225, 14.99831240506748, -4.75, cl_1};
Point(9) = {6.061246780253436, 30.47194530988896, -6.999999999999999, cl_1};
Point(10) = {6.061246780253431, 30.47194530988895, 7.000000000000001, cl_1};
Point(11) = {-6.061246780253529, 30.47194530988895, 6.999999999999999, cl_1};
Point(12) = {-6.061246780253525, 30.47194530988895, -7.000000000000001, cl_1};
Point(13) = {-4.05331978845584, 33.5888347684608, -7.000000000000001, cl_1};
Point(14) = {-1.31743470694308, 41.2050067034633, -7.000000000000001, cl_1};
Point(15) = {1.317434706943051, 41.20500670346338, -6.999999999999999, cl_1};
Point(16) = {4.05331978845576, 33.5888347684608, -6.999999999999999, cl_1};
Point(17) = {4.05331978845576, 33.5888347684608, 7.000000000000001, cl_1};
Point(18) = {-4.05331978845584, 33.5888347684608, 6.999999999999999, cl_1};
Point(19) = {1.317434706943051, 41.20500670346336, 7, cl_1};
Point(20) = {-1.31743470694308, 41.2050067034633, 7.000000000000001, cl_1};
Point(21) = {0.225, 36.70500670346338, -4.75, cl_1};
Point(22) = {-0.225, 36.70500670346338, -4.75, cl_1};
Point(23) = {-0.225, 36.70500670346338, 4.75, cl_1};
Point(24) = {0.225, 36.70500670346338, 4.75, cl_1};
Line(1) = {1, 2};
p2 = newp;
Point(p2 + 1) = {-1.491963279125907e-13, 2.775557561562892e-14, -7};
Circle(2) = {3, p2 + 1, 2};
Line(3) = {3, 4};
p4 = newp;
Point(p4 + 1) = {-1.50910833431397e-13, 2.775557561562892e-14, 7};
Circle(4) = {4, p4 + 1, 1};
Line(5) = {5, 6};
Line(37) = {5, 6};
p6 = newp;
```

Point(p6 + 1) = {-0.202501442942396, 14.99863304209213, 4.75};
Point(p6 + 2) = {-0.1800024302187768, 14.99891992785103, 4.75};
Point(p6 + 3) = {-0.1575030124586994, 14.99917306234418, 4.75};
Point(p6 + 4) = {-0.1350032402917206, 14.99939244557158, 4.75};
Point(p6 + 5) = {-0.1125031643473978, 14.99957807753322, 4.75};
Point(p6 + 6) = {-0.09000283525528777, 14.99972995822911, 4.75};
Point(p6 + 7) = {-0.06750230364494764, 14.99984808765925, 4.75};
Point(p6 + 8) = {-0.04500162014593442, 14.99993246582363, 4.75};
Point(p6 + 9) = {-0.02250083538780515, 14.99998309272226, 4.75};
Point(p6 + 10) = {-1.168787289174134e-13, 14.99999996835513, 4.75};
Point(p6 + 11) = {0.02250083538757341, 14.99998309272226, 4.75};
Point(p6 + 12) = {0.04500162014570855, 14.99993246582363, 4.75};
Point(p6 + 13) = {0.06750230364473173, 14.99984808765924, 4.75};
Point(p6 + 14) = {0.09000283525508565, 14.99972995822911, 4.75};
Point(p6 + 15) = {0.1125031643472136, 14.99957807753322, 4.75};
Point(p6 + 16) = {0.1350032402915582, 14.99939244557157, 4.75};
Point(p6 + 17) = {0.1575030124585626, 14.99917306234418, 4.75};
Point(p6 + 18) = {0.1800024302186698, 14.99891992785103, 4.75};
Point(p6 + 19) = {0.2025014429423226, 14.99863304209213, 4.75};
Spline(6) = {7, p6 + 1, p6 + 2, p6 + 3, p6 + 4, p6 + 5, p6 + 6, p6 + 7, p6 + 8, p6 + 9, p6 + 10, p6 + 11, p6 + 12, p6 + 13, p6 + 14, p6 + 15, p6 + 16, p6 + 17, p6 + 18, p6 + 19, 6};
Line(7) = {8, 7};
Spline(38) = {7, p6 + 1, p6 + 2, p6 + 3, p6 + 4, p6 + 5, p6 + 6, p6 + 7, p6 + 8, p6 + 9, p6 + 10, p6 + 11, p6 + 12, p6 + 13, p6 + 14, p6 + 15, p6 + 16, p6 + 17, p6 + 18, p6 + 19, 6};
Line(39) = {8, 7};
p8 = newp;
Point(p8 + 1) = {-0.2025000000000023, 14.99863306614388, -4.75};
Point(p8 + 2) = {-0.1800000000000045, 14.99891997342276, -4.75};
Point(p8 + 3) = {-0.1575000000000064, 14.99917312690413, -4.75};
Point(p8 + 4) = {-0.135000000000008, 14.99939252658798, -4.75};
Point(p8 + 5) = {-0.1125000000000094, 14.99957817247432, -4.75};
Point(p8 + 6) = {-0.09000000000001049, 14.99973006456314, -4.75};
Point(p8 + 7) = {-0.06750000000001136, 14.99984820285445, -4.75};
Point(p8 + 8) = {-0.04500000000001195, 14.99993258734824, -4.75};
Point(p8 + 9) = {-0.02250000000001232, 14.99998321804451, -4.75};
Point(p8 + 10) = {-1.243449787580175e-14, 15.00000009494327, -4.75};
Point(p8 + 11) = {0.02249999999998775, 14.99998321804451, -4.75};
Point(p8 + 12) = {0.04499999999998808, 14.99993258734824, -4.75};
Point(p8 + 13) = {0.06749999999998876, 14.99984820285445, -4.75};
Point(p8 + 14) = {0.08999999999998956, 14.99973006456314, -4.75};
Point(p8 + 15) = {0.1124999999999907, 14.99957817247432, -4.75};
Point(p8 + 16) = {0.1349999999999922, 14.99939252658798, -4.75};
Point(p8 + 17) = {0.1574999999999937, 14.99917312690413, -4.75};
Point(p8 + 18) = {0.1799999999999956, 14.99891997342276, -4.75};
Point(p8 + 19) = {0.2024999999999976, 14.99863306614388, -4.75};
Spline(8) = {8, p8 + 1, p8 + 2, p8 + 3, p8 + 4, p8 + 5, p8 + 6, p8 + 7, p8 + 8, p8 + 9, p8 + 10, p8 + 11, p8 + 12, p8 + 13, p8 + 14, p8 + 15, p8 + 16, p8 + 17, p8 + 18, p8 + 19, 5};
Spline(40) = {8, p8 + 1, p8 + 2, p8 + 3, p8 + 4, p8 + 5, p8 + 6, p8 + 7, p8 + 8, p8 + 9, p8 + 10,

p8 + 11, p8 + 12, p8 + 13, p8 + 14, p8 + 15, p8 + 16, p8 + 17, p8 + 18, p8 + 19, 5};
Line(9) = {9, 2};
Line(10) = {9, 10};
Line(11) = {1, 10};
Line(12) = {11, 4};
Line(13) = {11, 12};
Line(14) = {3, 12};
p15 = newp;
Point(p15 + 1) = {-5.843220120199492, 30.5145936777207, -7.000000000000003};
Point(p15 + 2) = {-5.646569116095066, 30.55150998963101, -7.000000000000003};
Point(p15 + 3) = {-5.438751968526832, 30.59768231786743, -7.000000000000003};
Point(p15 + 4) = {-5.240134258957463, 30.66767360852448, -7.000000000000003};
Point(p15 + 5) = {-5.053142502901895, 30.76181729524773, -7.000000000000003};
Point(p15 + 6) = {-4.877691643953241, 30.88011476759002, -7.000000000000003};
Point(p15 + 7) = {-4.716618413772618, 31.01987869230903, -7.000000000000003};
Point(p15 + 8) = {-4.570951083223504, 31.17842412944356, -7.000000000000003};
Point(p15 + 9) = {-4.448364944407608, 31.34220745227801, -7.000000000000003};
Point(p15 + 10) = {-4.347295548089637, 31.50827103889382, -7.000000000000003};
Point(p15 + 11) = {-4.262103216485357, 31.68094347486469, -7.000000000000003};
Point(p15 + 12) = {-4.191567540975719, 31.86032628265812, -7.000000000000003};
Point(p15 + 13) = {-4.134468112941675, 32.04652098474157, -7.000000000000003};
Point(p15 + 14) = {-4.089584533974398, 32.23962911261863, -7.000000000000003};
Point(p15 + 15) = {-4.056044712379846, 32.44006045147185, -7.000000000000003};
Point(p15 + 16) = {-4.033631744240455, 32.64880463187275, -7.000000000000003};
Point(p15 + 17) = {-4.022116073508605, 32.86684008717653, -7.000000000000003};
Point(p15 + 18) = {-4.021356904252023, 33.09522380401035, -7.000000000000003};
Point(p15 + 19) = {-4.031622484508785, 33.33537477554147, -7.000000000000003};
Spline(15) = {12, p15 + 1, p15 + 2, p15 + 3, p15 + 4, p15 + 5, p15 + 6, p15 + 7, p15 + 8, p15 +
9, p15 + 10, p15 + 11, p15 + 12, p15 + 13, p15 + 14, p15 + 15, p15 + 16, p15 + 17, p15 + 18,
p15 + 19, 13};
p16 = newp;
Point(p16 + 1) = {-4.059621482899755, 33.99998860623584, -7.000000000000001};
Point(p16 + 2) = {-4.030667793898976, 34.40878773303832, -7.000000000000001};
Point(p16 + 3) = {-3.979075572061298, 34.81447752481071, -7.000000000000001};
Point(p16 + 4) = {-3.908962641662942, 35.22008895108518, -7.000000000000001};
Point(p16 + 5) = {-3.823509913574644, 35.61994300233226, -7.000000000000001};
Point(p16 + 6) = {-3.724764631846288, 36.01492145375976, -7.000000000000001};
Point(p16 + 7) = {-3.613496704171113, 36.40723425355707, -7.000000000000001};
Point(p16 + 8) = {-3.490301802974394, 36.79725368231583, -7.000000000000001};
Point(p16 + 9) = {-3.355868436650492, 37.1849059244806, -7.000000000000001};
Point(p16 + 10) = {-3.210846908120189, 37.57013015433361, -7.000000000000001};
Point(p16 + 11) = {-3.055850304368443, 37.95287819955221, -7.000000000000001};
Point(p16 + 12) = {-2.891968650874093, 38.33190986808721, -7.000000000000001};
Point(p16 + 13) = {-2.721530353018921, 38.70315606757392, -7.000000000000001};
Point(p16 + 14) = {-2.544673159306746, 39.06758802167294, -7.000000000000001};
Point(p16 + 15) = {-2.361055653430663, 39.42690277624027, -7.000000000000001};
Point(p16 + 16) = {-2.170157770073208, 39.78276375330282, -7.000000000000001};
Point(p16 + 17) = {-1.971267542905925, 40.13683658894605, -7.000000000000001};

Point(p16 + 18) = {-1.763573285433414, 40.49078806977719, -7.000000000000001};
Point(p16 + 19) = {-1.546025303675059, 40.84628772841563, -7.000000000000001};
Spline(16) = {13, p16 + 1, p16 + 2, p16 + 3, p16 + 4, p16 + 5, p16 + 6, p16 + 7, p16 + 8, p16 + 9, p16 + 10, p16 + 11, p16 + 12, p16 + 13, p16 + 14, p16 + 15, p16 + 16, p16 + 17, p16 + 18, p16 + 19, 14};
p17 = newp;
Point(p17 + 1) = {8.57252759403147e-16, 0, -7};
Circle(17) = {15, p17 + 1, 14};
p18 = newp;
Point(p18 + 1) = {1.545973405538309, 40.8463667011001, -6.999999999999998};
Point(p18 + 2) = {1.763505458880102, 40.49088637662704, -6.999999999999998};
Point(p18 + 3) = {1.971206776434373, 40.13691293222307, -6.999999999999998};
Point(p18 + 4) = {2.17011651017291, 39.78279475551972, -6.999999999999998};
Point(p18 + 5) = {2.361036822018353, 39.42688228844525, -6.999999999999998};
Point(p18 + 6) = {2.544671352653141, 39.06752682693793, -6.999999999999998};
Point(p18 + 7) = {2.721538363348639, 38.70308127385721, -6.999999999999998};
Point(p18 + 8) = {2.891976539301108, 38.33186199060253, -6.999999999999998};
Point(p18 + 9) = {3.055849559059361, 37.95290117765861, -6.999999999999998};
Point(p18 + 10) = {3.210866416284228, 37.57012233293857, -6.999999999999998};
Point(p18 + 11) = {3.355917463232352, 37.18479511633608, -6.999999999999998};
Point(p18 + 12) = {3.490368133279744, 36.79703624554507, -6.999999999999998};
Point(p18 + 13) = {3.613557286893788, 36.40697128869291, -6.999999999999998};
Point(p18 + 14) = {3.724796596753962, 36.01473486913355, -6.999999999999998};
Point(p18 + 15) = {3.823493695757872, 35.61995363640006, -6.999999999999998};
Point(p18 + 16) = {3.908937857515054, 35.22007270800241, -6.999999999999998};
Point(p18 + 17) = {3.979075904363879, 34.81447695254942, -6.999999999999998};
Point(p18 + 18) = {4.030658570971088, 34.40875312676599, -6.999999999999998};
Point(p18 + 19) = {4.059618183244853, 34.00007580696644, -6.999999999999998};
Spline(18) = {15, p18 + 1, p18 + 2, p18 + 3, p18 + 4, p18 + 5, p18 + 6, p18 + 7, p18 + 8, p18 + 9, p18 + 10, p18 + 11, p18 + 12, p18 + 13, p18 + 14, p18 + 15, p18 + 16, p18 + 17, p18 + 18, p18 + 19, 16};
p19 = newp;
Point(p19 + 1) = {4.031839073001775, 33.33741413580277, -6.999999999999999};
Point(p19 + 2) = {4.021761966938088, 33.09959483324013, -6.999999999999999};
Point(p19 + 3) = {4.022598001195213, 32.873544197527, -6.999999999999999};
Point(p19 + 4) = {4.034022615446013, 32.65757141116707, -6.999999999999999};
Point(p19 + 5) = {4.056199465678046, 32.45040306329449, -6.999999999999999};
Point(p19 + 6) = {4.089398392316929, 32.25085652675384, -6.999999999999999};
Point(p19 + 7) = {4.13386155307427, 32.05772550670792, -6.999999999999999};
Point(p19 + 8) = {4.190626465449164, 31.87048371109485, -6.999999999999999};
Point(p19 + 9) = {4.261169616672662, 31.68898015050287, -6.999999999999999};
Point(p19 + 10) = {4.34696751661513, 31.51306385487597, -6.999999999999999};
Point(p19 + 11) = {4.449496675146936, 31.34258385415814, -6.999999999999999};
Point(p19 + 12) = {4.571459383580786, 31.1765556286288, -6.999999999999999};
Point(p19 + 13) = {4.714520243148685, 31.01856155660844, -6.999999999999999};
Point(p19 + 14) = {4.87624604779298, 30.87771596869668, -6.999999999999999};
Point(p19 + 15) = {5.052212659262638, 30.75979591667703, -6.999999999999999};
Point(p19 + 16) = {5.237754516124216, 30.6673600711189, -6.999999999999999};

Point(p19 + 17) = {5.436977806348509, 30.59798426746783, -6.999999999999999};
Point(p19 + 18) = {5.648196182558546, 30.55096210811703, -6.999999999999999};
Point(p19 + 19) = {5.84715832345151, 30.51384571267578, -6.999999999999999};
Spline(19) = {16, p19 + 1, p19 + 2, p19 + 3, p19 + 4, p19 + 5, p19 + 6, p19 + 7, p19 + 8, p19 + 9, p19 + 10, p19 + 11, p19 + 12, p19 + 13, p19 + 14, p19 + 15, p19 + 16, p19 + 17, p19 + 18, p19 + 19, 9};
p20 = newp;
Point(p20 + 1) = {5.847158323451508, 30.51384571267578, 7.000000000000001};
Point(p20 + 2) = {5.64819618255854, 30.55096210811702, 7.000000000000001};
Point(p20 + 3) = {5.436977806348507, 30.59798426746782, 7.000000000000001};
Point(p20 + 4) = {5.237754516124217, 30.6673600711189, 7.000000000000001};
Point(p20 + 5) = {5.052212659262638, 30.75979591667703, 7.000000000000001};
Point(p20 + 6) = {4.876246047792979, 30.87771596869668, 7.000000000000001};
Point(p20 + 7) = {4.714520243148685, 31.01856155660843, 7.000000000000001};
Point(p20 + 8) = {4.571459383580779, 31.1765556286288, 7.000000000000001};
Point(p20 + 9) = {4.449496675146928, 31.34258385415814, 7.000000000000001};
Point(p20 + 10) = {4.346967516615127, 31.51306385487597, 7.000000000000001};
Point(p20 + 11) = {4.26116961667266, 31.68898015050287, 7.000000000000001};
Point(p20 + 12) = {4.190626465449163, 31.87048371109485, 7.000000000000001};
Point(p20 + 13) = {4.13386155307427, 32.05772550670792, 7.000000000000001};
Point(p20 + 14) = {4.089398392316929, 32.25085652675384, 7.000000000000001};
Point(p20 + 15) = {4.056199465678046, 32.45040306329449, 7.000000000000001};
Point(p20 + 16) = {4.034022615446013, 32.65757141116707, 7.000000000000001};
Point(p20 + 17) = {4.022598001195212, 32.873544197527, 7.000000000000001};
Point(p20 + 18) = {4.021761966938086, 33.09959483324012, 7.000000000000001};
Point(p20 + 19) = {4.031839073001769, 33.33741413580276, 7.000000000000001};
Spline(20) = {10, p20 + 1, p20 + 2, p20 + 3, p20 + 4, p20 + 5, p20 + 6, p20 + 7, p20 + 8, p20 + 9, p20 + 10, p20 + 11, p20 + 12, p20 + 13, p20 + 14, p20 + 15, p20 + 16, p20 + 17, p20 + 18, p20 + 19, 17};
Line(21) = {16, 17};
Line(22) = {13, 18};
p23 = newp;
Point(p23 + 1) = {-4.031622484508784, 33.33537477554147, 6.999999999999999};
Point(p23 + 2) = {-4.021356904252022, 33.09522380401037, 6.999999999999999};
Point(p23 + 3) = {-4.022116073508605, 32.86684008717654, 6.999999999999999};
Point(p23 + 4) = {-4.033631744240455, 32.64880463187276, 6.999999999999999};
Point(p23 + 5) = {-4.056044712379846, 32.44006045147185, 6.999999999999999};
Point(p23 + 6) = {-4.089584533974398, 32.23962911261863, 6.999999999999999};
Point(p23 + 7) = {-4.134468112941674, 32.04652098474157, 6.999999999999999};
Point(p23 + 8) = {-4.191567540975719, 31.86032628265813, 6.999999999999999};
Point(p23 + 9) = {-4.262103216485357, 31.6809434748647, 6.999999999999999};
Point(p23 + 10) = {-4.347295548089637, 31.50827103889383, 6.999999999999999};
Point(p23 + 11) = {-4.448364944407608, 31.34220745227802, 6.999999999999999};
Point(p23 + 12) = {-4.570951083223504, 31.17842412944356, 6.999999999999999};
Point(p23 + 13) = {-4.716618413772618, 31.01987869230904, 6.999999999999999};
Point(p23 + 14) = {-4.87769164395324, 30.88011476759003, 6.999999999999999};
Point(p23 + 15) = {-5.053142502901895, 30.76181729524774, 6.999999999999999};
Point(p23 + 16) = {-5.240134258957462, 30.66767360852448, 6.999999999999999};

Point(p23 + 17) = {-5.438751968526833, 30.59768231786743, 6.999999999999999};
Point(p23 + 18) = {-5.646569116095074, 30.55150998963101, 6.999999999999999};
Point(p23 + 19) = {-5.843220120199496, 30.5145936777207, 6.999999999999999};
Spline(23) = {18, p23 + 1, p23 + 2, p23 + 3, p23 + 4, p23 + 5, p23 + 6, p23 + 7, p23 + 8, p23 + 9, p23 + 10, p23 + 11, p23 + 12, p23 + 13, p23 + 14, p23 + 15, p23 + 16, p23 + 17, p23 + 18, p23 + 19, 11};
p24 = newp;
Point(p24 + 1) = {4.059618183244853, 34.00007580696644, 6.999999999999998};
Point(p24 + 2) = {4.030658570971087, 34.408753126766, 6.999999999999998};
Point(p24 + 3) = {3.979075904363878, 34.81447695254941, 6.999999999999998};
Point(p24 + 4) = {3.908937857515054, 35.2200727080024, 6.999999999999998};
Point(p24 + 5) = {3.823493695757872, 35.61995363640006, 6.999999999999998};
Point(p24 + 6) = {3.724796596753961, 36.01473486913356, 6.999999999999998};
Point(p24 + 7) = {3.613557286893787, 36.4069712886929, 6.999999999999998};
Point(p24 + 8) = {3.490368133279742, 36.79703624554507, 6.999999999999998};
Point(p24 + 9) = {3.355917463232348, 37.18479511633608, 6.999999999999998};
Point(p24 + 10) = {3.210866416284227, 37.57012233293857, 6.999999999999998};
Point(p24 + 11) = {3.05584955905936, 37.9529011776586, 6.999999999999998};
Point(p24 + 12) = {2.891976539301108, 38.33186199060253, 6.999999999999998};
Point(p24 + 13) = {2.721538363348632, 38.70308127385721, 6.999999999999998};
Point(p24 + 14) = {2.544671352653134, 39.06752682693793, 6.999999999999998};
Point(p24 + 15) = {2.36103682201835, 39.42688228844523, 6.999999999999998};
Point(p24 + 16) = {2.170116510172909, 39.7827947555197, 6.999999999999998};
Point(p24 + 17) = {1.971206776434373, 40.13691293222305, 6.999999999999998};
Point(p24 + 18) = {1.763505458880095, 40.49088637662703, 6.999999999999998};
Point(p24 + 19) = {1.545973405538302, 40.84636670110011, 6.999999999999998};
Spline(24) = {17, p24 + 1, p24 + 2, p24 + 3, p24 + 4, p24 + 5, p24 + 6, p24 + 7, p24 + 8, p24 + 9, p24 + 10, p24 + 11, p24 + 12, p24 + 13, p24 + 14, p24 + 15, p24 + 16, p24 + 17, p24 + 18, p24 + 19, 19};
p25 = newp;
Point(p25 + 1) = {-8.572527594031433e-16, 0, 7};
Circle(25) = {19, p25 + 1, 20};
p26 = newp;
Point(p26 + 1) = {-1.546025303675058, 40.84628772841562, 6.999999999999998};
Point(p26 + 2) = {-1.763573285433414, 40.49078806977719, 6.999999999999998};
Point(p26 + 3) = {-1.971267542905924, 40.13683658894605, 6.999999999999998};
Point(p26 + 4) = {-2.170157770073207, 39.78276375330281, 6.999999999999998};
Point(p26 + 5) = {-2.361055653430661, 39.42690277624026, 6.999999999999998};
Point(p26 + 6) = {-2.544673159306745, 39.06758802167294, 6.999999999999998};
Point(p26 + 7) = {-2.721530353018929, 38.70315606757391, 6.999999999999998};
Point(p26 + 8) = {-2.891968650874095, 38.3319098680872, 6.999999999999998};
Point(p26 + 9) = {-3.055850304368442, 37.9528781995522, 6.999999999999998};
Point(p26 + 10) = {-3.210846908120188, 37.57013015433361, 6.999999999999998};
Point(p26 + 11) = {-3.355868436650492, 37.1849059244806, 6.999999999999998};
Point(p26 + 12) = {-3.4903018029744, 36.79725368231583, 6.999999999999998};
Point(p26 + 13) = {-3.613496704171113, 36.40723425355708, 6.999999999999998};
Point(p26 + 14) = {-3.724764631846287, 36.01492145375976, 6.999999999999998};
Point(p26 + 15) = {-3.823509913574643, 35.61994300233226, 6.999999999999998};

Point(p26 + 16) = {-3.908962641662941, 35.22008895108518, 6.999999999999998};
Point(p26 + 17) = {-3.979075572061299, 34.81447752481071, 6.999999999999998};
Point(p26 + 18) = {-4.030667793898976, 34.40878773303832, 6.999999999999998};
Point(p26 + 19) = {-4.059621482899755, 33.99998860623585, 6.999999999999998};
Spline(26) = {20, p26 + 1, p26 + 2, p26 + 3, p26 + 4, p26 + 5, p26 + 6, p26 + 7, p26 + 8, p26 + 9, p26 + 10, p26 + 11, p26 + 12, p26 + 13, p26 + 14, p26 + 15, p26 + 16, p26 + 17, p26 + 18, p26 + 19, 18};
Line(27) = {14, 20};
Line(28) = {19, 15};
Line(29) = {21, 5};
Line(41) = {21, 5};
Line(30) = {22, 21};
Line(45) = {22, 21};
Line(31) = {8, 22};
Line(42) = {8, 22};
Line(32) = {7, 23};
Line(44) = {7,23};
Line(33) = {23, 24};
Line(46) = {23, 24};
Line(34) = {24, 6};
Line(43) = {24, 6};
Line(35) = {21, 24};
Line(47) = {21, 24};
Line(36) = {22, 23};
Line(48) = {22, 23};
Line Loop(1) = {1, -2, 3, 4};
Line Loop(2) = {5, -6, -7, 8};
Ruled Surface(1) = {1,2};
Line Loop(3) = {1, -9, 10, -11};
Plane Surface(2) = {3};
Line Loop(4) = {3, -12, 13, -14,15,16,-17,18,19,9,-2};
Plane Surface(3) = {4};
Line Loop(5) = {2, -9, -51, -14};
Plane Surface(4) = {5};
Line Loop(6) = {19, -51, 15, -52};
Plane Surface (5) = {6};
Line Loop(7) = {52, 16, -17, 18};
Plane Surface(6) = {7};
Line Loop(8) = {20, -21, 19, 10};
Ruled Surface(7) = {8};
Line Loop(9) = {15, 22, 23, 13};
Ruled Surface(8) = {9};
Line Loop(10) = {4, 11, 49, 12};
Plane Surface(9) = {10};
Line Loop(11)= {49, -23, 50, -20};
Plane Surface(10)= {11};
Line Loop (12) = {50, 24, 25, 26};
Plane Surface (11) = {12};

Line Loop(13) = {26, -22, 16, 27};
Ruled Surface(12) = {13};
Line Loop(14) = {27, -25, 28, 17};
Ruled Surface(13) = {14};
Line Loop(15) = {24, 28, 18, 21};
Ruled Surface(14) = {15};
Line Loop(16) = {8, -29, -30, -31};
Plane Surface(15) = {16};
Line Loop(17) = {32, 33, 34, -6};
Plane Surface(16) = {17};
Line Loop(18) = {35, 34, -5, -29};
Plane Surface(17) = {18};
Line Loop(19) = {7, 32, -36, -31};
Plane Surface(18) = {19};
Line Loop(20) = {36, 33, -35, -30};
Plane Surface(19) = {20};
Line Loop(21) = {37, -38, -39, 40};
Ruled Surface(20) = {21};
Line Loop(22) = {40, -41, -45, -42};
Plane Surface(21) = {22};
Line Loop(23) = {44, 46, 43, -38};
Plane Surface(22) = {23};
Line Loop(24) = {47, 43, -37, -41};
Plane Surface(23) = {24};
Line Loop(25) = {48, 46, -47, -45};
Plane Surface(24) = {25};
Line Loop(26) = {39, 44, -48, -42};
Plane Surface(25)= {26};

Creation of Gear Body:
Surface Loop(1) = {1, 2, 3, 4, 5, 6, 7, 8, 9, 10, 11, 12, 13, 14, 15, 16, 17, 18, 19};
Volume(1) = {1};

Creation of the Insert Body:
Surface Loop(2) = {20, 21, 22, 23, 24, 25};
Volume(2) = {2};

Gather all the coincident volumes/surfaces/lines/points:
Coherence;
Physical Surface (1)={1};
Physical Surface (2)={2};
Physical Surface (3)={3};
Physical Surface (4)={4};
Physical Surface (5)={5};
Physical Surface (6)={6};
Physical Surface (7)={7};
Physical Surface (8)={8};
Physical Surface (9)={9};

Physical Surface (10)={10};
Physical Surface (11)={11,12,13,14,15};
Physical Surface (12)={16};
Physical Volume (1)={1};
Physical Volume (2)={2};

Appendix H.

Case SIF Hybrid Gear - Example

Case SIF code for the metallic insert steel created at Chapter 6:

Header

```
CHECK KEYWORDS Warn
Mesh DB "."
Include Path ""
Results Directory ""
End
```

Simulation

```
Max Output Level = 5
Coordinate System = Cartesian
Coordinate Mapping(3) = 1 2 3
Simulation Type = Steady state
Steady State Max Iterations = 2
Output Intervals = 1
Timestepping Method = BDF
BDF Order = 2
Timestep intervals = 1
Timestep Sizes = 1 Solver Input File = case.sif
Output File = case.dat
Post File = case.ep
Coordinate Scaling = 0.001
End
```

Constants

```
Gravity(4) = 0 -1 0 9.82
Stefan Boltzmann = 5.67e-08
Permittivity of Vacuum = 8.8542e-12
Boltzmann Constant = 1.3807e-23
Unit Charge = 1.602e-19
End
```

Heat Solver

Solver 1

```
Equation = Heat Equation
Procedure = "HeatSolve" "HeatSolver"
Variable = -dofs 1 Temperature
```

```
Exec Solver = Always
Stabilize = True
Bubbles = False
Lumped Mass Matrix = False
Optimize Bandwidth = True
Steady State Convergence Tolerance = 1.0e-5
Nonlinear System Convergence Tolerance = 1.0e-7
Nonlinear System Max Iterations = 20
Nonlinear System Newton After Iterations = 3
Nonlinear System Newton After Tolerance = 1.0e-3
Nonlinear System Relaxation Factor = 1
Linear System Solver = Iterative
Linear System Iterative Method = BiCGStab
Linear System Max Iterations = 500
Linear System Convergence Tolerance = 1.0e-10
Linear System Preconditioning = ILU0
Linear System ILUT Tolerance = 1.0e-3
Linear System Abort Not Converged = False
Linear System Residual Output = 1
Linear System Precondition Recompute = 1
End
```

Solver to save values of boundary conditions

```
Solver 2
Equation = SaveLine
File Append = Logical False
Procedure = "SaveData" "SaveLine"
Filename = temperature_coordinate_1_2.dat
Exec Solver = After Simulation
Save Flux = Logical True
Variable 1 = String Temperature
Variable 2 = Coordinate 1
Variable 3 = Coordinate 2
Variable 4 = Coordinate 3
Update Exported Variables = Logical True
Nonlinear Update Exported Variables = Logical True
End
```

Solver for output as VTU file format

```
Solver 3
Exec Solver = After Simulation
Equation = Result Output
Procedure = "ResultOutputSolve" "ResultOutputSolver"
Output Format = Vtu
Output File Name = Temperatures
Scalar Field 1 = Temperature
Single Precision = True
Output Directory = RefinedResults
```

End

Functions

Radius function definition as the square root of coordinate 1 (x) and coordinate 2 (y):

$ function raio(X) {_raio=$\sqrt{X(0)^2 + X(1)^2}$}

HeaviSide 0 for the imposed Heat Flux (average) from the power loss model:

$ function hs0(X) {_hs0=tanh (1000 · 1000 · ($\sqrt{X(0)^2 + X(1)^2}$-(raioA/1000)))}

HeaviSide 1 for the imposed Heat Flux (average) from the power loss model:

$ function hs1(X) {_hs1=((-tanh (1000· 1000· (($\sqrt{X(0)^2 + X(1)^2}$)-raioB/1000))+1)· (tanh (1000· 1000· ($\sqrt{X(0)^2 + X(1)^2}$-(raioA/1000-1e-4)))+1)/4)· ($qcof_1$(1)· (1000· $\sqrt{X(0)^2 + X(1)^2}$)^2+$qcof_1$(2)· 1000· $\sqrt{X(0)^2 + X(1)^2}$+$qcof_1$(3))}

HeaviSide 2 for the imposed Heat Flux (average) from the power loss model:

$ function hs2(X) {_hs2=((-tanh (1000· ($\sqrt{X(0)^2 + X(1)^2}$-raioC/1000))+1)· (tanh (1000· 1000· ($\sqrt{X(0)^2 + X(1)^2}$-raioB/1000))+1)/4)· ($qcof_2$(1)· (1000· $\sqrt{X(0)^2 + X(1)^2}$)^3+$qcof_2$(2)· (1000· $\sqrt{X(0)^2 + X(1)^2}$)^2+ $qcof_2$(3) · 1000· $\sqrt{X(0)^2 + X(1)^2}$+$qcof_2$(4))}

HeaviSide 3 for the imposed Heat Flux (average) from the power loss model:

$ function hs3(X) {_hs3=((-tanh (1000· 1000· ($\sqrt{X(0)^2 + X(1)^2}$-raioD/1000))+1)· (tanh (1000· 1000· ($\sqrt{X(0)^2 + X(1)^2}$-(raioC/1000-1e-4)))+1)/4)· ($qcof_3$(1)· (1000· $\sqrt{X(0)^2 + X(1)^2}$)^3+$qcof_3$(2)· (1000· $\sqrt{X(0)^2 + X(1)^2}$)^2+$qcof_3$(3)· 1000· $\sqrt{X(0)^2 + X(1)^2}$+$qcof_3$(4))}

HeaviSide 4 for the imposed Heat Flux (average) from the power loss model:

$ function hs4(X) {_hs4=((tanh (1000· 1000· ($\sqrt{X(0)^2 + X(1)^2}$-raioD/1000))+1)/2)· ($qcof_4$(1)· (1000· $\sqrt{X(0)^2 + X(1)^2}$)^2+$qcof_4$(2)· 1000· $\sqrt{X(0)^2 + X(1)^2}$+$qcof_4$(3))}

HeaviSide for heat transfer coefficients for meshing surface:

$ function ht1(X) {_ht1=((-tanh (1000· 1000· ($\sqrt{X(0)^2 + X(1)^2}$-raioE/1000))+1)· (tanh (1000· 1000· ($\sqrt{X(0)^2 + X(1)^2}$-(raioA/1000)))+1)/4)· ($pcof_3$(1)· (1000· $\sqrt{X(0)^2 + X(1)^2}$)^2+$pcof_3$(2)· (1000· $\sqrt{X(0)^2 + X(1)^2}$)+$pcof_3$(3))}

Equation 1
Name = "Equation 1"
Active Solvers(3) = 1 2 3
End

Definition of the first material properties:

Material 1
Name = "POM"
Heat Conductivity = 0.3
Heat Capacity = 1470
Density = 1415
Poisson ratio = 0.3
Mesh Poisson ratio= 0.3
Youngs Modulus = 2690000000

End

Definition of the second material properties:
Material 2
Name = "Steel"
Heat Conductivity = 41.8
Heat Capacity = 493
Density = 1415
Poisson ratio = 0.3
Mesh Poisson ratio= 0.3
Youngs Modulus = 210000000000
End

Definition of the polymeric gear properties:
Body 1
Name = "Polymeric Gear"
Material = 1
Equation = 1
End
Definition of the metallic insert properties:
Body 2
Name = "Metallic Insert"
Material = 2
Equation = 1
End

Body Force 1
Name = "BodyForce 1"
End

Symmetry 1:
Boundary Condition 1
Target Boundaries(1) = 2
Name = "Sym1"
Heat Flux = 0
Save Line = Logical True
End

Symmetry 2:
Boundary Condition 2
Target Boundaries(1) = 3
Name = "Sym2"
Heat Flux = 0
Save Line = Logical True
End

Gear side 1:
Boundary Condition 3

Target Boundaries(1) = 4
Name = "HeatTransferSides"
Heat Transfer Coefficient = Variable Coordinate 1, Coordinate 2
Real MATC "$pcof(1)$· (raio(tx))^2+$pcof(2)$· raio(tx)+$pcof(3)$"
External Temperature = 288.15
End

Non-meshing surface 1:
Boundary Condition 4
Target Boundaries(1) = 5
Name = "HeatTransferFaces"
Heat Transfer Coefficient = max(hs)/3
External Temperature = 288.15
End

Non-meshing surface 2:
Boundary Condition 5
Target Boundaries(1) = 6
Name = "HeatTransferFaces"
Heat Transfer Coefficient = max(hs)/3
External Temperature = 288.15
End

Gear side 2:
Boundary Condition 6
Target Boundaries(1) = 7
Name = "HeatTransferSides"
Heat Transfer Coefficient = Variable Coordinate 1, Coordinate 2
Real MATC "$pcof_2(1)$· (raio(tx))^2+$pcof_2(2)$· raio(tx)+$pcof_2(3)$"
External Temperature = 288.15
End

Meshing surface:
Boundary Condition 7
Target Boundaries(1) = 8
Name = "HeatSource"
Heat Flux = Variable Coordinate 1, Coordinate 2
Real MATC "hs0(tx)· (hs1(tx)+hs2(tx)+hs3(tx)+hs4(tx))"
Heat Transfer Coefficient = Variable Coordinate 1, Coordinate 2
Real MATC "ht1(tx)"
External Temperature = 288.15
End

Non-meshing surface 3:
Boundary Condition 8
Target Boundaries(1) = 9
Name = "HeatTransferFaces"
Heat Transfer Coefficient = max(hs)/3

External Temperature = 288.15
End

Non-meshing surface 4:
Boundary Condition 9
Target Boundaries(1) = 10
Name = "HeatTransferFaces"
Heat Transfer Coefficient = max(hs)/3
External Temperature = 288.15
End

Adiabatic surface (shaft/gear interface):
Boundary Condition 10
Target Boundaries(2) = 1 12
Name = "HeatFlux"
Heat Flux = 0
End

Polymer and metal interface - Heat gap:
Boundary Condition 11
Target Boundaries(1) = 11
Name = "Thermal Contact Conductance"
Heat Transfer Coefficient = hc
Heat Gap = Logical True
Save Line = Logical True
End

Appendix I.

Detailed analysis of the various insert profiles

I.1. T-Profile

I.1.1. Influence on tooth weight

As shown in Table I.1 the increment in mass is lower than 2% when comparing the normal profile to the new t-profile.

I.1.2. Tooth temperature results

Figures I.1a and I.1b represent the maximum and the minimum temperature for the various TCR tested, concluding that the maximum temperature is remarkably reduced when using a T-profile for the insert model. Therefore, the approximation of the insert to the heat font as a beneficial effect on the reduction of the maximum temperature.

The temperatures results over the different contact pressures as its percentages of the new geometry in comparison with the initial non hybrid POM gear are shown in Tables I.2 and I.3.

Table I.1.: Mass evaluation over the insert for t-profile and for normal section.

Weight evaluation		
Insert Profile	Insert Weight [g]	Total Weight [g]
POM Gear without insert	-	3.729
POM Gear	0.479	4.208
Rectangular Cuboid	0.924	4.653 (+ 10.575%)
POM Gear without insert	-	3.655
POM Gear	0.553	4.208
T-profile	1.067	4.722 (+ 12.215%)

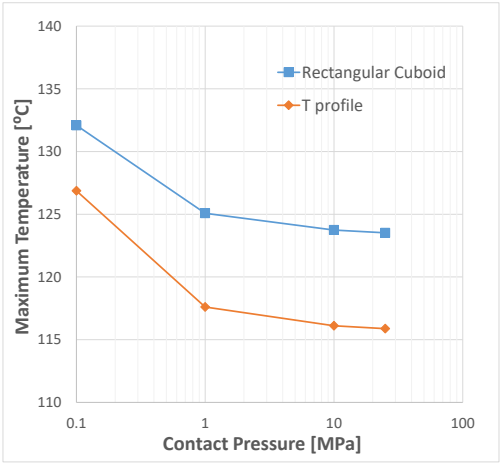

(a) Maximum temperature.

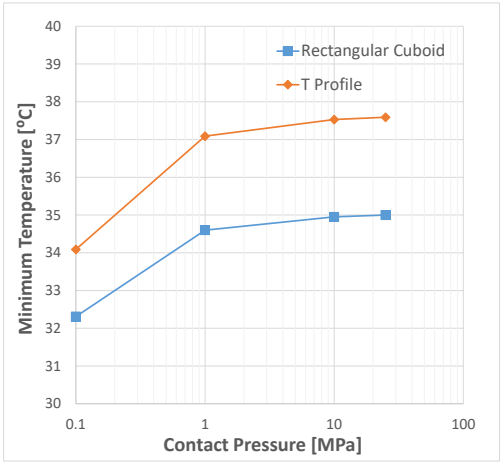

(b) Minimum temperature.

Figure I.1.: Maximum and minimum temperature for each insert profile (normal and t-profile) for the tested contact pressures.

Table I.2.: Maximum and minimum temperature for the insert profiles evaluation.

Temperature evaluation					
Insert Profile		**Contact Pressure**			
		0.1 MPa	1 MPa	10 MPa	25 MPa
Rectangular Cuboid	max(°C)	132.09	125.08	123.74	123.52
	min(°C)	32.31	34.60	34.95	35.00
T-profile	max(°C)	126.87	117.61	116.11	115.88
	min(°C)	34.09	37.09	37.53	37.59

Table I.3.: Percentage of temperature variation for the insert profiles evaluation.

Increment of temperature					
Insert profile		**Contact Pressure**			
		0.1 MPa	1 MPa	10 MPa	25 MPa
Rectangular Cuboid	max(%)	- 5.24	- 10.27	- 11.23	- 11.39
	min(%)	45.02	55.30	56.87	57.09
T-profile	max(%)	- 8.99	- 15.63	- 16.71	- 16.87
	min(%)	53.01	66.47	68.45	68.72

The new profile is able to reduce approximately 17% (reducing 140°C to 124°C) the maximum temperature, having a higher heat evacuated by the insert implementation, although raising the minimum temperature in the hybrid-gear body by 68.72% (increasing 22°C to 35°C). As for cuboid last profile it only has a increase of this minimum temperature of 57.09%.

For a better observation of the effect on the temperature distribution for the three cases (initial gear, normal insert profile and T-profile insert) the comparison has been done for a contacting pressure of 25 MPa, obtaining the results presented in Figure I.2.

Figures I.2b, I.2d and I.2f, representating the section of the various models for comparison, show that the temperature within the gear body and the insert has risen. Moreover, with the insert implementation more heat from a nearby zone in the meshing surface is getting evacuated, therefore, decreasing the maximum temperature, a clear effect seen in Figures I.2a, I.2c and I.2e, with a greener area, that is, a lower temperature than the above models.

The implementation of the T-profile has a better effect on reducing the heat evacuated and, therefore, reducing the maximum temperature, however having a consequence over the minimum temperature reached, which becomes higher.

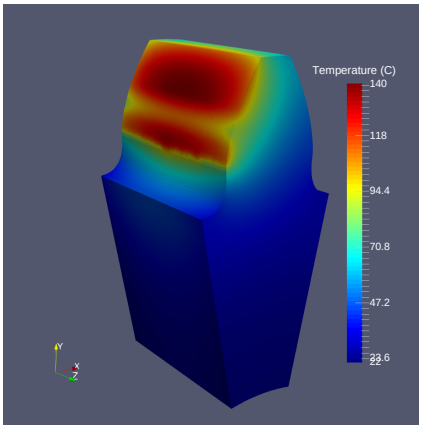

(a) Temperature without insert (T_{max}=139.40°C and T_{min}=22.28°C).

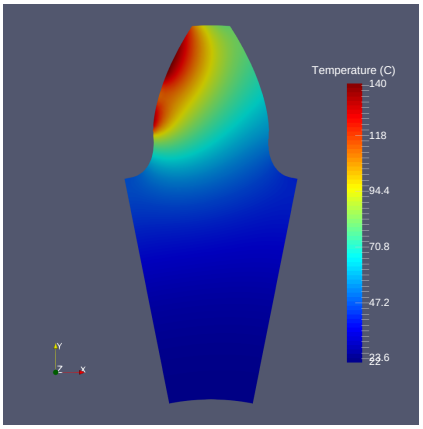

(b) Temperature cut without insert (T_{max}=139.40°C and T_{min}=22.28°C).

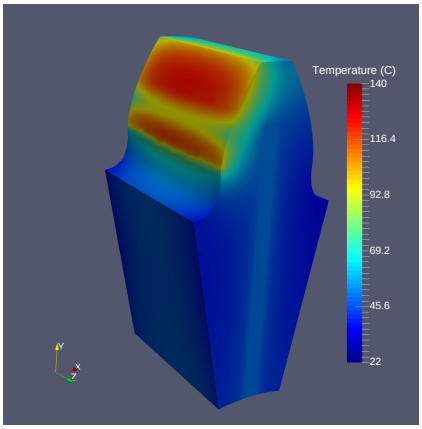

(c) Temp. result - Normal profile (T_{max}=123.52°C and T_{min}=35.00°C).

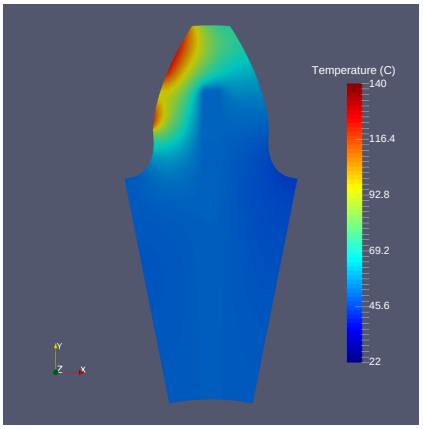

(d) Temp. result insert - Normal profile (T_{max}=123.52°C and T_{min}=35.00°C).

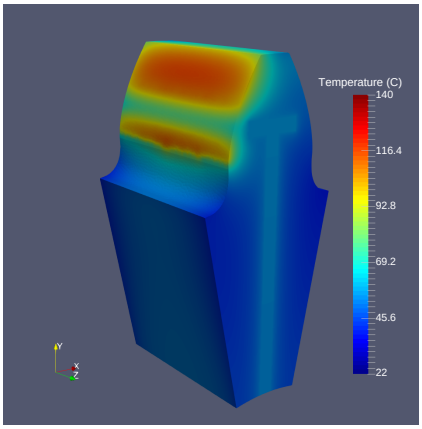

(e) Temperature result - T-profile (T_{max}=115.88°C and T_{min}=37.59°C).

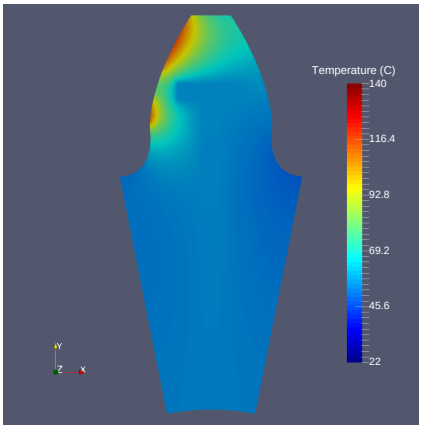

(f) Temperature result insert - T-Profile (T_{max}=115.88°C and T_{min}=37.59°C).

Figure I.2.: Temperature distribution for a normal gear and two hybrid gears, with a normal section or with a T-profile at 25MPa.

I.2. Double T-Profile

As the past case it was seen that adding an insert capable of evacuating the heat generated by frictional contact at meshing surface by the proximity at the meshing surface most aggravated points (the two "maximums" temperatures). Creating a double T-profile for that two points by creating a 2D cut representation of the double T-profile insert (Figure I.3a) and then generating the 3D hybrid-gear model(Figure I.3b) for the geometrical parameters of w_x=1.125 mm, t=2.25 mm, e=0 mm and vw=1.125 mm.

I.2.1. Influence on weight

As shown in Table I.4 the increment in mass is lower than 2% when comparing the T-profile to the double T-profile.

I.2.2. Influence on tooth temperature

Figures I.4a and I.4b represent the maximum and the minimum temperature results for the various contact pressures studies. Then, it is possible to infer that by creating another platform the evacuating heat flux generated by friction at the meshing gear on the two crucial points the maximum temperature is mostly reduced

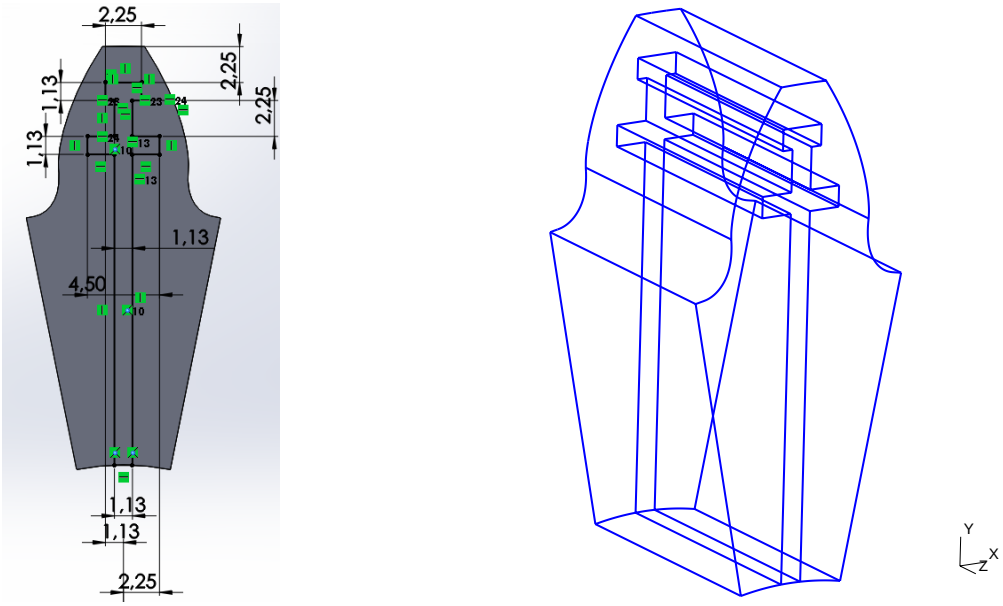

(a) Double T-profile - cut dimensions.

(b) 3D model of Double T-profile.

Figure I.3.: Dimension of the Double T-profile insert and hybrid-gear 3D model.

Table I.4.: Mass evaluation over the insert for double T-profile and for T-profile.

Weight evaluation		
Insert Profile	Insert Weight [g]	Total Weight [g]
POM Gear without insert	-	3.655
POM Gear	0.553	4.208
T-profile	1.067	4.722 (+ 12.215%)
POM Gear without insert	-	3.581
POM Gear	0.627	4.208
Double T-profile	1.211	4.792 (+ 13.878%)

than with the use of T-profile model. Therefore, it is more beneficial to have two "platforms" to decrease the bulk temperature at the meshing surface.

The temperatures results at the different contact pressures as its percentages of the temperature results for the new Double T-Profile when comparing with the initial non hybrid POM gear are shown in Tables I.5 and I.6. The new profile will be able to reduce approximately 23% of the maximum temperature reached (reducing 140°C to 107°C) compared to the 17% reduced with the implementation of the T-profile insert. Although always damaging the minimum temperature raising 75.31% (increasing 22°C to 39°C)as for the 68.72% (increasing 22°C to 38°C) of the T-profile model when comparing with the initial tooth.

For a more clear view of the effect of the double T-profile insert implementation at the hybrid-gear model Figure I.5 is presented with the insert section for observation of the temperature distribution on the gear tooth as well as the 3D model tooth for

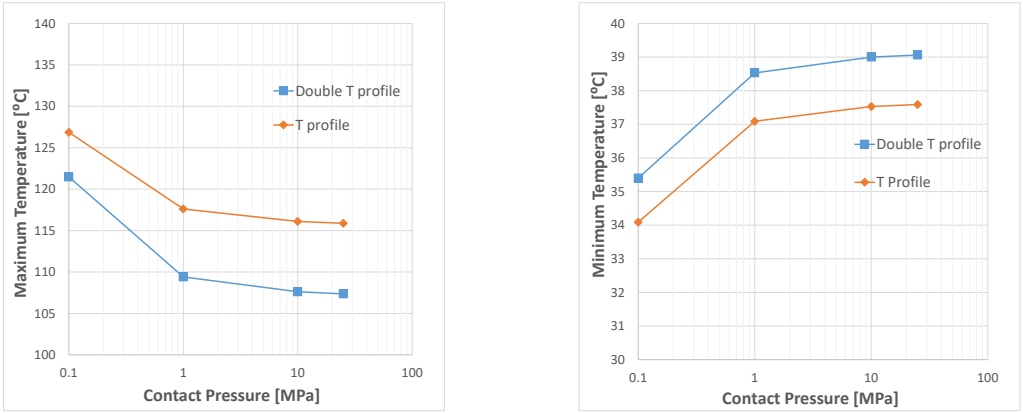

(a) Maximum temperature.

(b) Minimum temperature.

Figure I.4.: Maximum and minimum temperature for each insert profile (t and double t-profile) for the tested contact pressures.

Table I.5.: Maximum and minimum temperature for the insert T and double T-profiles evaluation.

Temperature evaluation					
Insert Profile		**Contact Pressure**			
		0.1 MPa	1 MPa	10 MPa	25 MPa
T-profile	max(°C)	126.87	117.61	116.11	115.88
	min(°C)	34.09	37.09	37.53	37.59
Double T-profile	max(°C)	121.48	109.41	107.62	107.36
	min(°C)	35.4	38.53	39	39.06

a constant contact pressure of 25 MPa.

Figures I.5b, I.5d and I.5f, representative of the section, showing that the temperature distribution has risen for the double T-profile guaranteed by increase of the minimum temperatures. However, the clear effect of adding a second "platform" at the insert model evacuates more heat through the insert and, consequently, diminishing the maximum temperature, as shown in Figures I.5a,I.5c and I.5e by the greener and yellower tone over the mesh surface.

Table I.6.: Percentage of temperature variation for the insert T and double T-profiles evaluation.

Increment of temperature					
Insert profile		**Contact Pressure**			
		0.1 MPa	1 MPa	10 MPa	25 MPa
T-profile	max(%)	- 8.99	- 15.63	- 16.71	- 16.87
	min(%)	53.01	66.47	68.45	68.72
Double T-profile	max(%)	- 12.86	- 21.51	- 22.80	- 22.98
	min(%)	58.89	72.94	75.04	75.31

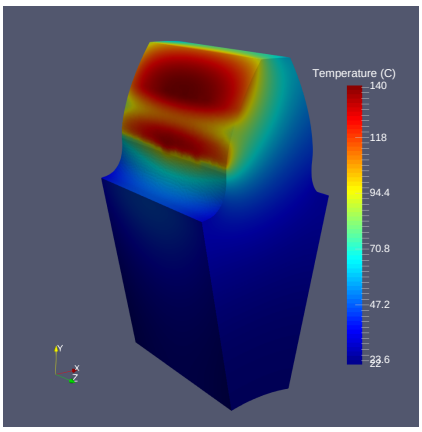

(a) Temperature without insert (T_{max}=139.40°C and T_{min}=22.28°C).

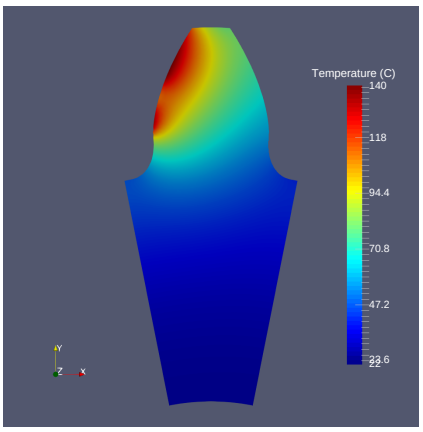

(b) Temperature cut without insert (T_{max}=139.40°C and T_{min}=22.28°C).

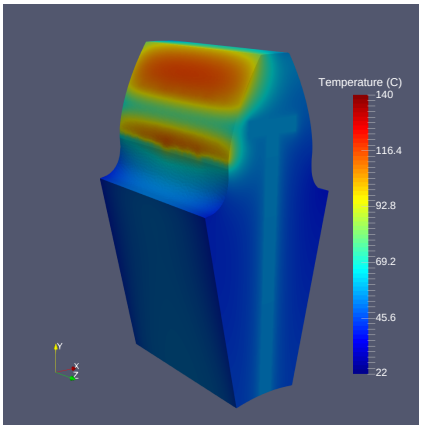

(c) Temperature result - T-profile (T_{max}=115.88°C and T_{min}=37.59°C).

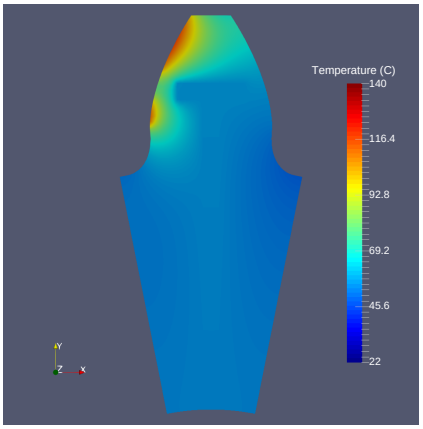

(d) Temperature result insert - T-Profile (T_{max}=115.88°C and T_{min}=37.59°C).

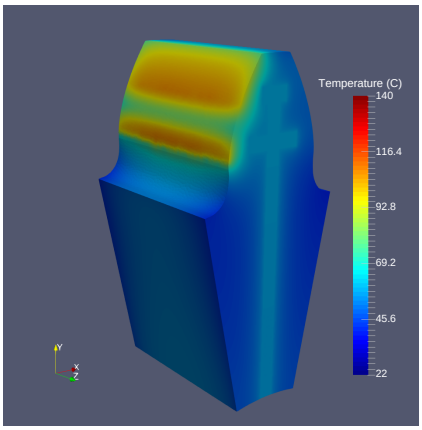

(e) Temp. result - Double T-profile (T_{max}=107.36°C and T_{min}=39.06°C).

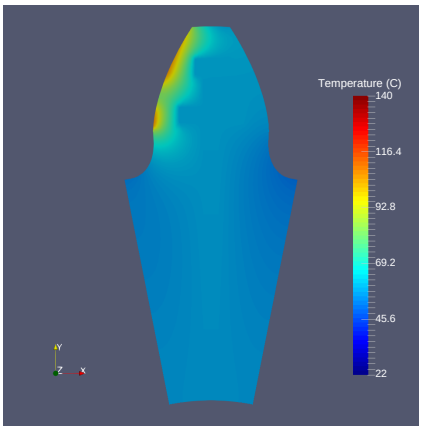

(f) Temp. result insert - Double T-profile (T_{max}=107.36°C and T_{min}=39.06°C).

Figure I.5.: Temperature distribution for a normal gear and two hybrid gears, with a T-profile or with a double T-profile at 25 MPa.

I.2.3. Increase of the Double T-profile "platforms"

For the study of the influence of the size of the two "platforms" for the Double T-profile to understand the influence over the closeness of the the insert and two points of higher heat flux generated another Double T-Profile (Double T-Profile I) was created. With the 2D section of the new double T-profile insert in Figure I.6a and the 3D hybrid-gear model in Figure I.6b for the geometrical parameters of w_x=1.125 mm, t=2.25 mm, e=0 mm and vw=1.125 mm.

Influence on tooth weight

As shown in Table I.7 the increment in mass is almost 2% when comparing the double T-profile to the double T-profile I.

Tooth temperature results

Figures I.7a and I.7b represent the maximum and the minimum temperature results for the various contact pressures studies in the Double T-Profile I when comparing with the initial non hybrid POM gear results. Deducing that the expansion of the two "platforms" of the double T-profile becomes a benefit in decreasing of maximum temperature. These expansion also reflects in a more heat evacuated by the new insert model, but having a huge effect at the increase of minimum temperature at

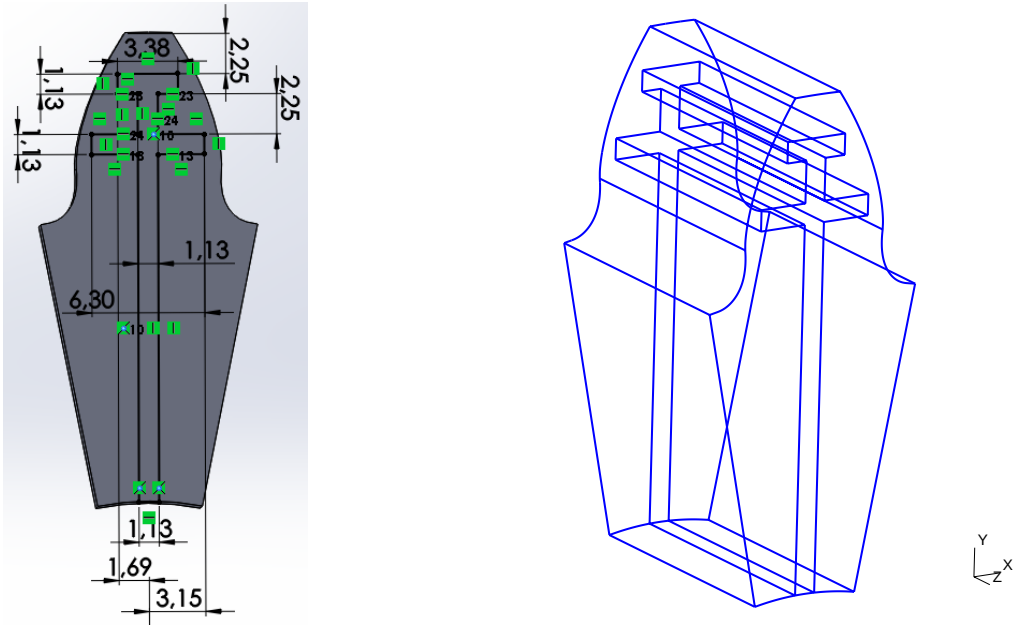

(a) Double T-profile I - cut dimensions.

(b) 3D model of Double T-profile I.

Figure I.6.: Dimension of the Double T-profile I insert and hybrid-gear 3D model.

Table I.7.: Mass evaluation over the insert for double T-profile and for double T-profile I.

Weight evaluation		
Insert Profile	Insert Weight [g]	Total Weight [g]
POM Gear without insert	-	3.581
POM Gear	0.627	4.208
Double T-profile	1.211	4.792 (+ 13.878%)
POM Gear without insert	-	3.516
POM Gear	0.692	4.208
Double T-profile I	1.335	4.851 (+ 15.280%)

the gear body.

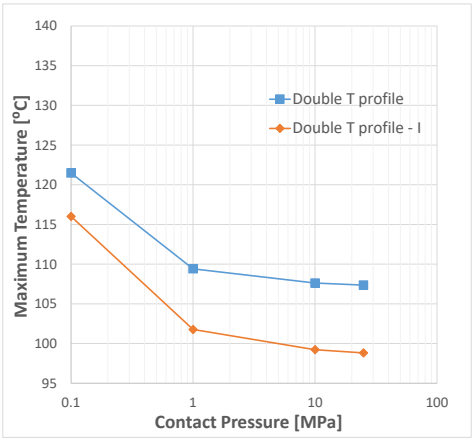

(a) Maximum temperature.

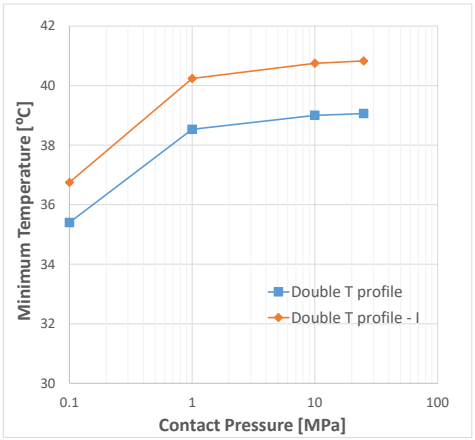

(b) Minimum temperature.

Figure I.7.: Maximum and minimum temperature for each insert profile (double t-profile and double t-profile I) for the tested contact pressures.

The temperatures results at the different contact pressures as its percentages pf the new hybrid gear model in comparison with the initial non hybrid POM gear are shown at Tables I.8 and I.9.

The new model (Double T-Profile I) is able to decrease the maximum temperature about 29% (reducing 140°C to 99°) instead of the 23% form the normal Double T-profile (reducing 140°C to 107°C), showing the clear impact of approximating the Double T-profile to near of the meshing surface. The expansion, the platforms sizes by 1.4 (4.5 to 6.3 mm and 2.25 to 3.375 mm) will conduce to a higher evacuation of the heat flux imposed at the contact surface.

On the other hand, as the heat dissipated by the insert is higher, so will the

Table I.8.: Maximum and minimum temperature for the insert double T-profile and double T-profile I evaluation.

Temperature evaluation					
Insert Profile		**Contact Pressure**			
		0.1 MPa	1 MPa	10 MPa	25 MPa
Double T-profile	max(°C)	121.48	109.41	107.62	107.36
	min(°C)	35.4	38.53	39	39.06
Double T-profile I	max(°C)	116.01	101.77	99.23	98.82
	min(°C)	36.75	40.24	40.75	40.83

Table I.9.: Percentage of temperature variation for the insert double T-profile and double T-profile I evaluation.

Increment of temperature					
Insert profile		**Contact Pressure**			
		0.1 MPa	1 MPa	10 MPa	25 MPa
Double T-profile	max(%)	- 12.86	- 21.51	- 22.80	- 22.98
	min(%)	58.89	72.94	75.04	75.31
Double T-profile I	max(%)	- 16.76	- 26.99	- 28.82	- 29.11
	min(%)	64.95	80.61	82.90	83.26

minimum temperature increase. For this case a raise of 83.26% (raising 22°C to 41°C) for the Double T-profile I instead of the 75.31% found for the previous Double T-profile (increase of 22°C to 39°C).

All this information is supported by Figure I.8, where Figures I.8a, I.8c and I.8e show the 3D gear model with the temperature result distribution and Figures I.8b, I.8d and I.8f represent the temperature result distribution in an insert section for a constant contact pressure of 25 MPa.

Figures I.8b, I.8d and I.8f shows that the temperature within the gear and within the insert increased, although lowering drastically the maximum temperature, as seen by the fading of the red/orange color over the mesh surface showed in Figures I.8a, I.8c and I.8e.

Finally, the maximum temperature decrease by the use of a more expanded insert model, however it is important to consider the possible negative effects at the region near the meshing surface.

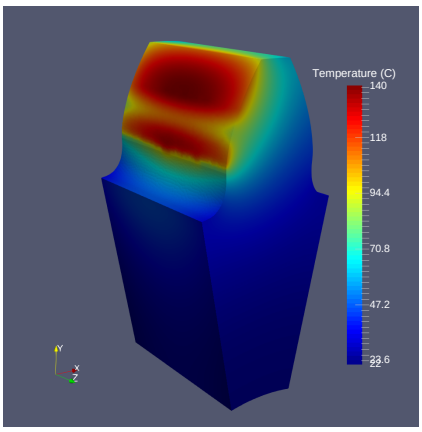

(a) Temperature without insert (T_{max}=139.40°C and T_{min}=22.28°C).

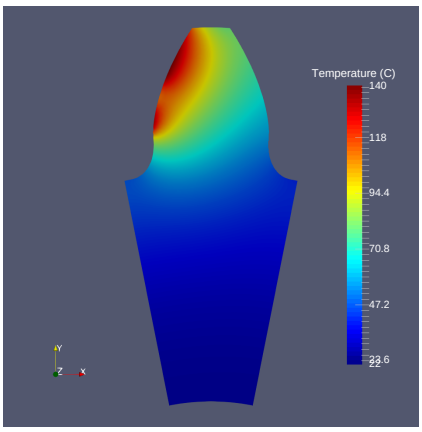

(b) Temperature cut without insert (T_{max}=139.40°C and T_{min}=22.28°C).

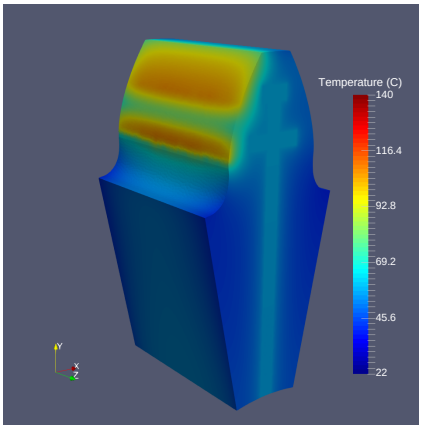

(c) Temp. result - Double T-profile (T_{max}=107.36°C and T_{min}=39.06°C).

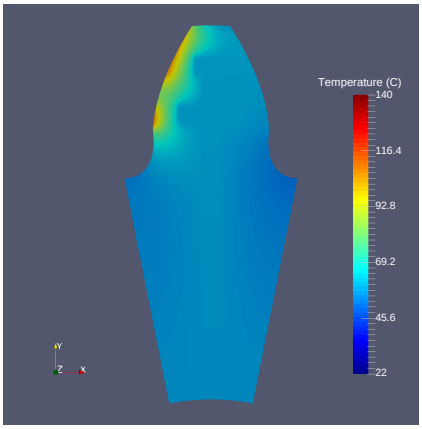

(d) Temp. result insert - Double T-profile (T_{max}=107.36°C and T_{min}=39.06°C).

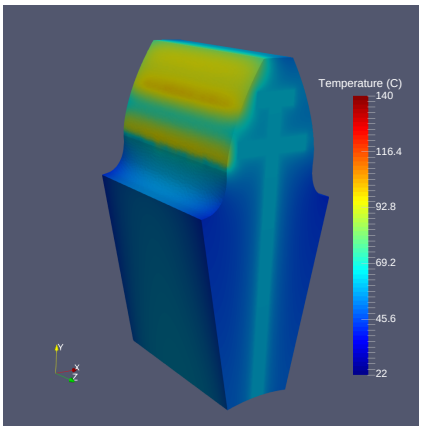

(e) Temp. result - Double T-profile I (T_{max}=98.82°C and T_{min}=40.83°C).

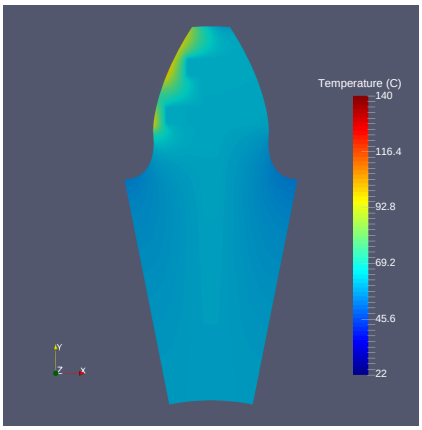

(f) Temp. result insert - Double T-Profile I (T_{max}=98.82°C and T_{min}=40.83°C).

Figure I.8.: Temperature distribution for a normal gear and two hybrid gears, with a double T-profile or with a double T-profile I at 25 MPa.

I.2.4. Influence of insert width (w_x) on a Double T-Profile I

Since the expansion of the "platforms" at the insert model drastically enhance the efficient of the insert and the evacuation of the heat generated at the meshing surface, some doubts were considered for the influence of the horizontal geometrical width of the insert, w_x. So, the next study will focus on the variation of the temperature for the insert width cases of 1.125, 0.788, 0.675 and 0.450 mm.

Influence on tooth weight

As shown in Table I.10 using the thinner width (0.450 mm) is possible a huge decrease in the weight from 15.280% of weight increment for 1.125 mm width to 8.935% weight increment for 0.450 mm of width.

Tooth temperature results

Figures I.7a and I.7b represent the maximum and the minimum temperature results, respectively, for the various contact pressures studies in the different geometries studied in comparison with the temperature results for the initial non hybrid POM gear. Therefore, the expand of the two "platforms" of the Double T-profile I are benefit for the decrease of maximum temperature. These expansion reflects on a more efficiency at heat evacuation by the new insert model, but having a huge effect

Table I.10.: Mass evaluation over the insert width for a Double T-profile I with variation of width.

Weight evaluation		
Width	Insert Weight [g]	Total Weight [g]
POM Gear without insert	-	3.516
POM Gear	0.692	4.208
w_x=1.125 mm	1.335	4.851 (+ 15.280%)
POM Gear without insert	-	3.660
POM Gear	0.548	4.208
w_x=0.788 mm	1.058	4.718 (+ 12.112%)
POM Gear without insert	-	3.708
POM Gear	0.500	4.208
w_x=0.675 mm	0.966	4.674 (+ 11.074%)
POM Gear without insert	-	3.803
POM Gear	0.405	4.208
w_x=0.450 mm	0.781	4.584 (+ 8.935%)

at the increase of bulk temperature at the gear body.

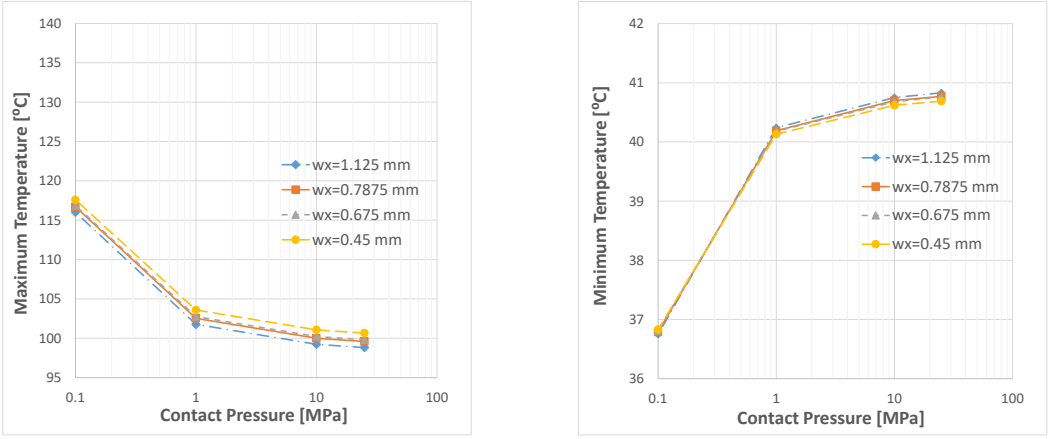

(a) Maximum temperature.

(b) Minimum temperature.

Figure I.9.: Maximum and minimum temperature for each insert width for a Double t-profile I for the tested contact pressures.

Tables I.11 and I.12 with the absolute values of minimum and maximum temperature for each insert width for each contact pressure and the percentages increment compared to the initial gear mode, respectively. Noticing that the insert width does not have a major impact over the maximum temperature or minimum temperature for a Double T-profile I, since the maximum and minimum temperatures for 1.125 mm width only differs from 0.450 mm width 2%. However, when the insert is thinner the maximum temperature increases and the minimum temperature decreases as it was concluded from the first studies.

Since the temperature results stay in the same range about 28% (reducing from 140°C to 101°C) for maximum temperature decrease and the minimum temperature increases 83% (rising from 22°C to 41°C) choosing the lower width (0.450 mm) the increment of weight of a gear tooth by the addiction of this insert type can be decrease by half (approximately 16% to 8%), reducing the inertia of the final gear.

Table I.11.: Maximum and Minimum temperature for each insert width for a Double T-profile I.

Temperature evaluation					
Width		**Contact Pressure**			
		0.1 MPa	1 MPa	10 MPa	25 MPa
w_x=**1.125 mm**	max(°C)	116.01	101.77	99.23	98.82
	min(°C)	36.75	40.24	40.75	40.83
w_x=**0.788 mm**	max(°C)	116.70	102.53	100.00	99.59
	min(°C)	36.79	40.19	40.70	40.77
w_x=**0.675 mm**	max(°C)	116.87	102.76	100.23	99.82
	min(°C)	36.81	40.18	40.68	40.75
w_x=**0.450 mm**	max(°C)	117.60	103.59	101.07	100.66
	min(°C)	36.83	40.13	40.62	40.69

Table I.12.: Percentage of temperature for each insert width for a double T-profile I.

Increment of temperature					
Width		**Contact Pressure**			
		0.1 MPa	1 MPa	10 MPa	25 MPa
w_x=**1.125 mm**	max(%)	- 16.76	- 26.99	- 28.82	- 29.11
	min(%)	64.95	80.61	82.90	83.26
w_x=**0.788 mm**	max(%)	- 16.28	- 26.45	- 28.26	- 28.56
	min(%)	65.13	80.39	82.68	82.99
w_x=**0.675 mm**	max(%)	- 16.16	- 26.28	- 28.10	- 28.39
	min(%)	65.22	80.34	82.59	82.94
w_x=**0.450 mm**	max(%)	- 15.64	- 25.69	- 27.50	- 27.79
	min(%)	65.31	80.12	82.32	82.63

I.2.5. Influence of vertical width (vw) on the Double T-profile I

As the effect of the expansion was studied on the previous section, it is importance to study the influence of the vertical width over the bulk temperature results.

The 2D model with the geometrical parameters of w_x=1.125 mm, t=2.25 mm and e=0 mm. However studying for a vertical width (vw) of 0.450 mm, as shown at Figures I.10a (the 2D cut of insert model created) and I.10b (3D global hybrid-gear model generated), and for a vw = 1.125 mm.

Influence on tooth weight

As shown in Table I.13 choosing a thinner insert at the vertical "platforms" will reduce by 2% of total weight when comparing with the previous case.

Tooth temperature results

Tables I.14 and I.15 list the temperature results for each vertical width studied at each contact pressure and the percentage increment over the temperatures results when comparing with the temperature results of the initial gear, respectively.

So, concluding when increasing the vertical width of the two "platforms" the maximum temperature will decrease, as shown in Figure I.11a, having a maximum

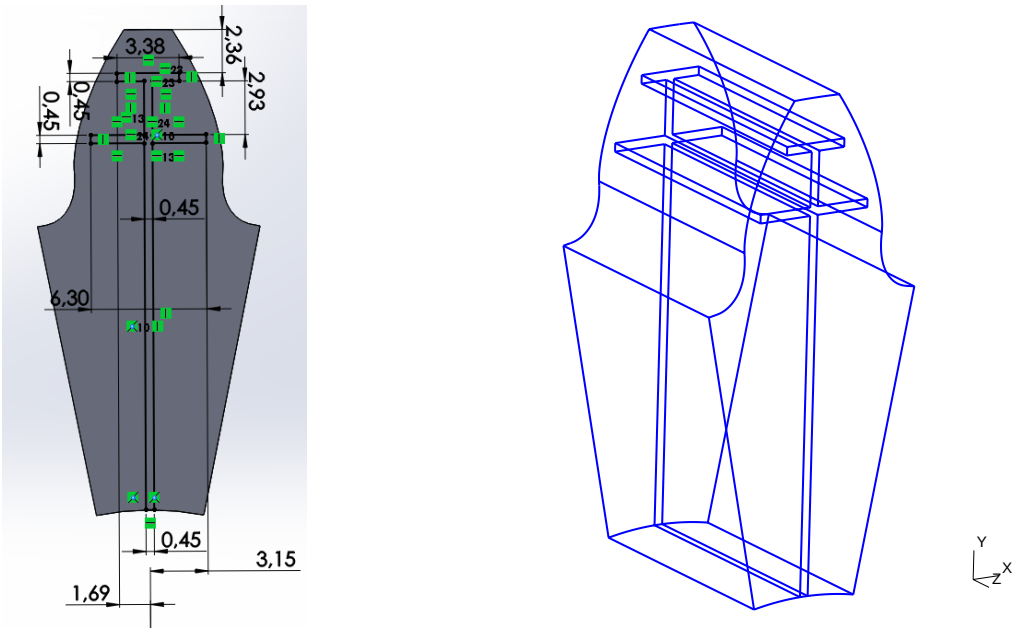

(a) Double T-profile I - cut dimensions.

(b) 3D model of Double T-profile I.

Figure I.10.: Dimension of the Double T-profile I 0.450 mm vertical width and its hybrid-gear 3D model.

Table I.13.: Mass evaluation for each vertical width on a Double T-profile I.

Weight evaluation		
Vertical Width	Insert Weight [g]	Total Weight [g]
POM Gear without insert	-	3.803
POM Gear	0.405	4.208
vw=1.125 mm	0.781	4.584 (+ 8.935%)
POM Gear	-	3.920
POM Gear	0.288	4.208
vw=0.450 mm	0.555	4.475 (+ 6.345%)

reduction over the maximum temperature of 28% (decrease from 140°C to 101°C) when *vw* is 1.125 mm and 26% (decrease from 140°C to 103°C) when *vw* value of 0.450 mm. The opposite happens when talking of the minimum temperature, where the increment of the minimum temperature is lower at a thinner insert, as seen in Figure I.11b, having a increasing of 80% for a vertical width of 0.450 mm and 83% for a *vw* of 1.125 mm.

Figure I.12, representing the global temperature result for the initial gear and for both of the vertical width at a Double T-profile I (Figures I.12a, I.12c and I.12e) as well as the a temperature distribution over a insert section (Figures I.12b, I.12d and I.12f) it becomes clear the impact of the vertical width at the final result. This is, observing the mesh surface at the global temperature result the maximum

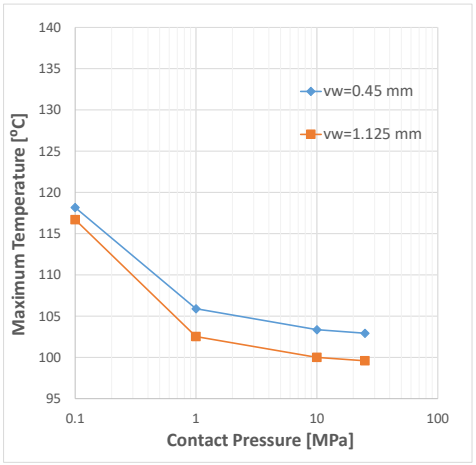

(a) Maximum temperature.

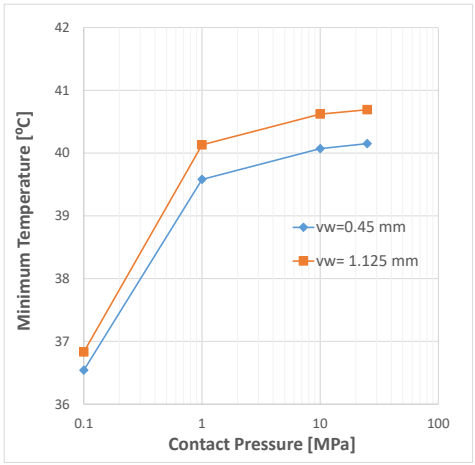

(b) Minimum temperature.

Figure I.11.: Maximum and minimum temperature for each vertical width for a Double T-profile I for the tested contact pressures.

Table I.14.: Maximum and Minimum temperature for each vertical width for a Double T-profile I.

Temperature evaluation					
Vertical Width		**Contact Pressure**			
		0.1 MPa	1 MPa	10 MPa	25 MPa
***vw*=1.125 mm**	max(°C)	117.60	103.59	101.07	100.66
	min(°C)	36.83	40.13	40.62	40.69
***vw*=0.450 mm**	max(°C)	118.17	105.90	103.36	102.93
	min(°C)	36.54	39.58	40.17	40.15

temperature is higher at the thinner vertical width since the gradient is more reddish when comparing with a larger vertical width. However, both results reveal good behavior when compared to the initial case since the result is temperature is more equally distributed. Concluding that the higher vertical width is the best solution taking into account the thermal result and the weight influence.

Table I.15.: Percentage of temperature for each vertical width width for a double T-profile I.

Increment of temperature					
Vertical Width (*vw*)		**Contact Pressure**			
		0.1 MPa	1 MPa	10 MPa	25 MPa
***vw*=1.125 mm**	max(%)	- 15.64	- 25.69	- 27.50	- 27.79
	min(%)	65.31	80.12	82.32	82.63
***vw*=0.450 mm**	max(%)	- 15.23	- 24.03	- 25.85	- 26.16
	min(%)	64.00	77.65	79.85	80.21

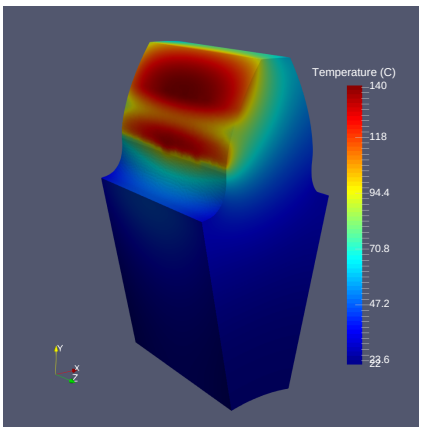

(a) Temperature without insert (T_{max}=139.40°C and T_{min}=22.28°C).

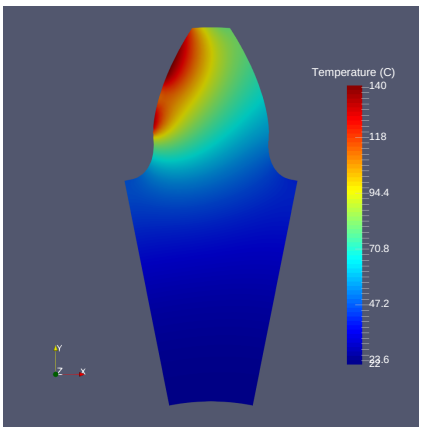

(b) Temperature cut without insert (T_{max}=139.40°C and T_{min}=22.28°C).

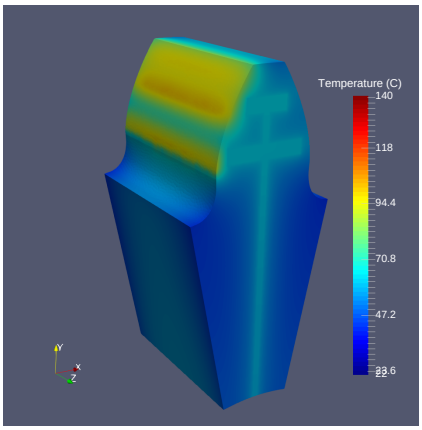

(c) Temperature result, vw=1.125 mm (T_{max}=100.66°C and T_{min}=40.69°C).

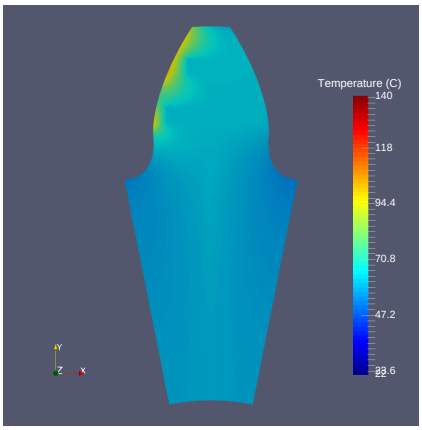

(d) Temperature result insert, vw=1.125 mm (T_{max}=100.66°C and T_{min}=40.69°C).

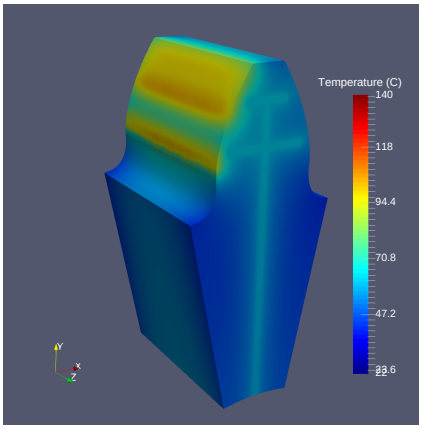

(e) Temperature result, vw=0.450 mm (T_{max}=102.93°C and T_{min}=40.15°C).

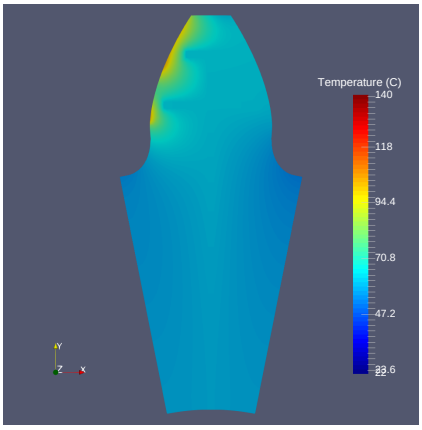

(f) Temperature result insert, vw=0.450 mm (T_{max}=102.93°C and T_{min}=40.15°C).

Figure I.12.: Temperature distribution for a normal gear and two hybrid gears, Double T-profiles I with 1.125 and 0.450 mm of vertical width at 25 MPa.

I.3. Involute profile

Influence on tooth weight

The weight evaluation at the shown in Table I.16 reveals that the difference between both profiles is negligible, being the cup profile 0.3% lighter than the Double T-profile

Tooth temperature results

Figures I.13a and I.13b show that the maximum temperature as almost negligible effect in terms of absolute value, although in terms of minimum temperature the results obtained by the involute profile are unfavorable when comparing to the Double T-profile I.

Table I.16.: Mass evaluation for a double T-profile and a involute profile.

Weight evaluation		
Insert type	Insert Weight [g]	Total Weight [g]
POM Gear without insert	-	3.803
POM Gear	0.405	4.208
Double T-Profile I	0.781	4.584 (+ 8.935%)
POM Gear without	-	3.818
POM Gear	0.390	4.208
Involute profile	0.752	4.570 (+ 8.603%)

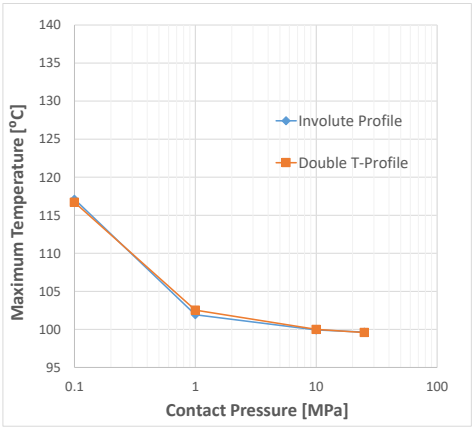

(a) Maximum temperature.

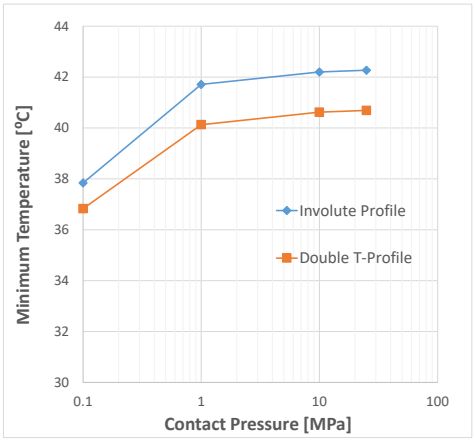

(b) Minimum temperature.

Figure I.13.: Maximum and minimum temperature for a double t-profile and a involute profile for the tested contact pressures.

Tables I.17, representing the absolute value of the minimum and maximum temperature for each profile at the tested contact pressure, and I.18, representing the percentages increments of minimum and maximum temperature when comparing with the initial gear, reenforce the above conclusions.

Since the implementation of the involute profile lead us to a reduction of maximum temperature of 27.79% (140°C to 100°C) instead of the 28.32% (140°C to 101°C) for the Double T-profile. However, when using a cup profile the minimum temperature increases from 82.63% (22°C to 40°C) to 89.72% (22°C to 41°C).

Moreover, Figures I.14b, I.14d and I.14f, representing the temperature distribution over the cut through the insert, show that with the implementation of the insert the bulk temperature will increase and more evenly distributed when compared with the initial gear. However, the temperature distribution over the new profile is more well distributed than the double T-profile.

Figures I.14a, I.14c and I.14f, show that the meshing surface temperature was clearly decreased supported by the brighter color marking the temperature decrease. It is curious to notice that the maximum temperature location for each profile is different, being at the tip of the tooth for the double T-profile and at the root of the tooth for the involute profile.

Table I.17.: Maximum and Minimum temperature for a double T-profile I and a cup profile.

Temperature evaluation					
Insert type		**Contact Pressure**			
		0.1 MPa	1 MPa	10 MPa	25 MPa
Double T-profile I	max(°C)	117.60	103.59	101.07	100.66
	min(°C)	36.83	40.13	40.62	40.69
Involute profile	max(°C)	117.11	101.93	99.93	99.64
	min(°C)	37.84	41.71	42.20	42.27

Table I.18.: Percentage of temperature for a double T-profile I and a involute profile.

Increment of temperature					
Insert type		**Contact Pressure**			
		0.1 MPa	1 MPa	10 MPa	25 MPa
Double T-profile I	max(%)	- 15.64	- 25.69	- 27.50	- 27.79
	min(%)	65.31	80.12	82.32	82.63
Involute profile	max(%)	- 15.99	- 26.88	- 28.31	- 28.32
	min(%)	69.84	87.21	89.41	89.72

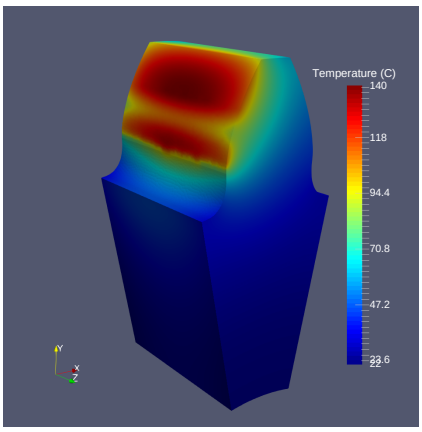

(a) Temperature without insert (T_{max}=139.40°C and T_{min}=22.28°C).

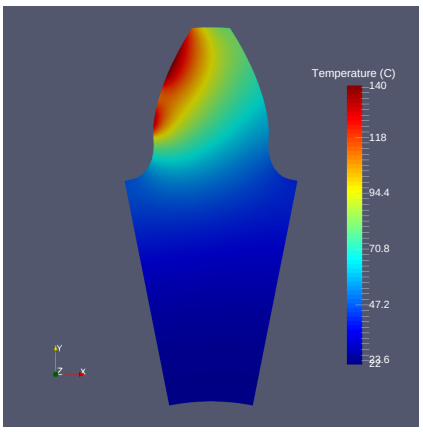

(b) Temperature cut without insert (T_{max}=139.40°C and T_{min}=22.28°C).

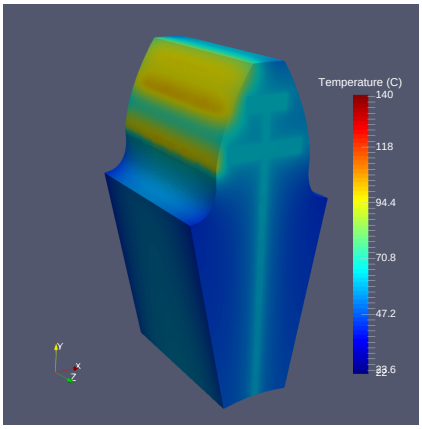

(c) Temp. result - Double T-profile I (T_{max}=100.66°C and T_{min}=40.69°C).

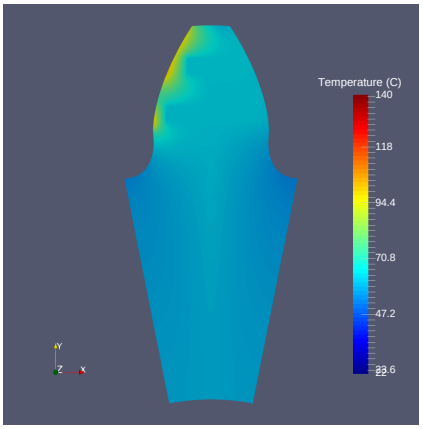

(d) Temp. result insert - Double T-profile I (T_{max}=100.66°C and T_{min}=40.69°C).

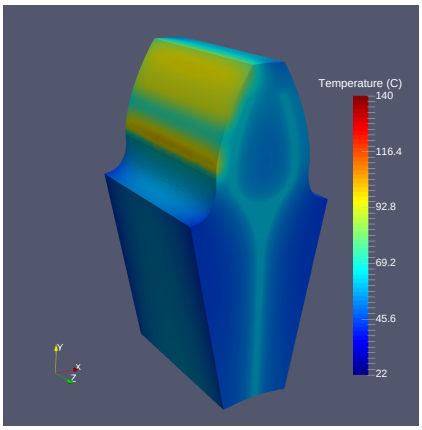

(e) Temperature result - involute (T_{max}=99.64°C and T_{min}=42.27°C).

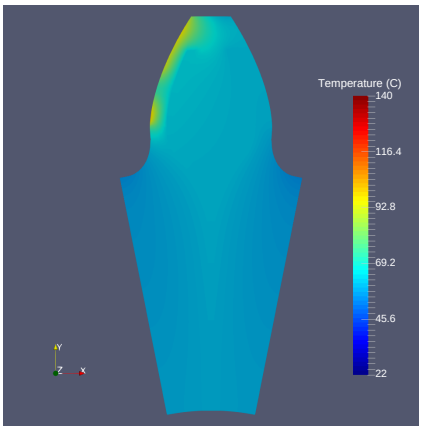

(f) Temperature result insert - involute (T_{max}=99.64°C and T_{min}=42.27°C).

Figure I.14.: Temperature distribution for a normal gear and two hybrid gears, double T-profile I and involute profile at 25 MPa.